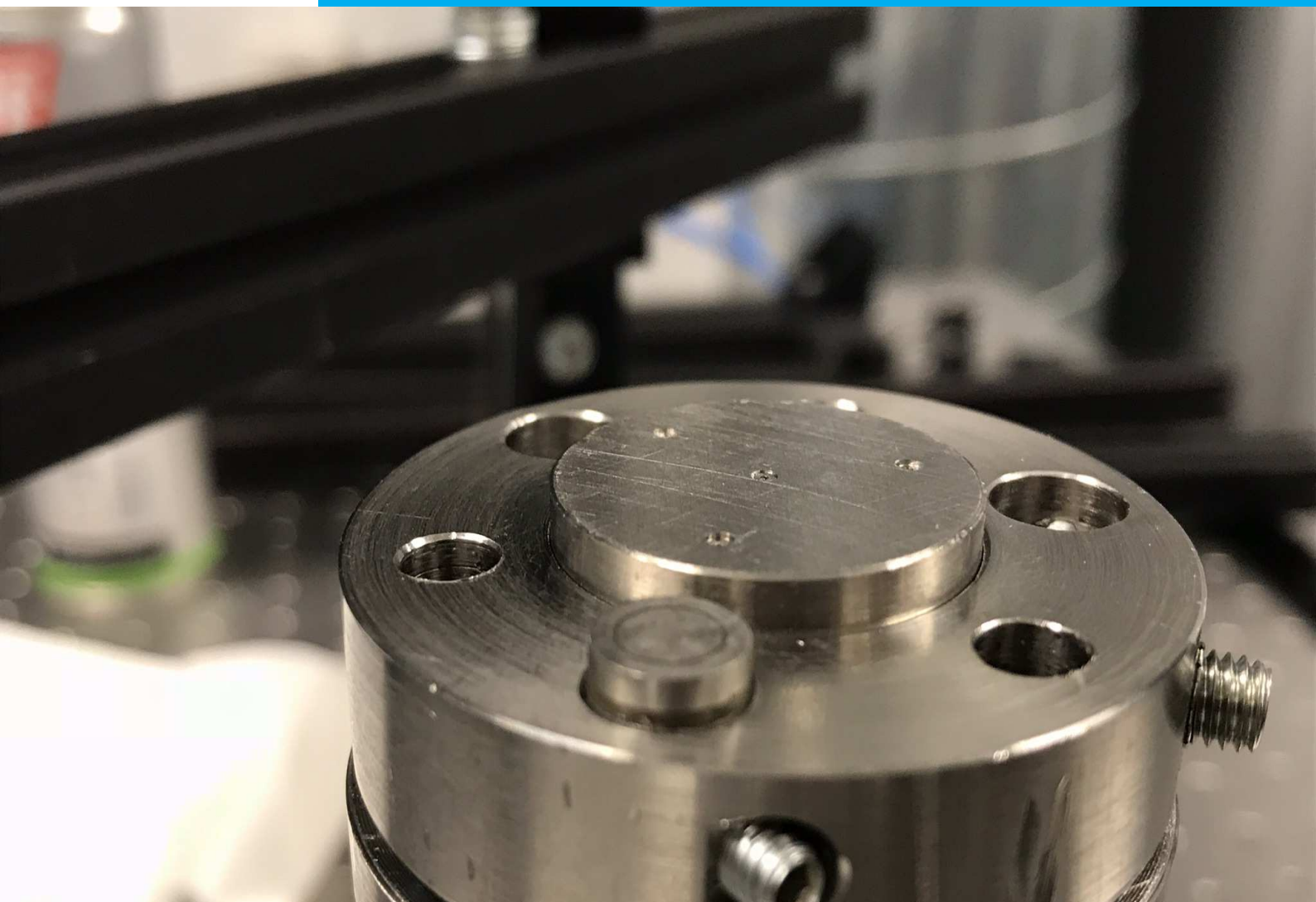


## Department of Precision and Microsystems Engineering

### Fundamentals of low-transmissibility aerostatic pads

Jeroen de Boom

Report no : 2019.030  
Coach : Dr. ir. R.A.J. van Ostayen  
Professor : Dr. ir. R.A.J. van Ostayen  
Specialisation : Mechatronic System Design  
Type of report : Master Thesis  
Date : 30th August 2019





# Fundamentals of low-transmissibility aerostatic pads

by

J. de Boom

to obtain the degree of Master of Science  
at the Delft University of Technology,  
to be defended publicly on Monday September 16, 2019 at 13:00.

Student number:	4143183	
Supervisor	Dr. ir. R.A.J van Ostayen	
Thesis committee:	Dr. ir. M. Langelaar,	TU Delft
	Ir. S.G.E. Lampaert,	TU Delft

*This thesis is confidential and cannot be made public until September 16, 2021.*

An electronic version of this thesis is available at <http://repository.tudelft.nl/>.



# Abstract

Air bearings are known for their low friction losses, constant viscosity and cleanliness, making them favourable in numerous high-tech applications. The relatively low aerostatic bearing stiffness, is topic in state of the art research. Some recently proposed concepts [8][29], are able to create infinite stiffness. This results in a strong coupling between the base and flying mass, enabling, unwanted propagation of base vibrations.

The initial idea of a zero-stiffness bearing, is proposed in [21], to reduce the thin-film coupling and transmission of base vibrations. The study, presents the concept of combining high- and low pressure aerostatic pads, to obtain a *static* low-stiffness design, see figure 1. Base vibrations are resulting in fly height perturbations, indicated with  $\Delta h$ . The low-stiffness fly height range, should cover the vibration's amplitude  $\Delta h$ , to be most effective. The concept of integrating the *passive* vibration isolation and bearing function, shows potential but needs further research.

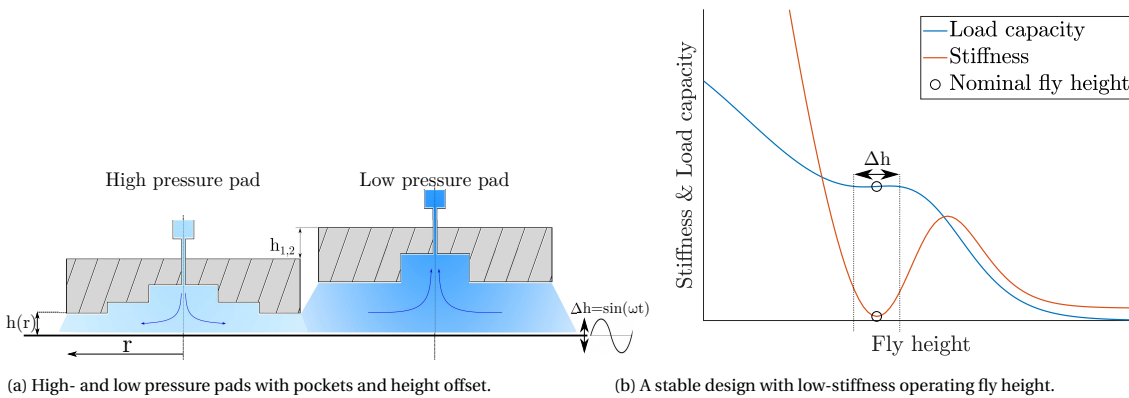
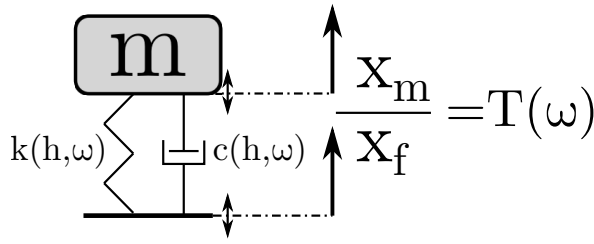
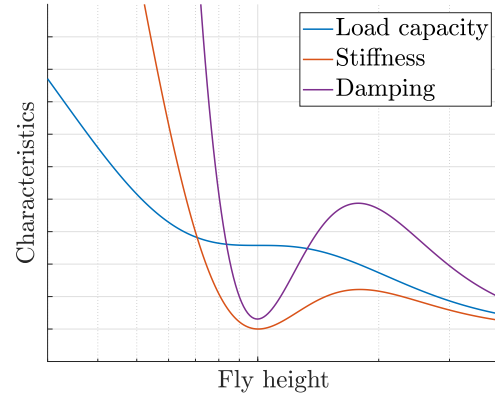


Figure 1: With a combination of a high- and low pressure pads, a stable low-stiffness bearing can be found.

The aim of this research is to optimise and validate the low-stiffness concept and to study the effect, of the *static* and *dynamic* pad characteristics, on the transmissibility function. A 2D numerical model, based on the compressible Reynolds equation is developed and different inlet-restriction flow models are studied. The flow characteristics of *standard* blunt syringe needles are measured and fitted with the laminar capillary flow model, which is valid for small pressure gradients. Then, the method of linear perturbation is implemented, to find the frequency dependent stiffness and damping characteristics of the aerostatic pads. The thin air film is represented by a single *nonlinear* mass-spring-damper, as shown in figure 2a. The stiffness and damping are linearised at the nominal fly height and the transmissibility function  $T(\omega)$  is found. The analysis, shows the importance of minimising *both* stiffness & damping to reduce  $T(\omega)$ . These findings are used to set-up a parametric optimisation to minimise stiffness & damping, while ensuring stability.



(a) The thin air film as shown in figure 1a, can be represented by a mass and non-linear spring and damper elements. The transmissibility at nominal fly height and a range of perturbation frequencies, is given by  $T(\omega)$ .



(b) Optimised design characteristics of a combined shallow-pocket and height-offset concept.

Figure 2: The lowest thin-film transmissibility is found when both stiffness & damping are minimised.

The optimised design, combines a relatively deep restriction-pocket, shallow-pocket and a pad height offset  $h_{1,2}$ . The characteristics at a low perturbation frequency, are given in figure 2b. It is found essential, to align the low- stiffness and damping operating fly heights, to maintain positive damping at increasing frequencies. This design has a low transmissibility, which can be improved, by further lowering the stiffness and damping. The influence of small design variations and displacement non-linearity, on: stiffness, damping and transmissibility, are studied in a sensitivity analysis. It is shown that small design perturbations in pressure, restriction conductivity or geometry, leads to relatively large stiffness and damping variations. These variations generally increase the thin-film transmissibility, furthermore, it is shown that further optimisation, leads to increased sensitivities, especially at low frequencies.

Measurements of a low-stiffness demonstrator are desired, to prove the concept of combining high- and low aerostatic pads and validate the model. Air bearings are known for their tight manufacturing tolerances, regarding surface waviness and restrictor mass flow. Different air bearing manufacturing methods are investigated, to create shallow surface pockets in a flat substrate. The shallow-pocket features can be created in a single plane, so there is no need to align different pads within micrometre precision. The shallow-pockets are etched in a thin polymer layer, which is spin-coated on a flattened stainless steel substrate. Shallow features are created with oxygen plasma- or wet etching in combination with a soft PDMS mask.

Manufacturability constraints are added to the optimisation procedure and a tip-tilt stable low-stiffness design is found. The design has one vacuum outlet surrounded by three inlets, see figure 3. The fly height is measured with three capacitive sensors, while continuously increasing the bearing load, under a changing inlet pressure. The measurements of the 'normal' bearing without shallow-pockets, are in agreement with the model. However, the shallow-pocket bearing, did not meet the required surface- and shallow-pocket manufacturing tolerances and a clear low-stiffness characteristic is not shown.

To conclude, this research started with the objective to optimise and validate the low-stiffness concept. Furthermore, the influence of the dynamic thin-film characteristics on vibration transmissibility needed further research. It is shown that *both* damping and stiffness need to be minimised to reduce transmissibility. An optimised design is presented, which shows challenging sensitivities. A demonstrator is manufactured with investigated techniques, validating the numerical model but it does not show a clear proof of the low-stiffness concept. A low-transmissibility aerostatic bearing is possible, but challenges need to be overcome.

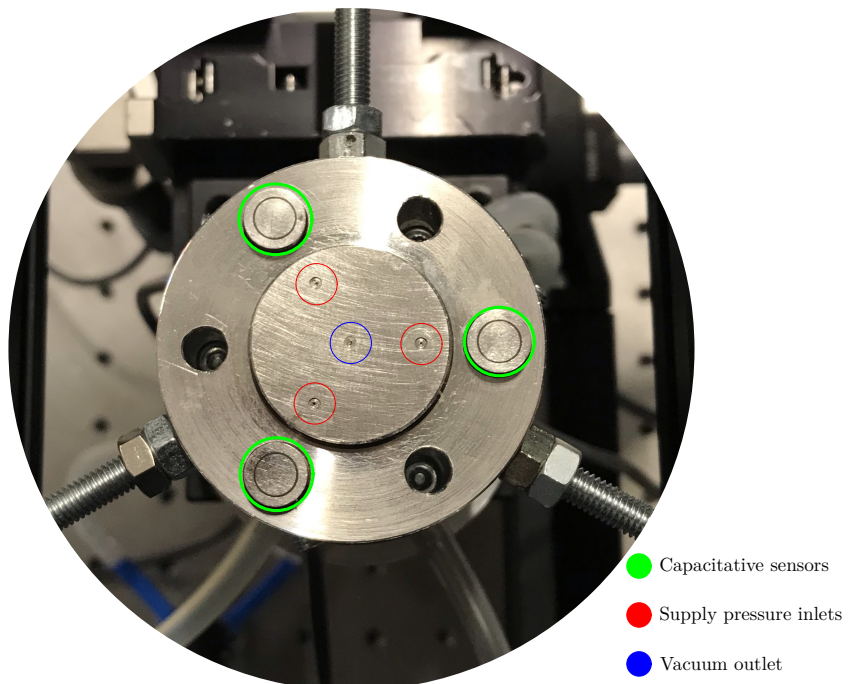


Figure 3: The tip-tilt stable shallow-pocket bearing with one vacuum outlet surrounded with three supply pressure inlets. The bearing is inside a sensor ring with three capacitive sensors, relative motion between ring and sensors, enables calibration.





# Preface

The results of my thesis study are presented in this report, which is the final stage of the Precision and Microsystems engineering master at the Delft University of Technology. It is already a while ago since I stopped by at Ron's office for the first time to discuss the concept of vibrations isolation in aerostatic bearings. I was appealed by the interesting combination of modelling, manufacturing and measuring and decided to accept the challenge. I started with the analysis of an existing linear air bearing stage to see if the proposed concept could be implemented directly. This idea turned out to be a bit too ambitious and the scope was narrowed. Within the research group we sometimes had discussions about the technology readiness levels (TRLs) of different projects. This scale starts at level 1 with basic research and ends in a working system at level 9. One of the things I noted during this thesis, is the fact that the path from level 1 to 9 is not necessarily monotonically increasing. I recon this is part of doing research, where answers often lead to new questions.

I would like to thank Ron for all his time and coaching during this project. I enjoyed our extensive discussions which often ended more than a few minutes too late. These meetings really helped to regain the energy to keep going and investigate new ideas. I especially appreciate your positivity and ability to find solutions when things got difficult. Your email response time is usually within 24 hours, even during weekends and holidays! Which is great.

Manufacturing this air bearing was a hard task and I would really like to thank the lab technicians Rob, Spiridon, Patrick and Harry and especially Wim from the workshop, for helping me with the measurement set-up and machinery. The weekly full-film meetings helped to get new ideas and to learn from each others work. I would like to thank Ron, Stefan, Joep and all students who attended these meetings. It was helpful to share an office with fellow graduation students to share ideas and coffee. Special thanks to Jelle, Niek, Roy, Kaz, Thomas, Ruben, Sarah, Bart, Savio, Ata, Lola, Abishek, Robert, Sander, Arjan and Korne, for all conversations and drinks. I would like to thank my family for supporting me all these years with advice and patience, I am sorry it took a while. Furthermore, I would like to thank all friends for putting things in perspective, special thanks to Tim and Dirk for proofreading parts of this report and mental support at our weekly dinners. Finally, I would like to thank Nikki for her patience and for listening to my often interesting, but sometimes boring thesis stories.

*J. de Boom*  
*Delft, September 2019*



# Contents

<b>1</b>	<b>Introduction</b>	<b>1</b>
1.1	Research context . . . . .	1
1.2	First principles . . . . .	1
1.3	State of the art . . . . .	2
1.3.1	Passive compensated air bearings . . . . .	3
1.3.2	Active compensated air bearings. . . . .	4
1.3.3	Discussion . . . . .	5
1.3.4	Low-stiffness bearing [21] . . . . .	5
1.4	Motivation . . . . .	6
1.5	Research objectives . . . . .	6
1.6	Contributions and thesis structure . . . . .	7
<b>2</b>	<b>Theory</b>	<b>9</b>
2.1	Thin-film modelling . . . . .	10
2.1.1	General Reynolds equation . . . . .	10
2.1.2	Perturbed Reynolds equation . . . . .	11
2.1.3	Dimensional analysis . . . . .	11
2.2	Restriction modelling and verification . . . . .	12
2.2.1	Capillary restriction . . . . .	13
2.2.2	Orifice restriction . . . . .	14
2.2.3	Syringe-needle flow modelling. . . . .	14
2.2.4	Validation . . . . .	16
2.3	Aerostatic bearing model . . . . .	17
2.3.1	Numerical model . . . . .	18
2.3.2	Analytical model and results . . . . .	19
2.4	Dynamics of aerostatic pads . . . . .	20
2.4.1	Transmissibility . . . . .	22
2.4.2	Stability . . . . .	24
2.4.3	2-pad analysis . . . . .	25
2.5	Conclusion . . . . .	28
<b>3</b>	<b>Optimisation &amp; Sensitivities</b>	<b>29</b>
3.1	Static optimisation . . . . .	29
3.1.1	Objectives and constraints. . . . .	30
3.1.2	Design variables . . . . .	31
3.1.3	Static optimisation results . . . . .	31
3.1.4	Combining shallow-pocket with height-offset . . . . .	34
3.2	Dynamic bearing characteristic . . . . .	34
3.3	Dynamic optimisation . . . . .	37
3.4	Transmissibility and stability . . . . .	39
3.5	Sensitivity analysis . . . . .	41
3.5.1	Design variable sensitivity . . . . .	41
3.5.2	Transmissibility sensitivity. . . . .	42
3.6	Conclusion . . . . .	42
<b>4</b>	<b>Manufacturing methods</b>	<b>45</b>
4.1	Manufacturing methods . . . . .	45
4.1.1	Materials. . . . .	46
4.1.2	Shallow-pocket manufacturing . . . . .	46
4.1.3	Surface topology . . . . .	48
4.1.4	Restrictor implementation. . . . .	48

4.2	Final recipe . . . . .	48
4.3	Conclusion . . . . .	51
<b>5</b>	<b>Design of a low-stiffness demonstrator</b>	<b>53</b>
5.1	Design . . . . .	53
5.2	Characteristics & tip-tilt stability . . . . .	54
5.3	Conclusion . . . . .	57
<b>6</b>	<b>Realisation &amp; validation</b>	<b>59</b>
6.1	Design realisation . . . . .	59
6.1.1	Bearing topology . . . . .	61
6.2	Experimental set-up . . . . .	63
6.3	Measurement procedure . . . . .	64
6.3.1	Challenges . . . . .	64
6.3.2	Measuring . . . . .	65
6.3.3	Post-processing . . . . .	65
6.4	Results . . . . .	66
6.4.1	Bearing without shallow pocket . . . . .	66
6.4.2	Shallow pocket bearing . . . . .	68
6.5	Conclusion . . . . .	70
<b>7</b>	<b>Conclusion</b>	<b>71</b>
<b>8</b>	<b>Towards the future</b>	<b>73</b>
<b>A</b>	<b>Reynolds equation</b>	<b>75</b>
A.1	Navier-Stokes equation . . . . .	75
A.2	Compressible Reynolds equation . . . . .	76
A.3	Solving the Reynolds equation . . . . .	78
<b>B</b>	<b>Restrictor measurements</b>	<b>81</b>
B.1	Measurement procedure . . . . .	81
B.2	Data processing G30 Measurement . . . . .	81
B.2.1	G30 measurement results . . . . .	83
B.2.2	G26 measurement results . . . . .	84
<b>C</b>	<b>General flow equations</b>	<b>87</b>
C.1	Laminar pipeflow equations . . . . .	87
C.2	Thin film flow . . . . .	88
<b>D</b>	<b>Extra dynamics single inlet bearing</b>	<b>89</b>
<b>E</b>	<b>Manufacturing</b>	<b>91</b>
E.1	Lathe . . . . .	91
E.2	Pulsed laser micromachining . . . . .	92
E.2.1	Stainless steel . . . . .	92
E.2.2	Silicon . . . . .	94
E.3	Oxygen plasma etching of Topas® . . . . .	100
E.3.1	Groove manufacturing . . . . .	101
E.4	Wet etching Si wafer . . . . .	103
E.5	Surface waviness . . . . .	105
E.5.1	Topas® sheets . . . . .	105
E.5.2	Reduce bearing area . . . . .	106
E.5.3	Flatten the Topas® bearing surface . . . . .	106
E.5.4	Find a counter surface with an exact opposite surface topology . . . . .	110
<b>F</b>	<b>Topas</b>	<b>113</b>
<b>G</b>	<b>Metrology specifications and settings</b>	<b>115</b>
	<b>Bibliography</b>	<b>119</b>

# Introduction

## 1.1. Research context

According to the Oxford dictionary: "A bearing is a part of a machine that allows one part to rotate or move in contact with another part with as little friction as possible". There is a large variety in bearing designs that uses different concepts in reducing friction between parts. A distinction is made between three principles: contact bearings, fluid interface bearings and non-contact bearing concepts. An overview is in figure 1.1. This report focusses on the design and manufacturing of linear aerostatic bearings.

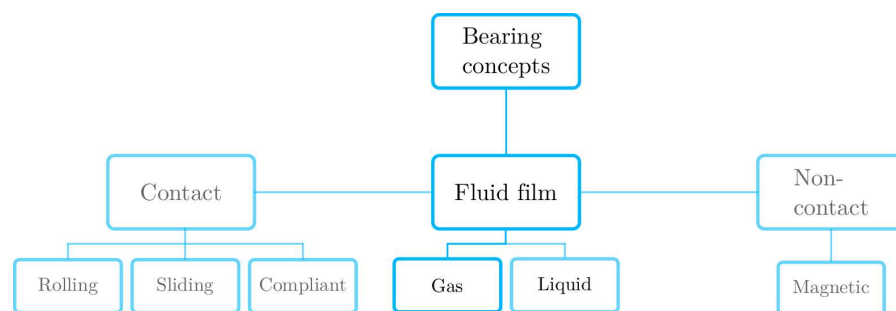


Figure 1.1: Overview of different bearing concepts.

Aerostatic bearings have major advantages when compared to contact bearings or fluid bearings that use oil or water as lubricant. One of the advantages is that air has very low frictional losses, this property makes air lubrication favourable in high speed precision machinery. Some other advantages are: hardly any change in viscosity over wide temperature ranges and air is an environmental friendly lubricant [18]. Some disadvantages are: the need of an external pressure source, lower stiffness and less load capacity compared to contact bearings and fluid bearings .

The concept of full film lubrication was first studied by Osbourne Reynolds in 1886 [37] after analysing experiments conducted by Mr. Tower. The experiments in [37] used oil as thin film lubricant. In 1897 Albert Kingsbury designed and built the first tilting pad externally pressurised air bearing [27]. During World War II, there was a demand for high precision, clean and maintenance free bearing systems [18]. From this time onwards more research has been done on gas-lubrication, resulting in numerous applications, for instance: precise positioning stages [38],[32], high speed spindles [16] and as basis in contactless position- and transportation systems [53],[43].

## 1.2. First principles

Before elaborating the state-of-the-art research, the fundamental principles of aerostatic bearings are briefly discussed. In figure 1.2 a simple single inlet axisymmetric aerostatic bearing is sketched. Air is fed into the system at a supply pressure  $P_s$ , the air is restricted before entering the thin film with film height  $h(r)$ . In this example a recess, also known as: pocket, is present at  $r < r_p$ . There is a pressure drop over the restriction,

pocket and thin film, until the pressure equals ambient pressure  $P_a$ . The feed pressure and geometry determine the bearing's characteristic. This characteristic can be expressed in terms of: load capacity, damping and stiffness.

When the external force is increased at a constant supply pressure  $P_s$ , the film height  $h$  decreases. This continues until the bearing- and external force reach equilibrium. The film height  $h$  can be increased by increasing the supply pressure  $P_s$ .

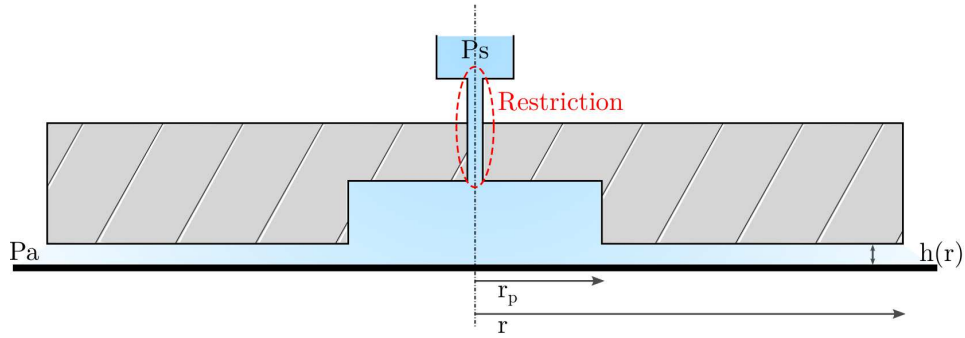


Figure 1.2: Simple single inlet axisymmetric aerostatic bearing.

### 1.3. State of the art

The starting point of a air bearing design, is often a static characterisation where the load capacity, stiffness and air consumption are expressed as function of fly-height. The static air bearing characteristic is mostly determined by the type of adopted feeding restrictor [35]. Consequently a lot of research, involving restrictor modelling is conducted. In [18]: the annular- and simple orifice [11] [13], slot [56], groove [57] and porous [9] restrictor types are discussed and compared. The state-of-the-art restriction research is focussed on combining different restrictor types, creating a compound restriction[18]. Combining the orifice-type and groove restrictor enhances tilt stiffness [49] [48] and therefore, reduces instability in high speed applications [45].

Once the static design meets the requirements, the dynamic properties are characterised. A common dynamic behaviour of aerostatic pads is an instability known as 'pneumatic hammer'. This phenomenon originates from the incompressibility of air, causing a phase delay between bearing clearance and the thin-film pressure variation [46]. Numerous methods in studying the pneumatic hammer instability have been developed [18]. Although quite some research has been done regarding this topic there are still a lot of unknowns. Especially when optimisation algorithms are used to optimise static bearing characteristics, the pneumatic-hammer likelihood seems to increase [8].

When new air bearing concepts are proposed in literature, the goal in general is to achieve high stiffness and sufficient damping. High stiffness causes a strong coupling between bearing and counterpart and eliminates low resonance frequencies. Higher stiffness can be achieved by using actively compensated air bearings. These type of bearings are able to compensate for a change in load or fly-height, resulting in an increased stiffness. An overview of active- and passive compensation methods is presented in [35]. Some of these concepts and their working principles are discussed, to give insight in existing air bearing techniques.

### 1.3.1. Passive compensated air bearings

Passive compensated air bearings have been developed since the 1970's [39]. In passive compensated air bearings, no energy is added to the system other than the external supply pressure. Furthermore, there is no need to implement sensors, resulting in lower costs and easier system integration. Different methods to increase bearing stiffness in a passive way have been developed. The concepts can be classified in three categories: 'flow resistance compensation' and 'geometrical compensation' or a combination of these two [35].

- A compliant membrane bearing surface [20],[44], [12] '*geometrical compensation*'
- X-shaped grooves combined with a spring [14] '*flow resistance compensation*'
- Elastic orifice [33] '*flow resistance compensation*'

Compliant membrane bearing surface.

An air bearing with a conically shaped airgap is often used as initial design for a compliant air bearing surface. A conical airgap has a higher load capacity and stiffness than bearings with parallel airgaps [44]. In [20], the fundamentals of using a flexible membrane are explained. High stiffness is achieved by increasing the slope of the load vs fly-height curve, see figure 1.3 by [20]. At nominal fly-height  $H_1 = b$  the airgap is parallel. When the 'static' bearing load increases, the fly-height tends to decrease, resulting in a higher film pressure. The increased film pressure pushes the membrane into a more convergent gap shape *a*. Both the increased pressure and the conical gap shape result in an increased load carrying capacity, without decreasing the gap height. During the membrane deformation, the inlet aperture is changed in an advantageous way, enhancing infinite stiffness. The compliant bearing developed by [44], is based on the same principles.

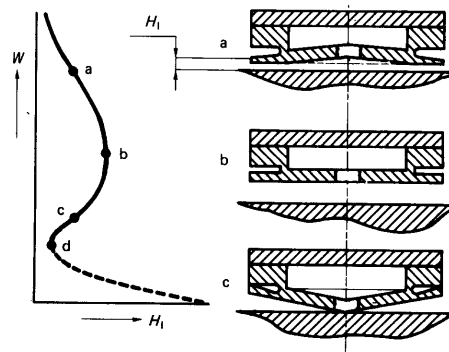


Figure 1.3: Deformable bearing pad with deformed positions: *a*, *b*, *c* drawn at right-hand side (from [20]).

X-shaped grooves combined with disk spring compensator.

This concept [14] uses a disk-spring to compensate changes in bearing load. The air-film- and spring pressures are in equilibrium, by means of a communal gas chamber, see figure 1.4. When the bearing load increases, the airgap tends to decrease. This causes a higher film pressure, which is compensated through the communal chamber by the disk-spring. The spring's reaction force restores the nominal fly-height after a load perturbation. In [14] the impulse response is studied, concluding that vibrations are reduced when using the compensated bearing.

Elastic orifice.

The orifice is normally a static element, relating pressure gradient and mass flow. In [33] compliant orifices are discussed. The orifice will deform as a result of pressure change inside the bearing pad. This results in higher flow in low airgaps and a decreased flow for larger airgaps. This passive orifice compensation can significantly improve air bearing stiffness. A downside is the low dynamic stability and the introduction of oscillations.

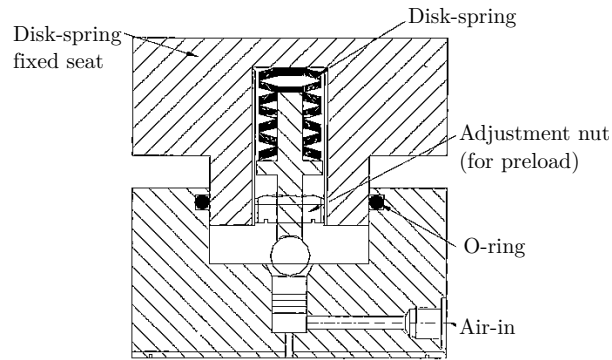


Figure 1.4: X-shaped groove aerostatic bearing with disk spring compensator (from [14])

### 1.3.2. Active compensated air bearings

The passive compensated air bearings are easy to integrate and have higher stiffness than standard air bearings. However, they can only reach infinite stiffness for maximum 20% of the load range and they have a relative low dynamic range, resulting in low system bandwidth [35]. Compensated air bearings can be further improved by implementing active components. Active compensated air bearings can be classified in the same three categories as passive compensated bearings. In [35] a further sub-categorisation is proposed by means of actuation type. An active system uses: external transducers, actuators and a controller, to control the airgap after a load perturbation. This increases the dynamic range and accuracy but leads to higher costs compared to passive systems. An extensive review study, discussing the state-of-the-art active compensation methods has been done by Raparelli in 2015 [35], therefore only the latest papers and most promising systems are discussed.

Hybrid compensation systems.

Most active compensation research is focussed on active flow resistance compensation methods. These active flow controlling components are placed upstream, inside the airgap or at an exhaust. When actuating the flow resistance, the pressure distribution inside the airgap is adjusted, compensating load variations. In [35] numerous concepts are discussed that use active flow resistance control. The main limitation in this type of active bearing control, is the limited bandwidth caused by the latency in response [8]. The dynamic performance can be improved by using active geometrical compensation, by means of conicity control. A hybrid active compensated air bearing is proposed and designed by A.L. Bender et al. [4],[8], [5]. The active bearing in figure 1.5 shows resemblance with the earlier discussed passive system in figure 1.3. However, the passive compliant membrane is replaced by a thin plate. The active conicity controlled system in [5] uses piezoelectric-stack actuators to deform the thin plate bearing surface.

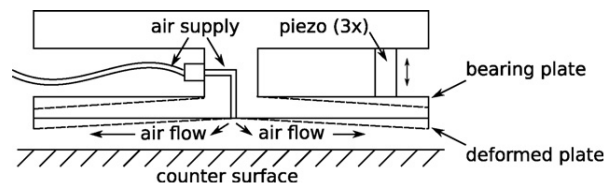


Figure 1.5: Active conicity controlled aerostatic bearing (from [5]).

In [8], the figure 1.5 concept is extended with pressure control and support control, to create a high bandwidth (300Hz) active compensation system. The implementation of PID control enables correction of small disturbances at high bandwidth. Furthermore, the system is able to follow a prescribed reference path, with minimal tracking error. 'This active bearing system is particularly suited for high performance ultra-precision positioning applications.'

The active compensation systems that are discussed in [35] including [8], need gap sensing. The performance of these systems rely on the resolution and linearity of the position sensor. In [29] an active aerostatic bearing with conicity actuation is presented, see figure 1.6. The active pad is actuated with Lorentz actuators



and controlled in closed loop without measuring the airgap. Instead the conicity is measured and the airgap and load capacity are calculated, using an iterative algorithm. This method requires a high level of open loop system identification to obtain a correct prediction. This concept has infinite static stiffness while maintaining the ability for macro positioning. The dynamic response of this system is not analysed yet, but will be in future research.

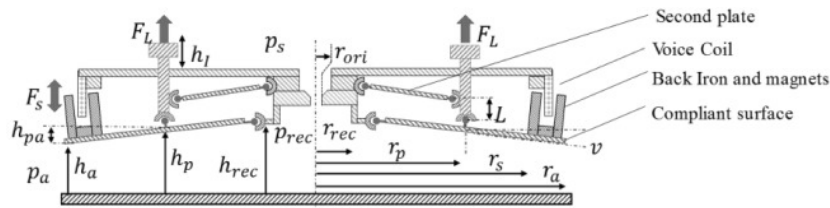


Figure 1.6: Active conicity controlled aerostatic bearing without airgap measurement (from [29]).

### 1.3.3. Discussion

Active compensation methods are a topic of latest research projects. These systems use concepts from the field of mechatronics, combined with air bearing research. The active systems are able to obtain infinite stiffness and high load capacity for wide loading range. The most advanced and complex system ([8]) is able to follow a prescribed (out-of-plane) trajectory. This is the only system that is able to compensate unwanted vibrations at high bandwidth. All other active (flow resistance) compensated bearing systems, are not capable of correcting a dynamic disturbance. Low bandwidth is caused by latency, which is inherent in flow controlled systems. The purpose of these active systems is to create an extremely stiff, out-of-plane connection between moving parts.

These types of bearings are used in high precision application like measuring instruments or precise positioning systems. External vibrations that are present at the machine's base, propagate through the system's stiff connections. In practice these systems are placed on top of active vibration isolation tables like [58], to eliminate vibrations before they enter the machine. Moving machine parts are a new source of undesired vibrations, that propagate to a point of interest. In general, vibration isolation needs to be placed as close as possible to the point of interest, to be most effective. Combining the bearing- and isolation function, can be promising and opposes current research, which mainly focuses on infinite stiff bearing connections. There is only one scientific report about creating less coupling between the surfaces in linear aerostatic bearings, written by R.P. Hoogeboom [21].

### 1.3.4. Low-stiffness bearing [21]

The integration of vibration isolation- and bearing function is proposed and studied in [21]. A time efficient numerical model is developed to compute the static and dynamic characteristics of axisymmetric bearing pads. It was decided to focus on minimising the static stiffness, using the developed numerical model. Manual optimisation resulted in a stable low-stiffness design with 'regular' damping at low frequencies. The manufacturing of this optimised design proved to be rather difficult and the low-stiffness bearing model could not be validated with measurement data. Instead, a bearing with normal stiffness and damping is tested, validating part of the model. From this work it is concluded that it is theoretically possible, to design a bearing with a stable low-stiffness operating point. This is done by combining a high- and low pressure pad, as shown in figure 1.7. The key elements in this design are: a shallow pocket, restricted in- and outlets, supply- and vacuum pressure and at last, a possible pad height offset.

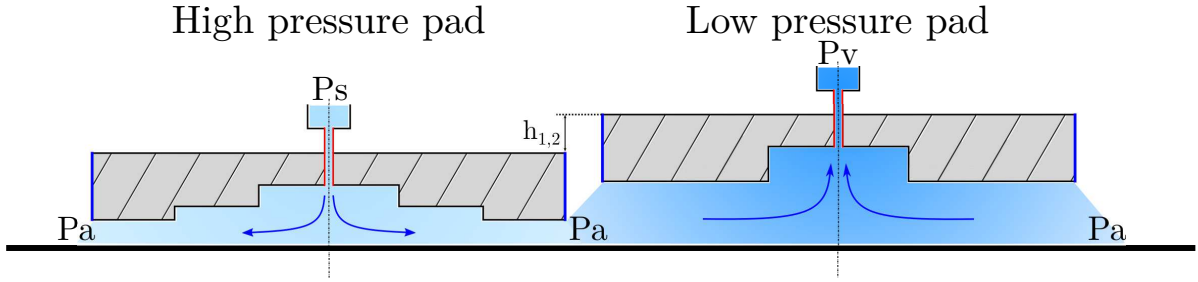


Figure 1.7: A combination of a high- and low-pressure pad with: height offset  $h_{1,2}$ , inlet- and outlet restriction and pockets. This type of design is proposed in [21] and enables a stable low-stiffness bearing characteristic.

## 1.4. Motivation

In figure 1.8 a schematic drawing of a linear stage is presented, the moving mass  $m$ , is supported by two aerostatic bearings. The bearings have a certain stiffness and damping characteristic in  $x$  direction, while planar friction is negligible, indicated by the frictionless rollers. The load carrying capacity of the bearings can be adjusted to compensate for small load misalignments. A disadvantage of this air bearing supported system, is the thin-film coupling between the floor and mass, which allows for the propagation of unwanted floor vibrations. These mass displacements  $x_m$  can be reduced by introducing active control elements, like the concepts in section 1.3.2. However, feedback controlled systems require precise position sensing and active bearing elements, making a passive or feed-forward controlled semi-active design favourable.

The thin-film transmission of floor vibrations, is a function of the frequency and fly-height dependent stiffness  $k(\omega, h)$  and damping  $c(\omega, h)$ . Minimising  $k(\omega, h)$  and  $c(\omega, h)$ , reduces thin-film coupling for a range of frequencies and vibration amplitudes ( $\Delta h$ ). A passive or semi-active feed-forward controlled system, is tuned *beforehand* and could be a straightforward vibration isolation concept, without the need of a real-time feedback control.

The linear stage in figure 1.8 is one of many possible applications. A single bearing element is indicated by the red circle.

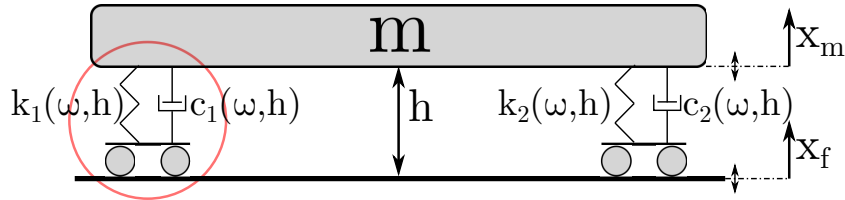


Figure 1.8: Schematic drawing of a linear stage supported with two aerostatic bearings represented by the 'non-linear' spring and damper elements  $k_{1,2}(\omega, h)$  &  $c_{1,2}(\omega, h)$ .

## 1.5. Research objectives

In this project the low-stiffness bearing concept is optimised and a demonstrator is build to verify the theoretical model. The existing low-stiffness air bearing fundamentals are expanded towards a low-transmissibility bearing design. This involves a study of the frequency dependent stiffness- and damping characteristics and their relation to the transmission of unwanted vibrations at different excitation frequencies. Summarising the objectives:

- *Optimise a stable zero-stiffness air bearing and build a demonstrator to validate this concept.*
- *Bridge the gap between the current low-stiffness bearing concept and the dynamic thin-film transmissibility.*

## 1.6. Contributions and thesis structure

The schematic overview in figure 1.9, presents the work done in this thesis project, the numbers correspond to the chapters. Two loops can be distinguished, the central design loop uses the numerical model to obtain the bearing pad characteristics, these are fed into the optimisation to improve the design. In the second loop, a final design is chosen and manufactured with the investigated methods, next experiments are done to validate the numerical model.

A numerical thin-film bearing model is set-up in chapter 2, using existing knowledge from literature. Different flow models from literature are combined with measurements and used to analyse a new type of inlet-restriction. In section 2.4, the dynamics of a two-pad aerostatic bearing concept are characterised and combined with the derived transmissibility function. Readers who are familiar with aerostatic bearing modelling, can go directly to section 2.4.

Chapter 3 focusses on the implementation of a parametric optimisation to find a stable design optimum. This chapter further elaborates on the dynamic stiffness and damping characteristics. A sensitivity study is presented, to analyse the effect of different design parameters on transmissibility.

In chapter 4, different bearing manufacturing methods are investigated and a final *manufacturable* design is presented in chapter 5. The optimised design is manufactured and integrated in a measurement set-up, to validate the theory in chapter 6.

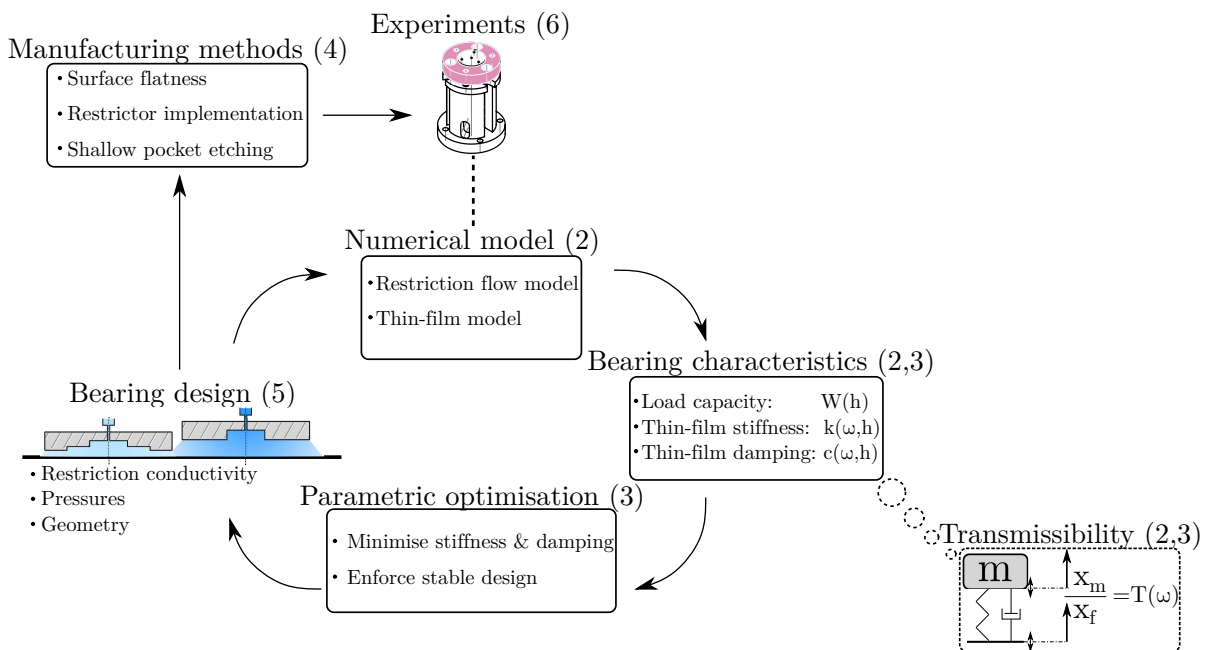


Figure 1.9: A schematic overview of all the treated topics in this thesis project. The arrows indicate the design and experimental validation loop. The numbers between the brackets, correspond to the report chapters.



# 2

## Theory

In the introduction, different state-of-the-art bearing concepts are discussed, concluding with the desire to build a low transmissibility thrust bearing. The current theory focusses on stiffness reduction by combining high- and low pressure pads in some stable configuration. The most basic, although, 'tip-tilt' unstable configuration with only two pads is depicted in figure 2.1. This chapter describes all theory that is needed to model these types of aerostatic bearing pads. The supply- and vacuum pressures:  $P_v < P_a < P_s$ , create a pressure gradient, which causes an airflow through the bearing gap. The thin-film pressure is modelled with the Reynolds equation [37]. The pad's characteristics are a function of bearing geometry, a restriction model and boundary conditions. A single inlet axisymmetric high pressure pad, with a cascaded pocket, is used to discuss the theory, see figure 2.2. This 'simple' axisymmetric geometry allows for an analytic study, to verify the developed numerical model. The inlet/outlet restriction has a large influence on the pad's characteristics, therefore various restriction models will be discussed and compared with measurement data. At last the principles of vibration *transmissibility* are studied and combined with the two-pad bearing's dynamics.

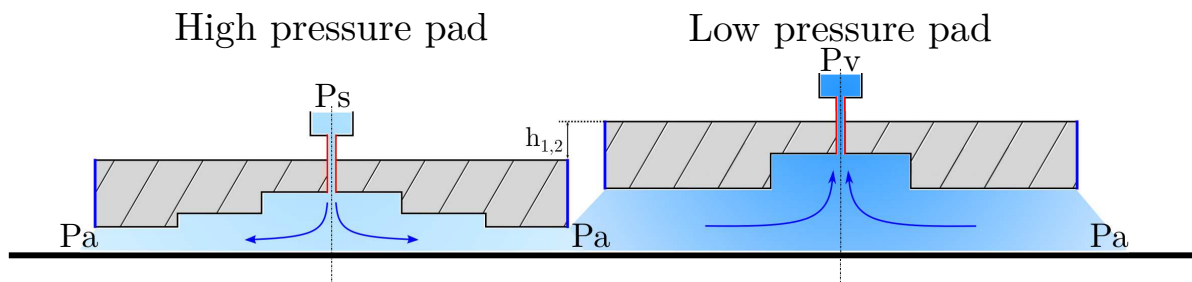


Figure 2.1: A combination of a high- and low-pressure pad with: height offset  $h_{1,2}$ , an inlet and outlet restriction and pockets. This type of design is proposed in [21] and enables a stable low-stiffness bearing characteristic.

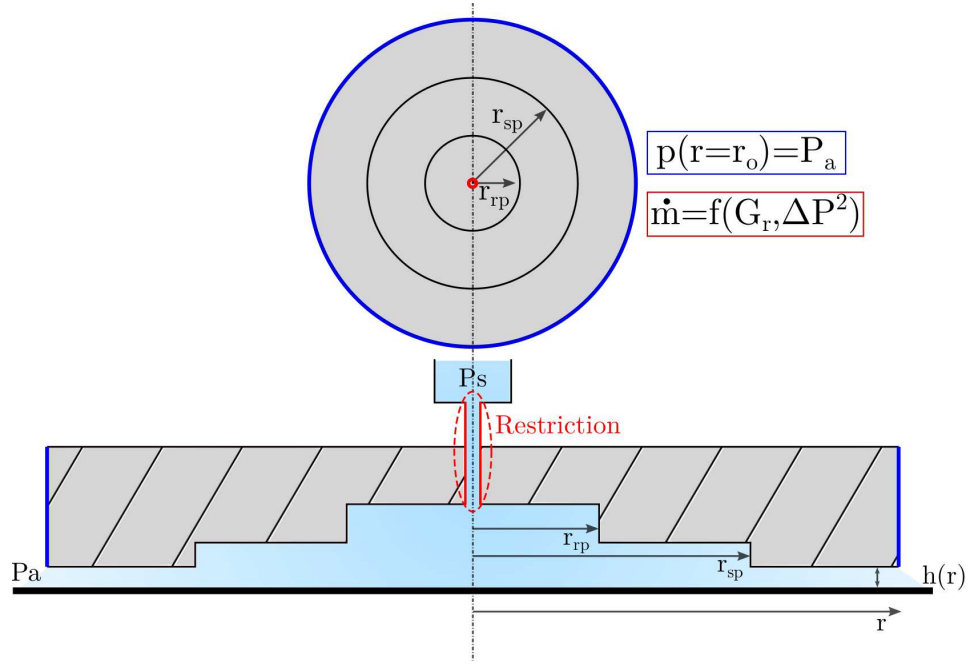


Figure 2.2: Top and side view of a single inlet axisymmetric aerostatic bearing, with a restriction-pocket  $r_{rp}$  and shallow-pocket  $r_{sp}$ . There are two boundary conditions: one Dirichlet B.C at the outer edge and the source term at the inlet, which is a function of quadratic pressure difference and restrictor properties.

## 2.1. Thin-film modelling

This section discusses the Reynolds equation and application in thin film aerostatic bearings. The Reynolds equation is used to calculate the pressure inside a thin film, bounded by two surfaces. The Reynolds equation can be derived from the Navier-Stokes equation or by writing down the force balance of a small volume element inside the thin film. In appendix A the derivation of the Reynolds equation is given and further elaborated in this section. The method of linear perturbation is used to obtain the dynamic bearing characteristics. At last the equations are made dimensionless to enhance numerical stability in future design optimisation.

### 2.1.1. General Reynolds equation

The compressible Reynolds equation in Cartesian coordinates is derived in appendix A under the following assumptions:

1. Constant viscosity.
2. Newtonian lubricant.
3. Thin film geometry, meaning a small film height compared to the film length, constant pressure over film height is assumed.
4. Body forces are neglected.
5. Laminar flow theory is applied, neglecting fluid inertial forces.
6. No slip at boundaries.
7. Air film is assumed to be isothermal.
8. Couette flow is neglected.
9. An ideal gas is assumed.

Rewriting the derived equation from appendix A yields the compact form compressible Reynolds equation. Where  $p$  stands for the pressure in the lubricating film,  $h$  the film height,  $\eta$  the air viscosity,  $R_s$  the specific gas constant,  $T$  the air film temperature and time  $t$ :

$$\underbrace{\nabla \left( \frac{h^3}{12\eta R_s T} p \nabla p \right)}_{\text{Poiseuille flow}} = \underbrace{\frac{1}{R_s T} \frac{\partial p h}{\partial t}}_{\text{Dynamic terms}} \quad (2.1)$$

This simplified Reynolds equation has a static part and a dynamic part represented by the Poiseuille flow and the dynamic terms respectively. No analytical solutions exist for this transient Reynolds equation and numerical solving methods are required. To find a solution for the dynamic part, the method of linear perturbation is used.

### 2.1.2. Perturbed Reynolds equation

A possibility is to use the method of linear perturbation to find the dynamic bearing characteristics. First a static solution is calculated, by using the static part of equation 2.1. Then the fly height and pressure are perturbed around this static equilibrium. The perturbed fly height and pressure in equation 2.2 are substituted in 2.1 to find 2.3. With the perturbed Reynolds equation 2.3, the perturbed pressure is found. The solution of the perturbed pressure and fly height is used to find the damping and stiffness of the air film. The subscript '0' indicates a static solution while the '~' represents the perturbed parameters. A complete derivation of the perturbed Reynolds equation is given in appendix A. The perturbed Reynolds equation is expressed in the frequency domain and shows a direct relation with perturbation frequency ' $\omega$ '. The stiffness is a function of the real part of the perturbed pressure and damping of the imaginary part, see equation 2.4.

$$\begin{aligned} h &= h_0 + \delta h(t) = h_0 + \tilde{h}e^{j\omega t} \\ p &= p_0 + \delta p(t) = p_0 + \tilde{p}e^{j\omega t} \end{aligned} \quad (2.2)$$

$$\frac{1}{12\eta R_s T} \nabla (p_0 h_0^3 \nabla \tilde{p} + (\tilde{p} h_0^3 + 3p_0 h_0^2 \tilde{h}) \nabla p_0) = \frac{1}{R_s T} j\omega (p_0 \tilde{h} + h_0 \tilde{p}) \quad (2.3)$$

$$\begin{aligned} k(\omega) &= -\frac{\int \Re(\tilde{p}) dA}{\tilde{h}} \\ c(\omega) &= -\frac{\int \Im(\tilde{p}) dA}{\omega \tilde{h}} \end{aligned} \quad (2.4)$$

### 2.1.3. Dimensional analysis

The Reynolds equation has a number of constants, namely: viscosity  $\eta$ , specific gas constant  $R_s$  and temperature  $T$ . Furthermore, the equation contains the following parameters, namely: a spatial coordinate, pressure  $p$  and fly height  $h$ . The perturbed equation has the same constants and parameters with the addition of perturbed- fly height  $\tilde{h}$  and pressure  $\tilde{p}$  and the perturbation frequency  $\omega$ . The inlet adds a source term to the equations, this increases the number of parameters even more, depending on the restriction model.

It is decided to make the equations dimensionless, by scaling with characteristic parameters. Without any scaling, large differences in order of magnitude are present, decreasing numerical stability. Numerical optimisation requires design variables being in the same order of magnitude, to improve convergence. The non-dimensional equations are clear and enable the comparison of different designs, without additional scaling. Only four dimensional parameters are needed to make the equations dimensionless, namely: length  $R$ , pressure  $P$ , height  $H$  and frequency  $\Omega$ . The parameters with a bar are dimensionless, relations are as follows:

$$\begin{aligned} r[m] &= \bar{r}[-]R[m] \\ p[Pa] &= \bar{p}[-]P[Pa] \\ h[m] &= \bar{h}[-]H[m] \\ \omega[\text{rads}^{-1}] &= \bar{\omega}[-]\Omega[\text{rads}^{-1}] \end{aligned} \quad (2.5)$$

The static part of equation 2.1 is used as starting point for the dimensional analysis rewriting gives:

$$C\nabla \cdot \mathbf{\Gamma} = \mathbf{0} \quad \text{with} \quad \nabla = \left[ \frac{\partial}{\partial x}, \frac{\partial}{\partial y} \right] \quad (2.6)$$

The constants  $\eta$ ,  $R_s$ ,  $T$  and scalar 12 are assembled in one constant named  $C$ . The pressure  $p$  and gap height  $h$  are functions of the spatial coordinates and are expressed as conservative flux ' $\mathbf{\Gamma}$ '. Constant ' $C$ ' and the conservative flux ' $\mathbf{\Gamma}$ ' and their correct SI units are given in equation 2.7.

$$\begin{aligned}\Gamma[\text{kg}^2 \text{s}^{-4}] &= \left[ p h^3 \frac{\partial p}{\partial x}, p h^3 \frac{\partial p}{\partial y} \right] \\ C[\text{s}^3 \text{kg}^{-1} \text{m}^{-1}] &= \frac{1}{12\eta R_s T}\end{aligned}\quad (2.7)$$

The constant 'C' can be removed entirely from equation 2.6 and the conservative flux 'Γ' can be made dimensionless using equation 2.5. This results in the non-dimensional conservative flux:

$$\bar{\Gamma}[-] = \frac{R}{p^2 H^3} \Gamma \quad (2.8)$$

The final non-dimensional static Reynolds equation becomes:

$$\bar{\nabla}(\bar{h}_0^3 \bar{p}_0 \bar{\nabla} \bar{p}_0) = 0 \quad (2.9)$$

Now the perturbed Reynolds equation 2.3 is used to find an expression for the dimensionless frequency, see equation 2.11.

The perturbed Reynolds equation 2.3 can be made dimensionless using the same method this gives equation 2.10.

$$\bar{\nabla}(\bar{p}_0 \bar{h}_0^3 \bar{\nabla} \bar{p} + (\bar{p} \bar{h}_0^3 + 3 \bar{p}_0 \bar{h}_0^2 \bar{h}) \bar{\nabla} \bar{p}_0) = j \bar{\omega}(\bar{p}_0 \bar{h} + \bar{h}_0 \bar{p}) \quad (2.10)$$

The dimensionless frequency ' $\bar{\omega}[-]$ ' can be converted to the dimensioned frequency when scaling with ' $\Omega$ '. This scaling parameter is derived from equation 2.3 and is a combination of the other scaling parameters and viscosity:

$$\omega[\text{rads}^{-1}] = \Omega[\text{rads}^{-1}] \bar{\omega}[-] = \frac{P H^2}{12\eta R^2} \bar{\omega}[-] \quad (2.11)$$

When the dimensionless Reynolds equations are used, all bearing characteristics are dimensionless as well. This enables easy comparison of different designs and gives insight in parameter sensitivities. However, scaling is necessary when constructing a final design or when quantitative insight in certain characteristics is desired. For easy conversion from dimensionless designs to a dimensioned design the following relations are deducted.

$$W[\text{N}] = P R^2 \bar{W}[-] \quad k[\text{Nm}^{-1}] = \frac{P R^2}{H} \bar{k}[-] \quad c[\text{Ns m}^{-1}] = \frac{P R^2}{\Omega H} \bar{c}[-] \quad \dot{m}[\text{kg m}^{-1} \text{s}^{-1}] = C \frac{H^3 P^2}{R} \bar{m}[-] \quad (2.12)$$

The dimensional scaling parameters in equation 2.5 should represent a design. when using the axisymmetric bearing in figure 2.2 as an example, the scaling parameters are chosen as follows: radius 'R' equals the outer bearing radius ( $R = r_o$ ), pressure 'P' equals ambient pressure ( $P = P_a$ ), height 'H' equals nominal fly height  $H = h(r)_{nom}$  and frequency ' $\Omega$ ' is a function of the other parameters and the viscosity. The following scaling parameters are chosen:  $R = 1 \times 10^{-2}$  m,  $P = 1 \times 10^5$  Pa,  $H = 1 \times 10^{-5}$  m.

## 2.2. Restriction modelling and verification

The Reynolds equation and the application in thin-film lubricated gas-bearings is discussed in the previous section. An important aspect when modelling thin-film lubricated systems is how the medium enters the thin-film. A restriction is placed between the air-supply and thin-film to create stiffness. When a restriction is omitted, the pressure distribution is constant and independent of film-height. The lack of any thin-film stiffness results in an inherently unstable system. Since restricting the supply pressure is of great importance a lot of research is done, regarding both passive- and active restrictions. Different restriction models are presented in literature. The restriction model relates geometry and pressure gradient, to the mass flow through the restriction that enters the thin film. In [52] basic flow equations for: capillary, porous and orifice restrictions are presented. In this section the capillary and orifice flow models are treated and the limitations of laminar and turbulent flow theory are assessed. In section 2.2.3 a small case study is presented, involving a hollow blunt syringe needle. This section is concluded with a mass flux measurement through the syringe needle and comparison with the discussed models.



### 2.2.1. Capillary restriction

The Capillary restriction is a long thin tube ( $l/d > 20$ ), figure 2.3a, where the volume flow is defined by equation 2.13. This model is based on laminar flow conditions ( $Re < 2300$ ) where viscous forces dominate inertial forces. This laminar flow condition results in a linear relation between flow and pressure, according to the Hagen-Poiseuille law [55, p. 357]. Inserting the ideal gas law in equation 2.13 gives the mass flow in equation 2.14. An extended laminar pipe flow analysis, including velocity profiles is given in appendix C.

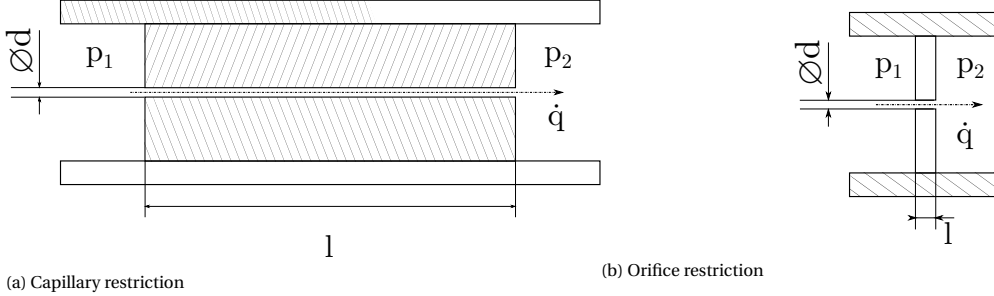


Figure 2.3

$$Q = \frac{\pi d^4}{128\eta L} (p_1 - p_2) \quad (2.13)$$

$$\dot{m}_{cap} = \frac{\pi d^4}{256L} \frac{p_1^2 - p_2^2}{\eta R_s T} \quad (2.14)$$

The mass flow through the capillary shows a linear relation with quadratic pressure difference  $p_1^2 - p_2^2$ . The flow becomes turbulent when the pressure gradient is too high, limiting the use of equation 2.14. The entrance length  $L_e$  for laminar pipe flow is a function of the Reynolds number and the pipe diameter:

$$\frac{L_e}{d} \approx 0.06 Re_d \quad (2.15)$$

The laminar flow model is only valid for low Reynolds numbers, therefore another flow model is discussed that takes the compressibility into account. When no heat exchange with the environment is assumed, an adiabatic Fanno flow model can be derived. The following assumptions are made: constant area straight duct, adiabatic flow, perfect gas, no shaft work and wall shear stress correlated by the Darcy friction factor. An extensive derivation of this type of flow is done in [55], the final result is in equation 2.16. With:  $\bar{f}$  the average friction factor along the duct,  $L^*$  the required length to develop a sonic flow,  $d$  the inner diameter and  $k$  the specific heat ratio.

$$\frac{\bar{f}L^*}{d} = \frac{1 - Ma^2}{kMa^2} + \frac{k+1}{2k} \ln \frac{(k+1)Ma^2}{2 + (k-1)Ma^2} \quad (2.16)$$

To find the mass flux as function of pressure difference one could use equation 2.16, this does not give a lot of insight. A set of two equations is derived by [51] and [50], relating the pressure- and temperature difference in equation 2.17, the mass flux is then calculated with equation 2.18.

$$\frac{k+1}{k} \ln \left( \frac{p_1 T_2}{p_2 T_1} \right) - \frac{k-1}{2k} \left( \frac{p_1^2 T_2^2 - p_2^2 T_1^2}{T_2 - T_1} \right) \left( \frac{1}{p_1^2 T_2} - \frac{1}{p_2^2 T_1} \right) + \frac{\bar{f}L}{d} = 0 \quad (2.17)$$

$$\dot{m} = A \sqrt{\frac{2k p_1^2 p_2^2}{(k-1)R_s} \left( \frac{T_2 - T_1}{T_1^2 p_2^2 - T_2^2 p_1^2} \right)} \quad (2.18)$$

As a result of the expansion and the adiabatic boundary condition the temperature decreases along the capillary, resulting in a lower air temperature at the outlet. This outlet temperature  $T_2$  can be calculated using equation 2.17 when the inlet temperature and pressure difference are both known. The average friction factor  $\bar{f}$  can be estimated using the Moody chart [55]. Once the outlet temperature is known, the mass flux can be determined using equation 2.18. These equations are only valid for turbulent subsonic flow  $Ma < 1$ .

For higher Mach numbers the flow becomes choked meaning there is no further increase in mass flux for increasing pressure difference. The Mach number is determined to check the validity of this flow model. The Mach number at the outlet is calculated in equation 2.19. Where the speed of sound  $c$  is determined using the bulk modulus:  $K_c = k * p$ , this gives:  $c_2 = (K_c / \rho_2)^{0.5}$ . The outlet density is determined using the ideal gas law.

$$Ma_2 = \frac{v_2}{c_2} = \frac{4\dot{m}}{\rho_2 \pi d^2} \frac{1}{c_2} = \frac{4\dot{m} R_s T_2}{p_2 \pi d^2} \frac{\sqrt{p_2}}{\sqrt{k p_2 R_s T_2}} \quad (2.19)$$

### 2.2.2. Orifice restriction

The orifice restriction in figure 2.3b is based on turbulent flow that is driven by inertia forces in the medium. In [42] and [43]) two types of orifice restrictions are discussed: the inherent orifice restriction and a pocketed orifice restriction. The mass flow rate of air through an orifice can be calculated as follows:

$$\dot{m}_0 = C_d \times \dot{m}_t$$

Where  $\dot{m}_t$  is the theoretical mass flow rate and  $C_d$  is the discharge coefficient. The discharge coefficient is a value between 0 and 1 and is a function of: orifice diameter and film thickness. In [13] it is shown that in a pocketed orifice restrictor the effects of: the supply pressure, bearing radius, pocket radius and pocket depth on the orifice discharge coefficient can be disregarded. The discharge coefficient can be estimated using correlations derived from experiments. Estimation of the discharge coefficient is fine for early stage models, however the real mass flow rate through the restrictor must be measured and compared to the model.

Only the inherent orifice will be analysed further because this type can be manufactured in a first prototype as will be explained later. The mass flow rate through this inherent orifice restrictor is given by [42] in equation 2.20. In equation 2.20:  $A$  is the surface area of the orifice, pressures  $P_1$  and  $P_2$  are indicated in figure 2.3b,  $R_s$  is the specific gas constant and  $T$  the temperature of the air. The ideal orifice equation consists of two parts where the first part is valid for sub-critical flow conditions and the second part for supercritical flow conditions. This means that when the flow becomes choked the mass flux does not increase for increasing pressure differences. Taking a heat capacity ratio  $\kappa$  of 1.4 the critical pressure ratio is:  $P_2/P_1 = 0.528$ .

$$\begin{aligned} \dot{m}_0 &= C_d A P_1 \sqrt{\frac{\kappa}{(\kappa-1)} \left[ \left( \frac{P_2}{P_1} \right)^{\frac{2}{\kappa}} - \left( \frac{P_2}{P_1} \right)^{\frac{\kappa+1}{\kappa}} \right] \frac{2}{R_s T}} \quad , \text{ if } \quad \frac{P_2}{P_1} \geq \left[ \frac{2}{\kappa+1} \right]^{\frac{\kappa}{\kappa+1}} \\ \dot{m}_0 &= C_d A P_1 \sqrt{\left( \frac{2}{\kappa+1} \right)^{2/(\kappa-1)} \left( \frac{\kappa}{\kappa+1} \right) \frac{2}{R_s T}} \quad , \text{ if } \quad \frac{P_2}{P_1} < \left[ \frac{2}{\kappa+1} \right]^{\frac{\kappa}{\kappa+1}} \end{aligned} \quad (2.20)$$

Besides the ideal model explained in equation 2.20 there is a simplified model introduced by Jobson [25]. This model is deduced by assuming a 1D flow through a simple inherent orifice at subcritical flow conditions. The Jobson equation for an ideal subcritical mass flow is given in equation 2.21.

$$\dot{m}_0 = \rho_0 C_d A \sqrt{\frac{2(p_1 - p_2)}{\rho_0}} = C_d A \sqrt{\frac{p_1^2 - p_2^2}{R_s T}} \quad (2.21)$$

### 2.2.3. Syringe-needle flow modelling

One of these restriction models should be implemented in the overall air bearing model. The choice of restriction model depends on the available restrictor elements, that can be used in the final design. It is useful to investigate the restrictor possibilities early in the design process. A standard restrictor element should have a consistent mass flux, independent of production errors. In the lab blunt hollow needles are available that are used in the field of microfluidics, see figure 2.4. These needles are available in different diameters, the smallest diameter that is in the lab is gauge 30 (G30), in table 2.1 a conversion to SI units is made together with the tolerances [28].

The blunt needles are standardized elements that can easily be connected to an air supply. The inner diameters are in the same range as the restriction elements used by [21] and [43]. For a small pressure difference  $p_1 - p_2$  and a ratio of  $L/d > 20$  the blunt needle can be modelled using the laminar capillary flow model of equation 2.14. All needles have a length of:  $L = 17$  mm, using this length the mass flux of needles with different inner diameters is determined, see figure 2.5. The contour plot in figure 2.5 gives the Reynolds number

Table 2.1: Syringe needle conversion table.

Gauge	Outer diameter (mm)	Inner diameter (mm)
30	0.3112 ± 0.0075	0.159 ± 0.019
26	0.46 ± 0.01	0.26 ± 0.019
18	1.27 ± 0.013	0.838 ± 0.038

of the flow through the capillary. At a Reynolds number of: 2300 the flow becomes turbulent and the laminar capillary flow model is invalid. The model assumes zero pipe friction and a fully developed flow, both are not the case in the real situation. These assumptions will overestimate the mass flux of the model compared to the real flux.

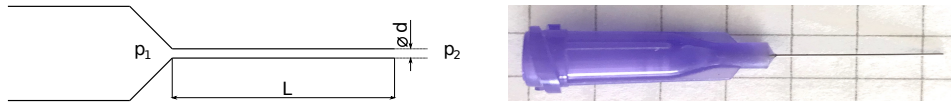


Figure 2.4: Blunt needle.

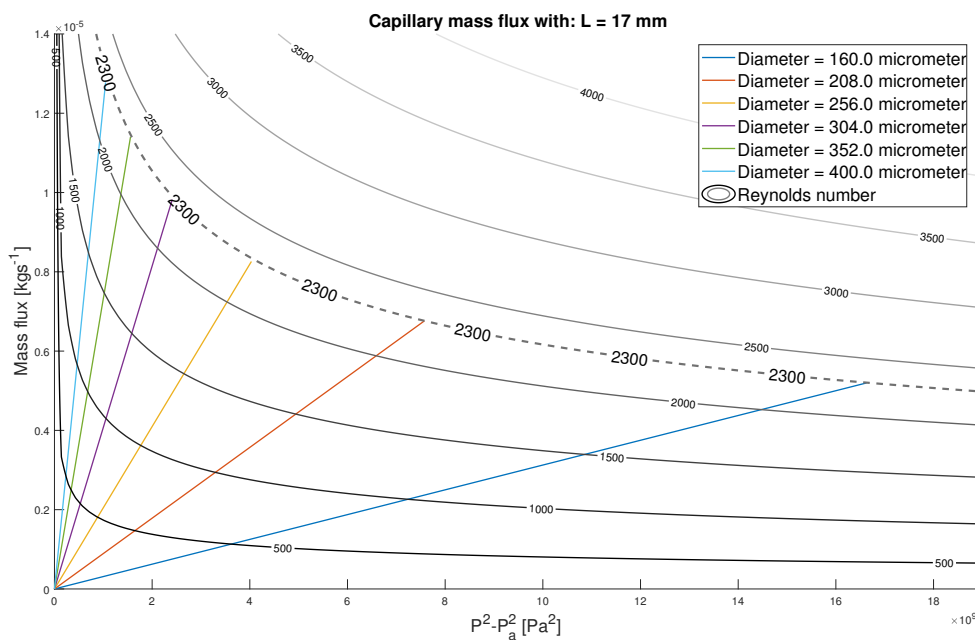


Figure 2.5: Laminar capillary flow.

As already stated, the laminar capillary flow model is only valid in fully developed flow conditions. The entrance length for laminar pipe flow conditions can be calculated with equation 2.22, according to [55].

$$L_e \approx 0.06 Re_d d \tag{2.22}$$

This means that the maximum laminar entrance length at:  $Re_d = 2300$  &  $d = 160\mu\text{m}$  is: 22.1 mm, which exceeds the needle length of 17 mm. An entrance length of 10% of the total length  $L$  corresponds to a Reynolds number of only:  $Re_d = 177$ . These very low Reynolds numbers are only the case at very low pressure differences over the needle restriction.

For higher Reynolds numbers  $Re_d > 2300$  the turbulent capillary flow model derived in [50] is used. The mass flux is calculated for a range of quadratic pressure differences using equations 2.17 and 2.18. The validity of the model is checked by calculating the Mach number at the outlet using equation 2.19. Calculating the Reynolds number is difficult in turbulent flow when compared to the laminar flow case. This is because

there is a set of coupled non-linear equations that have to be solved. However, for any pipe flow the Reynolds equation can be written as in equation 2.23. By solving the set of non-linear equations in: 2.17 and 2.18 simultaneously for a given pressure and mass flux, the diameter  $d$  and outlet temperature  $T_2$  are found. Substitution of the diameter  $d$  with the matching mass flux in equation 2.23 yields the Reynolds number.

$$Re = \frac{4\dot{m}}{\eta\pi d} \quad (2.23)$$

These calculations are done for a range of capillary diameters and with a constant length of:  $L = 17$  mm and a friction factor of:  $\bar{f} = 0.07$ . The result of these calculations are plotted in figure 2.6. In this graph the outlet Mach number equals one at the red dots, meaning that the theory is invalid at the right of the red dots because the flow is choked in that regime. The model is also invalid for low-full-laminar Reynolds numbers since a constant friction factor may only be assumed when considering turbulent flow.

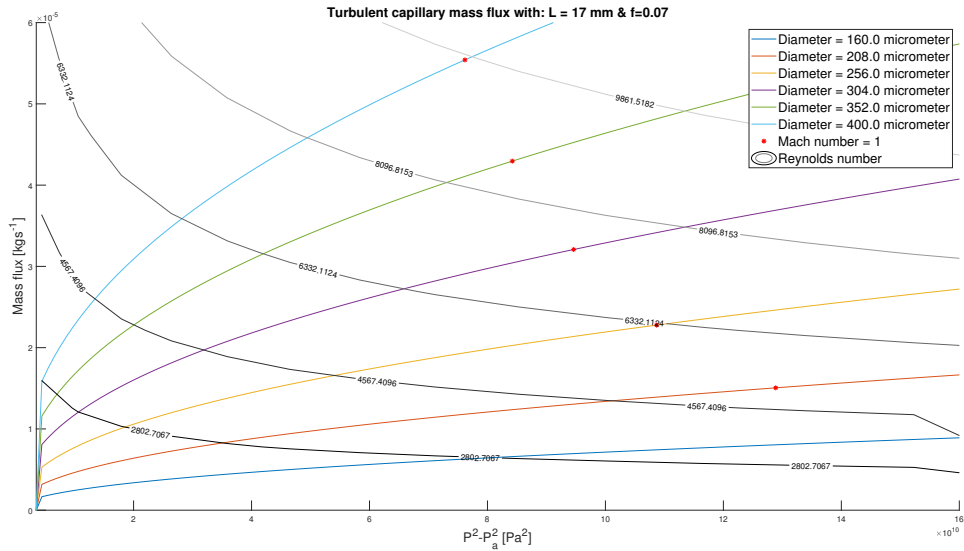


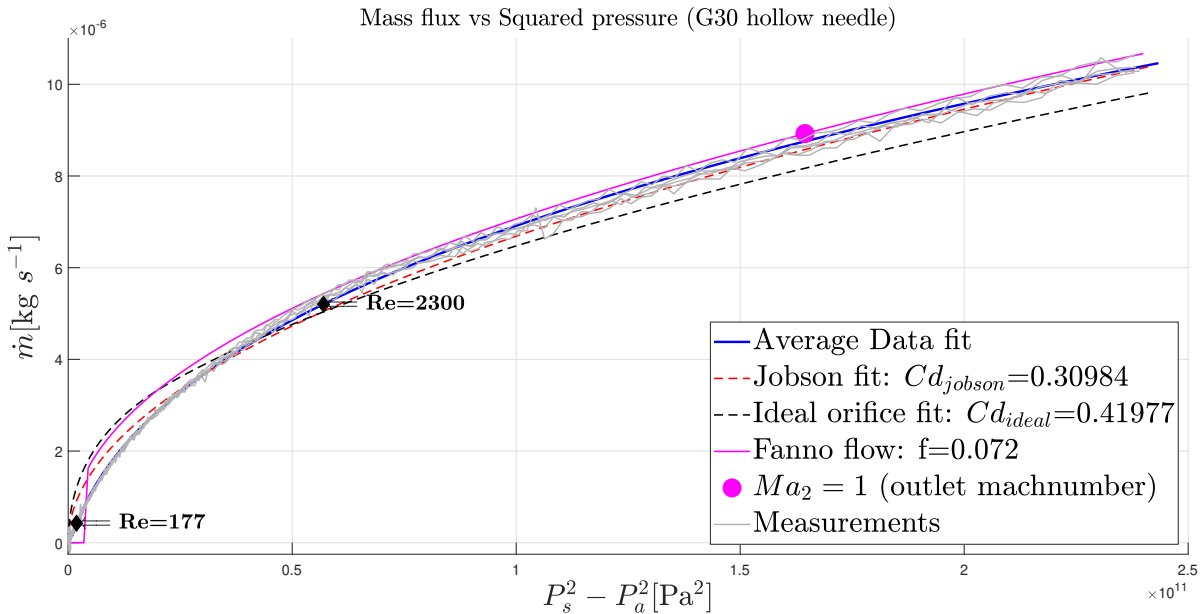
Figure 2.6: Turbulent adiabatic capillary flow.

### 2.2.4. Validation

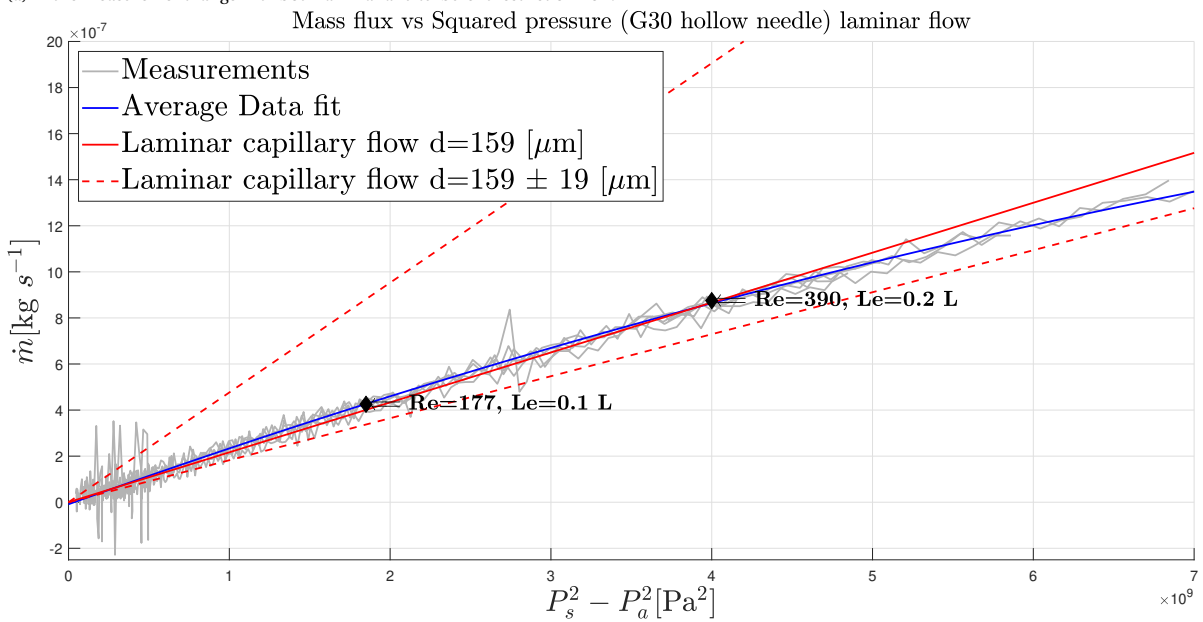
The syringe needle in figure 2.4 looks like a combination of a capillary- and orifice restriction. All the discussed flow models have limitations regarding the flow regime and probably none will fit the syringe flow for all pressure differences. An experimental set-up is build to measure the mass flow of six gauge 30 syringe needles, see appendix B. This measurement gives valuable information that can be used in the modelling phase. The mass flow versus quadratic pressure difference of the measured needles is plotted in figure 2.7a. The measurements are depicted by the grey lines and each line represents a different needle, the dark blue line represents the average of the measurements. From figure 2.6 it becomes clear that for:  $\Delta P^2 < 5 \times 10^{10} \text{ Pa}^2$  the flow is laminar. The three previously discussed turbulent pipe flow models are fitted to the measurement data with a least squares fit. For the ideal and Jobson orifice models the discharge coefficient,  $C_d$  is used as fitting parameter while for the adiabatic Fanno flow, the friction factor is used. The Jobson and Fanno flow models show a good fit in the turbulent regime at:  $\Delta P^2 > 5.7 \times 10^{10} \text{ Pa}^2$ , the latter still shows agreement for choked flow:  $Ma_2 = 1$  and the mass flux still increases. This could be a result of the adiabatic flow assumption, which is not completely valid when heat escapes through the thin restriction wall, reducing the outlet air temperature  $T_2$ .

The laminar flow regime is shown in figure 2.7b and the laminar capillary flow model from equation 2.14 is plotted with the manufacturing tolerances. The laminar capillary flow model is only valid for very low ( $Re \approx 177$  &  $Le = 0.1L$ ) Reynolds numbers, as a result of the entrance effects. It can be seen that the model starts to deviate when the entrance length exceeds 20% of the total needle length. Whether this linear flow model can be used, depends on the pressures and mass flux in the bearing application, these are a function of the thin-film resistance. However, a small restriction pressure difference is expected and it is decided

to use the laminar capillary flow model in further modelling. The linear relation between mass flow and squared pressure difference, simplifies the model and can be used as design variable, known as restriction conductivity:  $G_r = \frac{\pi d^4}{256L\eta R_s T}$ . These measurement results are used in chapter 5, when a final 'manufacturable' design is determined.



(a) Entire measurement range with both laminar and turbulent restriction flow.



(b) Laminar flow regime.

Figure 2.7: G30 size hollow syringe needle mass flow measurement with fitted restriction flow models, the laminar capillary flow model shows a proper fit for low Reynolds numbers.

### 2.3. Aerostatic bearing model

The previously discussed theory concerning thin film- and restriction modelling, is used to model the axisymmetric bearing in figure 2.2. The geometry is implemented in a 2D finite element Comsol model, that is able to calculate the static- and perturbed pressures inside the thin film. The 'static' part of the finite element model is validated analytically, using the method of multiple resistances (MR). This Comsol model will be used as starting point for more advanced designs and the parametric optimisation in chapter 3. A more

detailed drawing of the two pocket bearing in figure 2.2 is given in figure 2.8, the normalised design variables are given in table 2.2. It should be noted that these design variables are arbitrarily chosen to enable model validation.

Table 2.2: Single-inlet air bearing design parameters.

Variable	Value [-]	Description
$\bar{G}_r$	1	Restrictor conductivity
$\bar{r}_r$	0.003	Restrictor inlet radius
$\bar{r}_{rp}$	0.05	Restrictor pocket radius
$\bar{r}_{sp}$	0.25	Shallow pocket radius
$\bar{r}_o$	1	Outer radius
$\bar{h}_0$	1	Nominal fly height
$\bar{h}_{sp}$	0.1	Shallow pocket height
$\bar{h}_{rp}$	20	Restrictor pocket height
$\bar{p}_s$	3	Supply pressure
$\bar{p}_a$	1	Ambient pressure



Figure 2.8: Axisymmetric bearing design with dimensions and local (nodal) pressures.

### 2.3.1. Numerical model

When setting up a numerical model there is always a trade-off between computation time and model complexity. There is a challenge in capturing the system's physical behaviour correctly, without over-simplifying. The axisymmetric bearing can be modelled with a 1D numerical model. This reduces the number of elements drastically compared with a 2D model, decreasing computation time. However, a 2D model is chosen because it enables the analysis of more complicated designs at a later stage.

The dimensionless Reynolds equations presented in section 2.1.3, are implemented in a 2D Comsol model using the PDE study interface. The inlet restriction is modelled with the laminar capillary flow model described by equation 2.14. The equation is slightly rewritten by introducing the restrictor conductivity  $G_r$ , source pressure  $P_s$  and the restrictor pressure at the outlet  $r_r$ , see equation 2.24.

$$\dot{m}_{cap} = G_r (P_s^2 - P_r^2) \quad (2.24)$$

In the 2D model, the source term is scaled with the perimeter  $\mathcal{P}$  of the inlet hole, giving:

$$\dot{m}[\text{kgm}^{-1} \text{s}^{-1}] = \frac{G_r (P_s^2 - P_r^2)}{\mathcal{P}} \quad (2.25)$$

The conductivity, pressures and perimeter can be written in dimensionless form to obtain the dimensionless mass flux. To obtain the perturbed source term, the static mass flow is substituted with equation 2.2. The

dimensionless source terms that are used in the steady-state- and perturbed Reynolds equations, are given in equation 2.26 respectively.

$$\bar{m}_{cap} = \frac{\bar{G}_r(\bar{P}_s^2 - \bar{p}_0^2)}{\bar{\mathcal{P}}} \quad \text{steady-state source} \quad (2.26)$$

$$\tilde{m}_{cap} = \frac{-2\bar{G}_r\bar{p}_0\tilde{p}}{\bar{\mathcal{P}}} \quad \text{perturbed source} \quad (2.27)$$

The steady-state- and perturbed Reynolds equations are solved sequentially, using the Comsol MUMPS solver with a 'normal' size physics-controlled mesh. The load capacity is found by integrating the pressure distribution over the total bearing surface.

### 2.3.2. Analytical model and results

The design is axisymmetric and may therefore be expressed with only one 'normalised' spatial coordinate ( $r$ ). This means that the air bearing surface from  $r = 0$  to  $r = 1$  can be represented by multiple resistances in series. The mass that enters the system must pass through all resistances before it reaches the outer edge at ambient pressure. The mass flow through every resistance element must be the same, equating yields a system of equations resulting in the intermediate film pressures. The medium flows through the capillary restriction and three thin-film resistances, see figure 2.9. The mass flow through the thin-film shows a linear relation with quadratic pressure difference, see equation 2.28 and for derivation appendix C.2. The 'i' and 'o' subscripts indicate the thin film inlet and outlet respectively and conductivity  $G$  is the inverse of resistance  $R$ .

$$\bar{m} = \bar{G}_{tf}(p_i^2 - p_o^2) = \frac{\pi\bar{h}^3}{\ln(\bar{r}_o/\bar{r}_i)}(p_i^2 - p_o^2) \quad (2.28)$$

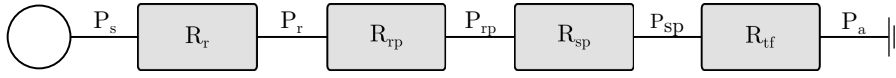


Figure 2.9: Axisymmetric bearing resistance scheme.

The mass flow through every element is equal giving the following equation:

$$\bar{m} = \bar{G}_r(\bar{P}_s^2 - \bar{P}_r^2) = \bar{G}_{rp}(\bar{P}_r^2 - \bar{P}_{rp}^2) = \bar{G}_{sp}(\bar{P}_{rp}^2 - \bar{P}_{sp}^2) = \bar{G}_{tf}(\bar{P}_{sp}^2 - \bar{P}_a^2) \quad (2.29)$$

The restrictor conductivity  $G_r$  is chosen to be unity while the thin-film conductivities are a function of radii and pocket height given in table 2.2.

To find the characteristic intermediate pressures indicated in figure 2.9, a system of equations is solved. Equation 2.29 is written in matrix form:  $Ax = b$ , see equation 2.30.

$$\begin{bmatrix} \bar{G}_r & 0 & 0 & 1 \\ -\bar{G}_{rp} & \bar{G}_{rp} & 0 & 1 \\ 0 & -\bar{G}_{sp} & \bar{G}_{sp} & 1 \\ 0 & 0 & \bar{G}_{tf} & -1 \end{bmatrix} \begin{bmatrix} \bar{P}_r^2 \\ \bar{P}_{rp}^2 \\ \bar{P}_{sp}^2 \\ \bar{m} \end{bmatrix} = \begin{bmatrix} \bar{G}_r\bar{P}_s^2 \\ 0 \\ 0 \\ \bar{G}_{tf}\bar{P}_a^2 \end{bmatrix} \quad (2.30)$$

This linear system of equations can be solved with the model parameters in table 2.2, resulting in the following intermediate pressures and mass flow:

$$\begin{bmatrix} \bar{P}_r \\ \bar{P}_{rp} \\ \bar{P}_{sp} \\ \bar{m} \end{bmatrix} = \begin{bmatrix} 2.15[-] \\ 2.15[-] \\ 1.71[-] \\ 4.38[-] \end{bmatrix} \quad (2.31)$$

Equation 2.32 describes the thin-film pressure profile between the nodes. Combining all results gives the pressure as function of the spatial coordinate  $r$ . It can be concluded that the results from the 2D numerical model match the analytical results perfectly, see figure 2.10a.

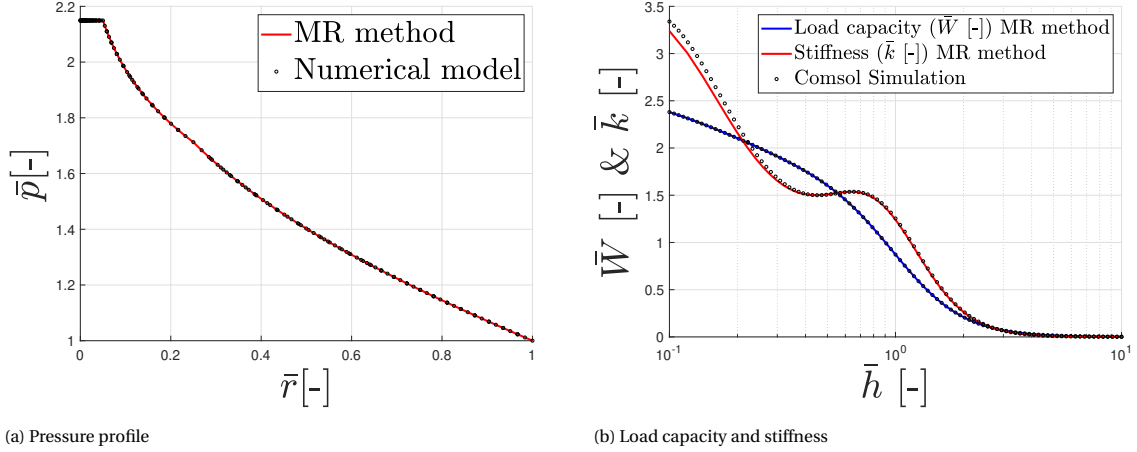


Figure 2.10: Numerical and analytically determined aerostatic bearing characteristics.

$$p(r) = p_o \sqrt{\left(\frac{p_i}{p_o}\right)^2 - \frac{\ln(r/r_i)}{\ln(r_o/r_i)} \left(\left(\frac{p_i}{p_o}\right)^2 - 1\right)} \quad (2.32)$$

To find the load carrying capacity, the pressure profile at a large number of fly-heights is calculated. Then these pressure profiles are integrated along the surface area to obtain the load carrying capacity, see equation 2.33. The integration of equation 2.32 can be done analytically according to [21] using the Gauss error function. However, it is decided to perform this integration numerically using the trapezoidal method since it is less cumbersome and fast.

$$\bar{W} = 2\pi \int_0^{\bar{r}_o} \bar{r} \bar{p}(r) d\bar{r} - \pi \bar{r}_o^2 \bar{p}_a \quad (2.33)$$

The stiffness is determined by taking the derivative of the load capacity  $\bar{W}$  w.r.t the fly-height  $\bar{h}_0$ , this is allowed for the static case. Both are depicted in figure 2.10b and compared to the Comsol simulation. The methods show excellent agreement and converge when increasing the number of fly height evaluations. The method of multiple resistances is unsuitable to find the damping in the system since no analytical solution of the perturbed Reynolds equation exists. Consequently, the frequency dependent stiffness and damping graphs are omitted.

## 2.4. Dynamics of aerostatic pads

The two-pocket-one-inlet bearing pad, depicted in figure 2.8 is used to study the influence of different design variables, on the high pressure pad's dynamics. An extensive study concerning the dynamic characteristics of circular centrally fed aerostatic bearings can be found in [6]. The method of linear perturbation discussed in section 2.1.2 is used, equation 2.10 gives:

$$-\frac{\partial}{\partial \bar{x}} \left( \bar{p}_0 \bar{h}_0^3 \frac{\partial}{\partial \bar{x}} \bar{p} + \bar{p} \bar{h}_0^3 \frac{\partial}{\partial \bar{x}} \bar{p}_0 + 3\bar{p}_0 \bar{h}_0^2 \bar{h} \frac{\partial}{\partial \bar{x}} \bar{p}_0 \right) - \frac{\partial}{\partial \bar{y}} \left( \bar{p}_0 \bar{h}_0^3 \frac{\partial}{\partial \bar{y}} \bar{p} + \bar{p} \bar{h}_0^3 \frac{\partial}{\partial \bar{y}} \bar{p}_0 + 3\bar{p}_0 \bar{h}_0^2 \bar{h} \frac{\partial}{\partial \bar{y}} \bar{p}_0 \right) + j\bar{\omega}(\bar{p}_0 \bar{h} + \bar{h}_0 \bar{p}) = 0 \quad (2.34)$$

This equation is applied to the geometry in figure 2.2, while prescribing a Dirichlet boundary condition at the outer edge:  $\bar{p}(r = r_o) = 0$ . The perturbed pressure is solved for the whole domain, using a small perturbation amplitude:  $\bar{h} \ll 1$ . The perturbed pressure is a complex number, the real- and imaginary part can be physically assigned to the thin-film stiffness and damping respectively. When following the theory in [6], the dynamic pressure can be written in the following form:

$$-\frac{\bar{p}}{\bar{h}} = p_k + j\omega p_c \quad (2.35)$$



The dynamic pressure components  $p_k$  and  $p_c$  are determined for the bearing design given in table 2.2. When the bearing geometry and supply pressure are considered constant, the dynamic pressure  $\bar{p}$  is only a function of the perturbation frequency  $\bar{\omega}$ . There are two limiting cases namely:  $\lim_{\bar{\omega} \rightarrow 0}$  and  $\lim_{\bar{\omega} \rightarrow \infty}$ .

For the first case, the transient term in equation 2.34 vanishes and the *real* part of the dynamic pressure profile ( $P_k$ ), *almost* mimics the shape of the static solution. When the frequency goes to infinity the dynamic term becomes dominant, yielding:

$$(\bar{p}_0 \bar{h} + \bar{h}_0 \bar{p}) = 0, \quad \bar{\omega} \rightarrow \infty \quad (2.36)$$

Rewriting gives:

$$-\frac{\bar{p}}{\bar{h}} = \frac{\bar{p}_0}{\bar{h}_0} \quad (2.37)$$

This means that, for large frequencies the perturbed- and steady-state solutions converge, resulting in a purely real solution. The absence of the complex part of the dynamic pressure distribution, indicates zero damping and is sometimes called: 'trapped gas' case [6]. This phenomenon becomes clear when the real  $P_k$  and complex  $P_c$ , pressure distributions are plotted at different perturbation frequencies. One half of the (symmetric) dynamic pressure distribution of the table 2.2 design is given in figure 2.11.

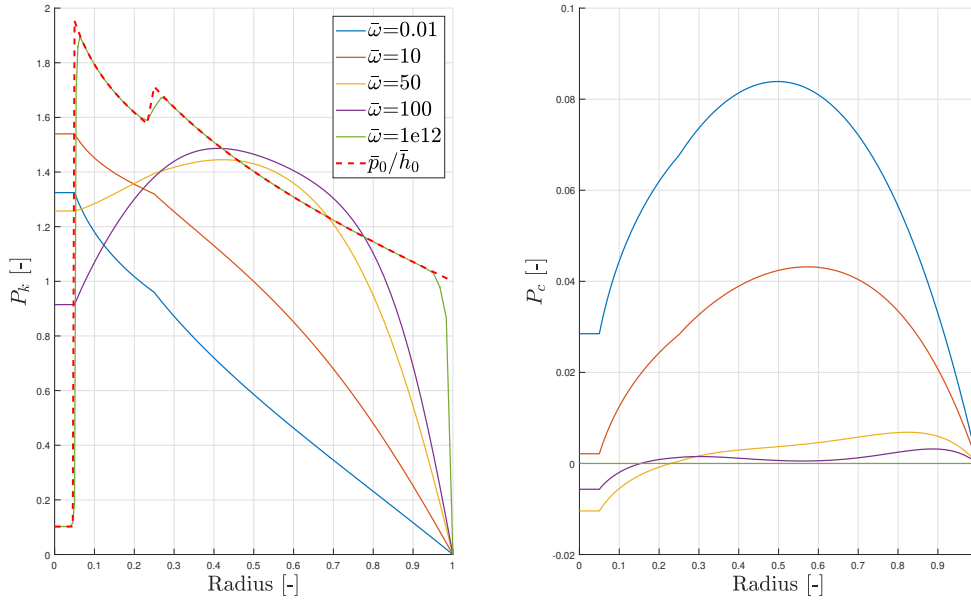


Figure 2.11: Dynamic pressure distributions  $P_k$  and  $P_c$ , of the circular centrally fed aerostatic bearing design (table 2.2).

At low frequencies the system has a high (complex) damping coefficient, as a result of the thin-film squeeze motion. When the perturbation frequency increases, there is no time for gas flow and the gas only gets compressed. At very high frequencies, the complex damping term vanishes and the perturbed solution converges to the steady-state solution (red dotted line). The  $P_c$  graph for high frequencies flattens in the middle, while the 'near' boundary pressure is relatively high, indicating the 'trapped gas' case (visible at:  $\bar{\omega} = 100$ ). The small 'dead' volume at the inlet causes a reduction of  $P_c$ , even negative values are present. When the 'dead' volume in the thin film becomes too large, instability occurs known as 'pneumatic hammer'.

This inlet-pocket volume has a large influence on the dynamic bearing characteristics, while not affecting statics. The stiffness and damping are found with the dynamic pressure, see equations 2.4. These results are given for a range of frequencies and increasing restriction pocket depth  $h_{rp}$ , see figure 2.12.

Both the stiffness and damping are clearly a function of perturbation frequency and restriction pocket depth. The blue line in figure 2.12 corresponds with the pressure distributions in figure 2.11. The damping in this configuration stays positive for all frequencies, indicating a stable system. Increasing the restriction-pocket depth reduces the damping for low frequencies, even zero or negative damping is possible, see figure 2.12b. Negative damping should be avoided, since it causes self-excited vibrations, known as: 'pneumatic

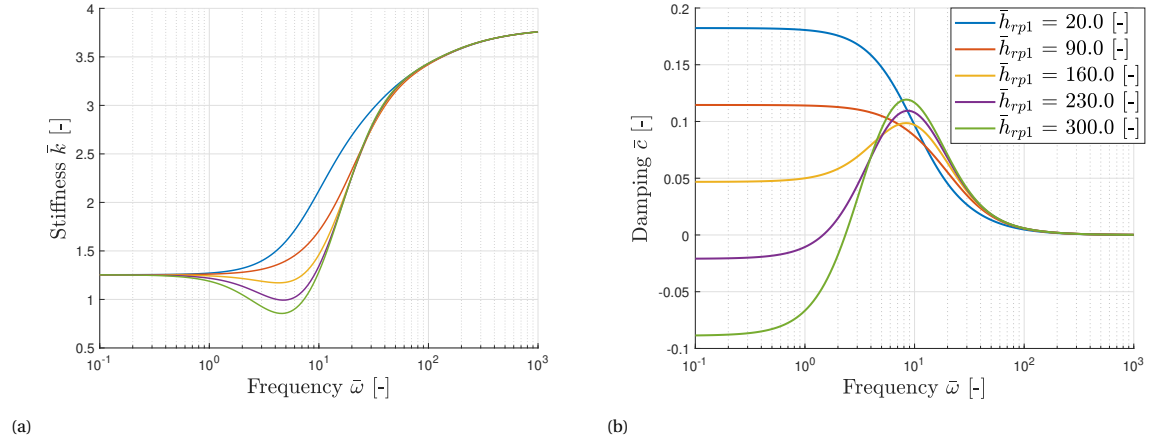


Figure 2.12: Stiffness and damping at different frequencies and restrictor pocket depths for a single pad with:  $P_s = 3[-]$

hammer'. The damping increases again, when the gas film undergoes a transition from the squeeze film state to the trapped gas state, resulting in the damping peak around  $\bar{\omega} = 10$ . The stiffness graphs all originate from the same point, indicating that  $h_{rp}$  does not influence the static bearing stiffness. However, the increased restriction-pocket volume, does influence the stiffness characteristic; the stiffness declines when damping starts to rise and vice versa [6].

The restriction-pocket depth is not the only design variable changing the dynamic bearing behaviour. In [6] the influence of the feed hole radius  $r_{rp}$ , supply pressure  $P_s$  and inlet flow is discussed. These design variables have a large influence, on the static bearing characteristics and are therefore, less suitable when tuning dynamics. Furthermore, altering the restriction-pocket height, gives a monotonic transition of stiffness and damping. Changing the feed hole radius  $r_{rp}$  gives a non-monotonic stiffness and damping ratio. Supplementary graphs of the dynamic influence of different design variables can be found in appendix D, all are in agreement with [6].

The graphs in figures 2.11 and 2.12 depict the single pad characteristics at a supply pressure of:  $P_s = 3[-]$ , the same equations and theory are applicable in case of vacuum pressure. The same design from table 2.2 is used, to analyse the vacuum pad characteristics at a vacuum pressure of:  $P_s = 0.1[-]$ . It should be noted that, as a result of the *static* negative stiffness, a vacuum pad needs to be combined with a supply pressure pad, to create a stable system. These purely theoretical single vacuum pad characteristics are depicted in figure 2.13. The stiffness starts negative but increases at higher perturbation frequencies, the restriction-pocket depth influences the constant stiffness bandwidth. A deeper restriction-pocket results in an earlier stiffness increase than a shallower pocket, this opposes the supply pad characteristics in figure 2.12a. The damping characteristic in figure 2.13b, show an increased damping at low-frequencies for larger pocket volumes, opposing the supply pressure pad characteristic.

It is known that adding a vacuum outlet, pre-loads the bearing system and leads to an increased damping characteristic at lower frequencies. The aforementioned relation between: the 'dead' restriction-pocket volume and damping, has been studied in literature for supply pressure pads. The increased damping when 'dead' volume is added around a vacuum outlet, has never been studied as far to the authors knowledge. This phenomenon could be of use in high damping applications, however, in this study the damping is minimised and a small vacuum restriction-pocket depth is favourable.

#### 2.4.1. Transmissibility

The thin air film couples the bearing- and counter surface, transmitting forces and displacements. The goal of this research is to reduce the transmissibility of the thin air-film, for a wide range of perturbation frequencies. The thin-film can be represented by frequency dependent spring and damper elements, see figure 2.14. The equation of motion for this single mass spring damper system is given by 2.38.

$$m\ddot{x}_m + c(\omega)(\dot{x}_m - \dot{x}_f) + k(\omega)(x_m - x_f) = 0 \quad (2.38)$$

The transmissibility is defined as the ratio of base-to-target displacement and can be derived from the

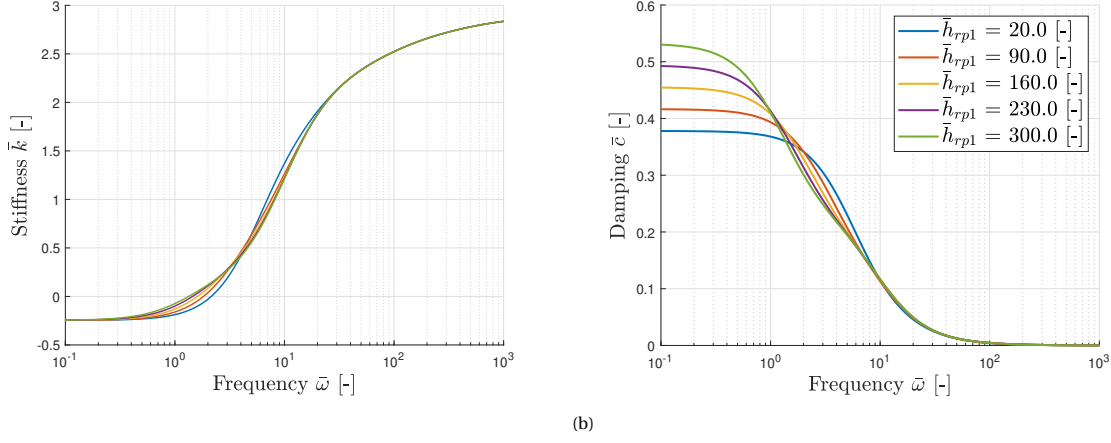


Figure 2.13: Stiffness and damping at different frequencies and restrictor pocket depths for a single vacuum pad with:  $P_s = 0.1[-]$ .

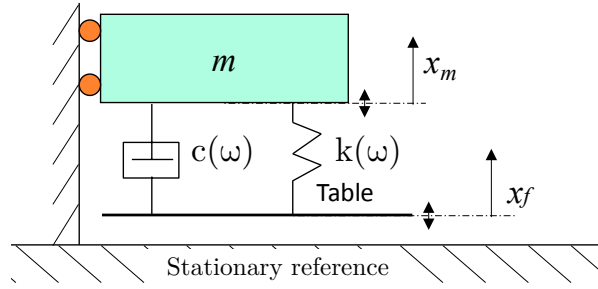


Figure 2.14: Simple dynamic model of an air bearing, transmissibility is defined by the ratio of  $x_m$  and  $x_f$  (from (40)).

equation of motion. First the Laplace transform of equation 2.38 is taken, rewriting gives:

$$x_m (ms^2 + c(\omega)s + k(\omega)) = x_f (c(\omega)s + k(\omega)) \quad (2.39)$$

When a sinusoidal system response is assumed, the Laplace operator  $s$  can be replaced with the Fourier term:  $j\omega$ . This gives the frequency-domain expression that describes the transmissibility, see equation 2.40. This linearised expression, assumes fly-height independent and frequency dependent stiffness and damping coefficients.

$$T(\omega) = \frac{x_m(\omega)}{x_f(\omega)} = \frac{c(\omega)j\omega + k(\omega)}{-m\omega^2 + c(\omega)j\omega + k(\omega)} \quad (2.40)$$

All the modelling is done with dimensionless parameters, these can be substituted with their correct scaling factors in equation 2.40. The appropriate scaling factors for the stiffness, damping and frequency are in equation 2.12. The mass can be expressed in load capacity by means of the gravitational acceleration  $g = 9.82 \text{ ms}^{-2}$ :

$$m[\text{kg}] = \frac{W[\text{N}]}{g[\text{ms}^{-2}]} = \frac{PR^2[\text{N}]\bar{W}[-]}{g[\text{ms}^{-2}]} \quad (2.41)$$

Implementation of the dimensionless variables in equation 2.40 gives:

$$T(\bar{\omega}) = \frac{\bar{c}(\bar{\omega})j\bar{\omega} + \bar{k}(\bar{\omega})}{-\frac{H\Omega^2\bar{W}}{g}\bar{\omega}^2 + \bar{c}(\bar{\omega})j\bar{\omega} + \bar{k}(\bar{\omega})} \quad (2.42)$$

This equation 2.42 scales the mass term to obtain a correct ratio between the mass, damping and stiffness. However, this equation needs the dimensional scaling factors, namely:  $P$ ,  $H$ ,  $R$  and  $\eta$ . The bearing radius determines the effective load capacity and must be chosen realistically. This gives:  $P = 1 \times 10^5 \text{ Pa}$ ,

$H = 1 \times 10^{-5}$  m,  $R = 12.5 \times 10^{-3}$  m and  $\eta = 18 \times 10^{-6}$  Pas. With these dimensional scaling factors the mass scaling term becomes:

$$\frac{H\Omega^2}{g} = 0.0894[-] \quad (2.43)$$

The transmissibility of the single supply pressure pad, is determined by substituting the stiffness and damping characteristics from figure 2.12 in equation 2.42. These results are depicted in the figure 2.15 Bode plot at different restriction-pocket depths. The reduced damping originating from the increased pocket depth, causes an eigenfrequency shift and a larger resonance peak, while it reduces the phase-lag in the system.

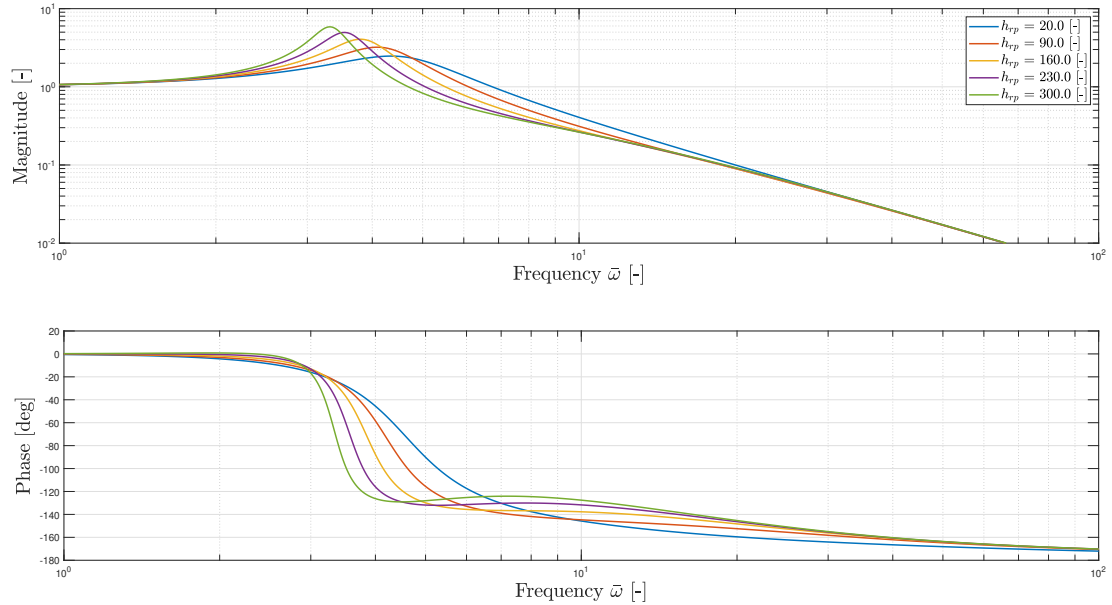


Figure 2.15: Transmissibility of the single inlet air bearing with the figure 2.12 stiffness and damping characteristics. The mass corresponds to the load capacity of a bearing with an outer radius of:  $r_o = 12.5 \times 10^{-3}$  m.

The goal is to obtain a low thin-film transmissibility for a large range of perturbation frequencies. The magnitude of the transmissibility shows a strong decay for frequencies above the eigenfrequency. This is the reason most commercial vibration isolation tables, have a low stiffness and a high mass. However, a large moving mass is undesirable within the context of high speed stages, because it introduces high forces and limits acceleration. Consequently, only the stiffness is used to reduce the eigenfrequency.

When the frequency rises the damping term becomes more dominant, this creates a stronger connection with the vibrating floor. Minimising the damping is therefore desired, this even shifts the 'damped' eigenfrequency further to the 'left'. The downside of very low damping is the potentially high resonance peak at a low eigenfrequency. This introduces a trade-off between a fast transmissibility decay and limiting the eigenfrequency amplification.

Analysis of the transmissibility expression in 2.42 at the limit frequencies, yields:

$$\lim_{\bar{\omega} \rightarrow 0} T(\bar{\omega}) = 1 \quad \lim_{\bar{\omega} \rightarrow \infty} T(\bar{\omega}) = 0 \quad \text{when,} \quad c, k > 0 \quad (2.44)$$

It can be seen that for positive stiffness and damping, the transmissibility always starts at one. To obtain zero transmissibility through the thin-film, the numerator must be zero:  $|\bar{c}(\bar{\omega})j\bar{\omega} + \bar{k}(\bar{\omega})| = 0$ . When the system has an absolutely zero stiffness and damping, it will act like a free floating mass, unaffected by floor vibrations.

### 2.4.2. Stability

Minimisation of the stiffness and damping can lead to instabilities, therefore it is decided to use a pole-zero plot to analyse the stability at different frequencies. The poles are found by solving equation 2.42 for the

Laplace operator  $s = j\bar{\omega}$  and equating the denominator to zero [40]. At constant stiffness and damping, the system would have two poles  $p_{1,2}$  and one zero  $z$ , defined as follows:

$$z = -\frac{\bar{k}}{\bar{c}} \quad p_{1,2} = \frac{-\bar{c} \pm \sqrt{\bar{c}^2 - 4 \frac{H\Omega^2 \bar{W}}{g} \bar{k}}}{2 \frac{H\Omega^2 \bar{W}}{g}} \quad (2.45)$$

However, the stiffness and damping are a function of the perturbation frequency, resulting in an infinite number of poles and zeros. To find the poles and zeros the stiffness and damping are linearised at a large number of frequencies. The poles of the single supply pad are plotted in the complex plane for a range of frequencies:  $1 \times 10^{-1} < \bar{\omega} < 1 \times 10^3$  and restriction-pocket depths:  $20 < h_{rp} < 300$ , see figure 2.16. The system is stable if both poles have a negative *real* part, the zero does not affect the stability. The poles are situated at the black markers for low perturbation frequencies and follow the trajectory towards the stable limit at:  $\Re(p_{1,2}) = 0$ ,  $\bar{\omega} = 1 \times 10^3$ . The bearing configurations with the deep restriction pockets  $h_{rp} = 230, 300$ , have negative damping at low frequencies. This places the poles at the positive side of the stable limit, indicating an unstable system as is expected with negative damping. It becomes clear that stability is a function of perturbation frequency. This means that, theoretically an unstable system could be stable, if it is solely excited at a single stable frequency, which has poles in the left-half plane of figure 2.16.

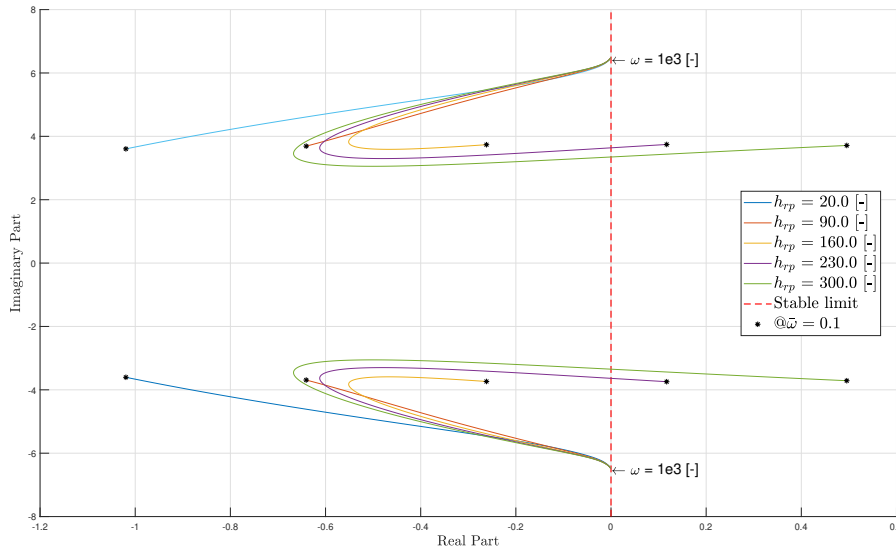


Figure 2.16: Pole stability plot for different restriction-pocket depths and perturbation frequencies. A deep pocket introduces 'dead' volume in the thin-film which results in negative damping and 'pneumatic hammer'.

### 2.4.3. 2-pad analysis

In the previous paragraphs the dynamic properties of the supply- and vacuum pads and the concept of thin-film transmissibility are analysed. With a combination of two pads, it is possible to create a stable 'static' low-stiffness bearing design as proposed in [21]. However, from the transmissibility function it appears that damping needs to be minimised as well. A parametric analysis is done to obtain insight in the frequency dependent relations, between stiffness, damping and thin-film transmissibility. The analysis is based on artificial stiffness and damping characteristics of a two-pad bearing design. This study gives insights in the dynamic characteristics and stability, without the need of a real completely optimised design.

The characteristics in figure 2.12 are parametrised and represented by discrete lines between transition frequencies. The schematic stiffness and frequency graphs are in figure 2.17. At low frequencies  $\bar{\omega} < \bar{\omega}_1$  the stiffness is equal to the static bearing stiffness  $k_0$  and the damping is  $c_0$ . Increasing  $h_{rp}$  reduces the damping without influencing static bearing characteristics. However, the dynamic stiffness is proportionally affected by the damping, indicated by  $\alpha$ , see figure 2.17a. In systems with low damping, the stiffness shows a 'dip' for:  $\bar{\omega}_1 < \bar{\omega} < \bar{\omega}_2$ . The following trend is observed:

$$\begin{array}{lll}
 \alpha > 0 & \text{when,} & c_0 < \bar{c}(\bar{\omega} = \bar{\omega}_2) \\
 \alpha = 0 & \text{when,} & c_0 = \bar{c}(\bar{\omega} = \bar{\omega}_2) \\
 \alpha < 0 & \text{when,} & c_0 > \bar{c}(\bar{\omega} = \bar{\omega}_2)
 \end{array}$$

This means that the stiffness decreases when the damping increases and vice versa, as is also observed by [6]. A 'static' low-stiffness design with small damping, can get a negative stiffness in the:  $\bar{\omega}_1 < \bar{\omega} < \bar{\omega}_2$  frequency bandwidth. This phenomenon must be taken into account since it might cause unwanted instabilities. At frequencies:  $\bar{\omega}_2 < \bar{\omega} < \bar{\omega}_3$ , the stiffness and damping converge towards a final value. The stiffness and damping characteristics of different  $\bar{k}(\bar{\omega})$  &  $\bar{c}(\bar{\omega})$  combinations are plotted in figure 2.17. The transmissibility of all different characteristics is calculated with equations 2.42 and 2.43, see figure 2.18.

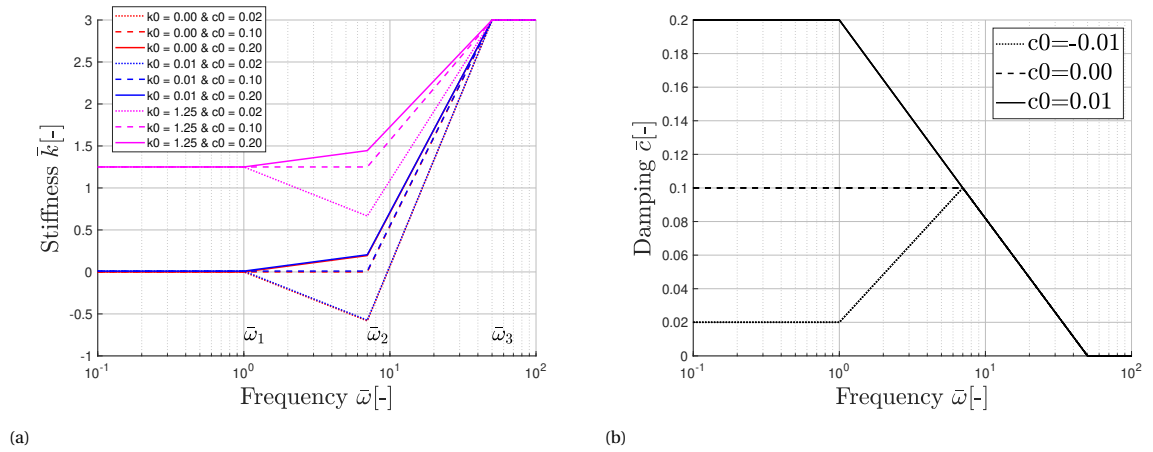


Figure 2.17: Artificial but realistic stiffness and damping characteristics for an arbitrary air bearing. The gradients of the  $\bar{k} - \bar{\omega}$  and  $\bar{c} - \bar{\omega}$  graphs always have an opposing sign [6].

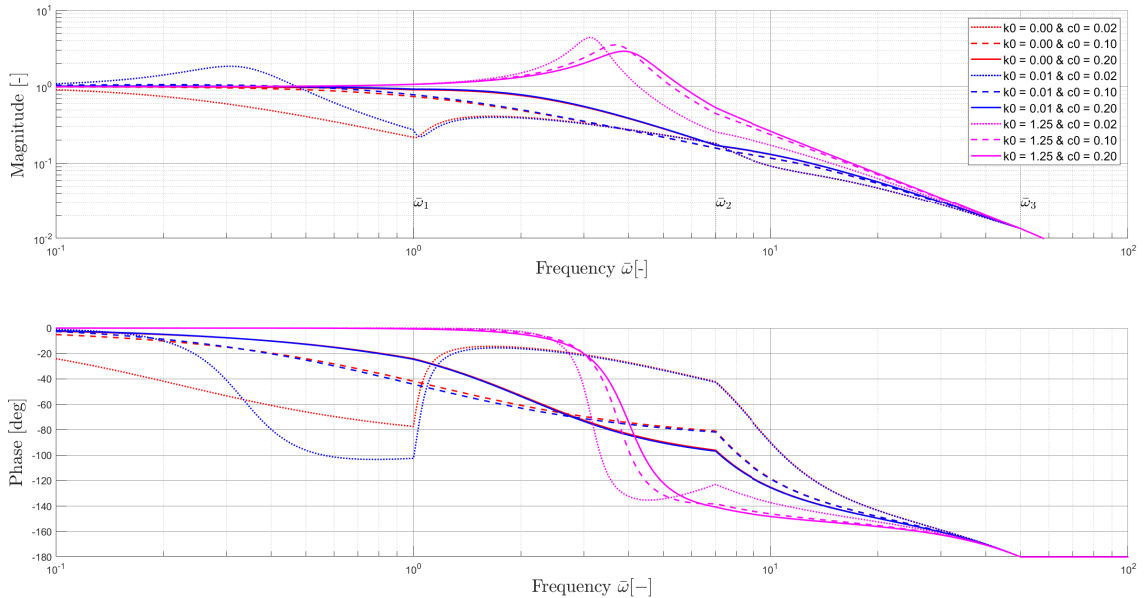


Figure 2.18: Transmissibility of the stiffness and damping characteristics in figure 2.17, the negative stiffness at:  $\bar{\omega}_1 < \bar{\omega} < \bar{\omega}_2$  causes an instability.

The solid purple line represents a 'standard' single inlet air bearing with normal stiffness and damping. Decreasing the damping causes an eigenfrequency shift and a reduced transmissibility at the mid-frequency range. These three purple characteristics show the same trend as the bearing in figure 2.15, indicating the validity of this discrete representation.

The effect of a low-stiffness and zero-stiffness design, is represented by the blue and red lines respectively. Both lines show the same trend for normal and medium damping. This means that an absolute zero-stiffness design, is not required for a strong transmissibility reduction. When the damping is reduced to almost zero, there is even less coupling in the system. However, when examining the phase, a big 'jump' is spotted between  $\bar{\omega}_1$  and  $\bar{\omega}_2$ . The system has an *unstable pole*, emerging from the negative stiffness that places the pole in the right half plane, see equation 2.45. The negative stiffness in this frequency band 'slightly' amplifies unwanted vibrations but is limited by the increasing positive damping.

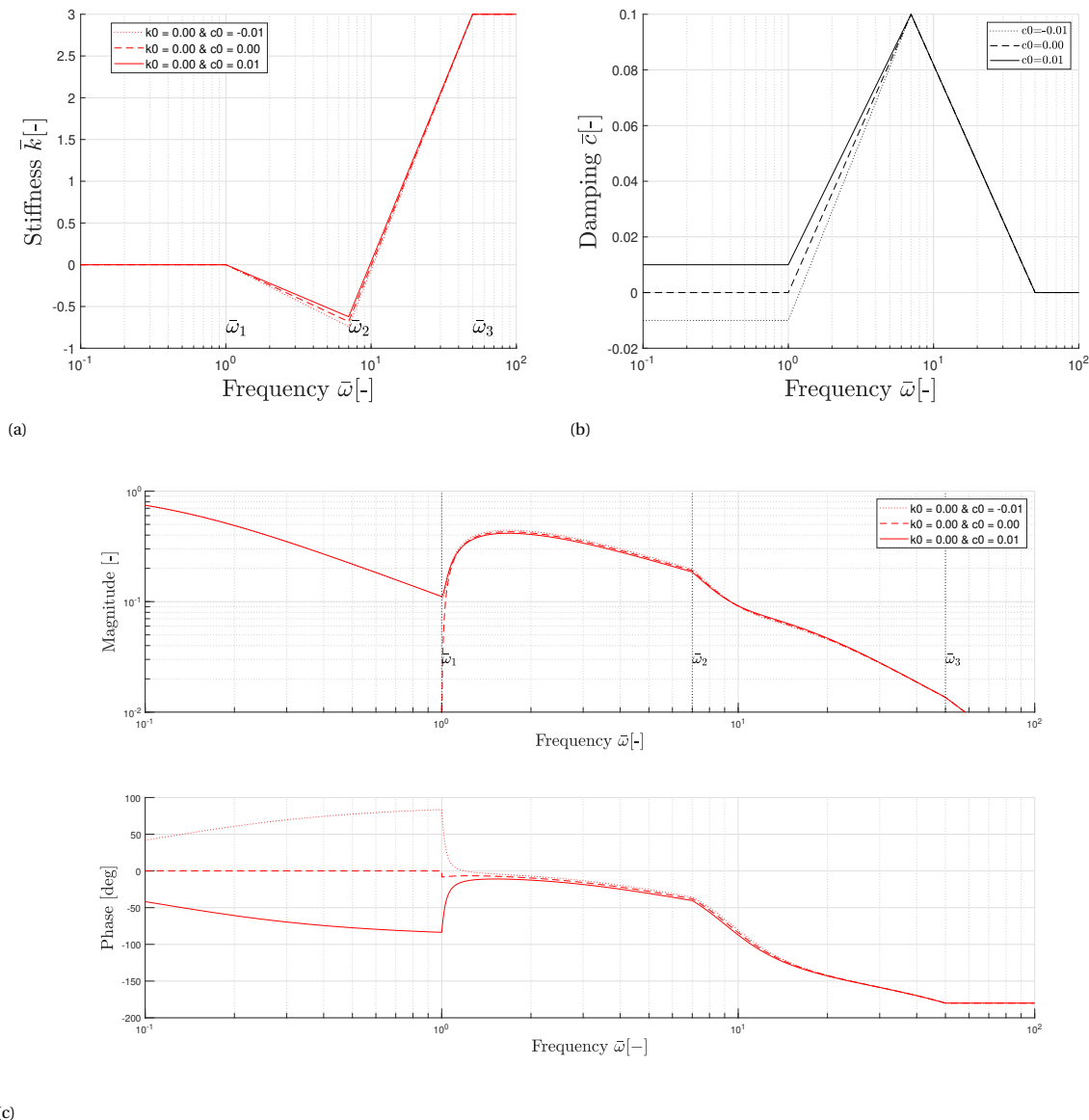


Figure 2.19: A bearing design with a statically zero- stiffness and damping characteristic. At increased frequencies the damping starts to rise and the stiffness becomes negative, creating an unstable system in limit-cycle oscillation. A slight positive damping, immediately couples the system at low frequencies, while negative damping results in a pneumatic hammer instability.

Even in a system with zero stiffness, the transmissibility starts at one because of the damping term. In theory the damping can be made zero for frequencies:  $\bar{\omega} < \bar{\omega}_1$ . In this region the stiffness stays positive, ensuring the stability. In figure 2.19 the transmissibility is plotted for a zero-stiffness system at slightly different

damping characteristics. Zero stiffness & damping is represented with the dashed line and gives zero transmissibility as expected. When  $\bar{\omega} > \bar{\omega}_1$ , the damping starts to increase causing a decreasing stiffness which immediately becomes negative. The negative stiffness yields positive *unstable* poles, placing the system in a limit cycle oscillation. The oscillation is initiated by the negative stiffness but bounded by the increasing damping.

In practice it is probably quite difficult to maintain exactly zero stiffness and damping, therefore graphs with slightly positive and negative damping are added. This gives a small transmissibility with a -1 slope in the stable frequency band and an increased transmissibility in the *unstable* region:  $\bar{\omega}_1 < \bar{\omega} < \bar{\omega}_2$ .

The negative stiffness resulting from a low damping design, gives instabilities and can be avoided in the following ways.

1. In a static zero-stiffness design, the damping  $\bar{c}(\bar{\omega})$ , should be a monotonically decreasing function, resulting in:  $\alpha \geq 0$ .
2. The static stiffness can be optimised at:  $k_0 = k(\bar{\omega} = \bar{\omega}_2, \alpha)$ , allowing a low damping design with:  $\alpha < 0$  and  $\bar{k}(\bar{\omega}) \geq 0$ .

This means there is a trade-off between minimising the stiffness or damping, depending on the magnitude of  $\alpha$ . However, limiting the minimisation of damping has a large influence on the low frequency ( $\omega < \omega_1$ ) transmissibility, the difference is illustrated by the dashed and dotted red lines in figure 2.18. The magnitude of the limit-cycle oscillations in the unstable region are unknown and might be acceptable. With the current model it is not possible to do an extensive (time-domain) analysis of these non-linear oscillations, this is left as recommendation.

## 2.5. Conclusion

The two-pad bearing model from [21] is further explored and modelled with the dimensionless compressible Reynolds equation. To be able to determine the dynamic characteristics, the method of linear perturbation is used. Besides thin-film modelling, different 'existing' inlet-restriction models are discussed. A small case study is done with mass flow measurements of syringe needles, these are used in the prototyping phase. The laminar capillary flow model, shows a good fit for small pressure differences and is used in further modelling. A two-dimensional numerical model is created and validated with an analytic study of a 'simple' axisymmetric geometry. At last a dynamic analysis is done, to obtain insights in the relation between thin-film transmissibility and air bearing dynamics.

The combination of high- and low pressure pads is a good starting point to reduce the 'static' stiffness. From the transmissibility function it becomes clear that the damping must be reduced as well. The restriction-pocket depth does not affect the static bearing characteristics and can be used to decrease damping. However, the reduced damping starts to rise at increasing perturbation frequency and can cause negative stiffness at a certain bandwidth. The negative stiffness results in a positive pole, indicating an instability. The instability is bounded by the positive increasing damping and puts the system in a limit cycle. An optimisation procedure is applied on the numerical model in the next chapter, to help find an optimal bearing design.



# 3

## Optimisation & Sensitivities

The dynamic study in section 2.4, shows that air-film stiffness and damping have a strong influence on transmissibility. In this chapter, a twofold static & dynamic optimisation procedure is proposed. The optimal air bearing characteristics are quantified and used in objective- and constraint functions. The starting point is stiffness minimisation, however, when the goal is to minimise transmissibility, dynamic optimisation is indispensable. The challenge is to obtain a statically and dynamically stable optimal design. After the optimisation, the transmissibility of a 'standard' air bearing (figure 2.2) and the optimised bearing are compared. With a sensitivity analysis, the influence of small design variations on stiffness and damping are studied. This analysis is further expanded to the transmissibility sensitivity to variations in stiffness and damping.

### 3.1. Static optimisation

A low-stiffness bearing design can be accomplished with a combination of high- and low pressure bearing pads [21]. A restricted vacuum sink adds negative stiffness to the system. To obtain a *stable* low-stiffness design, a shallow pocket or pad-height offset is needed. The shallow pocket introduces a thin-film resistance with a strong fly height dependence. This causes a change in load capacity as can be seen in figure 2.10b at  $h_0 = 0.5$ . A height offset of the low pressure pad, will shift the negative stiffness curve to larger fly heights, enabling a stable design. One of these methods, or a combination must be used to find a feasible optimum. The two-pad bearing is modelled with the Reynolds equation and laminar capillary flow theory, discussed in chapter 2. The high- and low pressure pads with geometric design variables, are depicted in figure 3.1.

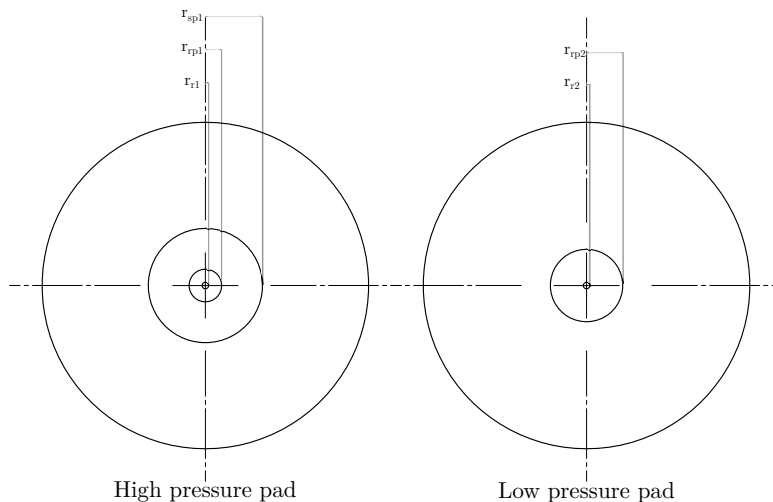


Figure 3.1: The high- and low pressure pad that is used in the optimisation, with geometric design parameters.

The static optimisation procedure is based on the  $W - h$  and  $K - h$  curves found by [21]. An optimal low stiffness air bearing characteristic, for an arbitrary design is given in figure 3.2. The optimised design must

have sufficient load carrying capacity and a stable low stiffness working point ( $h_c$ ). Stability is enforced by the increased load capacity at smaller fly heights ( $h_a$ ) and decreased load capacity at increased fly heights ( $h_e$ ). This gives a 'valley' shaped stiffness profile represented with the orange line. The low-stiffness domain is situated between fly heights  $h_b$  and  $h_d$ . The domain size limits the 'covered' vibration amplitude and should therefore be maximised.

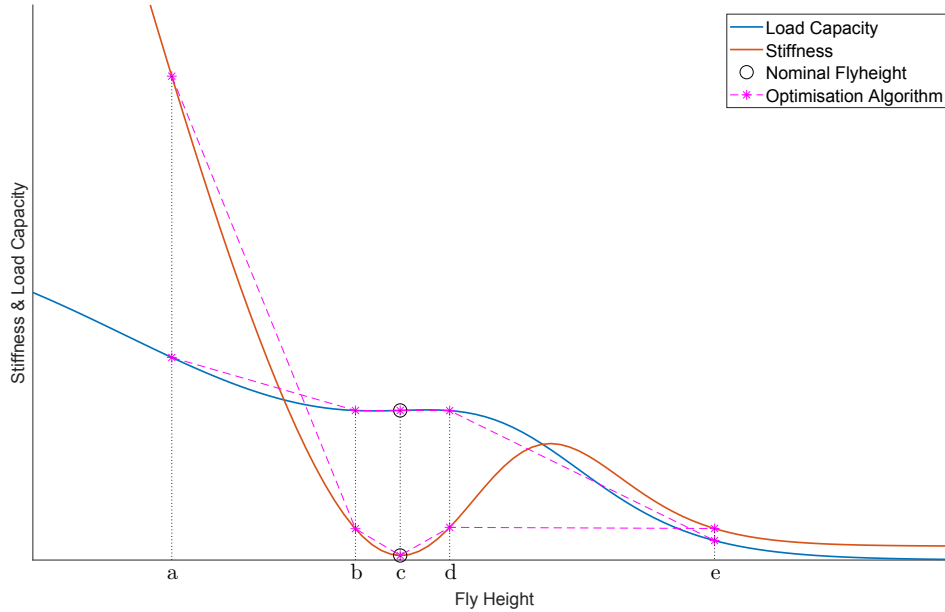


Figure 3.2: Graphical representation of a low stiffness stable air bearing design.

An objective function is defined by using the  $W - h$  and  $K - h$  graphs in figure 3.2. At every design perturbation that is initiated by the optimiser, the load capacity and stiffness are evaluated at a small number of different fly heights. Calculating the complete  $W - h$  and  $K - h$  graphs would make the model too computationally expensive and therefore impractically slow. The data obtained after every design iteration can be expressed by:  $W_n$  and  $K_n$ , where subscript  $n$  corresponds to fly heights  $a$  until  $e$ . In figure 3.2,  $W_n$  and  $K_n$  are indicated with pink asterisks connected by dotted lines, yielding a simplified bearing characteristic.

### 3.1.1. Objectives and constraints

The problem is defined as a minimisation problem with objective function:  $f(W_n(\mathbf{x}), K_n(\mathbf{x}))$ . The objective function  $f$ , is a function of load capacity  $W_n$  and stiffness  $K_n$ , which are a function of the design variables in  $\mathbf{x}$ . The total objective function consists of seven terms and is written in equation 3.1. This objective represents the desired load capacity curve in the first four terms. This results in decreasing load capacity at increasing fly height and a flat plateau around nominal fly height. The fifth term maximises the load capacity at nominal fly height. The last two terms minimise the stiffness around the nominal fly height.

$$f(\mathbf{x}) = \left(\frac{W_b}{W_a} + 1\right)^2 + \left(\frac{W_e}{W_d} + 1\right)^2 + (W_c - W_b)^2 + (W_c - W_d)^2 + \left(\frac{K_c}{W_c}\right)^2 + \left(\frac{K_b - K_d}{b - d} + 1\right)^2 + (K_b + K_c + K_d + 1)^2 \quad (3.1)$$

This objective function represents a desired bearing characteristic. Now constraint functions are used to enforce certain characteristics and to limit the total design space to a feasible design space. To find a feasible low-stiffness design, the  $W - h$  curve must be monotonically decreasing. This is already implemented in the objective function but is accentuated by using both equality- and inequality constraints, represented

by:  $h(W_n(\mathbf{x}), K_n(\mathbf{x})) = 0$  and  $g(W_n(\mathbf{x}), K_n(\mathbf{x})) \leq 0$  respectively. All six constraints are shown in equation 3.2. Constraints  $g_1$ ,  $g_2$ ,  $h_3$  and  $h_4$  ensure a monotonically decreasing  $W - h$  curve, constraint  $g_5$  enforces positive stiffness at nominal fly height and constraint  $g_6$  optimises the load capacity to a desired numerical value:  $W_n$ .

$$g_1 = \frac{W_b - W_a}{b - a} \quad g_2 = \frac{W_e - W_d}{e - d} \quad h_3 = W_b - W_c \quad h_4 = W_c - W_d \quad g_5 = -K_c \quad g_6 = W_n - W_c \quad (3.2)$$

An optimisation algorithm tries to find a global minimum in a design space. The objective and constraint functions are the link between a mathematical global minimum and the desired optimal design. When the objective- and constraint functions are not well defined, the found minimum is not a representation of an optimal design. The functions in equations 3.1 and 3.2 are iteratively determined by examining the outcome of the optimiser. After adjusting these functions a couple of times, the problem is well defined. All the terms in the objective function 3.1 are quadratic to have faster convergence.

### 3.1.2. Design variables

There are a number of design variables that are used by the optimiser to find an optimal design. The model has a high- and low pressure pad, five radii are indicated which are usable as design parameters, see figure 3.1. Besides these radii, every pocket has a certain depth, resulting in another three design variables. Both pads have an inlet pressure and a restrictor conductivity. This gives a grand total of twelve independent design variables. When the relative height between the pads is used, this becomes thirteen design variables. These design variables are collected in vector  $\mathbf{x}$ . All dimensionless independent design variables with their corresponding numerical range, are given in table 3.1.

When all the design parameters in table 3.1 are used, an optimum has to be found in a thirteen dimensional design space. In this numerical model, the design space is discontinuous, meaning that no analytical derivatives are available. A derivative free algorithm must be used in which derivatives are approximated. This results in increased computation time with increasing number of design variables since the differences are small.

Reducing the number of the design variables in table 3.1 is possible. For instance, the restrictor radii  $r_{r1}$  and  $r_{r2}$  can be taken constant. The number of design variables can be further decreased by fixing the shallow pocket depth or the radius of one of the restrictor pockets. However, oversimplifying the optimisation problem might result in overconstraining, making it impossible to find an optimum.

The restrictor pocket is used to increase or decrease the radius of a constant pressure area around the inlet or outlet. A constant pressure is only the case, if the restrictor pocket contains enough 'dead' volume of air. The volume in this pocket is a function of pocket radius and pocket depth. The pocket radius effects the static bearing characteristic, while the pocket depth only influences the dynamic characteristics. This means that the restrictor pocket depths:  $h_{rp1}$  and  $h_{rp2}$  can be omitted from the static optimisation and used to enhance dynamics in a later stage.

### 3.1.3. Static optimisation results

The used Comsol software provides a variety of different derivative free solvers. After trying different solvers and comparing computation time and the ability to find an optimum, COBYLA [34] showed the best performance in most cases. The design variables in table 3.1 are used while keeping the depth of both restrictor-pockets constant at:  $h_{rp1} = h_{rp2} = 50$ . The shallow pocket and height offset concept are based on different principles and are initially evaluated separately. It appears that the algorithm is not able to find one global optimum. Therefore six different vectors with initial design variables are used, see tables 3.2 and 3.3. The sets with initial parameters in tables 3.2 and 3.3 all show convergence. The optimality tolerance of the COBYLA solver is set at:  $1 \times 10^{-3}$ , with a maximum of 250 model evaluations.

Table 3.1: Optimisation design variables with their range of normalised values.

	<b>Parameter</b>	<b>Range</b>	<b>Description</b> dynamic/static optimisation
Thrust pad	$\bar{G}_{r1}$	(0,10]	Inlet conductivity (static)
	$\bar{P}_{s1}$	[1,7]	Supply pressure(static)
	$\bar{h}_{sp1}$	[0.05,1]	Shallow pocket depth (static)
	$\bar{h}_{rp1}$	[0,1000]	Restrictor pocket depth (dynamic)
	$\bar{r}_{r1}$	0.003	Restrictor radius
	$\bar{r}_{rp1}$	[0.15,1]	Restrictor pocket radius
	$\bar{r}_{sp1}$	[0.2,1]	Shallow pocket radius (static)
Vacuum pad	$\bar{G}_{r2}$	(0,10]	Outlet conductivity (static)
	$\bar{P}_{s2}$	[0.4,1]	Vacuum pressure (static)
	$\bar{h}_{rp2}$	[0,50]	Restrictor pocket depth (dynamic)
	$\bar{r}_{r2}$	0.003	Restrictor radius
	$\bar{r}_{rp2}$	[0.1,1]	Restrictor pocket radius (static)
General	$\bar{h}_{1,2}$	(0,1]	Height difference (static)
	$a; b; c; d; e$	0.05; 0.4; 0.6; 0.8; 3	Discrete fly height evaluations

Table 3.2: Initial design variables shallow pocket concept.

	$\mathbf{x}_{01}$	$\mathbf{x}_{02}$	$\mathbf{x}_{03}$
$\bar{G}_{r1}$	1	3	8
$\bar{P}_{s1}$	2	1.5	1.25
$\bar{h}_{sp1}$	0.1	0.1	0.1
$\bar{r}_{rp1}$	0.2	0.2	0.1
$\bar{r}_{sp1}$	0.28	0.5	0.7
$\bar{G}_{r2}$	2.5	3	3.5
$\bar{P}_{s2}$	0.7	0.5	0.5
$\bar{r}_{rp2}$	0.25	0.4	0.6

Table 3.3: Initial design variables height offset concept.

	$\mathbf{x}_{01}$	$\mathbf{x}_{02}$	$\mathbf{x}_{03}$
$\bar{G}_{r1}$	1	3	8
$\bar{P}_{s1}$	2	1.5	1.25
$\bar{r}_{rp1}$	0.2	0.2	0.1
$\bar{h}_{1,2}$	0.5	0.5	0.5
$\bar{G}_{r2}$	2.5	3	3.5
$\bar{P}_{s2}$	0.7	0.5	0.5
$\bar{r}_{rp2}$	0.25	0.4	0.6

Every set of initial variables converges to a different local optimum in the design space, see the optimisation results in tables 3.4 and 3.5. The optimised geometries with their pressure distribution at nominal fly height, are depicted in figure 3.4. When only examining the value of the objective function  $f(\mathbf{x})$ , design  $\mathbf{x}_1$  is supposed to be most optimal for both concepts. The load capacity and stiffness of the optimised designs are plotted in figure 3.3, the vertical grey lines indicate the evaluated fly-heights in the optimiser. A lower objective value does not necessarily indicate the 'best' design. One could argue that design  $\mathbf{x}_3$  is optimal, since it covers a larger low-stiffness domain. A downside of this design is the smaller stiffness and load capacity at low fly heights, explaining the higher objective value.

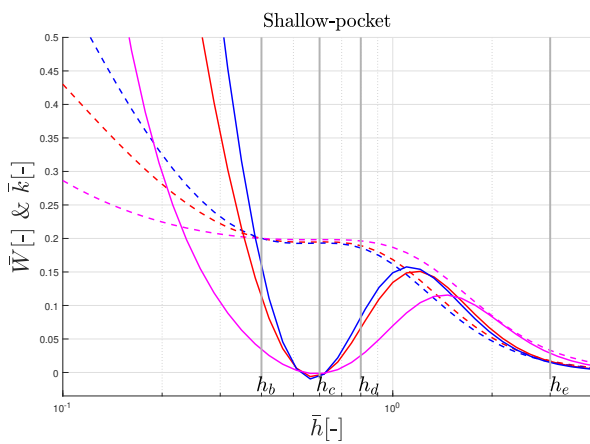
The optimised shallow pocket designs have a lower final objective value than the height offset concepts. This translates to a lower load capacity at small fly heights, indicating a less stable design. Furthermore, the height offset concept has a strong transition in load capacity, at the boundaries of the zero-stiffness domain. Contrary, the shallow pocket shows a smoother transition in load capacity. Based on these results, both concepts are perfectly usable in a bearing application. The shallow-pocket bearing, shows slightly better results.

Table 3.4: Optimised shallow pocket concept.

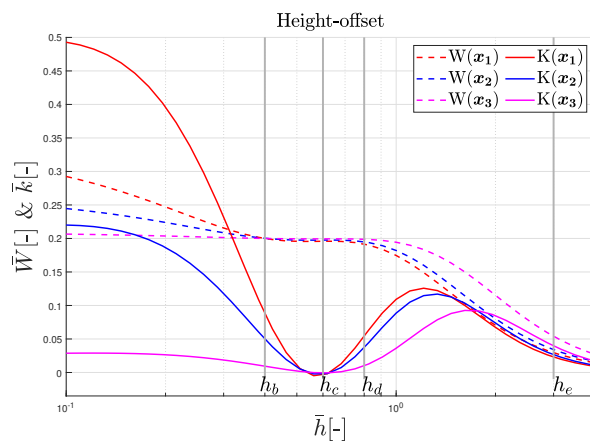
	$\mathbf{x}_1$	$\mathbf{x}_2$	$\mathbf{x}_3$
$\bar{G}_{r1}$	2.1387	3.204	7.998
$\bar{P}_{s1}$	1.6802	1.542	1.316
$\bar{h}_{sp1}$	0.074	0.047	0.048
$\bar{r}_{rp1}$	0.145	0.160	0.278
$\bar{r}_{sp1}$	0.515	0.645	0.830
$\bar{G}_{r2}$	2.559	2.997	3.439
$\bar{P}_{s2}$	0.497	0.656	0.802
$\bar{r}_{rp2}$	0.336	0.305	0.270
$f(\mathbf{x})$	0.85434	0.87526	0.94566
Time [s]	257	290	270
Evaluations	123	93	121

Table 3.5: Optimised height offset concept.

	$\mathbf{x}_1$	$\mathbf{x}_2$	$\mathbf{x}_3$
$\bar{G}_{r1}$	2.0443	3.1594	8.2351
$\bar{P}_{s1}$	2.1838	1.9483	1.6171
$\bar{r}_{rp1}$	0.14581	0.1474	0.1494
$\bar{h}_{1,2}$	0.9269	0.3712	0.2599
$\bar{G}_{r2}$	2.426	2.9765	3.7879
$\bar{P}_{s2}$	0.4958	0.5043	0.3994
$\bar{r}_{rp2}$	0.4610	0.3709	0.1229
$f(\mathbf{x})$	0.99531	1.0817	1.2116
Time [s]	204	149	154
Evaluations	92	70	88



(a) Shallow pocket concept



(b) Height-offset concept

Figure 3.3: Static optimisation results for the shallow-pocket and height-offset concept. The shallow-pocket designs generally have a higher stability, as a result of the increased stiffness at low fly heights.

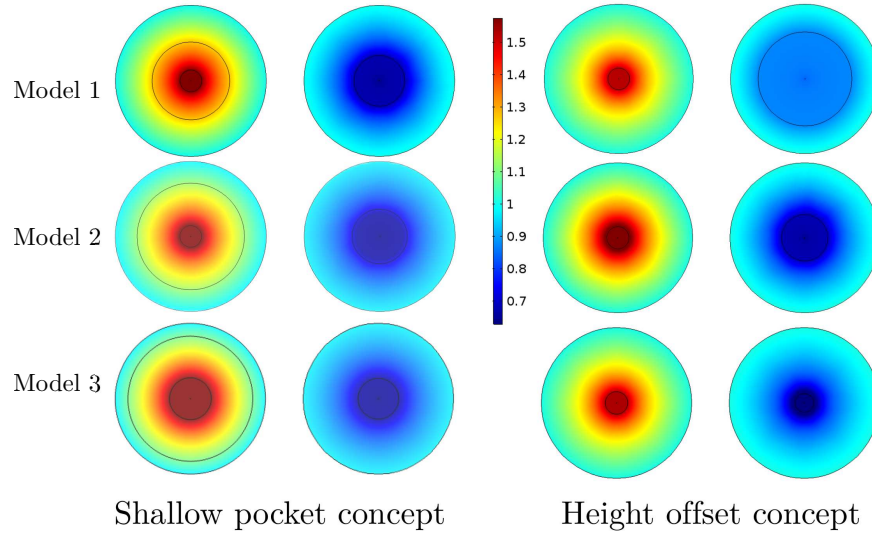
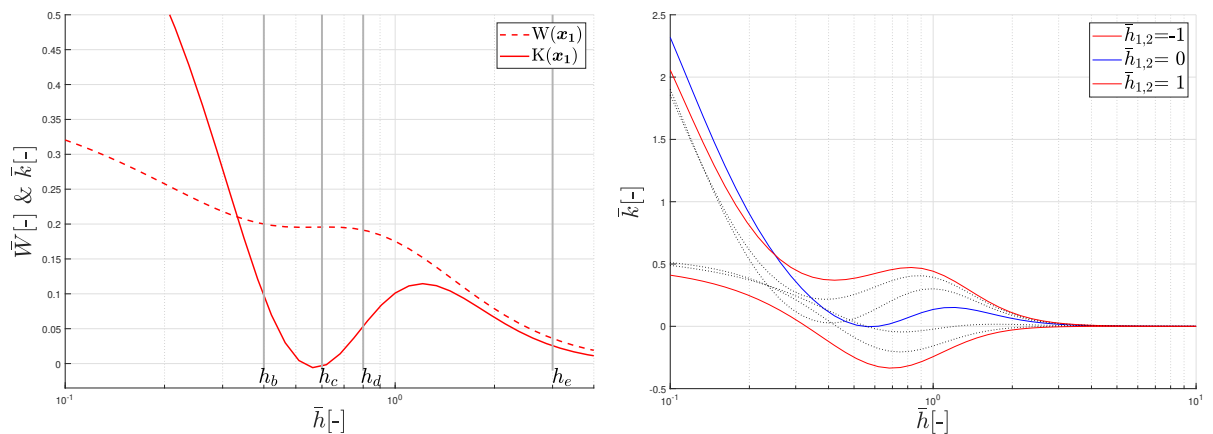


Figure 3.4: Bearing geometries for six optimised designs with pressure distribution at nominal 'low-stiffness' fly height.

### 3.1.4. Combining shallow-pocket with height-offset

Combining a shallow pocket with a pad height-offset, might improve the results that are found in the previous section. For both concepts, the optimised design  $\mathbf{x}_1$  in tables 3.4 and 3.5 has the lowest objective function value. These optimisation results are chosen as initial conditions for a hybrid design, in case of mutual design variables the mean value has been used. The optimised characteristics of this hybrid design are depicted in figure 3.5a. This hybrid characteristic does not show a clear improvement, when compared with the individual concepts. There is, however, the possibility of adjusting the height-offset to tune the design. The influence of the relative pad height-offset on the bearing stiffness, is shown in figure 3.5b. The blue line is the optimised shallow-pocket bearing from the previous section. The stiffness characteristic shows a shift when a pad height-offset with a range of:  $(-1 < \bar{h}_{1,2} < 1)$  is applied, the maxima are plotted in red. The stiffness graph maintains its characteristic 'valley' shaped curve. Therefore variable  $\bar{h}_{1,2}$  is suitable to increase or decrease the low-stiffness operation point, without losing its stability.

A hybrid design combines the higher stability of a shallow pocket, with the ability to apply small changes in stiffness. The latter is only true for an adaptive bearing design, without a fixed pad offset.



(a) Optimised hybrid bearing design with:  $\bar{h}_{sp} = 0.046[-]$  &  $\bar{h}_{1,2} = 0.84[-]$ .

(b) Optimised shallow-pocket stiffness at various pad height-offsets.

Figure 3.5: Hybrid bearing design characteristics.

## 3.2. Dynamic bearing characteristic

The optimised shallow pocket bearing design  $\mathbf{x}_1$ , from table 3.4 and figures 3.3 & 3.5b, is used for dynamic analysis. The influence of scaling parameters, possible pad-offset and restriction-pocket depth, on the overall dynamic performance is studied. First the frequency dependent stiffness and damping are determined at the

nominal 'static-low-stiffness' fly height:  $h_0 = 0.6$ , see figure 3.6. Then the influence of perturbation frequency and fly height on stiffness and damping is discussed. Based on these findings, the *static* design  $\mathbf{x}_1$ , is dynamically optimised to get a stable low-transmissibility design.

The dynamic stiffness and damping characteristics, are a function of the thin-film 'dead' restriction-pocket volume, as stated in section 2.4. Adding 'dead' volume to the high-pressure pad, reduces low-frequency damping, while the opposite is true for the low-pressure pad. So adding volume to the vacuum restriction-pocket  $r_{rp2}$ , increases low-frequency damping.

In figure 3.6 the:  $\bar{k} - \bar{\omega}$  and  $\bar{c} - \bar{\omega}$  graphs are depicted, at a constant fly height of  $\bar{h} = 0.6$  and at different restriction-pocket depths. At low frequencies the stiffness equals the optimised static stiffness, which is close to zero. When the damping increases, negative stiffness occurs, this is in agreement with the preliminary findings in section 2.4.

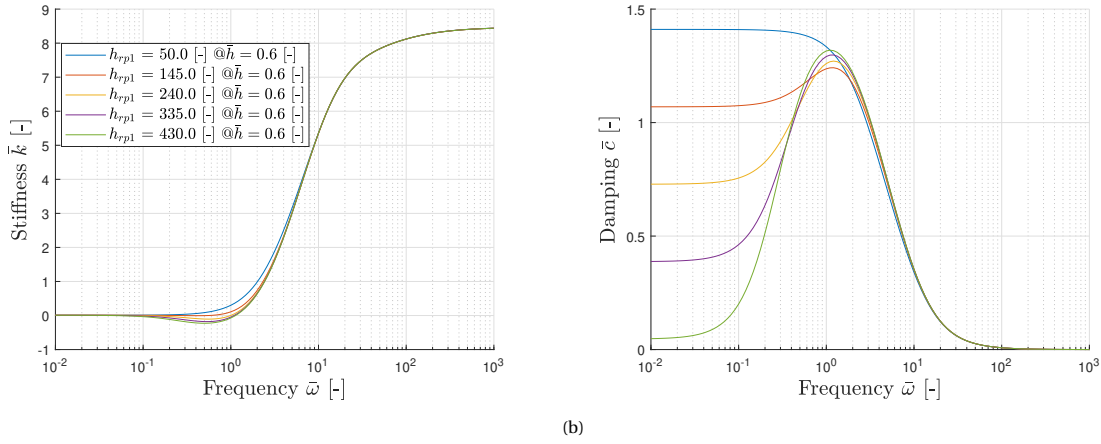


Figure 3.6: Stiffness and damping at different frequencies and restrictor pocket depths.

The characteristics in figure 3.6 are evaluated at a constant fly height, although the perturbation amplitude has a significant influence on the characteristics. Therefore, the  $\bar{k} - \bar{h}$  and  $\bar{c} - \bar{h}$  graphs are given in figure 3.7, at a constant low frequency and various restriction-pocket depths. All stiffness graphs overlap as is expected from figure 3.6a, however, the damping shows a strong fly height dependence that is non-monotonic for:  $h_{rp1} > 145$ . The minimum negative damping occurs around a fly height of:  $\bar{h} = 1$  for all  $\bar{h}_{rp1}$ . The low-stiffness operating point at:  $\bar{h}_0 = 0.65$  (dotted line) and the fly height where minimum damping occurs do not overlap. For:  $\bar{h}_{rp1} > 145$ , the bearing will be immediately unstable if the fly height is increased by a small input perturbation. Once damping is negative, the bearing becomes self-exciting, increasing the vibration amplitude.

Negative damping should be avoided for all fly heights and perturbation frequencies. To do so, the amount of 'dead' restriction-pocket volume can be reduced. However, this increases the damping at the optimised nominal low-stiffness fly height, yielding higher transmissibility. A solution is to align the low-stiffness fly height with the low damping fly height. Damping scales cubically with fly height, making it impossible to shift  $\min(\bar{c})$  to the lower fly heights. However, shifting the low stiffness point to the larger fly heights is possible by changing the relative pad offset  $h_{1,2}$ , see figure 3.5b. These findings are used to dynamically optimise the 2-pad bearing concept in section 3.3.

The characteristics in figure 3.7 are evaluated at a low perturbation frequency of:  $\bar{\omega} = 1 \times 10^{-2}$ . From figure 3.6 the following is known. in case of  $\bar{h}_{rp1} = 50$ , the stiffness increases and damping decreases monotonically, when perturbation frequency increases. For a deeper restriction-pocket, the stiffness first shows a decrease, while damping first rises before convergence to  $\bar{c}_{\bar{\omega} \rightarrow \infty} = 0$ . The influence of perturbation frequency on  $\bar{k}$  &  $\bar{c}$ , is now studied for a range of fly heights, see figure 3.8. The linear frequency increment between each plotted line is:  $\Delta\bar{\omega} = \bar{\omega}_{i+1} - \bar{\omega}_i = 0.41[-]$ .

For  $\bar{h}_{rp1} = 50$ , the stiffness- and damping show a monotonic increase- and decrease respectively, at increasing perturbation frequency. The carefully optimised *static* low-stiffness curve holds its shape at low frequencies. The local low-stiffness minimum shifts to higher fly heights when increasing frequency, while the damping stays positive at all fly heights and decreases. For  $\bar{h}_{rp1} = 430$ , the stiffness shape is preserved

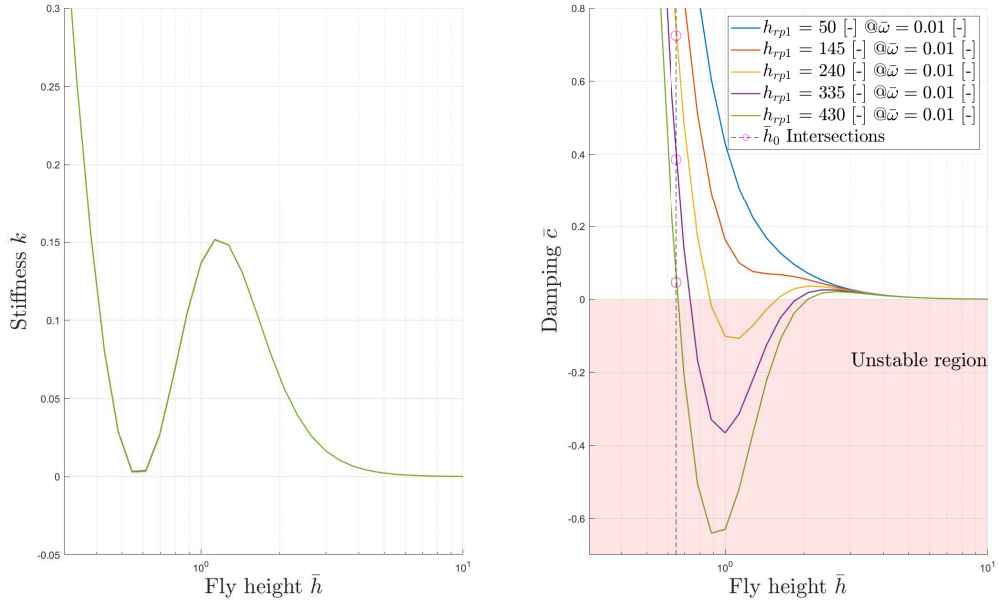


Figure 3.7: Characteristics of the statically optimised shallow-pocket bearing, design  $\mathbf{x}_1$  in table 3.4. The stiffness is not affected by an increased 'dead' restriction-pocket volume for low perturbation frequencies. The minimum damping- and the operating fly height do not coincide, yielding an unstable system.

for a larger range of 'low to mid' range frequencies, because, before the stiffness rises, it becomes negative first. The same trend of fly height shifting, of the minimum stiffness operating point, is visible. Damping is negative at larger fly heights and low frequencies, yielding an unstable system.

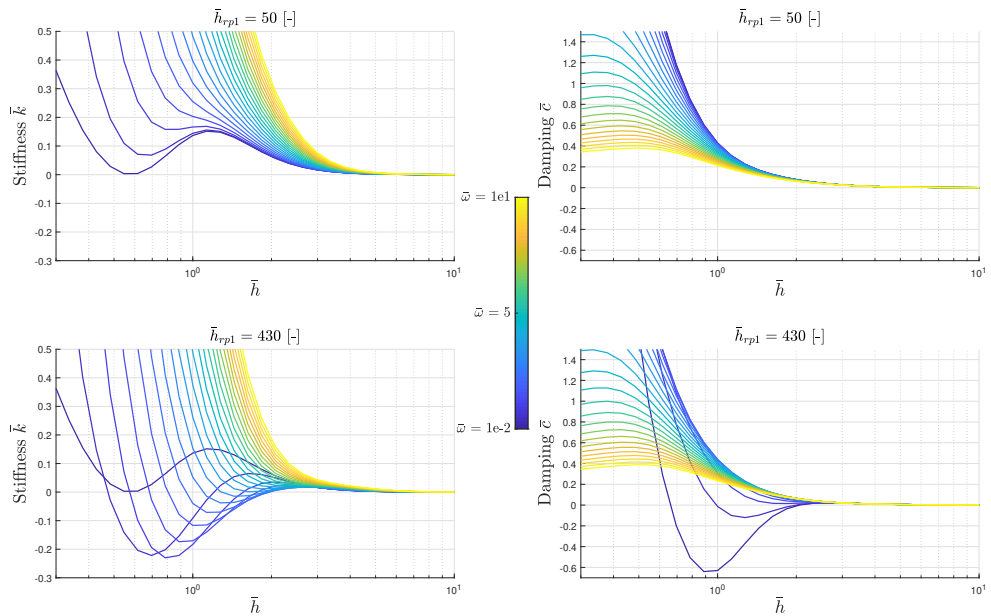


Figure 3.8: Stiffness and damping as function of fly height and perturbation frequency at restriction-pocket depths of  $h_{rpl} = 50$  and  $h_{rpl} = 430$ . The characteristics belong to the statically optimised low-stiffness shallow pocket bearing, design  $\mathbf{x}_1$  in table 3.4. A deep restriction-pocket, leads to negative stiffness at the low to mid-frequency range and negative damping at larger fly heights.



### 3.3. Dynamic optimisation

The static optimisation in the first section, leads to a stable low-stiffness air bearing design with relative high damping. When the perturbation frequency increases, the low-stiffness operating point increases, while shifting to a larger fly height. The addition of 'positive' - and 'negative' *dead* volume, by enlarging  $h_{rp1}$  and  $h_{rp2}$  respectively, decreases or increases damping. In the current optimised static designs, the low-stiffness operating point and low damping point do not coincide. This results in a range of fly heights with negative damping and stiffness in a certain frequency bandwidth. In this section the dynamic bearing properties are enhanced by reducing the damping, while ensuring it stays positive for all fly heights. It is investigated, whether it is possible to coincide the stiffness- and dynamic nominal fly heights. Starting point for the dynamic optimisation, is the statically optimised shallow pocket bearing:  $\mathbf{x}_1$  in table 3.4.

The goal is to minimise and align the stiffness- and damping characteristics, to create a stable low-transmissibility bearing design. The objective and constraint functions from section 3.1.1 are used and extended with additional terms. The same design variables that are used in the static optimisation are applicable, see table 3.1. However, the restriction-pocket depths:  $h_{rp1}$  and  $h_{rp2}$  will be used as design variables to change the damping. Furthermore, the discrete fly height evaluation points:  $a, b, c, d, e$  are adapted, to enable stiffness and damping alignment. Only one objective term and two constraint terms are added to equations 3.1 and 3.2 respectively, see equation 3.3.

$$\begin{aligned}
 f(\mathbf{x}) &= f(\mathbf{x})_{static} + 3 \times (C_c + 1)^2 \\
 g_7 &= -C_c \\
 g_8 &= \frac{C_c - C_b}{c - b} + 0.005
 \end{aligned} \tag{3.3}$$

The additional objective term minimises the damping at the nominal fly height evaluation point:  $\mathbf{h}_c$ , a scaling factor of *three* appears to give the most promising results. Not all design variables in table 3.1 are used in this optimisation. Better results are found when keeping the geometry of the statically optimal shallow pocket bearing unaltered and when using a smaller set of design variables. However, the pressures, restriction conductivities, pad offset and restriction-pocket depth are used to find a new 'shifted' optimum. From the damping graphs in figure 3.8, it appears that the low damping fly height is situated around:  $\bar{h} = 1$ . The fly height evaluation as depicted in figure 3.2, are chosen as follows:  $\mathbf{h}_a = 0.05$ ,  $\mathbf{h}_b = 0.88$ ,  $\mathbf{h}_c = 1$ ,  $\mathbf{h}_d = 1.15$ ,  $\mathbf{h}_e = 3$ . Increasing the nominal fly height will inevitably decrease the load capacity. It is therefore necessary to relax constraint  $g_6$  in equation 3.2 or to change  $W_n$  to a lower, more realistic value.

The initial design variables and the final optimised result are given in figure 3.9. The individual high- and low pressure pad characteristics, are depicted with dotted and dashed lines. The combined pads yield a relative low load capacity, almost zero stiffness and very small damping at:  $\bar{h}_0 = 1$ . Increasing the load capacity  $\bar{w}$ , seems to be impossible at this low damping fly height region. Increasing the perturbation frequency, yields the damping and stiffness characteristics in figure 3.10. The design with:  $\bar{h}_{rp1} = 130$  has a less critical damping characteristic and positive stiffness for all perturbation frequencies. Any increase of dead volume, e.a  $\bar{h}_{rp1} > 130$ , leads to a bandwidth of negative stiffness. The optimised low-damping design with  $\bar{h}_{rp1} = 401.63$ , has positive damping for all frequencies but develops negative stiffness.

	$\mathbf{x}_0$	$\mathbf{x}$
$\bar{G}_{r1}$	3.0	2.94
$\bar{P}_{s1}$	1.8	1.6103
$\bar{h}_{rp1}$	400	401.63
$\bar{h}_{1,2}$	0.5	0.4
$\bar{h}_{sp1}$		0.074
$\bar{r}_{sp1}$		0.515
$\bar{r}_{rp1}$		0.145
$\bar{r}_{r1}$		0.003

$\bar{G}_{r2}$	3.5	3.88
$\bar{P}_{s2}$	0.5	0.61456
$\bar{r}_{rp2}$		0.336
$\bar{h}_{rp2}$		1.5
$\bar{r}_{r2}$		0.003

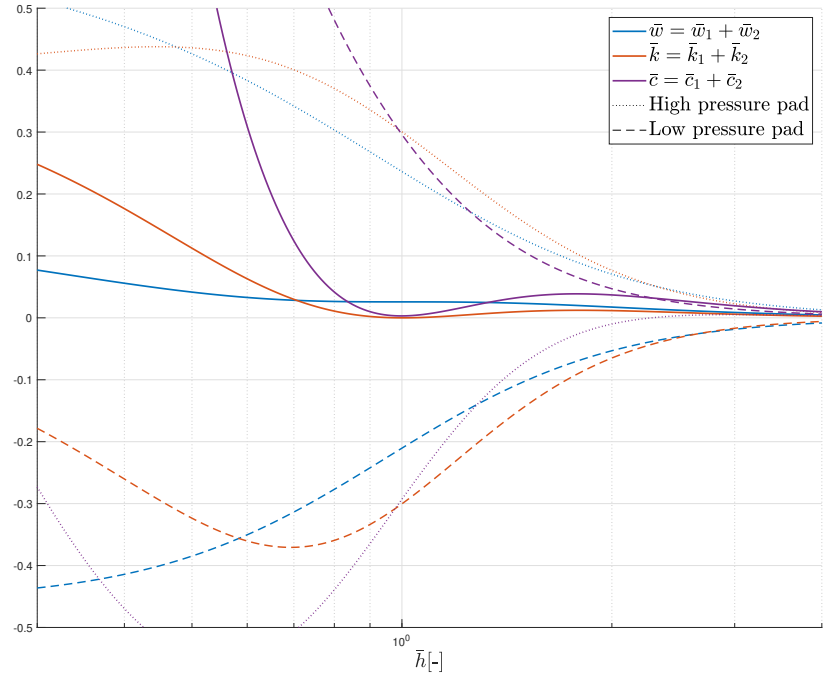


Figure 3.9: Table with initial design variables and the final optimised design, the graph gives the individual pad- and total bearing characteristics at  $\bar{\omega} = 0.01$ .

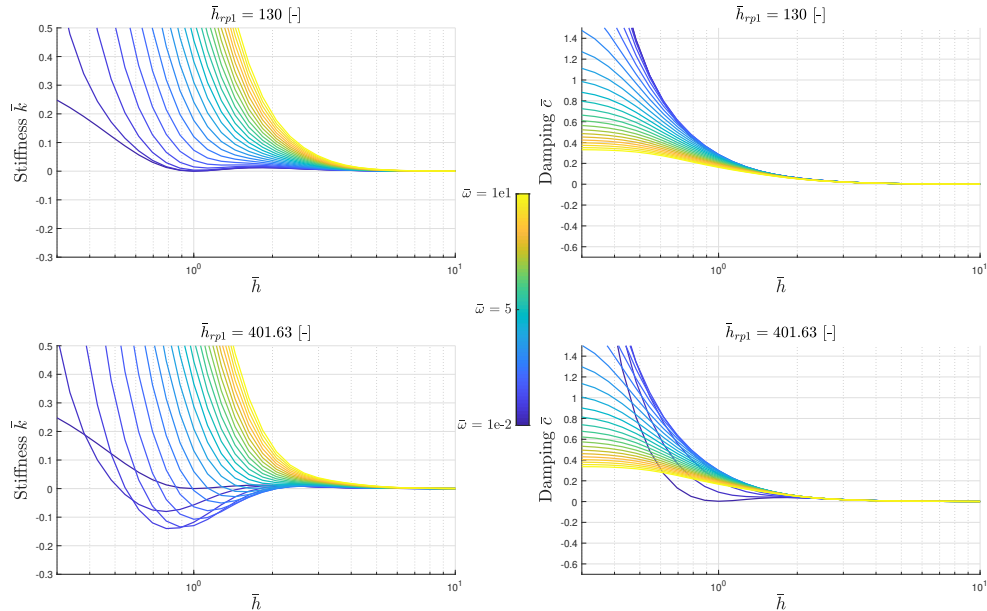


Figure 3.10: Stiffness and damping as function of fly height and perturbation frequency at restriction-pocket depths of  $h_{rp1} = 130$  and  $h_{rp1} = 401.63$ . The characteristics belong to the statically & dynamically optimised low-stiffness & low-damping bearing design, from figure 3.9. The  $h_{rp1} = 401.63$  design has low damping and stiffness but develops negative stiffness at increasing frequency

### 3.4. Transmissibility and stability

The characteristics in figure 3.10 are used in the transmissibility equation as shown in equation 3.5. This relation is only valid if  $\bar{k}$  and  $\bar{c}$  are assumed linear with displacement, so a small perturbation amplitude. However, the non-linearity caused by an increase in perturbation frequency, has more impact on  $\bar{k}$  and  $\bar{c}$  than small displacements:

$$\Delta\bar{k}(\Delta\bar{h}) < \Delta\bar{k}(\Delta\bar{\omega}) \quad \& \quad \Delta\bar{c}(\Delta\bar{h}) < \Delta\bar{c}(\Delta\bar{\omega}) \quad (3.4)$$

The transmissibility of the system is determined at:  $\bar{h} = \bar{h}_0 = 1$  with  $\bar{k}(\bar{\omega})$  and  $\bar{c}(\bar{\omega})$ , using equation 3.5.

$$T(\bar{\omega}) = \frac{\bar{c}(\bar{\omega})j\bar{\omega} + \bar{k}(\bar{\omega})}{-\frac{H\Omega^2\bar{W}}{g}\bar{\omega}^2 + \bar{c}(\bar{\omega})j\bar{\omega} + \bar{k}(\bar{\omega})} \quad (3.5)$$

The 'mass' term in equation 3.5 is a collection of dimensional scaling parameters that have a large influence on  $T(\bar{\omega})$ , rewriting gives:

$$\frac{H\Omega^2\bar{W}}{g} = \frac{P^2H^5\bar{W}}{144\eta^2gR^4} \quad (3.6)$$

The scaling parameters  $R$  and  $H$ , determine the final bearing's radii and feature heights respectively, see equation 2.5. The dimensionless frequency is scaled with  $\Omega$ , causing a 'horizontal' shift of  $T(\omega)$  depending on the scaled design. In table 3.6 the scaling height  $H$  is determined at a number of possible final nominal fly heights, furthermore the influence of  $H$  and  $R$  in equation 3.6 is determined. A combination of a low nominal fly height with a relative large bearing radius, gives the smallest scaling factor:  $H^5/R^4 = 1.3 \times 10^{-16}$  [m]. This gives a rather low 'mass' term in equation 3.6 and therefore a larger transmissibility.

Table 3.6: Scaling the bearing to different fly heights and radii

$h_{desired}$ [μm]	$\bar{h}$	$H$ [μm]	$R$ [mm]	$\frac{H^5}{R^4} * 1 \times 10^{16}$ [m]
10	1	10	12.5	1.3107
15	1	15	6	5.8594
20	1	20	3	395.06

The 'mass' term in equation 3.6 gives insight in the physics affecting the transmissibility of the system. Increasing the load capacity  $\bar{W}$ , gives a larger moving mass and consequently a lower eigenfrequency and transmissibility. An increase in fly height  $H$  causes a 'third order' decrease in damping and a small decrease of stiffness, this is in agreement with equation 2.12 and [15]. The bearing radius  $R$  has an opposite effect on both damping and stiffness. The damping shows a 'fourth order' increase with  $R$  at low frequency squeezing motion, resulting from the increased thin film area. An increase in bearing area yields higher load capacity, this effect is however subordinate to the higher damping. Besides, an increase in moving mass is undesired in this application. The damping and stiffness characteristics are also a function of perturbation amplitude. An effort is made to maximise the low-stiffness fly height region by increasing the distance between points **b** and **d** in figure 3.2.

The stability and transmissibility of the optimised bearing is analysed at: various restriction-pocket depths, a nominal fly height of  $h_0 = 20\mu\text{m}$  and a bearing radius of  $R = 5\text{mm}$ . This particular bearing radius gives a load capacity of a few grams, just enough to support a small silicon wafer. The real pole parts of different bearing designs are plotted as a function of frequency in figure 3.11. The system has negative poles for  $\bar{h}_{rp1} = 130$  and corresponds to the blue lines in the transmissibility plot, see figure 3.12. The relatively high damping does not increase, resulting in a positive stiffness at all frequencies. This damping causes a slow decay of the transmissibility. This characteristic is only slightly 'better' than a standard single inlet bearing with equal load capacity. The standard reference bearing has no shallow pocket and vacuum outlet and a low supply pressure of  $P_s = 105\text{kPa}$  is chosen to match the load capacities. The stiffness of the reference bearing is 615 times larger than the stiffness of the optimised designs at lower frequencies. This difference results in a eigenfrequency that is 24 times larger. This explains the resonance peak at 100Hz for the reference bearing design and the absence of a clear peak in the optimised low-stiffness  $\bar{h}_{rp1} = 130$  design.

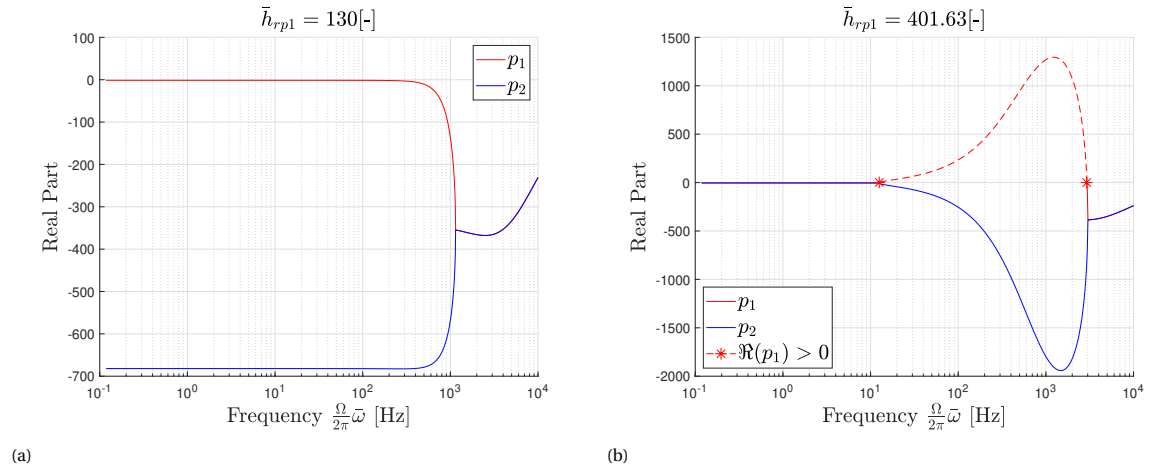


Figure 3.11: Real pole locations as a function of perturbation frequency for two restriction-pocket depths. With scaling parameters:  $H = 20\mu\text{m}$ ,  $R = 5\text{mm}$ . A deep restriction-pocket develops negative stiffness at a frequency bandwidth of:  $10 < \bar{\omega} < 3\text{kHz}$ , giving an unstable pole.

The comparison of the standard reference bearing with the low-stiffness normal-damping  $h_{rp1} = 130$  bearing, clearly illustrates the importance of damping reduction. The low-damping designs are also plotted in figure 3.12, where the  $h_{rp1} = 401$  bearing has the lowest damping. This design shows a resonance peak around 4 Hz, resulting from the lack of damping. It is possible to shift this peak to lower frequencies by further reducing the stiffness. However, it is decided to study the model sensitivities and their relation to the stiffness and damping first. Since an extremely small supply-pressure variation may already have a significant effect on performance. The deep restriction-pocket leads to negative stiffness and a positive pole, see figure 3.11b. The red markers in figures 3.11 & 3.12, indicate the frequencies where the stiffness just becomes negative. The amplitude of the negative stiffness is very small at mid-frequency range and oscillations are bounded by a proportionally increasing damping. A limit cycle analysis would give more insight in the exact behaviour of the system at this frequency band, this is left for future work.

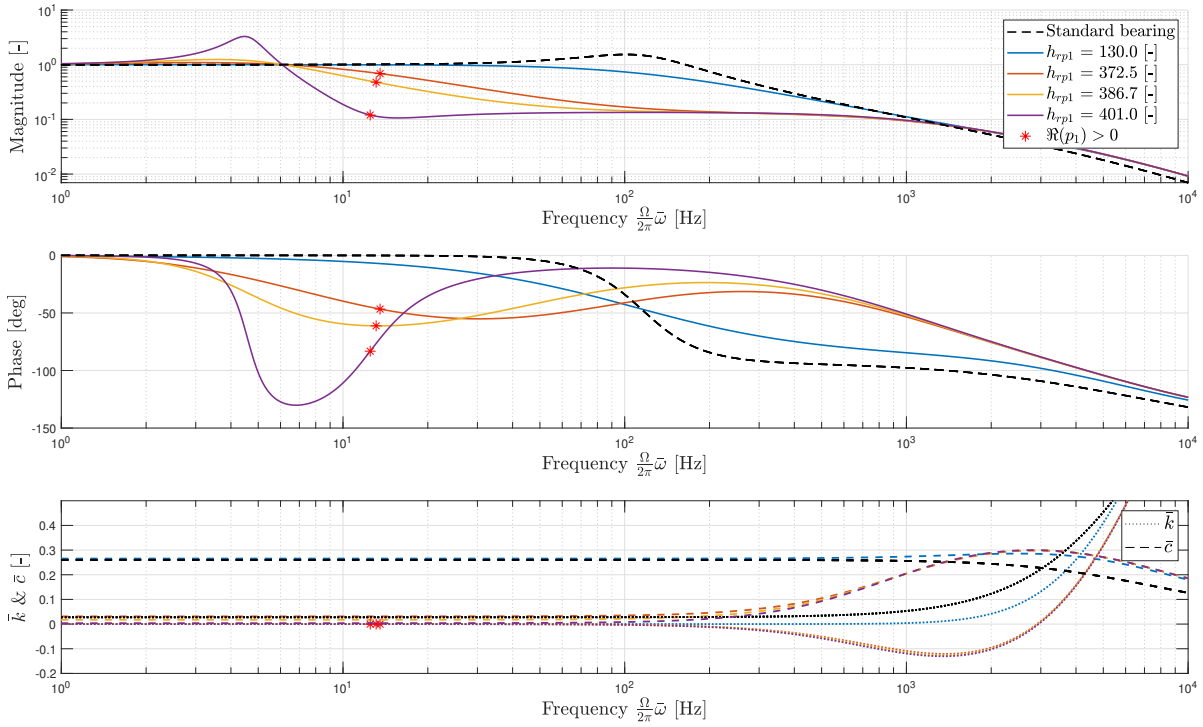


Figure 3.12: Transmissibility of the optimised shallow pocket bearing at different restriction-pocket depths, with:  $H = 20\mu\text{m}$  and  $R = 5\text{mm}$ , the deep restriction-pocket shows a positive real pole, resulting from negative stiffness. The bottom plot shows the damping and stiffness, the latter becomes negative at the red markers.

### 3.5. Sensitivity analysis

The previous sections show that it is possible to minimise stiffness and damping in a two-pad bearing design. The final eigenfrequency of the optimised designs in figure 3.12, is found to be 4 Hz. Further fine-tuning towards a lower eigenfrequency, can easily be done and will reduce the transmissibility, especially at low frequencies. However, this must be proportional to possible system variations, like: small fly height non-linearities of  $\bar{k}$  &  $\bar{c}$  around the operating point and small design perturbations during operation. Therefore, the influences of design variables on the bearing characteristics are studied in a sensitivity analysis, this is done in two steps. First the design variable sensitivities are determined, then the influence on the thin-film transmissibility is studied. At last the influence of fly height non-linearities on transmissibility is discussed.

#### 3.5.1. Design variable sensitivity

The following variables are analysed: supply- and vacuum pressure, restriction conductivities and shallow pocket depth. The optimised model from figure 3.9 is used as reference and each variable is slightly varied. Each design perturbation from the optimised operating point, directly leads to worse stiffness and damping as expected. All the original and perturbed characteristics are visualised in figure 3.13. The sensitivities are calculated by taking the partial derivatives of  $\bar{k}$  and  $\bar{c}$  with respect to the design variables at the operating fly height  $\bar{h}_0 = 1$  &  $\bar{\omega} = 0.01$ , see table in figure 3.13.

The supply- and vacuum pressures have a large influence on the stiffness and damping and suffer from supply-line variations during operation. Any offset in restriction conductivity or pockets will change the characteristics, but these geometric variables remain constant after manufacturing and are unlikely to change during bearing operation. The low-stiffness 'static' optimum in figure 3.12 is currently:  $\bar{k}(\omega = 1\text{ Hz}) = 5 \times 10^{-5}$ , a slight change in supply pressure of 100 Pa yields a stiffness increase of:  $\Delta\bar{k} = 5.4 \times 10^{-4}$ . This means that the operating-point stiffness, is a factor 12 higher than the initial optimal value, the same holds for the damping. A small decrease of supply pressure can therefore also lead to negative stiffness and damping, resulting in instabilities.

It can be concluded that both stiffness and damping are very sensitive to small design perturbations. The main disadvantage is the large supply pressure sensitivity, since it is hard to control within these tolerances. The influence of stiffness and damping on the transmissibility function is studied in the next section.

### 3.5.2. Transmissibility sensitivity

Now that the influence of small design perturbations on stiffness and damping is known, the effect on the transmissibility function is studied. The sensitivity to stiffness and damping can be derived analytically, by taking the partial derivatives of equation 3.5, this gives the functions in equation 3.7. The stiffness sensitivity function, is inversely quadratic proportional with frequency, giving a '-2' slope at higher frequencies, while the damping sensitivity function is inversely proportional, giving a '-1' slope at higher frequencies.

$$\left| \frac{\partial T(\bar{\omega})}{\partial \bar{k}} \right|_{\bar{h}=\bar{h}_0} = \left| \frac{-\frac{H\Omega^2 \bar{W}}{g} \bar{\omega}^2}{\left(-\frac{H\Omega^2 \bar{W}}{g} \bar{\omega}^2 + \bar{c}(\bar{\omega}) j \bar{\omega} + \bar{k}(\bar{\omega})\right)^2} \right| \quad \left| \frac{\partial T(\bar{\omega})}{\partial \bar{c}} \right|_{\bar{h}=\bar{h}_0} = \left| \frac{-\frac{H\Omega^2 \bar{W}}{g} \bar{\omega}^3 j}{\left(-\frac{H\Omega^2 \bar{W}}{g} \bar{\omega}^2 + \bar{c}(\bar{\omega}) j \bar{\omega} + \bar{k}(\bar{\omega})\right)^2} \right| \quad (3.7)$$

The sensitivities of the previously discussed bearing transmissibility from figure 3.12, are depicted in figure 3.14. The standard bearing (black lines) has a high stiffness, when compared with the low-stiffness designs (coloured lines). The blue design has a low-stiffness operating point, resulting in an strong sensitivity increase at lower frequencies. The damping sensitivity also shows an increase, when the thin-film damping is decreased in the *red, yellow, purple* designs. Both sensitivity functions, show a clear peak around the optimised design resonance frequency of 4Hz. A further reduction of the stiffness in the system pushes the resonance frequency to the 'left', while following the -2 slope in case of stiffness sensitivity lines and the -1 slope for the damping sensitivities. The stiffness and damping are only present in the denominator of the sensitivity functions. This means that any optimisation of the bearing's transmissibility by a stiffness and damping reduction, will lead to increased sensitivities. This makes the system's performance vulnerable to small design variable perturbations, especially in the low frequency domain.

To visualise the importance of stiffness on the bearing's transmissibility, different graphs at shifted stiffness values are plotted in figure 3.15. A supply pressure fluctuation of only:  $\Delta P_{s1} = 10\text{Pa}$  leads to a 100% stiffness variation giving a transmissibility somewhere between the blue and the green graphs. Furthermore the stiffness is a non-linear function of displacement, this is not included in the current linearised model. The optimised design in figure 3.9, shows a relatively large stiffness variation around nominal fly height of:  $\bar{k}(\bar{h} = 1.1) = 20 \times \bar{k}(\bar{h} = \bar{h}_0 = 1)$ . This means that only very small (sub-micron) perturbation amplitudes are allowed, unless the low-stiffness fly height domain is increased. Figure 3.15, combined with the sensitivity analysis, gives a clear picture of the difficulties in transmissibility minimisation.

## 3.6. Conclusion

In this chapter, a twofold static & dynamic optimisation procedure is developed and applied on the two-pad bearing. First, the properties of a stable low-stiffness design are quantified and objective and constraint functions are formed. The static optimisation yields promising results for the shallow-pocket and height-offset concepts. In the second phase the optimisation is extended and the damping is minimised. A pad height-offset must be used to align the low- stiffness and damping fly heights. The final result yields a bearing with positive damping at all frequencies and 'slight' negative stiffness in a certain frequency bandwidth. The negative stiffness emerges from the minimised damping at lower frequencies and the rising damping at mid-range frequencies.

The transmissibility of different optimised designs is studied and the dimensioning ( $H$  &  $R$ ), has a great influence on the transmissibility. A bearing with a small radius and a relatively large nominal fly height, has the largest 'mass' term and therefore a faster transmissibility decay. The design with normal damping, has a slightly better performance than the standard bearing design. If also the damping is reduced, the transmissibility shows a much faster decay than the standard bearing. A 'time-domain' limit-cycle analysis is needed, to investigate the exact system behaviour in case of 'small' negative stiffness. Although further fine-tuning towards a better optimum is possible, it is decided to do a sensitivity analysis on: design variables, stiffness & damping and transmissibility.

First the sensitivities of small design variations on stiffness and damping are determined. From this analysis it becomes clear, that small supply pressure variations have a large effect on the operating point stiffness and damping. These variations also have an effect on the transmissibility, as more optimal designs result in increased sensitivities. This high transmissibility sensitivity, directly limits the allowed amplitude of floor vibrations.

In the following chapter, different techniques to manufacture these type of bearing pads are discussed. This information is used in chapter 5, to find a feasible design which can be constructed.

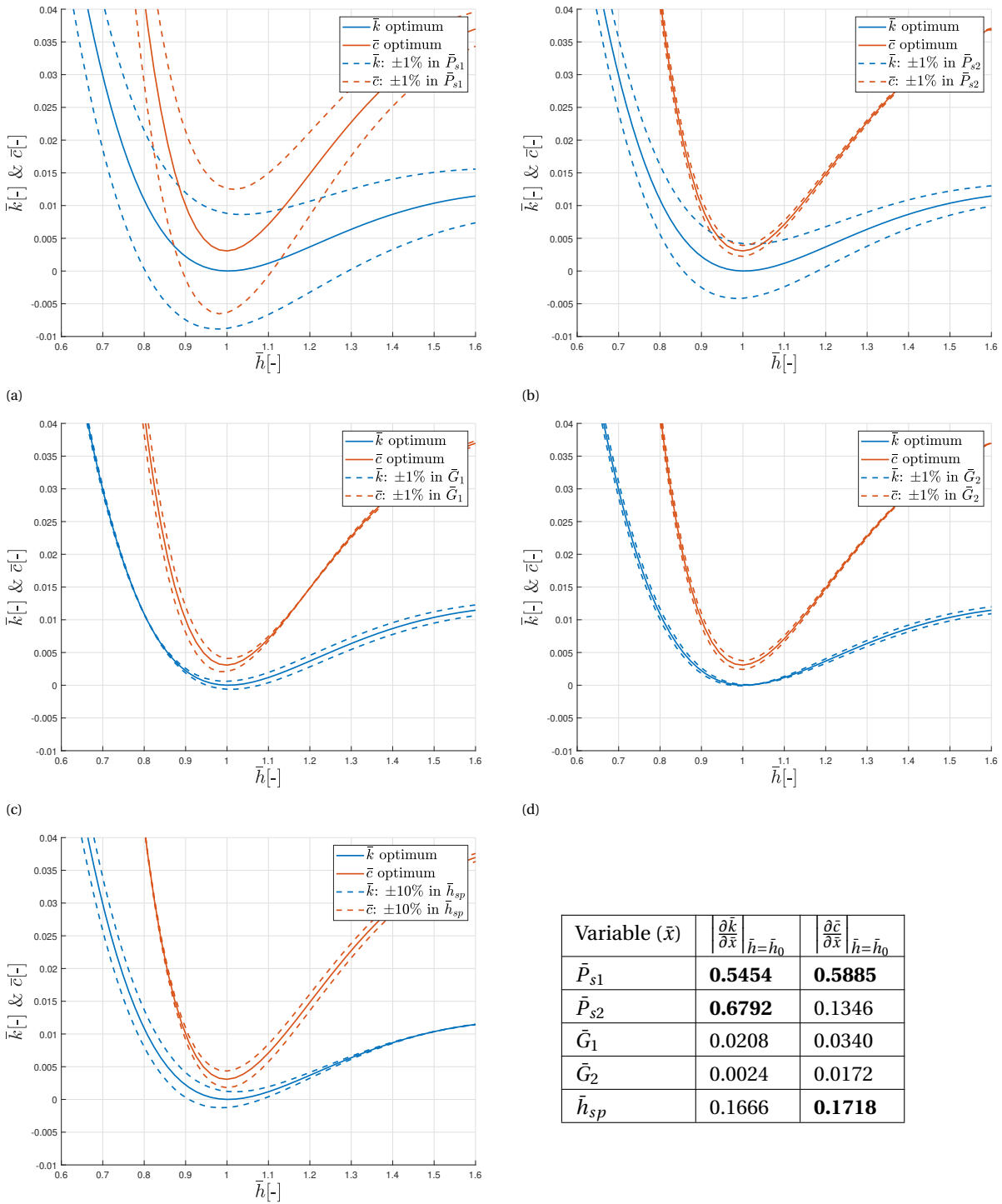


Figure 3.13: The effect of small design-variable changes on the 'low-frequency' stiffness and damping around the nominal fly height.

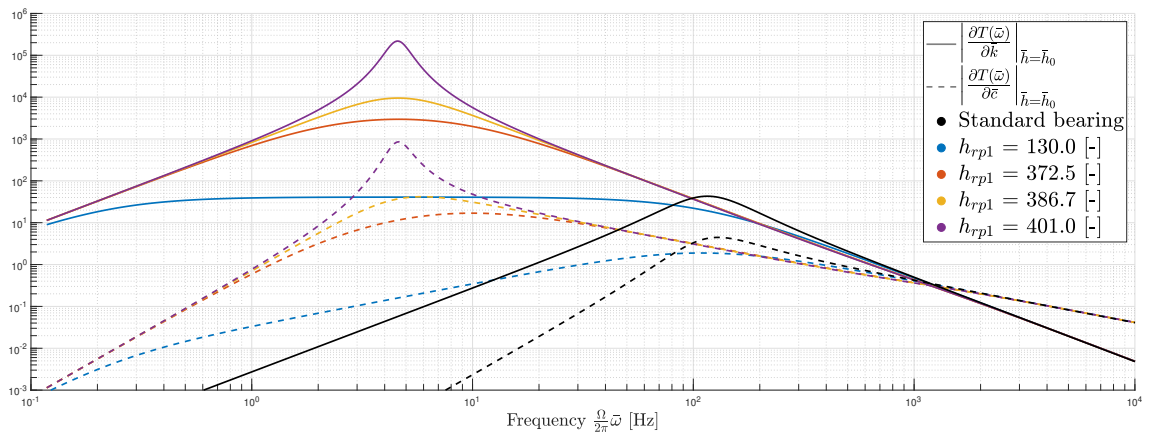


Figure 3.14: Stiffness and damping sensitivity lines of bearing designs with a decreasing damping characteristic. Any reduction of stiffness and damping optimises the overall transmissibility graph but results in higher sensitivities, making the system vulnerable to small design perturbations.

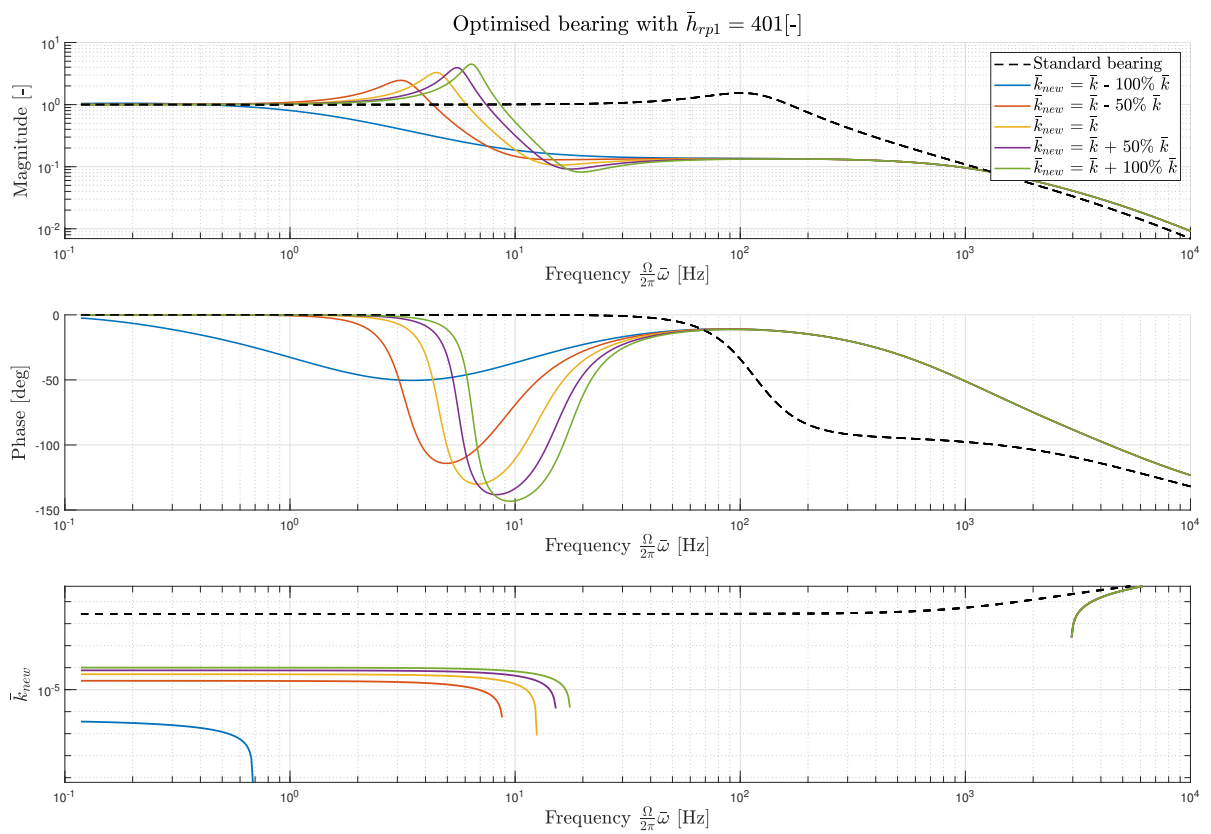


Figure 3.15: The  $\bar{h}_{rp1} = 401$  low damping design is used to show the influence of stiffness shifts on the transmissibility. A 100% variation of stiffness is easily initiated by a slight design perturbation, as a result of the high sensitivities.



# 4

## Manufacturing methods

Already in an early stage of this project, it was decided that the fabrication and testing of a stable zero-stiffness prototype, would be valuable as a proof of concept. From findings in [21], it appears to be rather difficult to construct such bearing design, with the available methods and within a reasonable amount of time. Aero-static thrust bearings are known for their tight manufacturing tolerances, regarding surface-roughness and -waviness. Furthermore, the implementation of a surface texture and air restriction proves to be a challenge.

To enable fast and low-cost prototyping of aerostatic bearings, different manufacturing techniques, available at the faculty were tested. This chapter briefly describes all the investigated techniques and concludes with a recipe to build a zero-stiffness bearing, which is tested in a measurement set-up. Beforehand, it must be decided whether a shallow pocket, height offset or a hybrid bearing design is manufactured, since it involves different techniques. The results in chapter 3, show that a shallow pocket bearing has higher load capacity and stiffness at low- and high fly heights, when compared with the height offset designs. A disadvantage of only implementing a shallow pocket, is a bearing geometry, that can not be changed after production. The only variables that can be tuned are the load and the supply- and vacuum pressures. Based on these findings a hybrid bearing would be ideal to use in a test set-up.

However, a prototype should have multiple high pressure pads to be tip-tilt stable. Aligning all pads perfectly without any tilt and introducing an adjustable pad offset mechanism, seems hard to realise with conventional machinery. Especially since multiple parts, made in a different clamping, need to be combined. The shallow pocket bearing surface can have multiple inlets that are all in the same plane. This means that the whole geometry including the shallow pockets and inlets, can be made in a single piece of material that does not need any alignment. Based on the bearing performance and expected manufacturing difficulties, it is decided to develop a non-adjustable shallow pocket bearing. This continues the work from [21], but with a different approach on manufacturing methods.

### 4.1. Manufacturing methods

The construction of an aerostatic thrust bearing like in figure 2.2 can be divided in three major challenges. Namely: the construction of micrometre-scale surface textures like pockets, an overall flat surface topology and the implementation of the supply pressure through a restricted inlet. Besides these features, there are different materials that can be used as bearing surface. An overview of the tested materials and methods is given in figure 4.1. The final process must yield a low surface roughness  $R_a < \approx 0.1 \mu\text{m}$  and small peak to peak waviness  $R_{p2p} < \approx 0.1 h_0$ . Furthermore, there must be the ability to produce well defined micrometre pockets, with a depth of:  $1 \mu\text{m} < \approx h_{sp} < \approx 3 \mu\text{m}$  and millimetre-scale radius. There must be the opportunity to integrate a restriction tube or needle, like the tested blunt needles in section 2.2.4. At last there is the wish to develop a fast and cheap 'in-house' production method. This enables faster prototyping and testing of promising designs and can be used in future projects.

An extended overview of the tested manufacturing methods is given in appendix E, accompanied with test results and used machine settings. In this section a short overview is presented, explaining why certain methods are suitable or not.

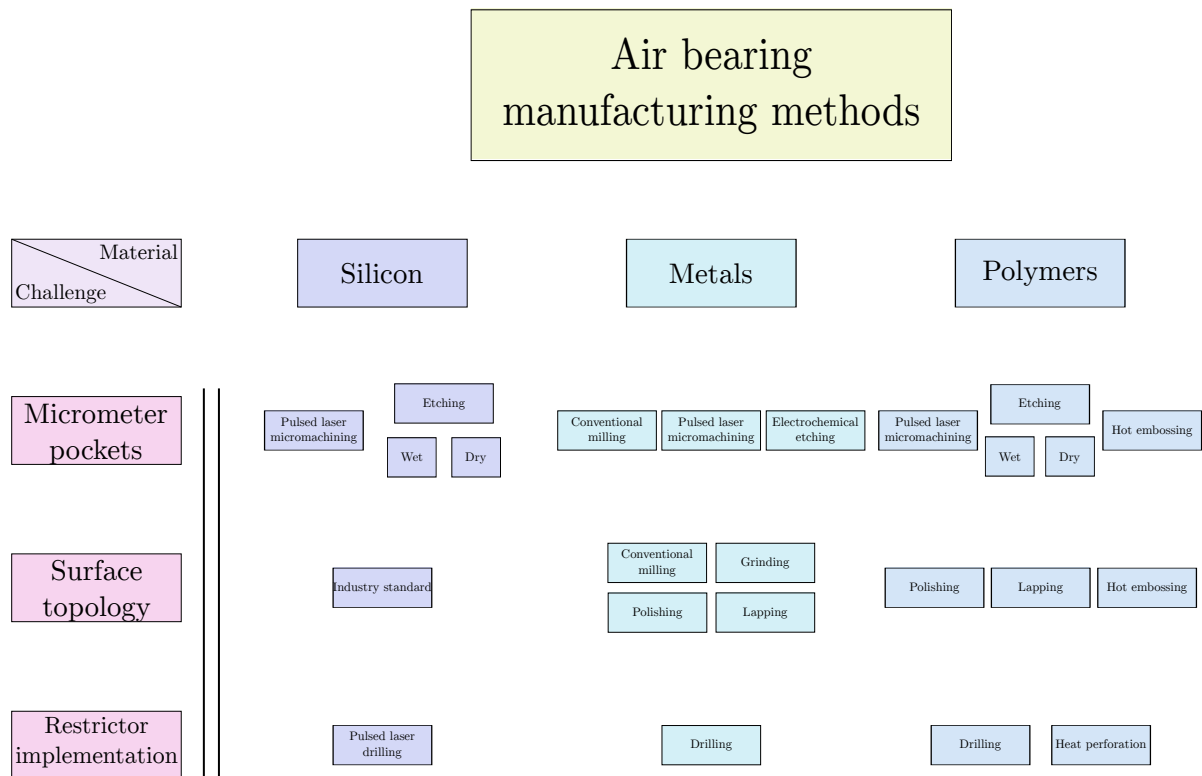


Figure 4.1: Overview of all considered and tested manufacturing methods

#### 4.1.1. Materials

To assess a larger variety of production techniques to create micrometre-scale pockets, three different materials are chosen. In industrial bearing applications, metals are the default material. Metals can be machined with conventional milling techniques and a metal bearing surface is stiff and retains its shape. Silicon is available as wafers and has a superb surface quality. Features can be machined with pulsed laser micromachining or with etching techniques, unfortunately the material is very brittle but it has high wear resistance. Some types of polymers can be conventionally machined, etched or deformed with pressure and heat. Clear, low-surface energy polymers like PMMA and cyclic olefin copolymer (COC), generally have very low surface roughness.

The surface waviness of the silicon wafer and polymer sheet is subjective to deformations and is therefore 'partly' determined by the flatness of a support material. Firstly, the different materials are individually examined for micrometre-pocket manufacturability and surface topology. Later the combination of materials is studied.

#### 4.1.2. Shallow-pocket manufacturing

The shallow pocket manufacturing in different materials is studied first, since it is the key feature in this type of low-stiffness bearing. In [21] some techniques are studied to make a shallow-pocket in a stainless steel surface. The discussed methods are: 'standard' pulse laser engraving, electrochemical etching and lathing. Only the last method gave good results after endless testing since a micrometer pocket exceeds normal machine tolerance. However, the major disadvantage is the inability to produce multiple shallow pockets in one surface and single machine clamping. It is decided not to use any of these methods and to explore some novel techniques.

Since some time the faculty owns a short pulse UV laser (Optec), that should be able to etch micrometre size features in silicon or stainless steel. The laser settings are different for each material and determine the ablation characteristics. The settings are not trivial and need to be determined experimentally, in [24] laser settings are determined for some operations. The settings to etch a thin layer of material are not present and the minimum etch depth is unknown. Different laser parameters like: pulse frequency, speed, number of repetitions, hatch patterns and laser power are altered and the surfaces are evaluated with a white light

interferometer, see appendix E. The best results were found in silicon, a well defined pocket with a depth of:  $h \approx 8 \mu\text{m}$  and very little debris is possible. This pocket depth does not meet the requirements and is therefore not useful in this particular bearing application. A shallower pocket with a depth of:  $h \approx 4 \mu\text{m}$  was possible, but without a clear height step and high pocket roughness. An extra step that involves a wet KOH etch did not improve this. To conclude, the etched surface is rough and contains craters, at some points the material is still present, also the repeatability was an issue. After numerous tests it is decided not to continue with this method.

When a small amount of material needs to be removed to create a feature with high aspect ratio:  $r/h \gg 1$ , etching techniques can be used. This technique is used on a large scale in the semi-conductor industry and can be categorised in wet- and dry etching techniques. Wet etching uses a mask and chemical baths to remove material, the removal rate is a function of temperature and concentration. Very well defined micro structures can be etched in silicon. This is done inside a cleanroom and comes with high costs and low flexibility, making it not suitable to use in this project. At the faculty an oxygen plasma cleaner is available to remove contamination from (silicon) samples. After consulting the micro and nano department, the idea of using this machine for dry-etching arose. Since the machine is designed for decontamination of samples, it is less powerful than a designated plasma etching device, increasing the etch time.

The high energetic oxygen plasma is generated in a low pressure chamber by high power radio waves, any interaction of free radicals with a substrate will generate heat. Different types of gases are used to etch different materials. In this set-up only oxygen is available, meaning that only polymers can be used. The free radicals in the oxygen plasma, react both chemically and kinetically with a polymer sample, removing an 'unprotected' surface. A polymer with a high thermal resistance is needed to withstand the thermal energy involved during this process. After testing different polymers good results were found with a combination of a PDMS mask and a cyclic olefin copolymer (COC) named Topas<sup>®</sup>. Different grades with various glass transition temperatures ( $T_g$ ) are available, grades: 6015S-04 or 6017S-04 with  $T_g = 158^\circ\text{C}$  and  $T_g = 178^\circ\text{C}$ , yield the best results see appendix E.3.

Different geometries can be made in the soft PDMS mask, the mask adheres to a clean Topas<sup>®</sup> surface and uncovered areas are removed by the plasma. The pocket depth depends on the etch duration, oxygen mass flow, power and mask geometry- and thickness. After approximately two hours of etching the pocket is well defined, with a depth of a few micrometres and low overall surface roughness, see figure 4.2. Some small spots are not removed, this is probably caused by local surface contamination. This is a promising result and after few more tests, it is decided to continue with this concept.

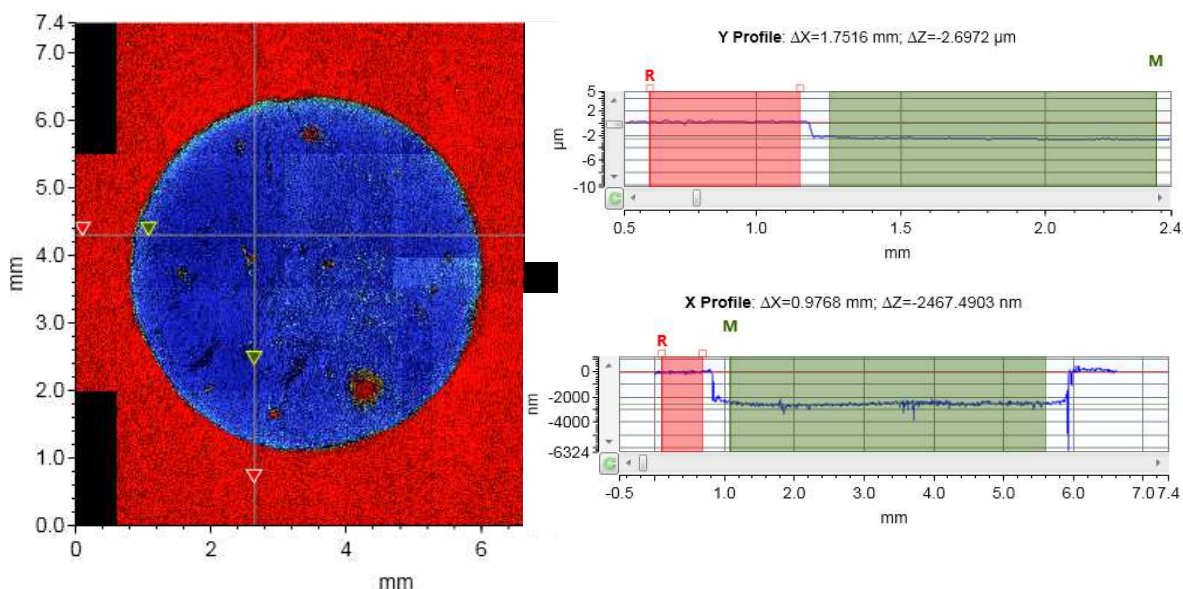


Figure 4.2: Circular pocket  $r \approx 2.5 \text{ mm}$  etched in Topas 6017S-04 after 2h of etching at 99 W. A small height step of  $h \approx 2.5 \mu\text{m}$  is clearly visible.

### 4.1.3. Surface topology

Another challenge is to ensure a flat bearing surface that has low roughness and waviness. The Topas<sup>®</sup> is available as 5 mm thick moulded sheets that have very low roughness. The waviness is examined by analysis of an A5 size sheet with the white light interferometer and measuring the peak to peak distances. The sheets show some slight bending in the order of tenths of micrometre. It was impossible to find a small circular area with small (micrometre range) height differences. This will cause contact between bearing- and counter surface at a range of low fly heights. The sheets are quite rigid but can be deformed when loaded, this will inevitably change the surface waviness. Therefore, a piece of sheet material is adhered to a rigid steel base with an epoxy glue, to overcome this problem. Then an attempt was made to flatten the Topas<sup>®</sup> surface, by using various abrasive methods and by plastic deformation with pressure and heat (hot-embossing), see appendix E.5.

It appeared to be difficult to flatten, even a small area of adhered Topas<sup>®</sup>. The abrasive methods use a polishing paste with small abrasive particles to remove material. Edge-effects caused a non-uniform material removal which results in an 'umbrella' shaped surface. Embossing the sample with a supported flat silicon wafer at  $T \approx T_g$  and different pressures, did not yield a flat surface. The sample is clearly deformed by this process but internal stresses might cause unwanted deformations after removing the pressure. A very long cool-down period and a gradually releasing pressure, did not improve results. Besides this, there were problems with the adhesive at higher temperatures and the formation of micro-cracks when using abrasive polishing methods. Adhering Topas<sup>®</sup> sheet material to a rigid base is a source of multiple problems. It is therefore decided to investigate different possibilities. This is done in the last section where a final manufacturing recipe is presented, to achieve a low-waviness surface with micrometre deep pockets.

### 4.1.4. Restrictor implementation

In chapter 2 different restriction flow models are discussed and the mass flow of blunt syringe needles is experimentally determined in section 2.2.4. The advantage of using these industry standard needles is their consistent mass flow and the availability of different inner diameters. The tubing can be connected with a standard air-tight Luer lock fitting. The drilled hole *A* and milled pocket *C* in figure 4.3 are separated by a few millimetres of stainless steel. Then a very small drill with a size close to the outer restriction diameter, is used to drill hole *B*. A small ball is used as temporary insert to align the inlet restriction, then an adhesive is used for fixation.

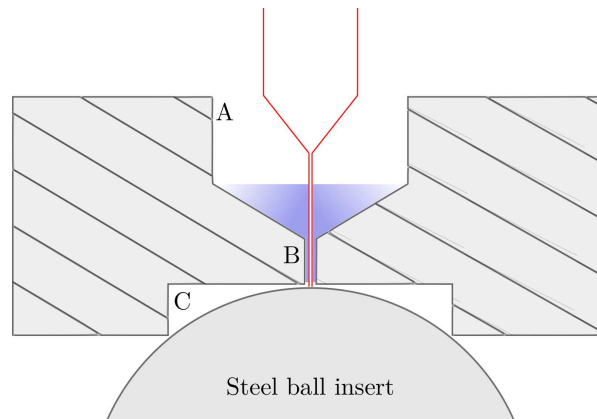


Figure 4.3: Schematic draft of the restrictor implementation, a ball is used for alignment. (not to scale).

## 4.2. Final recipe

Different methods are investigated to produce a flat bearing surface with well defined shallow pockets. It is possible to etch shallow pockets in Topas<sup>®</sup> sheet material. Unfortunately this sheet material has large surface waviness making it unsuitable as a bearing surface. Different methods to improve the waviness of this sheet material were not successful. If it is possible to use a thin polymer coating on a rigid flat substrate, there is no need to use the 'wavy' sheet material in combination with an adhesive. It is possible to apply a thin polymer film on a substrate by using a spin-coater [26]. The spin coat process uses a Topas<sup>®</sup>-toluene solution. A substrate is covered with the solution and rotated at high speed for a short period. All the toluene evaporates

and a thin uniform film of Topas<sup>®</sup> covers the substrate's surface. It should be noted that toluene is highly flammable and toxic, all the correct safety measures are taken in accordance with the lab staff.

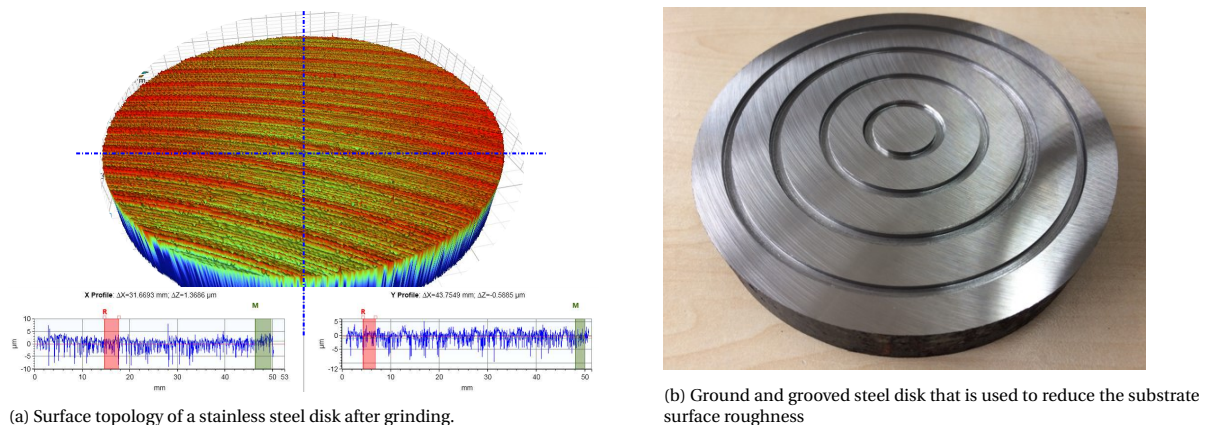


Figure 4.4

The flat substrate is made by grinding the surface of a stainless steel disk with a grinder that is recently purchased by the workshop. This gives a flat surface with low waviness, see figure 4.4a. The process does however, introduce micro grooves, leading to some surface roughness. These micro grooves are a problem for the spin coating process, since they lead to a polymer film with higher roughness than the substrate. This roughness needs to be reduced while maintaining the flatness. A solution is found with the ground steel disk with a diameter of: 130 mm, in figure 4.4b. The shape is inspired by commercially available lapping plates that are used to flatten surfaces. The figure 4.4a substrate is placed on the disk in figure 4.4b, with a small amount of abrasive diamond paste (3 $\mu$ m grade). Rubbing the two surfaces in a 8-figure pattern reduces the grinding-groove roughness, while maintaining the overall flatness.

This 'smoothed' substrate is now spin coated with the Topas<sup>®</sup>-toluene solution. Tests are done at different rotation speeds and weight percentages of the solution, while using findings from [26] as a guideline. A thin polymer film with a thickness around 4 $\mu$ m, is obtained with a Topas<sup>®</sup> 6017S-04 20wt% solution and spinning the substrate at 1500 RPM for 45s. The surface topology of a spin coated single-inlet test sample is given in figure 4.5. The surface waviness is under two micrometers and the sample shows some roughness. The latter seems hard to determine correctly with the white light interferometer, as a result of the reflective and transparent nature of the thin polymer film. The deep pocket that is milled in the stainless steel, causes some accumulation of polymer around the edge. Furthermore, there are some so called 'comets', which are small (dust) particles causing a trace on the surface. If a particle is embedded in the polymer film, it will be worn off during bearing application, increasing overall flatness. A reduction of the diameter decreases waviness, enabling lower fly heights.

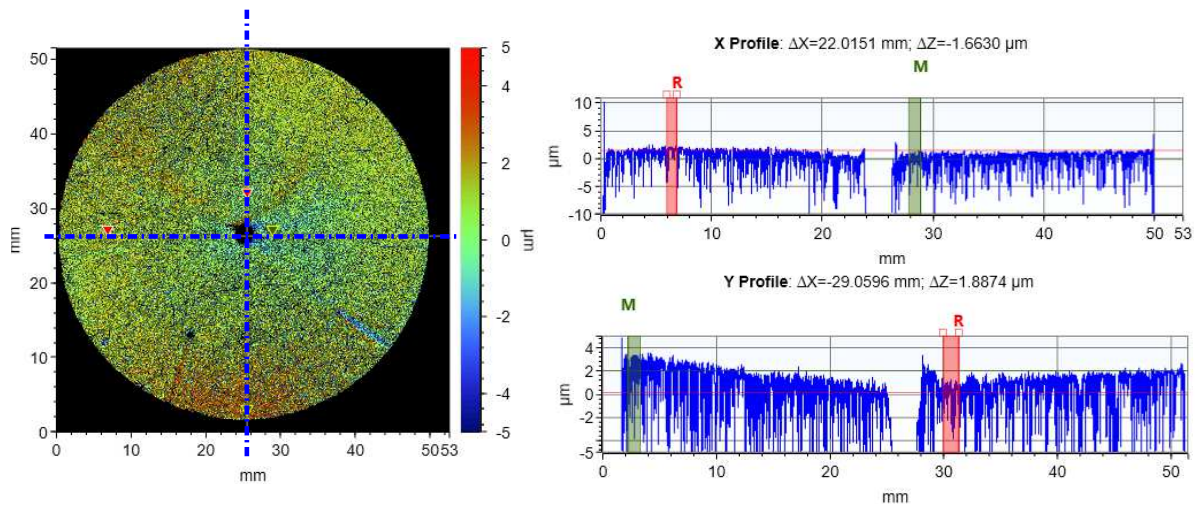


Figure 4.5: A sample disk that is flattened by using the figure 4.4b disk and diamond paste. Then a thin polymer film is applied with a spin coating process, the x-y profiles and height differences are given.

The shallow pocket features can be etched with the oxygen plasma process, in combination with a soft PDMS mask, as described above. Any geometry can be etched using this technique, giving more design freedom. There are however, some process disadvantages: heat generation, time consumption, limited machine's chamber space and a hard to control oxygen mass flow, resulting in a low process repeatability. At a later stage, an easier, more reliable method was found, to create circular pockets in the polymer surface. This method is based on insights gained during the spin coating process, when a faulty polymer layer was removed from the steel substrate. The thin Topas<sup>®</sup> layer, dissolves in toluene or sec-butylbenzene, this property is used to selectively remove parts of the thin polymer film. Again a PDMS mask is used to cover and protect parts of the substrate. Then a cotton bud with a small amount of toluene is used to locally remove the Topas<sup>®</sup> film, the removed shape is defined by the PDMS mask. With this method it is not possible to have different pocket depths, the depth is defined by the polymer layer thickness. A circular pocket with a diameter of 5 mm, is etched in the figure 4.5 test sample, using this method, see figure 4.6.

When the thin polymer film is applied and the desired shallow pockets are etched, the inlet- and outlet restrictions are implemented. All individual manufacturing processes are executed in a specific order, an overview of all steps is given in figure 4.7.

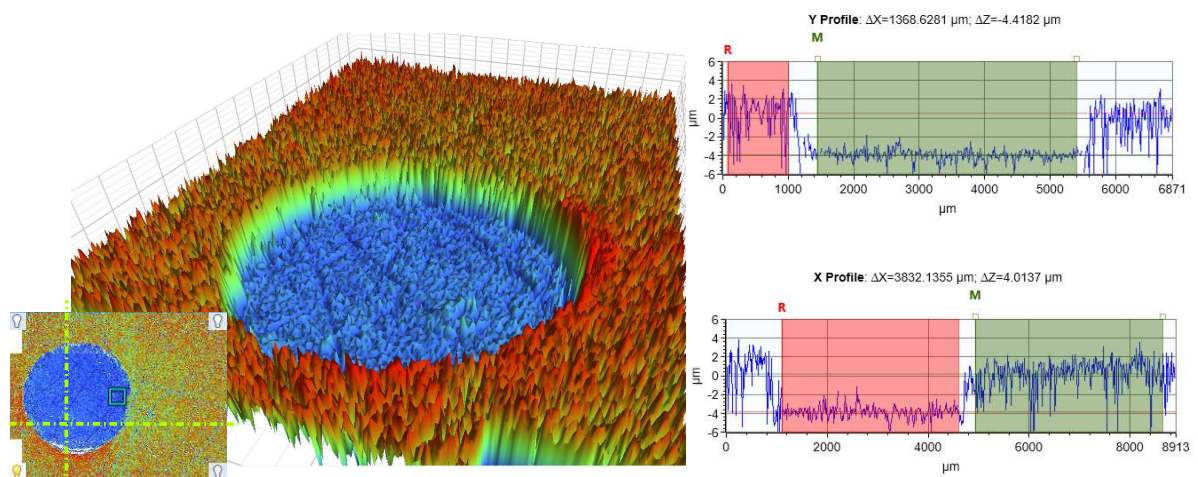


Figure 4.6: Surface image of the spin-coated polymer layer with an etched shallow-pocket, the pocket is created by locally dissolving the film through a soft PDMS mask.

### 4.3. Conclusion

In this chapter an overview of the considered and final manufacturing methods is presented. First, the problem is separated in three individual challenges, namely: shallow-pocket manufacturing, surface topology and restrictor implementation. A lot of effort was put into exploring the possibilities of short pulse laser micromachining. This method looked promising, but it was not able to create well defined micrometre scale pockets. Besides the creation of shallow surface features, achieving a flat surface topology turned out to be difficult. A solution is found, in spin-coating a thin polymer film on a flattened stainless steel substrate. The shallow pockets are created in the polymer top-layer, by means of plasma etching or by locally dissolving the film, both processes require a soft PDMS mask.

In theory the process is fast and flexible, because a polymer layer with a different thickness can be applied and various mask shapes can be used, giving lots of design freedom. In practice, it is hard to find the correct spin-coat settings to obtain the right film thickness. Besides this, the surface quality of the coating must be good and without presence of air bubbles or particles. Sometimes delamination of the layer occurred, starting at the outer edge. Despite these problems, the method is used in further prototyping. The restrictor alignment and implementation delivered good results. These findings are used in chapter 5, to design a low-stiffness bearing, which can be manufactured with the discussed techniques.

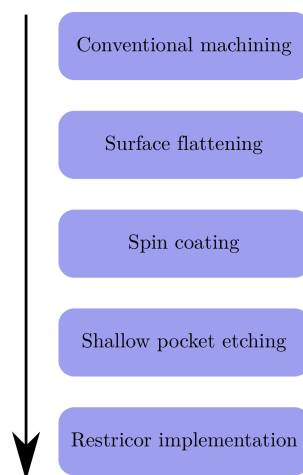


Figure 4.7: Overview of the process steps to manufacture a shallow pocket bearing.





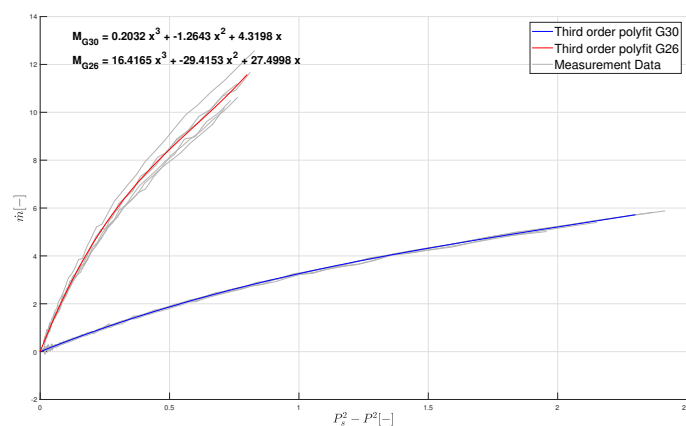
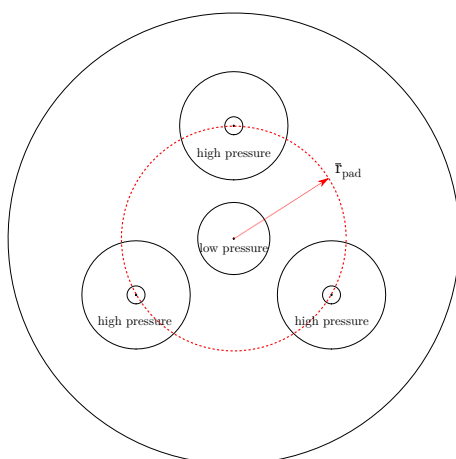
# 5

## Design of a low-stiffness demonstrator

To validate the concept of a low-stiffness aerostatic bearing a demonstrator is designed, build and tested. Despite the lower *post-manufacturing* flexibility, the shallow pocket concept is chosen from the manufacturing point of view to have all surface features in a single plane. The analysis in chapter 3, shows that a low-damping design is beneficial, in terms of transmissibility. However, minimising the damping by introducing 'dead' thin-film volume, easily leads to an unstable system. Therefore, it is decided to focus on validating the 'static' low-stiffness concept, with the use of 'integrated' high- and low pressure pads. The optimisation procedure is used to find a *tip-tilt* stable design, with multiple high pressure inlets. Manufacturing constraints are added to the optimisation, to obtain a feasible manufacturable optimum. After a design is found, the tip-tilt stability is analysed as function of bearing pad orientation.

### 5.1. Design

The optimised two-pad designs in chapter 3 are not tip-tilt stable and therefore unsuitable to use in a demonstrator. Placing multiple high pressure pads around a low pressure core yields a stable design, see figure 5.1a. Increasing the radius of the high pressure pads:  $\bar{r}_{pad}$ , gives a higher tip-tilt resistance. The inlets, pockets and outlet are in the same plane for easy manufacturing. This configuration does not have a Dirichlet boundary condition around each integrated pad. The pressure interaction between the pads, makes a simple scaling operation of a 2-pad optimised design not valid. Despite the changed boundary conditions, a scaled 2-pad optimum is used as initial configuration. To maintain the high- and low pressure pad ratio, the surface area of three high pressure pads is scaled, the following scaling factor applies for  $n$  high pressure pads  $r_{scaling} = \sqrt{r^2/n} = \sqrt{1/3} = 0.58$ .



(a) A tip-tilt stable design; a vacuum pad surrounded by three high pressure pads (b) Polynomial fit of G30 and G26 restriction measurement data

The design variables in table 3.1 allow for a large design space that might be impossible to construct with the available methods. For this reason the restriction-pocket radius and depth are removed from the

list of design variables. Furthermore, the measured restriction mass flux of the gauge 30 and gauge 26 blunt syringe needle is used, this eliminates  $\bar{G}_{r1}$  and  $\bar{G}_{r2}$  as design variables. At this point an outer bearing radius of 12.5mm is chosen. This makes it easier to obtain a flat bearing surface and it is large enough to integrate all surface features and restrictions. The restriction-pockets are milled directly in the stainless steel surface, using a tool with a diameter of:  $d = 1.5$  mm. The G30 and G26 blunt restriction needles have an outer diameter of 0.31 mm and 0.46 mm respectively. The smallest possible drill size to make through-hole  $B$  in figure 4.3 is 1 mm. The mass flow measurement data of the G30 and G26 restrictions is scaled with the dimensionless numbers from section 2.1.3. The mass flux for both restrictions as function of a quadratic pressure difference is given in figure 5.1b. The flow models discussed in section 2.2 do not give a perfect fit for this type of restriction. Therefore, it is chosen to use a third order polynomial-fit in the numerical model to eliminate reduce any error.

Table 5.1: The reduced set of design variables for optimisation with applied manufacturability constraints

	<b>Parameter</b>	<b>Range</b>	<b>x<sub>01</sub></b>	<b>x<sub>1</sub></b>	<b>x<sub>02</sub></b>	<b>x<sub>2</sub></b>	<b>x<sub>03</sub></b>	<b>x<sub>3</sub></b>
Thrust pad	$\bar{G}_{r1}$	$f(\dot{m}, \Delta P^2)$						
	$\bar{P}_{s1}$	<b>[1,7]</b>	1.3	1.27	2	1.4	1.6	1.36
	$\bar{h}_{sp1}$	<b>[0.05,1]</b>	0.07	0.08	0.1	0.2	0.05	0.11
	$\bar{h}_{rp1}$	30						
	$\bar{r}_{r1}$	0.01						
	$\bar{r}_{rp1}$	0.06						
	$\bar{r}_{sp1}$	<b>[0.07,0.2]</b>	0.15	0.18	0.2	0.14	0.1	0.16
Vacuum pad	$\bar{G}_{r2}$	$f(\dot{m}, \Delta P^2)$						
	$\bar{P}_{s2}$	<b>[0.3,1]</b>	0.9	0.80	0.3	0.37	0.4	0.60
	$\bar{h}_{rp2}$	10						
	$\bar{r}_{r2}$	0.006						
	$\bar{r}_{rp2}$	0.06						
General	$\bar{h}_{1,2}$	0						
	$a; b; c; d; e$	0.05;0.8;1;1.2;2						
	$\bar{r}_{pad}$	0.7						

## 5.2. Characteristics & tip-tilt stability

Three different initial design configurations are used as starting point, they all converge to a feasible low-stiffness optimum. All design variables are given in table 5.1, the variables used by the optimiser are bold and a range is given. To increase tip-tilt stability the inlets are placed at a normalised radius of  $\bar{r}_{pad} = 0.7$ . The load capacity, stiffness and damping at  $\bar{\omega} = 0.01$  of all optimised designs, is given in figure 5.2. All designs show a stable low-stiffness operating point at  $\bar{h} = \bar{h}_0 = 1$  with sufficient damping. Design 1 has the largest low-stiffness operating range with high stiffness at low fly heights. The absence of deep restriction-pockets results in a stable bearing with positive stiffness and damping for all fly-heights and frequencies, see figure 5.3.

The *static* tilt characteristics of the bearing are studied, to see the influence of an eccentric loading on bearing performance. Furthermore, the influence of pad radius  $\bar{r}_{pad}$  and axis of rotation  $\beta$  are examined. The tilt of the counter surface can be defined in two different ways. The first considers only a rotation around the centre of the load without any vertical translation. This causes a decrease of the nominal fly-height at one half of the bearing, see theory in [7]. The second method adds a translation, to ensure the minimum fly height equals the nominal fly height. This second method will be used to model static tilt of this bearing, a schematic drawing is given in figure 5.4a.

For convenience the problem is defined in polar coordinates with  $r$  the radius and  $\theta$  the angular coordinate. The fly height is now not only a function of the spatial coordinates, but also a function of tilt angle  $\alpha$ .

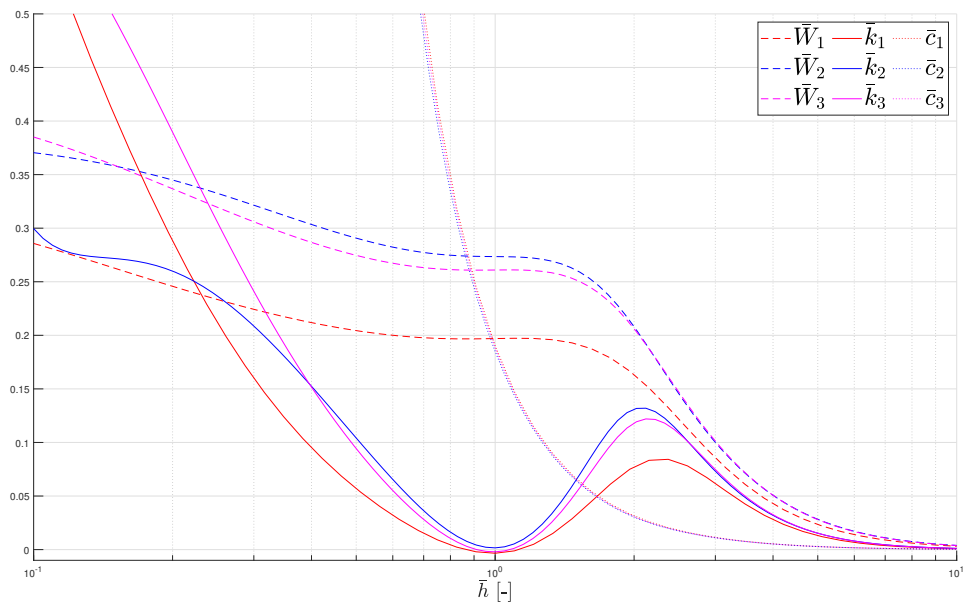


Figure 5.2: Optimised bearing characteristics for three different initial conditions. All designs show the desired stable low-stiffness behaviour with only small differences in load capacity and overall stability. The bearing has a relatively high damping at the operating fly height, reducing the change of pneumatic-hammer.

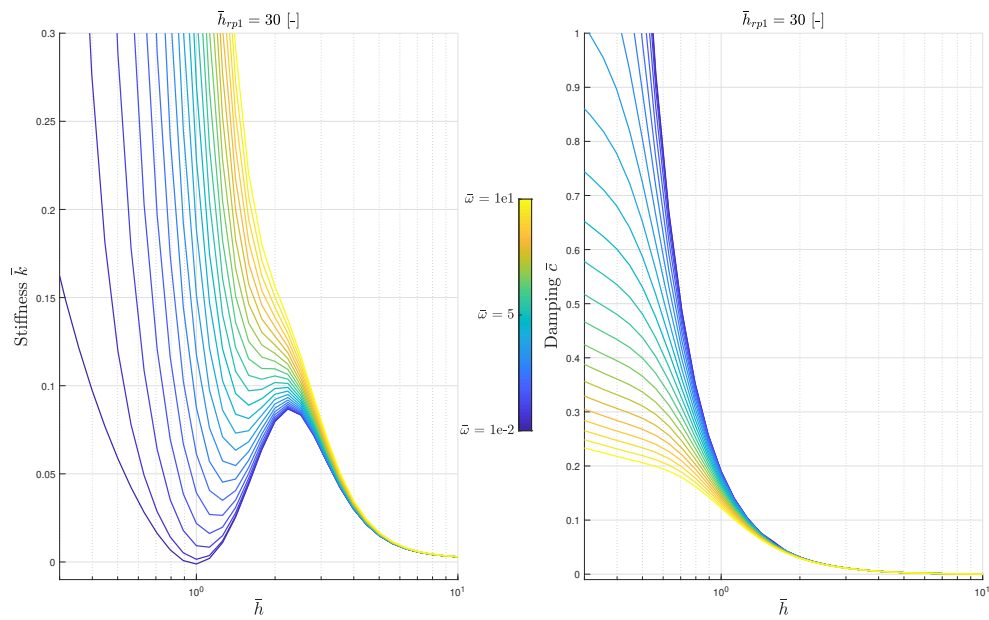


Figure 5.3: The stiffness and damping characteristics of optimised design **x1** for increasing perturbation frequency.

The dimensionless fly height can be expressed as follows:

$$\bar{h} = \bar{h}_0 + \bar{r} \cos\theta \sin\bar{\alpha} + R \sin\bar{\alpha} \quad (5.1)$$

The dimensionless tilt moment  $\bar{T}$ , is calculated by integrating the pressure profile while multiplying with the moment arm. The equation for tilt moment is:

$$\bar{T} = \int_0^{2\pi} \int_0^R (\bar{p} - P_a) r \cos\theta r dr d\theta \quad (5.2)$$

The angular stiffness can now be calculated by taking the derivative of tilt moment w.r.t. the tilt angle:

$$\bar{k}_\alpha = -\frac{\partial \bar{T}}{\partial \bar{\alpha}} \quad (5.3)$$

The dimensionless angular stiffness:  $\bar{k}_\alpha$  and tilt moment  $\bar{T}$  can be dimensionally scaled with the following relations:  $T[\text{Nm}] = PR^3 \bar{T}[-]$  and  $k_\alpha[\text{Nm rad}^{-1}] = \frac{PR^4}{H} \bar{k}_\alpha[-]$ , when:  $\alpha[\text{rad}] = \frac{H}{R} \bar{\alpha}[\text{rad}]$ . The tilt axis of rotation is indicated in figure 5.4a at:  $\theta = 90$  deg. This means that one inlet is located on the axis of rotation and the other two can create a moment. To study the influence of the inlet positions on tilt stiffness  $\bar{k}_\alpha$ , the bearing is rotated at an angle  $\beta$ , see figure 5.4b.

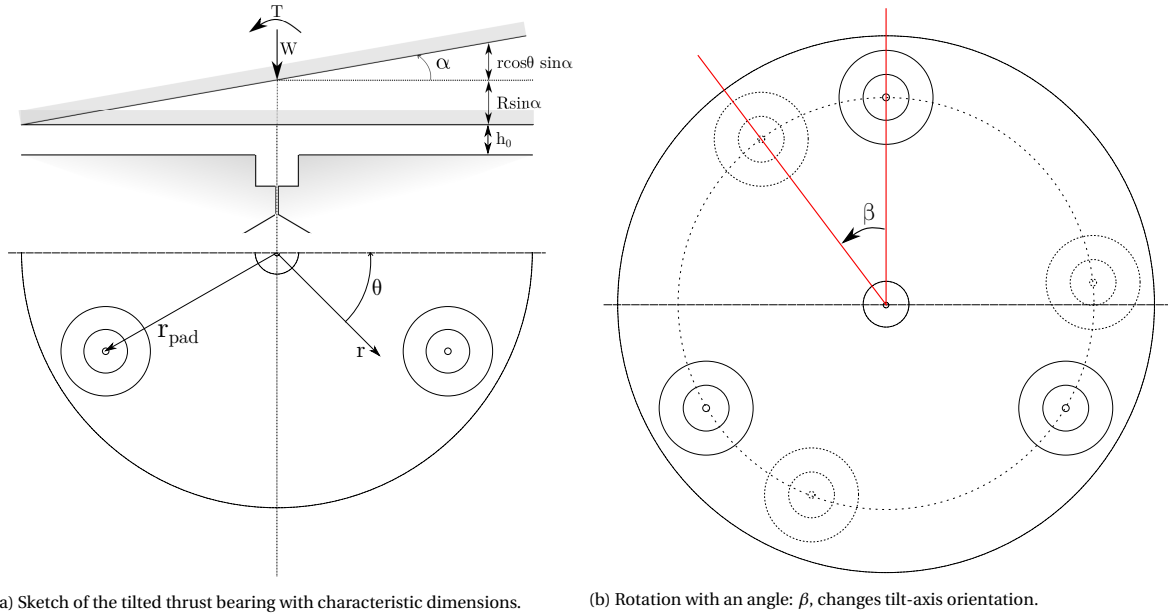


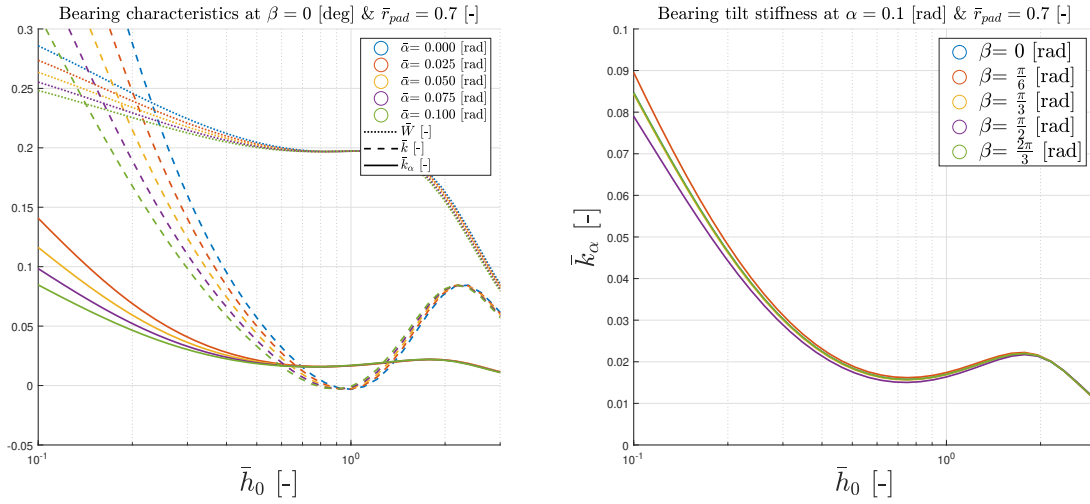
Figure 5.4

The results in figure 5.5a show the influence of a small tilt angle on the bearing characteristics. When evaluating the characteristics in the operating point:  $\bar{h}_0 = 1$ , there is hardly any change of load capacity and stiffness at increasing tilt angle. The influence of tilt angle becomes dominant at lower fly heights, causing a decrease of load capacity, stiffness and angular stiffness. The orientation of the inlets towards the tilt axis of rotation, is studied by introducing rotation angle:  $\beta$ . The results are depicted in figure 5.5b and show a minor influence on the angular stiffness. The bearing orientations at  $\beta = 0$  and  $\beta = \frac{2\pi}{3}$  are the same, so they overlap. The biggest difference of  $\bar{k}_\alpha$  occurs at a bearing orientation of:  $\beta = \frac{\pi}{6}$  and  $\beta = \frac{\pi}{2}$ . However, the effect of the bearing orientation is small, when compared to the influence of the tilt angle and may therefore be neglected.

To gain more insight in the angular stiffness and corresponding moment, caused by an eccentric load, the value for:  $\bar{k}_\alpha(\bar{h}_0 = 1) = 0.017[-]$ , is dimensionally scaled with  $H = 10\mu\text{m}$  and  $R = 12.5\text{mm}$ . Using the above mentioned relation, the following is obtained:  $k_\alpha = \frac{PR^4}{H} \bar{k}_\alpha = 4.15\text{Nm rad}^{-1}$ , for  $\alpha = \frac{H}{R} 0.1 = 8 \times 10^{-5}$  rad. This gives a tilt moment of:  $T = \frac{k_\alpha}{\alpha} = 51.8\text{kNm}$ , which can be equated to an eccentric load with an eccentricity of  $\epsilon[\text{m}]$ , yielding:  $T = W \times \epsilon$ . The load capacity at nominal fly height is:  $W(\bar{h}_0) = PR^2 \times 0.2 = 3.12\text{N}$ , this gives an eccentricity of:  $\epsilon = \frac{T}{W} = \frac{51.8\text{kNm}}{3.12\text{N}} = 1.7 \times 10^4\text{m}$ . This means that an extraordinary misalignment is needed to

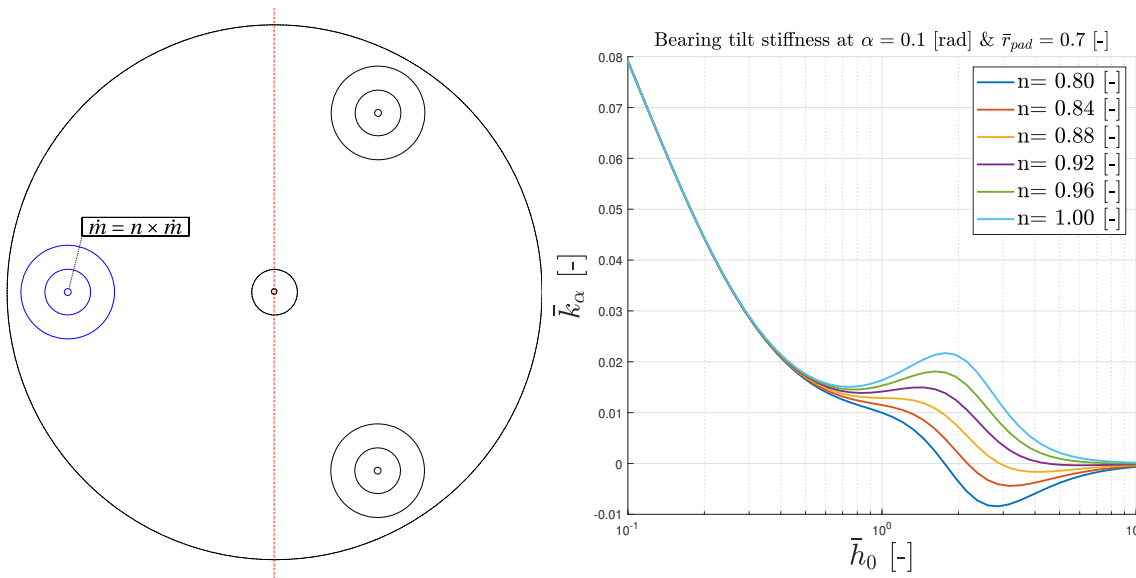
cause a deflection of:  $\Delta h = R \sin \alpha = 1 \mu\text{m}$ , at the outer radius of the bearing. This is only the case when the bearing is symmetric and all inlets have the same conductivity.

To study the effect of different inlet flows, a scaling is applied to one of the inlets. One (blue) inlet is set perpendicular to the red tilt axis, see figure 5.6a and the mass flow is scaled with  $n$ . A tilting angle of  $\bar{\alpha} = 0.1$  is assumed giving a reduced film thickness at the 'left' side of the bearing. The influence of decreasing mass flow at the angular stiffness is depicted in figure 5.6b. It should be realised this is only an indicative figure, since the exact tilt magnitude and direction are unknown. However, a decreased mass flow in one of the inlets, does affect the angular stiffness around the operating fly height and above.



(a) The load capacity, stiffness and angular stiffness at various tilt angles. (b) The angular stiffness at various bearing orientations.

Figure 5.5



(a) Bearing orientation with unequal inlet mass flows. (b) The angular stiffness when one inlet has a reduced inlet mass flow.

Figure 5.6

### 5.3. Conclusion

The two-pad concept from chapter 3, is integrated in a single bearing to create a tip-tilt stable design. The same optimisation procedure is used, but with a reduced set of design parameters, to fulfil all manufacturing

constraints. The previously measured restriction characteristics are directly used in the model. Furthermore, the restriction-pocket radii and depths are constrained and based on available mill sizes and machine tolerances. This results in three feasible optima with similar *stable* characteristics. The tip-tilt stability is analysed and the influence of tilt angle on the (angular) stiffness and load capacity is presented. The tilt angle has hardly any influence on the low-stiffness operating point, although, it has at lower fly heights. This analysis is used in chapter 6, to clarify measurement errors resulting from load misalignments.

# 6

## Realisation & validation

In this chapter, the static low-stiffness air bearing design is realised with the manufacturing techniques discussed in chapter 4. Then a measurement set-up is built to validate the theoretical model of a bearing, with and without shallow-pockets.

### 6.1. Design realisation

All three optimised designs in chapter 5 have an identical stainless steel bearing base, the only geometrical differences are the shallow pocket- radius and depth. A final bearing radius of  $R = 12.5$  mm is chosen, so the inlets are placed at  $r_{pad} = 8.75$  mm from the centre. Furthermore, a cavity is created, to house four restriction needles. The bearing is integrated in the measurement set-up, so mounting-holes and sensor cut-outs are machined. The design is depicted in figure 6.1, it should be noted that the restriction needles are not drawn in this figure. The vacuum pocket at the centre has a depth of  $h_{rp2} = 0.1$  mm, the other restriction-pockets are:  $h_{rp1} = 0.3$  mm. A small drill with a diameter of 0.1 mm, is used to link the inside cavity:  $d = 21$  mm, with all pockets. This small hole is used to align and guide, all restriction needles at a later stage.

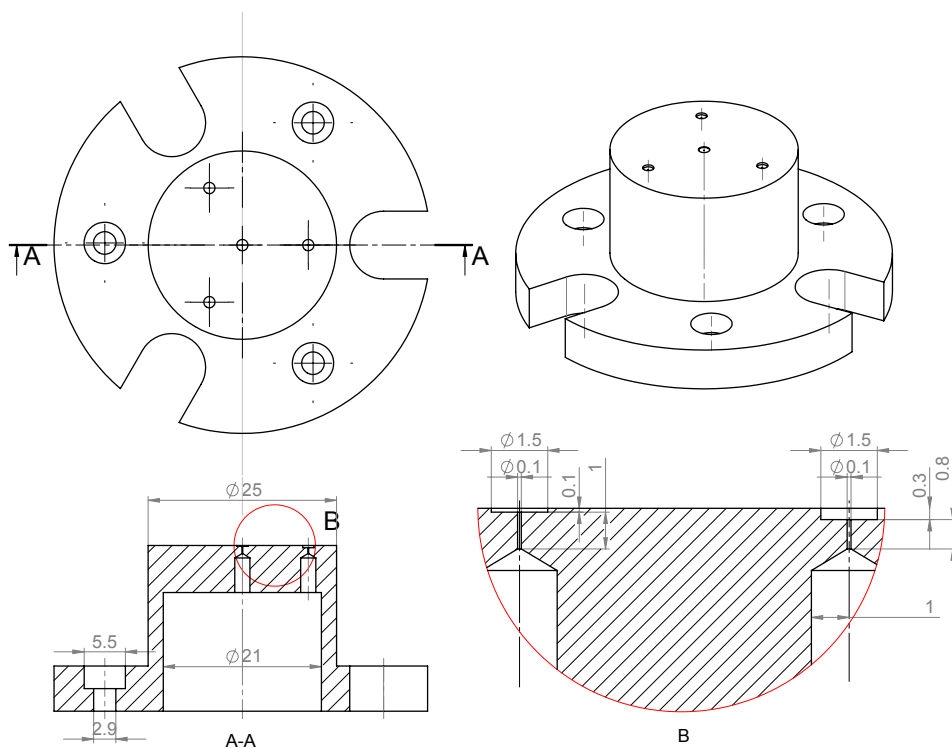
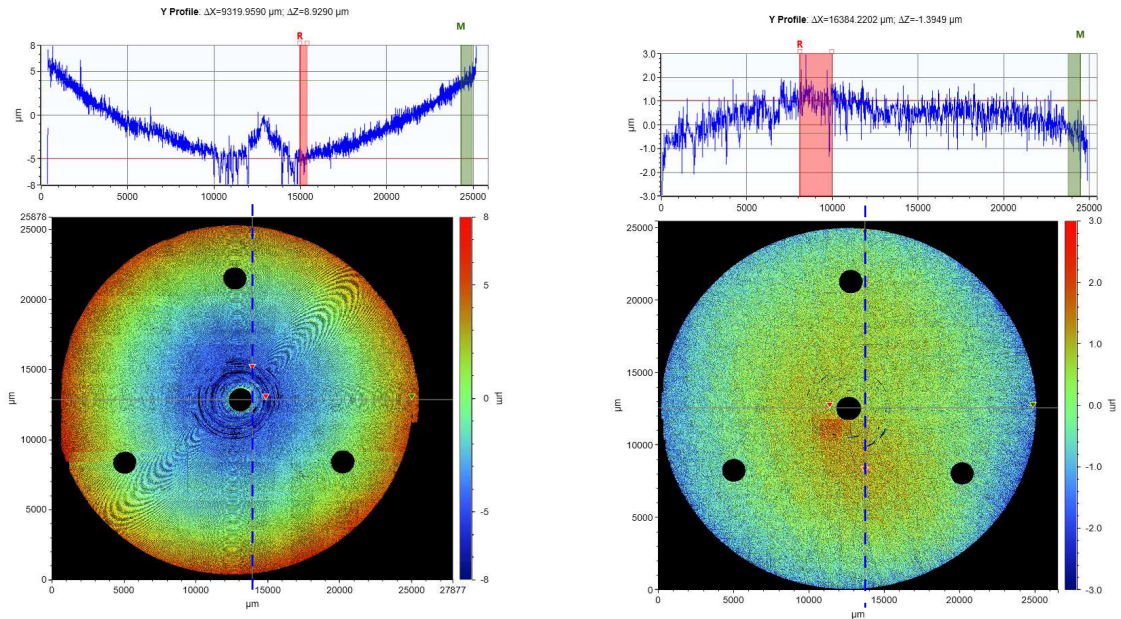


Figure 6.1: The stainless steel bearing base that is realised with conventional machining techniques, all dimensions are in millimetre.

After machining the base from a single piece of stainless steel, the bearing surface is flattened with the tool in figure 4.4b. The white light interferometer is used to obtain a height map of the surface before and after flattening, see figure 6.2. The relatively large waviness that resulted from lathing is strongly reduced and the small bumps around the restriction-pockets are removed.

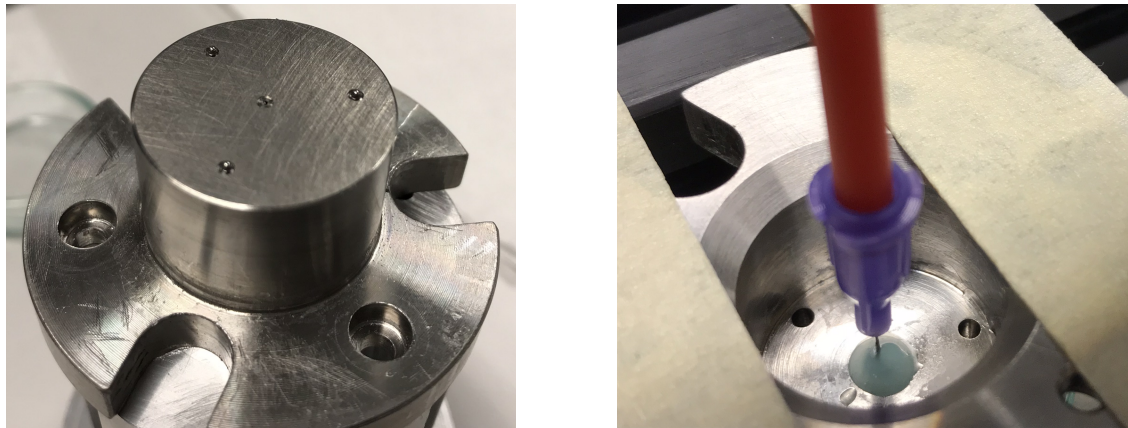


(a) Bearing surface after finishing conventional machining techniques.

(b) Bearing surface after treatment with the figure 4.4b tool.

Figure 6.2

The restrictions are aligned by placing small steel balls inside the restriction pockets, adding epoxy glue to lock them in place. In figure 6.3b, the 'gauge 30' restriction is placed in the bearing's centre vacuum outlet, the red rod holds it in place while the glue cures. The machined bearing surface with all pockets is depicted in figure 6.3a, three steel balls ( $d = 1$  mm) are visible in the outer pockets.



(a) Bearing surface with restriction-pockets and 3 steel ball inserts.

(b) Fixating one of the restrictions with epoxy glue.

Figure 6.3: Surface topology of the stainless steel bearing surface, measured with the white-light interferometer

When all the restriction needles are in place, the cavity is filled with hot glue to increase overall robustness. Then, small stickers are placed inside the restriction-pockets to cover the inlets, preventing any inlet blockage after spin coating. The bearing is placed in a nylon clamping and secured in the spin coater with vacuum pressure, see figure 6.4a. A 15wt% Topas<sup>®</sup> 6017S-04 solution is then spin coated at 2000 RPM for 45 seconds, resulting in a thin polymer film. A soft PDMS mask with three holes, corresponding to a shallow pocket radius of  $r_{sp1} = 2.5$  mm, is applied at the Topas<sup>®</sup> bearing surface. It is chosen not to use the plasma etching process,



since it involves a lot of heat which affects the glue. Instead, the thin film is removed using a cotton bud with little solvent. The exact shape of the removed sections is defined by the soft PDMS mask in figure 6.4b.



(a) The bearing inside a nylon holder to enable spin coating.



(b) The soft PDMS mask with holes at the shallow pocket positions.

Figure 6.4

### 6.1.1. Bearing topology

After spin coating and etching of the shallow pockets, the surface is analysed, using white light interferometry. Different wavelengths and other settings are tried, to find the best way to measure the surface topology of thin transparent film. The transparency results in a 'double' measurement, one of the top Topas<sup>®</sup> layer and a second measurement of the stainless steel just below, yielding a distorted measurement. A special transparent film module is available in the software but this was not able to improve results. The area around all pockets is measured individually, see figure 6.5. The whole surface is measured as well, yielding different results, see figure 6.6. The individually measured pockets, have a depth around  $4\mu\text{m}$  and a depth of  $2\mu\text{m}$ , when compared to the stitched surface area. The pocket depth is in the right order of magnitude and the film surface is flat, with a small amount of defects. Therefore, it is decided to keep this particular topology, to do measurements.

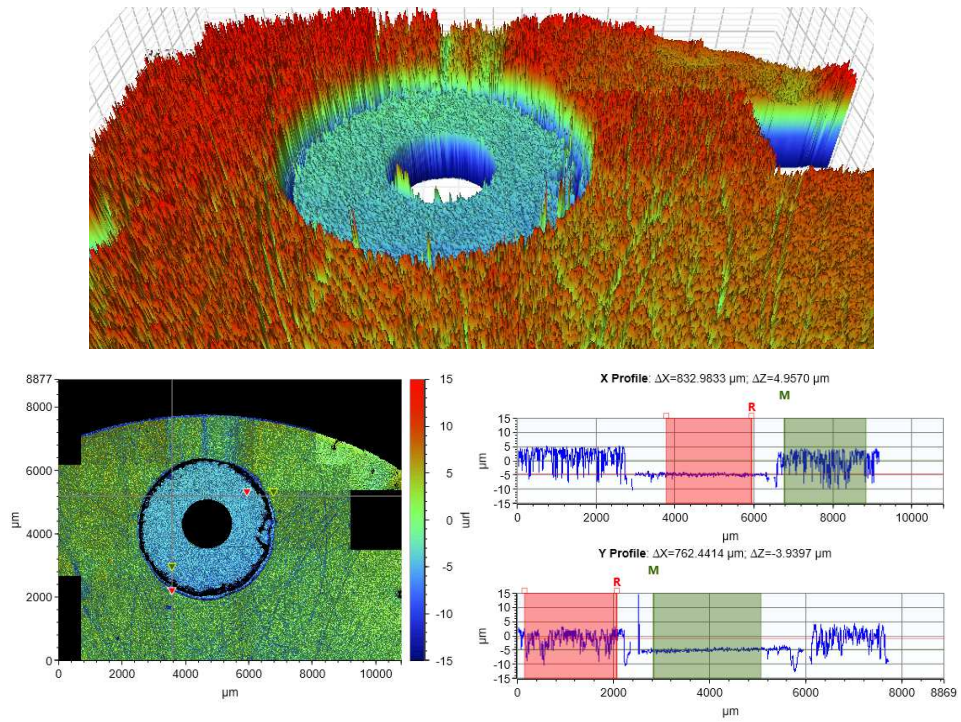


Figure 6.5: Section of the air bearing surface after etching the shallow pockets, the pocket depth is  $\approx 4\mu\text{m}$  when compared with the surrounding area.

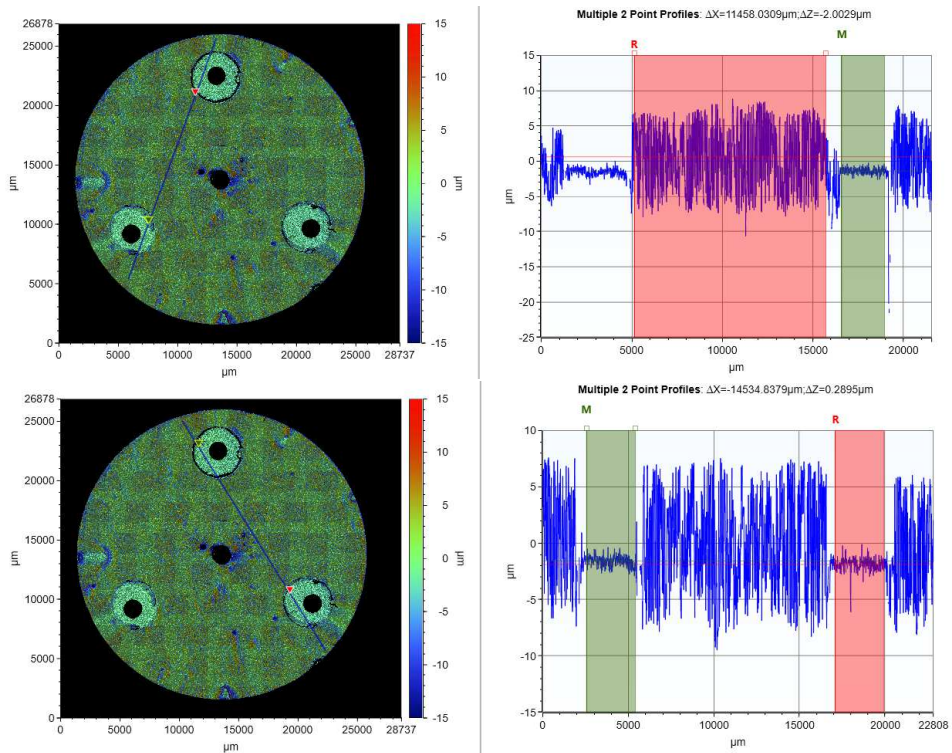


Figure 6.6: Top-view of the air bearing surface after etching the shallow pockets, the depth is  $2\mu\text{m}$  when compared with the whole 'stitched' bearing surface area.

## 6.2. Experimental set-up

An experimental set-up is build to validate the discussed theoretical model and to verify the low-stiffness concept. The set-up is designed to measure the fly height at different loads and inlet pressures. First, pneumatic tubes are added to the bearing which is mounted on a stand to create enough space for the tubing and sensors. Then, a stainless steel ring, with three capacitive sensors is placed over the bearing's cylinder. A minimum of three sensors is required to measure tip-tilt motion, the combination of all sensors yields the fly height. Capacitive sensors are chosen because of their nanometre resolution over a micrometre range and their availability in the lab. The bearing and the ring with the sensors, are placed on: one tip-tilt- and two linear stages. This results in 4 degrees of freedom, namely: two rotations and two translations in the X-Y plane, see figure 6.7. Then an additional stage is implemented, to allow a relative motion between the bearing surface and the sensor ring:  $\Delta Z$ . This is used to adjust the 'sensing-distance' ( $S$ ) between the sensors and counter-surface. The counter-surface is constrained in the X-Y plane by steel strings. This results in two planar tension forces ( $F_x$  &  $F_y$ ), which are proportional to the bearing's tip-tilt angle. The sensors measure relative displacements  $\Delta h$ , the offset:  $\delta = s - h$  is measured at zero supply pressure when the surfaces make contact.

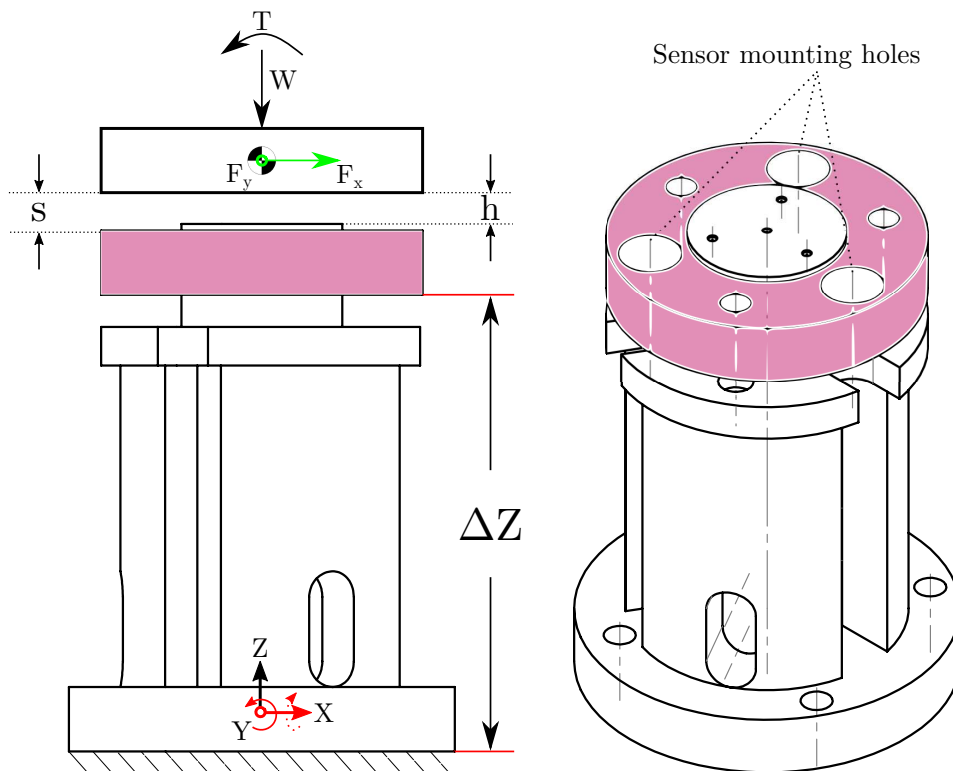


Figure 6.7: Schematic drawing of the air bearing and sensor-ring and their degrees of freedom, the counter-surface experiences planar string forces:  $F_x$  and  $F_y$ .

The supply- and vacuum air flow passes through a number of 'flow'-elements before arriving at the bearing restrictions, a schematic flow diagram is given in figure 6.8. The 2 litre sized tanks create a large volume to compensate sudden pressure differences in the supply line. Right after the tank, proportional valves are installed to adjust the feeding pressure. A Festo proportional valve is implemented, to enable a controlled change of feeding pressure during measurements, the vacuum pressure is taken constant.

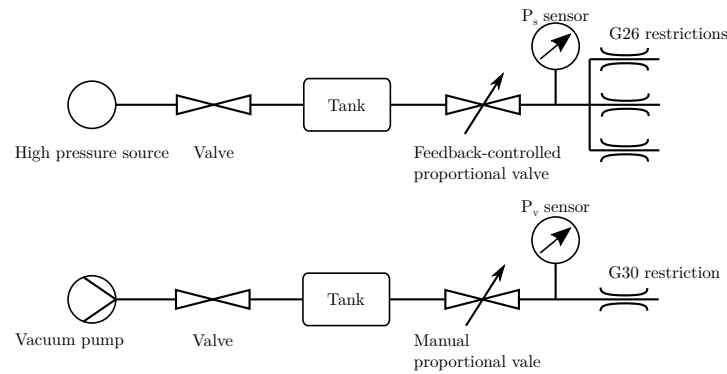
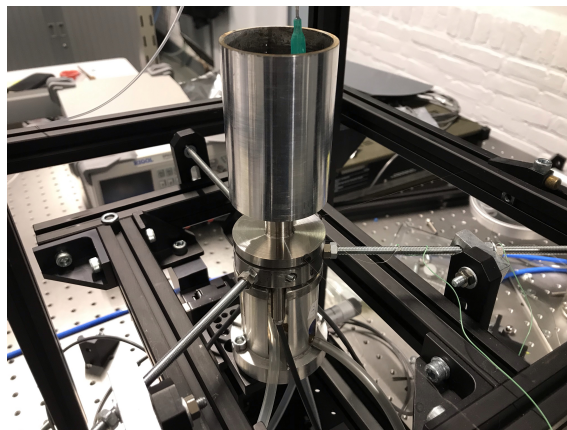
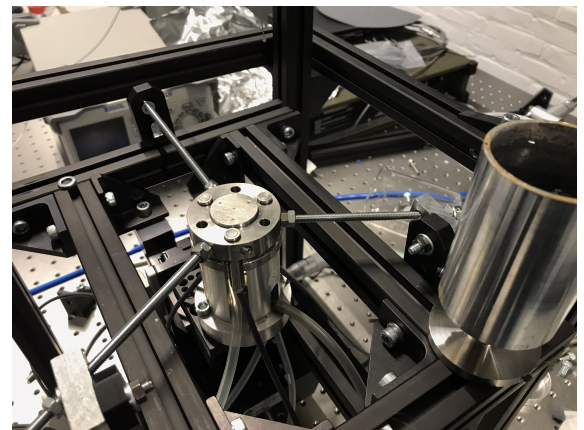


Figure 6.8: Pneumatic flow diagram from source to the air bearing restrictions, the tanks reduce any source pressure variation.

The counter-surface mass can be increased in a discrete or continuous way. Initially, the load was increased by manually adding small weights. Every time a weight is added to the system, the bearing is touched causing a disturbance, also the alignment of individual weights is an issue. This manual method is time consuming and not suitable in the low-stiffness fly height region. It is decided to use a continuous flow of water to increase the load, therefore a water-reservoir is fitted on the counter-surface. In figure 6.9 photos of the set-up with counter-surface and reservoir are depicted. A syringe pump with a volume of: 120 ml, is used to add water with a continuous, well-defined mass flow. The exact sensor specifications can be found appendix G, along with information about the data acquisition and other set-up components.



(a)



(b)

Figure 6.9: Pictures of the final measurement set-up with the counter-surface containing a volume of water.

### 6.3. Measurement procedure

Before the final measurement procedure was established, some tests were done to increase repeatability. During these preliminary tests some problems were encountered that needed a solution. In the final measurement procedure, the loading and supply pressure are simultaneously altered. This means extensive post-processing of the data is needed, to obtain the  $W - h$  graph at a constant supply pressure. The fundamentals of post-processing the measurement data, are discussed in section 6.3.3.

#### 6.3.1. Challenges

At first, measurements were done at a constant pressure by tuning the proportional valve before each measurement. The valve should control the pressure to keep it constant, even when the mass flow changes. However, in practice the proportional valve is affected by a mass flow change, which is a result of the fly height reduction during a measurement. A solution is found by sweeping the supply pressure on purpose, by feeding a sawtooth shaped voltage signal to the electronic proportional valve. Post-processing the data in Matlab gives the correct fly height at constant supply pressure and load.

The alignment of the load and bearing surfaces, affects the minimum achievable fly height before the surfaces make contact. To reduce misalignment of the counter-surface a procedure is followed before each measurement. First, the surfaces are aligned by eye, then the flying mass is gradually increased at constant pressure, this decreases fly height. When all three sensors show the same decreasing trend, the two surfaces stay parallel during motion, indicating perfect alignment. If this is not the case, the bearing shows a tip-tilt motion, indicating mass misalignment. In this case the bearing is slightly displaced with the X-Y stages to realign the flying mass, this is repeated until the surfaces are parallel. These steps reduce the initial alignment error, however the error increases again when water is added as a result of the small intended tilt of the bearing. Measures to reduce the alignment error by introducing a point load instead, were considered but it was unable to implement.

### 6.3.2. Measuring

Two sets of measurements are done, first the bearing without shallow pockets is tested at different supply- and vacuum pressures, the second set of measurements is done after etching the shallow pockets. This gives the ability to compare the regular bearing and shallow pocket bearing. Before a measurement is started, the counter-surface is aligned by following the discussed procedure. From now on the measurement is automated. A voltage signal is sent to the electronic proportional valve, starting at zero supply pressure to determine the height offset. Then a periodic sawtooth signal is generated and the syringe pump with constant flow rate is switched on. At every point in time the system has a certain supply pressure, load and fly height. The maximum water capacity of the syringe pump and reservoir is 120 ml, this gives a maximum load increment of 1.17N per measurement. To measure different parts of the  $W - h$  curve, weights are added to create a load offset and the automated sequence is repeated.

### 6.3.3. Post-processing

The measured fly heights of individual sensors, for one complete measurement cycle and corresponding pressures, are plotted in figure 6.10. The pressure follows the sawtooth signal with a period of 60 s, when pressure increases the fly height increases as well. The time on the horizontal axis, is proportional to the applied load, causing a decreasing fly height over time. The whole measurement creates a large dataset containing: supply pressures, fly heights and loads. A small windowed moving average filter, is applied on all the data, then points of equal pressure are sought among all periodic sections. The dotted lines indicate all points of equal pressure throughout the measurement. Then the corresponding fly heights and loads at this particular pressure and time are selected, giving the  $W - h$  graph at constant supply pressure. The diamond shaped markers indicate when the load starts flying, meaning there is no contact between the surfaces. The periodic fly height data that is at the 'left' of these markers, is invalid because there is still contact between the surfaces.

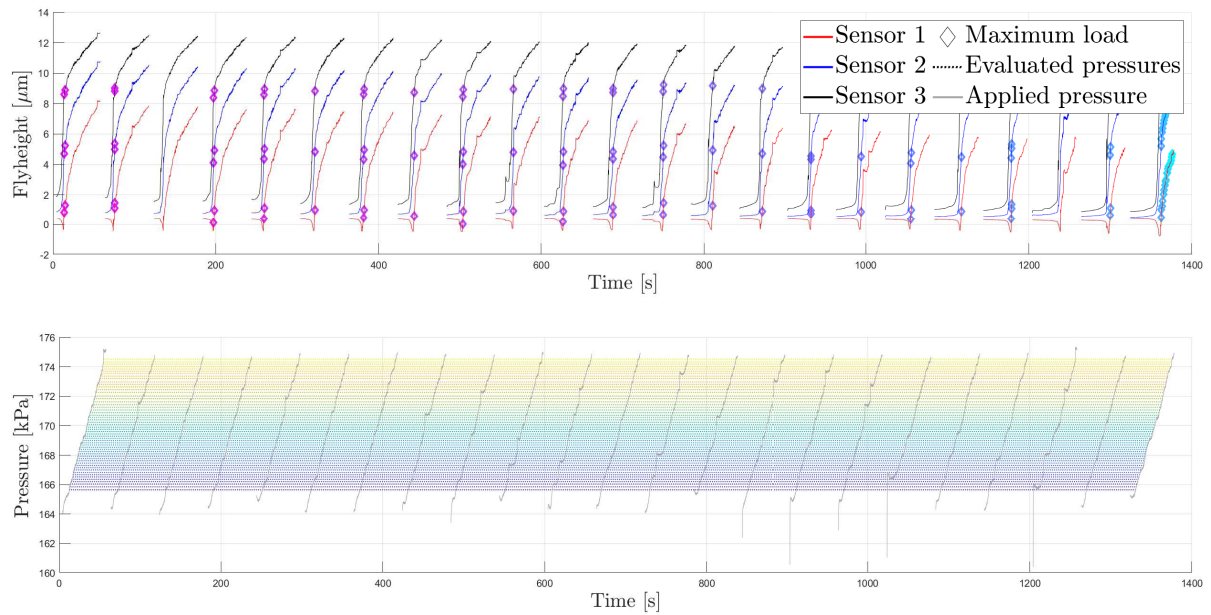


Figure 6.10: The sensor fly height and pressure data for a single automated measurement sequence. The linear increasing pressure 'lifts' the counter mass, the point of no-contact is indicated with the diamond shaped marker. The mass linearly increases with time and the points of equal 'evaluated' pressure are indicated with the coloured dotted lines.

## 6.4. Results

First, a large amount of measurements are done without a shallow pocket, after evaluation of these results the shallow pockets are etched and the measurements are repeated. The results are used to validate the numerical model. The differences between the measurements and the model are analysed and the model is fitted, by allowing small design- and tilt angle corrections.

### 6.4.1. Bearing without shallow pocket

The bearing without any shallow pockets is measured at different supply pressures and applied loads. The minimum achieved fly height before the bearing surfaces make contact is:  $\approx 5\mu\text{m}$  and the bearing became unstable for fly heights exceeding:  $\approx 16\mu\text{m}$ . To measure this complete fly height domain, three load offsets are applied, giving three blocks of data, see figure 6.11. In total three of these measurement sequences are done, with  $166 < P_s < 174\text{kPa}$  and no vacuum. Measurement errors are made when determining the applied load correctly. Sources of errors are: residual water in the reservoir and a time delay between switching on the pump and an actual increase of the load. As discussed previously, the sensor offset is determined before each measurement block. This is an error source in determining the exact fly height, since the orientation of the counter-surface may slightly change. Furthermore, the tip-tilt moment that is created by a load misalignment, influences the load capacity, especially at lower fly heights.

Despite the presence of these measurement errors, the data in figure 6.11 looks promising. This measurement is combined with other measurements and the data at  $P_s = 170\text{kPa}$  is used to validate the numerical model. A small number of data points is used to fit the model, using a least-squares optimisation procedure. From this analysis, it appears there is a systematic error in the measured fly height of:  $1.8\mu\text{m}$ . This is probably a result of a slightly tilted counter-surface, when determining the sensor offset at the start of each measurement. The measurement data in figure 6.12 is shifted accordingly. The model is fitted by allowing a correction of the load capacity ( $\times 1.006$ ) and tilt angle ( $\alpha = 2.1 \times 10^{-4}$  rad), both the original and fitted models are depicted.

The measured bearing has a lower load capacity than is expected by the model, the difference is  $0.08\text{kg}$ . A small part of this difference, is caused in determining the exact applied load. The other source of error is the actual bearing pad radius. To eliminate the latter, the bearing radius is measured with the white light interferometer and is found to be:  $r_o = 12.2\text{mm}$ . Furthermore, the pressure could be overestimated, as a result of a pressure drop between sensor location and actual restriction inlet. The ambient pressure is measured at the

start of each measurement with the same sensor.

A proper fit of the model is found with the applied tilt angle, caused by load misalignment and imperfections in bearing symmetry. This measurement without shallow-pockets validates the used model. In the next section, the shallow-pocket bearing characteristics are measured.

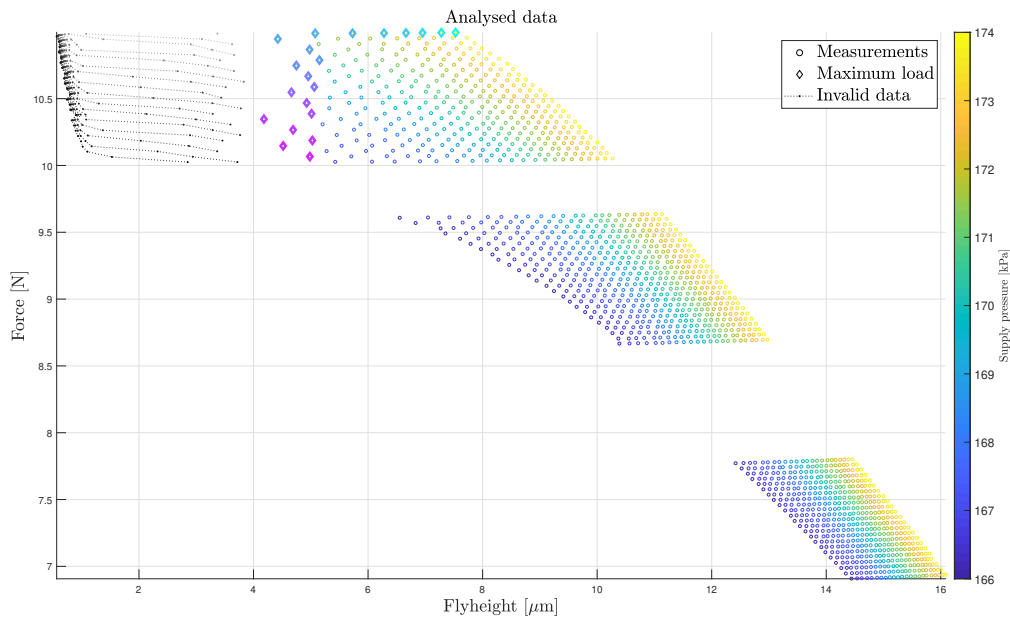


Figure 6.11: A fly height measurement of the bearing without shallow pocket at a range of supply pressures.

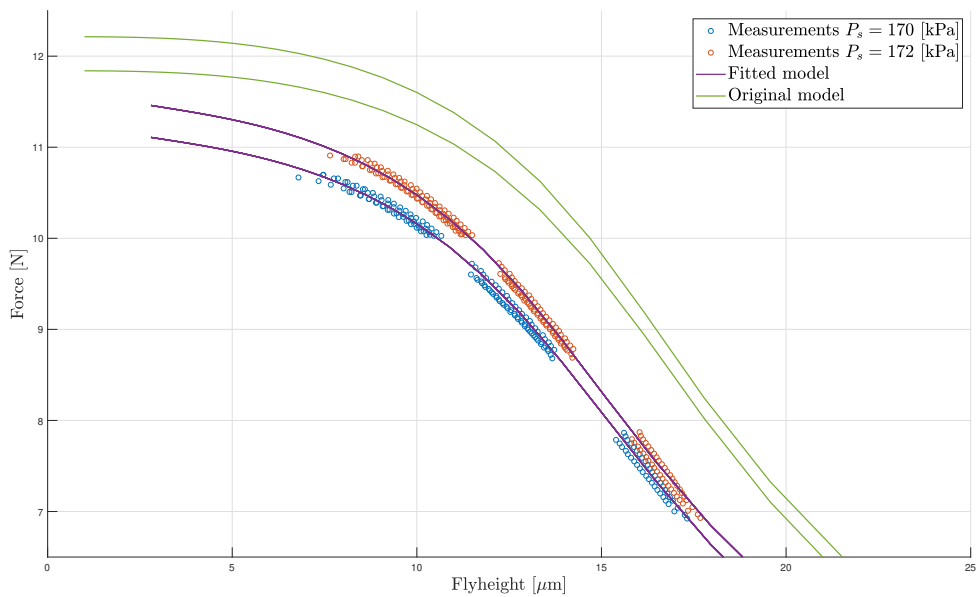


Figure 6.12: Data of three measurements that is corrected for the systematic fly-height error. The data is fitted with the numerical model and is corrected for: the fly-height offset, loading error and tilt angle.

### 6.4.2. Shallow pocket bearing

The pockets are etched in the thin polymer film with the previous described methods. Then, measurements are done with and without vacuum pressure, the results clearly distinct from the bearing without shallow pockets. Unfortunately, none of these measurements showed the low-stiffness characteristic as was designed in chapter 5.

In figure 6.13 an extended measurement is done of the shallow pocket bearing without turning on the vacuum, giving ambient pressure at the centre outlet. The vacuum supply is enabled in figure 6.14 and a measurement is done for a range of supply pressures. From these measurements and observations, it appears that a lower fly height is achieved than the bearing without shallow pockets. Furthermore, there is no sign of a decreasing load capacity at any fly height.

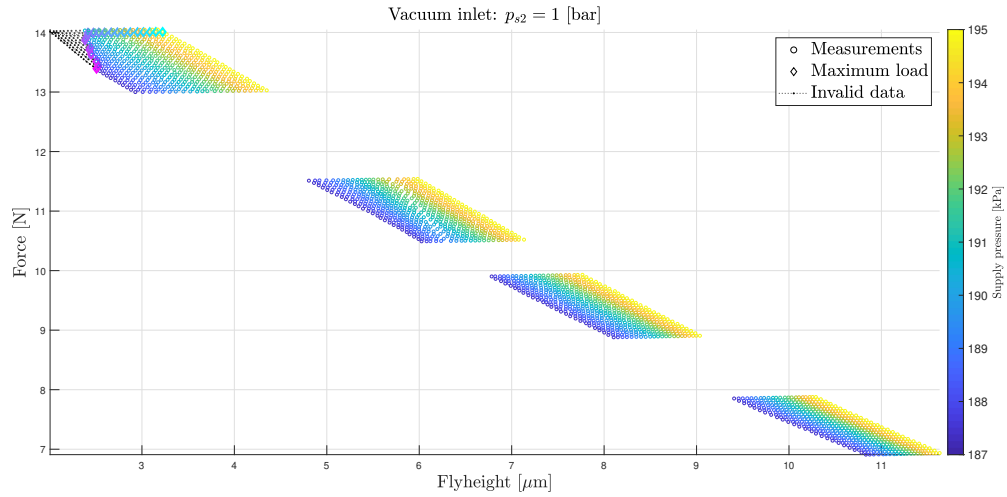


Figure 6.13: A fly height measurement of the bearing with shallow pocket at a range of supply pressures without vacuum.

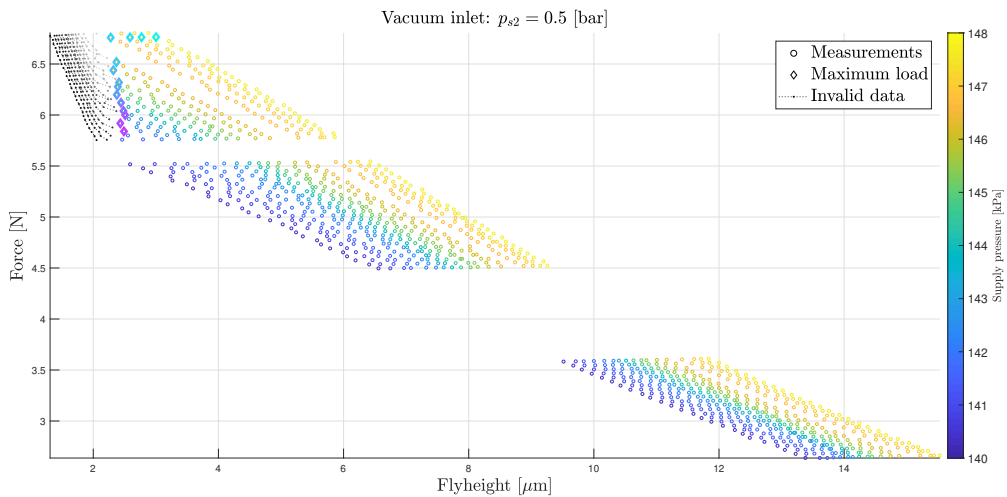


Figure 6.14: A fly height measurement of the bearing with shallow pocket at a range of supply pressures and vacuum pressure.

The data of some measurements at different supply- and vacuum pressures, is further analysed and compared with the numerical model in figure 6.15. The measurements are not in agreement with the original model. It is decided to focus on the measurements with enabled vacuum pressure, since they should represent a low-stiffness operating point somewhere in the fly height domain. The model already proved its validity in section 6.4.1, so the measurement error most likely originates from the modified surface topology and the implementation of shallow pockets.



The model is fitted with a least-squares optimisation, from this it appears that the measured fly height must be smaller than the real fly height. This shifts all measurements in figure 6.16 to the right, reducing the 'gap' between the measured and modelled load capacities. To fit the model, a fly height shift of:  $\approx 6.5\mu\text{m}$  is needed. This means the bearing was unable to reach low range fly-heights, possibly caused by local surface defects.

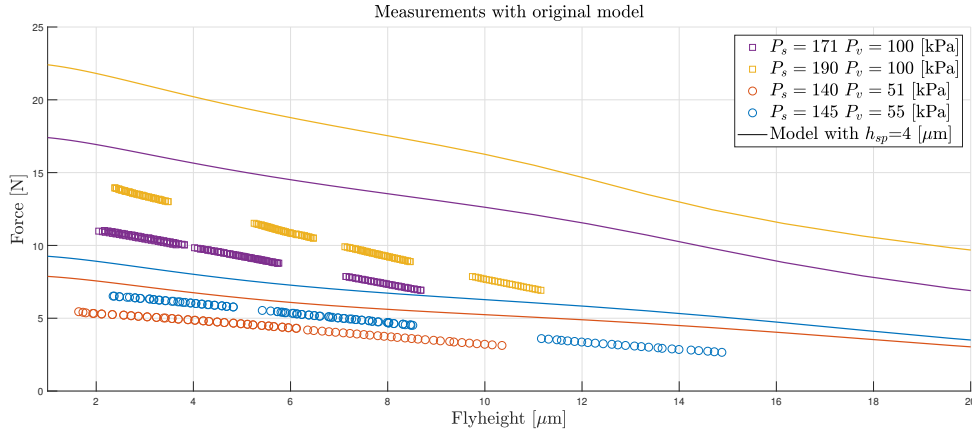


Figure 6.15: Data of four different measurements with the original model from chapter 5, evaluated at a shallow pocket depth of:  $h_{sp} = 4\mu\text{m}$ .

The model is fitted by allowing load and fly height corrections of the measured data, furthermore the tilt angle  $\alpha$  and shallow pocket depth  $h_{sp}$  are used as fitting parameters. The measurements fit the model when taking a shallow pocket depth of:  $h_{sp} = 5.2\mu\text{m}$ , this corresponds with the findings in figure 6.5. The tilt angles  $\alpha$  for the  $P_s = 140$  and  $P_s = 145$  measurements are:  $1 \times 10^{-4}$  rad and  $2 \times 10^{-4}$  rad respectively. From these findings, it appears that the bearing surface did not satisfy the flatness and roughness requirements to achieve lower fly heights. It was expected that any local height offsets in the polymer film, would wear off after some time, like it was the case in section 6.4.1. After a number of measurements, delamination of the polymer film at the bearing's outer pocket edges is observed, although the fundamental geometry stayed intact. This could cause a thickening of the polymer film around the shallow-pockets and explain the fly height offset of  $6.5\mu\text{m}$ .

The purple lines of the fitted model in figure 6.16, do not show a clear *horizontal segment*, indicating zero-stiffness. This is a result of the shallow-pockets being slightly too deep. There was no time to replace the polymer layer to create new shallow-pockets, furthermore, the success rate of the proposed manufacturing steps turned out to be low. Fortunately, the measurements without shallow-pockets, validated the numerical model. Although, the measured low-stiffness bearing characteristics are in agreement with the model, they are not clear enough to validate the concept.

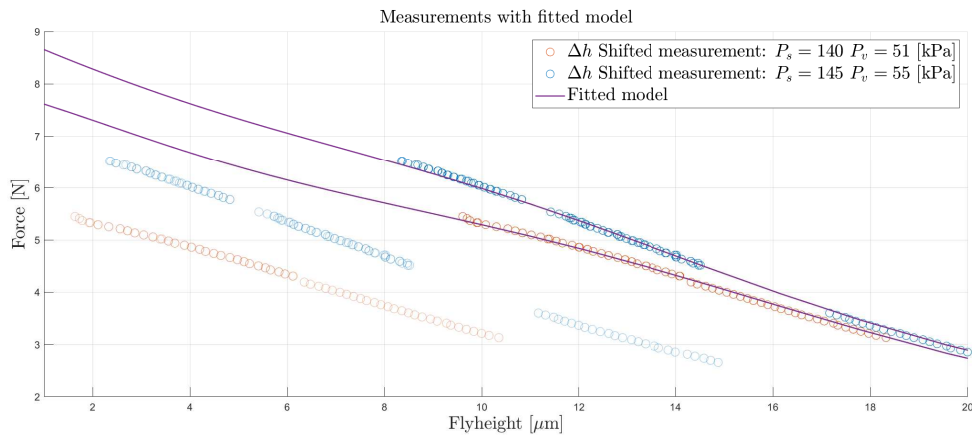


Figure 6.16: The original measurements are shifted to a larger fly height and the model is fitted by adjustment of the: tilt angle and shallow pocket depth. The latter is slightly too deep, 'softening' the zero-stiffness characteristic.

## 6.5. Conclusion

The design from chapter 5, has been manufactured and is integrated in a measurement set-up. The base of the prototype is made of stainless steel and houses the previously measured restriction needles. The actual bearing surface is made from a thin polymer film, in which shallow-pockets are etched. The bearing is placed on an aluminium stand to be able to integrate the tubing and sensors. Multiple linear micrometer stages are used to adjust the sensor gap, tip-tilt angle and to enable precise counter-surface alignment. The fly height is measured while continuously increasing the *counter-surface's* load, under a periodically changing inlet pressure.

Extensive post-processing of the measurement data, gives the  $W - h$  characteristics for a range of inlet pressures. The bearing without shallow-pockets validates the used model, when corrected for a systematic fly height- and tip-tilt error. The measurements with shallow-pocket, do not show a clear low-stiffness region, as was designed in chapter 5. Surface defects made it impossible to achieve lower fly heights and the shallow-pocket turned out to be too deep, this 'softens' the designed stiffness characteristic. The proposed production techniques did not deliver the expected results, making it hard to adapt the prototype in a later stage.

To conclude, the numerical model is validated and it is likely that a static low-stiffness design exists, although this could not be clearly validated, due to manufacturing difficulties.

# 7

## Conclusion

The goal of this research, is to optimise and validate the low-stiffness bearing concept, by studying the relation, between dynamic thin-film characteristics and the transmissibility function. To achieve this goal, a 2D numerical model is made, which is based on the compressible Reynolds equation and measured restriction-flow characteristics. The model is used, to study the static and dynamic characteristics of aerostatic bearing pads and their relation to thin-film transmissibility. To obtain a stable and manufacturable design, an optimisation procedure is implemented. The optimisation constraints, are 'partly' based on newly explored shallow-pocket bearing manufacturing techniques. An optimised shallow-pocket bearing is manufactured, by using spin-coating and polymer etching techniques and is tested in a measurement set-up. The measured bearing characteristics validate the numerical model, however, the low-stiffness concept could not be proved.

The desire to validate the low-stiffness concept required early design optimisation and demonstrator manufacturing to stay within project time. During this initial phase questions arose about the effect of low-stiffness on thin-film transmissibility. The research was extended, to a more fundamental study of dynamic bearing properties and their relation with transmissibility. New insights are found, concerning the importance of damping and overall design variable sensitivity. Despite these findings it is still valuable to construct a low-stiffness design to validate the concept and as starting point in transmissibility minimisation. The following conclusions can be drawn from this study.

The numerical model, is suitable to find both *static & dynamic* bearing pad characteristics and is applicable to non-symmetric designs. The flow properties of *industry standard*, blunt syringe needles are measured and different flow models from literature are discussed. The laminar capillary flow model, shows a proper fit for small pressure gradients and Reynolds numbers. Furthermore, the tested restriction elements have a small variance, resulting in a repeatable inlet flow.

The thin-film can be modelled, with a single mass and non-linear spring and damper elements. The transmissibility function is derived and describes the coupling between the vibrating base and flying mass, as function of perturbation frequency. The 'mass' term is a collection of the bearing's dimensional scaling factors and has a large influence on the transmissibility function. The dynamic characteristics of low- and high pressure pads are described and the effect of 'dead' pocket volume on damping is studied. The analysis shows the importance of reducing *both* stiffness and damping to achieve lower transmissibility.

It is found that a combination of the shallow-pocket and height-offset concepts (hybrid design) does not improve the low-stiffness design. However, with the hybrid design it is possible to shift the low-stiffness operating point to a different fly height. A hybrid design, with aligned low-stiffness and low-damping operating fly heights is presented. This results in a positive damping at all fly heights and perturbation frequencies. The minimised damping causes small negative stiffness in a certain frequency band.

The operating point stiffness and damping, shows a high sensitivity to small design changes, especially to supply pressure variations. Furthermore, it is shown that small stiffness and damping variations have a large influence on the transmissibility. Further design optimisation by reducing the stiffness and damping increases transmissibility sensitivity with the strongest effect at low frequencies. The high sensitivities limit

the allowed perturbation amplitude, because of the stiffness and damping non-linearities with displacement.

A method is found to create shallow-pocket bearings with different geometries and pocket depths, by using available techniques. The proposed method spin-coats a thin polymer film on a stainless steel substrate. Plasma- or wet etching techniques are combined with a soft mask, to etch shallow surface features in the polymer film. The surface quality and thickness of the spin-coated film were difficult to control, making the total process prone to errors.

A low-stiffness shallow-pocket bearing with three supply inlets and one vacuum outlet is optimised and manufactured. A small counter-surface tilt angle, has negligible influence on the zero-stiffness operating point characteristics. A tilt angle, does however, reduce the load capacity and stiffness at lower fly heights. The orientation of the inlets relative to the tilt rotational axis, hardly influences the angular stiffness.

The bearing is integrated in a measurement set-up and the fly height is measured at different loads and inlet pressures. A novel semi-automatic measurement procedure is used, where the load is continuously increased, while periodically changing the supply pressure. This method works around the problem of small pressure variations, caused by a changing mass flow and internal valve hysteresis. The capacitive sensors are capable to measure fly height changes with nanometre resolution. However, a systematic fly height error is introduced, when determining the sensor offset, at ambient inlet pressure and surface contact.

Measurements with- and without shallow-pockets are done, the latter shows good agreement with the model, when compensating for small tilt- and loading errors. After etching the shallow-pockets, measurements are repeated. A large fly-height offset is observed, meaning the bearing could not reach lower fly heights. This is caused by local thickening of the polymer layer, possibly resulting from surface defects and film delamination. Furthermore, it appears that the pockets were slightly too deep, resulting in an unclear low-stiffness characteristic. This means that the model is validated, although the low-stiffness concept could not be clearly proven, due to manufacturing difficulties.

The research objectives stated in chapter 1 are partially fulfilled. The low-stiffness concept is further analysed, optimised and a demonstrator is manufactured. Measurements of a bearing without zero-stiffness characteristic, prove the validity of the numerical model. It is likely that the *static* zero stiffness concept is valid, although manufacturing a demonstrator is challenging. The underlying principle of stiffness minimisation, is to reduce the thin-film transmissibility. In this study new insights are presented, showing the possibilities and difficulties of low-transmissibility aerostatic pads. In the next chapter recommendations are given on future research.

# 8

## Towards the future

The current study gives a fundamental view on the concept of low-transmissibility aerostatic pads. The used model, is perfectly suitable to analyse the frequency dependent bearing characteristics. However, the stiffness and damping are linearised at the operating fly height, introducing an error. The error increases when larger perturbation amplitudes are considered. These small deviations of stiffness and damping, affect the transmissibility function. The following recommendations are given regarding the used *model*:

- Develop a more advanced non-linear dynamic bearing model covering *both* displacement and frequency non-linearity.
- Implement the ability to get a time-domain solution of the non-linear model to perform a limit-cycle oscillation analysis and assess the stability in all frequency bandwidths.

The study shows that, *both* stiffness and damping reduction is necessary to reduce the transmissibility. It is also found, that optimisation leads to higher design variable sensitivities. The following needs further investigation when designing a low-transmissibility system.

- The high design sensitivities require adjustment of key design features after manufacturing. One could investigate the possibilities of a compliant bearing surface, with an adjustable pad height offset and restriction-pocket volume. This way both stiffness and damping can be tuned.
- This research focussed on *passive* vibration isolation and this is found to be challenging. Future research could investigate the possibilities of (semi) active bearing control.
- The system shows a high sensitivity to variations in supply- and vacuum pressure, these are the only design variables prone to change, during bearing operation. Methods to reduce this particular pressure sensitivities, could be explored, combined with the use of advanced proportional (*piezo*) valves.

The used measurement set-up with continuously increasing load and periodic pressure variations functioned properly but can be improved. The following improvements are suggested:

- The volume of the counter-surface water reservoir and syringe pump, should be increased. This gives the possibility, to measure a larger range of fly heights in a single measurement sequence. Resulting in reduced loading error and faster measurements.
- The current set-up, uses a controllable proportional valve on the supply pressure and a manual valve on the vacuum pressure. The latter could be replaced with a controllable valve, to enable a periodic vacuum sweep during measurements.
- The three capacitive sensors are perfectly suitable to measure small fly height changes and tilt. It appeared to be difficult, to determine the sensor offset at zero fly-height, introducing a systematic error. Increasing the surface quality of the bearing- and counter surface, possibly reduces this error.

- The current set-up does not have a vibrating base, to enable dynamic bearing characterisation. The available shakers generally have an amplitude of a few millimetres. A *piezo* element, can be a solution to vibrate the bearing at small amplitudes and high frequencies, while delivering enough force.

Future low-transmissibility bearing research, should start with enhancing the current model with the implementation of the discussed improvements. A demonstrator with *adjustable* elements can be manufactured, to validate the low- stiffness and damping design at different perturbation frequencies. Such demonstrator, can also be used to empirically determine the influence of all *adjustable* bearing elements, on the transmissibility function. Active feedback control may be applied, although, it opposes the current *passive* or *feed-forward* controlled bearing philosophy and results in: increased- complexity and costs and limited bandwidth .

Some interesting findings from this study, could be used outside the context of low-transmissibility. The optimisation procedure, can be used to *separately* tune: thin-film stiffness, damping and load capacity, within certain limits. This means that a combination of aerostatic pads, can be used as adjustable spring damper elements, with a predetermined eigenfrequency and damping factor. Furthermore, it is found that implementation of a vacuum outlet with large restriction-pocket volume, increases damping. This relation might be a solution for *pneumatic hammer* in certain applications.

The tested blunt syringe needle restriction elements are characterised and fitted with different models. Blunt needles with various inner diameters are available, these might be suitable in other bearing applications with a restricted inlet flow.

# A

## Reynolds equation

The Reynolds equation describes a pressure field between two surfaces which are separated by a thin film. The Reynolds equation was first derived by Osbourne Reynolds in 1886 and is used in thin film lubrication. The two dimensional compressible Reynolds equation can be derived in two common ways. The first method is simplification of the Navier-Stokes equation and the second method is by writing down the force balance of an infinitesimal small volume element inside the thin film. Both derivation methods are treated in [19, p. 147], in this section the Navier-Stokes equation is used as starting point. All assumptions are written down, alongside the derivation of the two dimensional Reynolds equation.

### A.1. Navier-Stokes equation

As a starting point in deriving the Reynolds equation, the Navier-Stokes equation can be used. The Navier-Stokes equation describes the motion of viscous fluids, a derivation can be found in [55].

The basic differential momentum equation for an infinitesimal element is given in equation A.1, see [55, p. 241]. When written in a sentence: gravity force per unit volume + pressure force per unit volume + viscous force per unit volume = density  $\times$  acceleration.

$$\rho \mathbf{g} - \nabla p + \nabla \cdot \boldsymbol{\tau}_{ij} = \rho \frac{d\mathbf{V}}{dt} \quad (\text{A.1})$$

where

$$\frac{d\mathbf{V}}{dt} = \frac{\partial \mathbf{V}}{\partial t} + u \frac{\partial \mathbf{V}}{\partial x} + v \frac{\partial \mathbf{V}}{\partial y} + w \frac{\partial \mathbf{V}}{\partial z} \quad (\text{A.2})$$

This equation is valid for all fluids in any general motion. It becomes useful when the viscous stresses ( $\boldsymbol{\tau}_{ij}$ ) are written in terms of velocity components. When frictionless flow is assumed ( $\boldsymbol{\tau}_{ij} = 0$ ) equation A.1 becomes *Eulers' equation* which forms the basis for the *Bernoulli equation*. For now an isotropic Newtonian medium is considered and the relation in equation A.3 is valid. Note that the viscosity ( $\mu$ ) is considered as a constant and does therefore, not change over film height.

$$\boldsymbol{\tau}_{ij} = \mu \left( \frac{\partial v_i}{\partial x_j} + \frac{\partial v_j}{\partial x_i} \right) \quad (\text{A.3})$$

Equation A.3 is substituted in the momentum equation A.1. All the components that 'hide' in the vector notation are written throughout, see equation A.4 from [55, p. 242].

$$\begin{aligned} \rho g_x - \frac{\partial p}{\partial x} + \mu \left( \frac{\partial^2 u}{\partial x^2} + \frac{\partial^2 u}{\partial y^2} + \frac{\partial^2 u}{\partial z^2} \right) &= \rho \frac{du}{dt} \\ \rho g_y - \frac{\partial p}{\partial y} + \mu \left( \frac{\partial^2 v}{\partial x^2} + \frac{\partial^2 v}{\partial y^2} + \frac{\partial^2 v}{\partial z^2} \right) &= \rho \frac{dv}{dt} \\ \rho g_z - \frac{\partial p}{\partial z} + \mu \left( \frac{\partial^2 w}{\partial x^2} + \frac{\partial^2 w}{\partial y^2} + \frac{\partial^2 w}{\partial z^2} \right) &= \rho \frac{dw}{dt} \end{aligned} \quad (\text{A.4})$$

The second-order partial differential equation A.4, is known as the incompressible flow *Navier-Stokes equation*. This equation has four unknowns:  $p$ ,  $u$ ,  $v$ ,  $w$  respectively. The continuity equation A.5, describing the conservation of mass, is added to solve the system with four unknowns.

$$\frac{\partial \rho}{\partial t} + \frac{\partial}{\partial x} \rho u + \frac{\partial}{\partial y} \rho v + \frac{\partial}{\partial z} \rho w = 0 \quad (\text{A.5})$$

The continuity equation A.5 requires no assumptions, while the Navier-Stokes equation A.4 has the following.

- Incompressible medium
- Constant viscosity
- Newtonian medium
- Constant density

Equations A.4 and A.5 will be used as basis to derive the compressible Reynolds equation, changing the aforementioned assumptions.

## A.2. Compressible Reynolds equation

The *Navier-Stokes equation* A.4 is further simplified by making more assumptions. First thin film geometry is assumed, meaning body forces are negligible ( $\rho g_i = 0$ ). Furthermore, steady flow is assumed so the transient terms ( $\rho \frac{du}{dt}$ ) become zero. At the walls, no-slip boundary conditions are applied and the pressure gradient becomes zero ( $\frac{\partial p}{\partial z} = 0$ ), because of the thin film assumption. These assumptions simplify equation A.4 drastically, yielding equation A.6.

$$\begin{aligned} \frac{\partial p}{\partial x} &= \mu \frac{\partial^2 u}{\partial z^2} \\ \frac{\partial p}{\partial y} &= \mu \frac{\partial^2 v}{\partial z^2} \end{aligned} \quad (\text{A.6})$$

In figure A.1 a thin film bearing gap of height  $h$  between two surfaces is drawn. Both surfaces have six degrees of freedom. Displacement of the surfaces or a pressure gradient results in a velocity profile. This profile consists of a pressure driven part and a velocity driven part, known as Poiseuille and Couette flow respectively. This pressure profile is found by integrating equation A.6 twice and applying the no-slip B.C:  $u(z=0) = u_1$ ,  $u(z=h) = u_2$ ,  $v(z=0) = v_1$  and  $v(z=h) = v_2$ , see equation A.7. This pressure profile is only valid in laminar flow conditions.

$$\begin{aligned} u(x, z) &= \frac{1}{2\mu} \frac{\partial p}{\partial x} (z^2 - hz) + \frac{z}{h} (u_2 - u_1) + u_1 \\ v(y, z) &= \frac{1}{2\mu} \frac{\partial p}{\partial y} (z^2 - hz) + \frac{z}{h} (v_2 - v_1) + v_1 \end{aligned} \quad (\text{A.7})$$

The mass flow through the gap can easily be found by integrating the velocity profile over the film thickness  $h$  and multiplying with the density. The mass flow per unit length is given in equation A.8.

$$\begin{aligned} m_x &= \rho \int_0^h u(x, z) dz = -\frac{\rho h^3}{12\eta} \frac{\partial p}{\partial x} + \frac{\rho h}{2} (u_1 - u_2) \\ m_y &= \rho \int_0^h v(y, z) dz = -\frac{\rho h^3}{12\eta} \frac{\partial p}{\partial y} + \frac{\rho h}{2} (v_1 - v_2) \end{aligned} \quad (\text{A.8})$$

Now the mass flow inside the gap is expressed, the equation of continuity A.5, is needed to preserve conservation of mass. Equation A.5 is slightly rewritten to obtain the mass balance in equation A.9, substitution of equation A.8 gives the second part in A.9. Note that the mass flow  $m_z$  is zero because of the thin film assumption and may therefore be neglected.

$$\begin{aligned} \frac{\partial \rho h}{\partial t} &= \frac{\partial m_x}{\partial x} + \frac{\partial m_y}{\partial y} + \frac{\partial m_z}{\partial z} \\ \frac{\partial \rho h}{\partial t} &= \frac{\partial}{\partial x} \left( \frac{\rho h^3}{12\eta} \frac{\partial p}{\partial x} \right) + \frac{\partial}{\partial x} \left( \frac{\rho h (u_1 - u_2)}{2} \right) + \frac{\partial}{\partial y} \left( \frac{\rho h^3}{12\eta} \frac{\partial p}{\partial y} \right) + \frac{\partial}{\partial y} \left( \frac{\rho h (v_1 + v_2)}{2} \right) \end{aligned} \quad (\text{A.9})$$



The dynamic part in this equation is represented by the term at the left of the equal sign:  $(\frac{\partial \rho h}{\partial t})$ . This dynamic part is analysed further by using the product rule, see equation A.10.

$$\frac{\partial \rho h}{\partial t} = \rho \frac{\partial h}{\partial t} + h \frac{\partial \rho}{\partial t} \quad (\text{A.10})$$

The second term  $h \frac{\partial \rho}{\partial t}$  describes local expansion in the thin film and refers to a change in density over time, this could be caused by adding heat to the system. The first term  $\rho \frac{\partial h}{\partial t}$  describes the change in film height  $h$  over time and is called 'squeeze' effect. This effect can be caused by simple up and down motion of surface 1 and 2 or by a translation over an inclined plane. The dynamic equation is rewritten in expanded form in A.11.

$$\frac{\partial \rho h}{\partial t} = \rho (w_2 - w_1) - \rho u_2 \frac{\partial h}{\partial x} - \rho v_2 \frac{\partial h}{\partial y} + h \frac{\partial \rho}{\partial t} \quad (\text{A.11})$$

The final Reynolds equation consists of pressure driven flow (Poiseuille flow), external driven flow by moving surfaces (Couette flow) and the Dynamic (squeeze) effects. The Reynolds equation written in Cartesian coordinates is given in A.12

$$\frac{\partial}{\partial x} \left( \frac{\rho h^3}{12\eta} \frac{\partial p}{\partial x} \right) + \frac{\partial}{\partial y} \left( \frac{\rho h^3}{12\eta} \frac{\partial p}{\partial y} \right) = \frac{\partial}{\partial x} \left( \frac{\rho h (u_1 - u_2)}{2} \right) + \frac{\partial}{\partial y} \left( \frac{\rho h (v_1 + v_2)}{2} \right) + \rho \left( w_2 - w_1 - u_2 \frac{\partial h}{\partial x} - v_2 \frac{\partial h}{\partial y} \right) + h \frac{\partial \rho}{\partial t} \quad (\text{A.12})$$

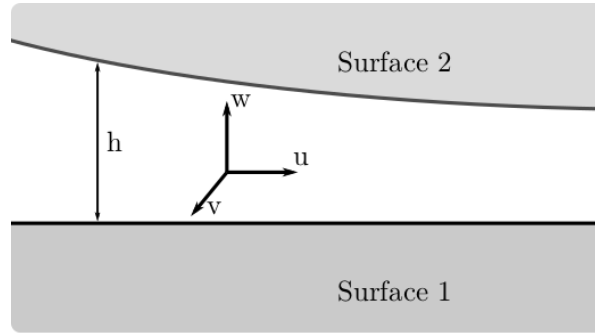


Figure A.1: Two surfaces separated that are with a thin film of thickness  $h$

The presented Reynolds equation in A.12 can be modified to make it more suitable to use with compressible lubricants like air. The density ( $\rho$ ) has a strong relation with the local film pressure and can be described with the ideal gas law:

$$\rho = \frac{p}{R_s T} \quad (\text{A.13})$$

This equation is substituted in A.12 while assuming constant temperature  $T$  and  $R_s$  the specific gas constant of the medium, this yields A.14.

$$\underbrace{\frac{\partial}{\partial x} \left( \frac{p h^3}{12\eta R_s T} \frac{\partial p}{\partial x} \right) + \frac{\partial}{\partial y} \left( \frac{p h^3}{12\eta R_s T} \frac{\partial p}{\partial y} \right)}_{\text{Poiseuille flow}} - \underbrace{\frac{\partial}{\partial x} \left( \frac{p h (u_1 - u_2)}{2} \right) - \frac{\partial}{\partial y} \left( \frac{p h (v_1 + v_2)}{2} \right)}_{\text{Couette flow}} + \frac{1}{R_s T} \left( \underbrace{(w_1 - w_2) p}_{\text{Normal squeeze}} + \underbrace{u_2 \frac{\partial h p}{\partial x} + v_2 \frac{\partial h p}{\partial y}}_{\text{Translational squeeze}} \right) - \underbrace{\frac{h}{R_s T} \frac{\partial}{\partial t} p}_{\text{Local expansion}} = 0 \quad (\text{A.14})$$

The derived Reynolds equation A.14 is written in Cartesian coordinates and therefore applicable to non-symmetric geometries. The equation consists of different parts, with distinct physical significance as described in [19]. The Poiseuille terms describe the net flow rates due to pressure gradients. The Couette terms describes the flow rate, resulting from surface displacements. The squeeze terms and the local expansion

originate from a transient term in the Reynolds equation. The normal squeeze term describes the flow when the two surfaces are pressed together. This term directly creates a pressure in the film, proportional with the relative displacement. This effect is sometimes described as the 'cushioning' effect and is of great importance when studying the dynamic characteristics. The translational squeeze, results from translation of an inclined bearing surface and is proportional to the rate of which the film thickness decreases. The local expansion term describes the change in film pressure over time. This self-induced term is related to the density of the medium, which is a function of temperature. Equation A.14 is not always valid, the following assumptions are made during derivation:

1. Constant viscosity.
2. Newtonian lubricant.
3. Thin film geometry, meaning a small film height compared to the film length, constant pressure over film height is assumed.
4. Body forces are neglected.
5. Laminar flow theory is applied neglecting fluid inertial forces.
6. No slip at boundaries.
7. Air film is assumed to be isothermal.

The Couette flow can be neglected if the sliding velocities of the bounding surfaces are small. This simplifies the general Reynolds equation A.14 into equation A.15

$$\frac{\partial}{\partial x} \left( \frac{ph^3}{12\eta R_s T} \frac{\partial p}{\partial x} \right) + \frac{\partial}{\partial y} \left( \frac{ph^3}{12\eta R_s T} \frac{\partial p}{\partial y} \right) - \frac{1}{R_s T} \frac{\partial hp}{\partial t} = 0 \quad (\text{A.15})$$

### A.3. Solving the Reynolds equation

Solving the second order partial differential equation can be challenging and most problems require the use of finite element or finite difference methods. Analytical solutions for the *static* Reynolds equation exist, but only for simple geometries. However, when the dynamics need to be studied the method of linear perturbation is used, in combination with finite element methods. The perturbed Reynolds equation is found by substitution of a perturbed fly height and pressure. These fly height and pressure are consisting of a static part and a dynamic part that introduces a sinusoidal 'squeezing' motion around a static solution, see equation A.16.

$$\begin{aligned} h &= h_0 + \delta h(t) = h_0 + \tilde{h}e^{j\omega t} \\ p &= p_0 + \delta p(t) = p_0 + \tilde{p}e^{j\omega t} \end{aligned} \quad (\text{A.16})$$

The stiffness is found by taking the partial derivative of the load capacity with respect to the fly height. The damping is obtained by differentiating the load capacity with respect to the velocity. Both equations for dynamic stiffness and damping are derived in equation A.17

$$\begin{aligned} k &= -\frac{\partial W}{\partial h} \approx -\frac{\delta W - W_0}{(h_0 + \delta h) - h_0} = -\frac{\int p_0 + \delta p dr - \int p_0 dr}{(h_0 + \delta h) - h_0} = -\frac{\int \tilde{p}e^{j\omega t} dr}{\tilde{h}e^{j\omega t}} = -\frac{\int \tilde{p} dr}{\tilde{h}} \\ c &= -\frac{\partial W}{\partial \dot{h}} \approx -\frac{\delta W - W_0}{(\dot{h}_0 + \delta \dot{h}) - \dot{h}_0} = -\frac{\int p_0 + \delta p dr - \int p_0 dr}{(\dot{h}_0 + \delta \dot{h}) - \dot{h}_0} = -\frac{\int \tilde{p}e^{j\omega t} dr}{j\omega \tilde{h}e^{j\omega t}} = -\frac{\int \tilde{p} dr}{j\omega \tilde{h}} \end{aligned} \quad (\text{A.17})$$

Now the perturbed Reynolds equation is determined, see equation A.18. This is done by substitution of equation A.16 in equation A.15 while neglecting higher order terms in  $\delta$ . With this perturbed Reynolds equation, the perturbed pressures can be calculated in the thin film of air. These perturbed pressures are used in equation A.17 to get the frequency dependent stiffness and damping.

$$\begin{aligned}
& -\frac{1}{12\eta R_s T} \left( \frac{\partial}{\partial x} \left( p_0 h_0^3 \frac{\partial}{\partial x} \tilde{p} + \tilde{p} h_0^3 \frac{\partial}{\partial x} p_0 + 3p_0 h_0^2 \tilde{h} \frac{\partial}{\partial x} p_0 \right) + \frac{\partial}{\partial y} \left( p_0 h_0^3 \frac{\partial}{\partial y} \tilde{p} + \tilde{p} h_0^3 \frac{\partial}{\partial y} p_0 + 3p_0 h_0^2 \tilde{h} \frac{\partial}{\partial y} p_0 \right) \right) \\
& + \frac{1}{R_s T} j\omega (p_0 \tilde{h} + h_0 \tilde{p}) = 0 \quad (\text{A.18})
\end{aligned}$$

In equation A.18 the static solution is needed, these static solutions which are indicated by a 0 subscript are found by solving the static part of equation A.15. After a small perturbation around this static solution the stiffness and damping is found.



# B

## Restrictor measurements

To obtain the exact mass flow properties of a restriction element a measurement is done. This particular measurement is also performed by: [54] [21] and [43] but for different restrictor types. Using the same set-up, the mass flow of the needle restriction elements discussed in section .. are measured.

### B.1. Measurement procedure

The air pressure before entering the restrictor is measured while deflating a pressurized tank of 2 litres. To measure the air pressure a NXP MPX5700A absolute sensor is used in combination with a NI-USB-6211 (16-bit) data acquisition system. The computer program Labview is used to log the pressure data with a time step of: 10ms. The pressure sensor has a 7 bar pressure range so the tank is pressurized just below this value. Pressurizing the tank is done by closing valve 2 and opening valve 1, when the tank has a pressure between 6 and 7 bar valve 1 is closed. Now the measurement is started while valve 2 remains closed, this is done to measure the correct ambient air pressure. After a few seconds valve 2 is opened and the tank deflates through the restriction. During this deflation the upstream air pressure is measured.

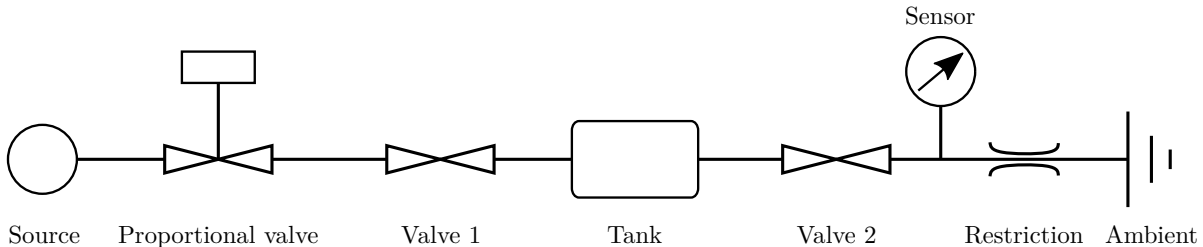


Figure B.1: Restriction measurement set-up

The mass inside the tank is calculated using the tank's volume and the ideal gas law. By taking the derivative of the mass over time the mass flow is determined, see equation B.1. It is assumed that the temperature and the volume remain constant during the measurement. The minus sign indicates that there is a negative flow from the tank through the restrictor.

$$\dot{m} = - \frac{\partial p}{\partial t} \frac{V}{R_s T} \quad (\text{B.1})$$

### B.2. Data processing G30 Measurement

The upstream pressure is measured for six G30 size blunt needles when deflating the compressed air-tank, see figure B.2. The initial tank pressure is around 7 bar, it can be seen that all needles have the same characteristic except the third measurement, which has a higher pressure drop. The pressure data from the measurement shows some high frequent scatter when zoomed-in. The raw pressure data is analysed using the fast Fourier transform (FFT) method, a power spectral density plot is made to determine the dominant frequencies in the signal, see figure B.3a. The discharge of the tank is a slow process that is represented by the high spectral

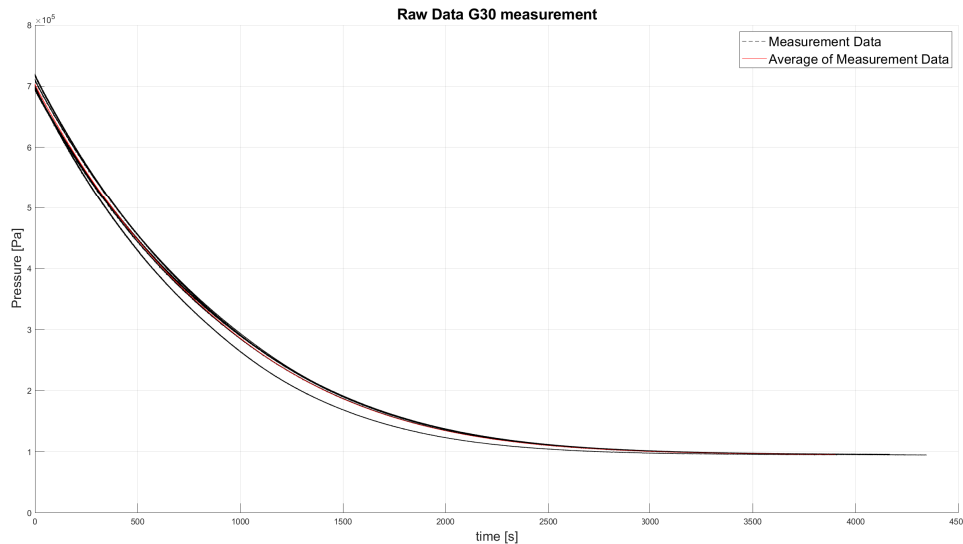
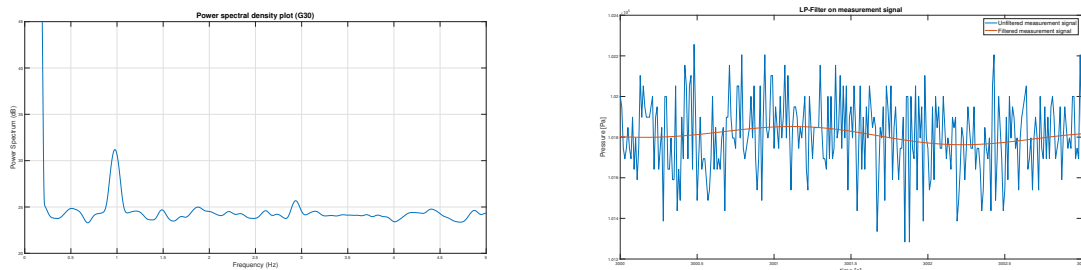


Figure B.2: Absolute pressure of G30 needles

density for frequencies under: 0.25Hz. Another peak is visible at a frequency of: 1 Hz. The noise on the signal is captured in the:  $1\text{ Hz} < f < 50\text{ Hz}$  band and can be filtered using a low-pass filter. So before further processing is done the data is filtered using a first-order low-pass filter with: a pass-band-frequency and a stop-band-frequency of 1 Hz and 1.5 Hz respectively. In figure B.3b a section of the original unfiltered measurement signal and the filtered signal are plotted. It can be seen that the high frequency noise is removed and a smooth signal is obtained.



(a) Power spectral density of pressure signal

(b) Filtered signal using first order LP-Filter

Figure B.3: Processing of raw data

It is decided to remove the third measurement since it deviates too much from the other needles. The data of the five remaining restrictor needles is analysed further and the mass flux versus quadratic pressure difference is plotted, see figure B.4. All five measurements have a similar mass flux and a sudden increase in mass flux at high pressure differences. This unexpected increase in mass flux at the beginning of each measurement is called: "measurement flag" and is observed in [54] as well. In [54] some tests are done to explain the origin of this unexpected measurement 'flag'.

According to [54] the temperature in the tank plays a role. Some tests were done with filling the tank and resting it for a couple of hours to be sure the temperature inside the tank equals the ambient temperature, this did not remove the 'flag'. It could be that the air temperature is underestimated at the start of the measurement resulting in a higher mass flux. This higher air temperature might be a result of initial dynamic effects before the system reaches a steady-state. It is considered to measure the real-time temperature inside the tank but it takes too much time to implement an airtight thermocouple. Instead the ambient air temperature is measured twice during each measurement and used in further calculations. The initial start-up effects at

the beginning of each measurement are removed in further analysis.

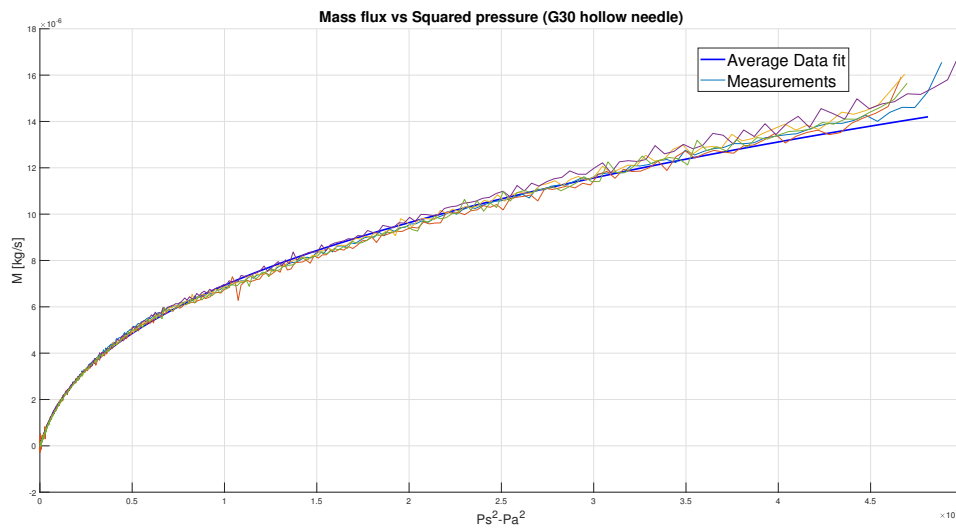


Figure B.4: Mass flux G30 needle restrictions

### B.2.1. G30 measurement results

The results from the measurement are processed in appendix.. and will be further analysed. The flow models that are discussed in the theory section are applied on the measurement data, see figure B.5. The discharge coefficient for the ideal- and Jobson fit are in the displayed in the legend and are: 0.42 and 0.31 respectively. The best fit for the adiabatic Fanno flow model is achieved with a friction coefficient of: 0.072 which corresponds with a rough wall.

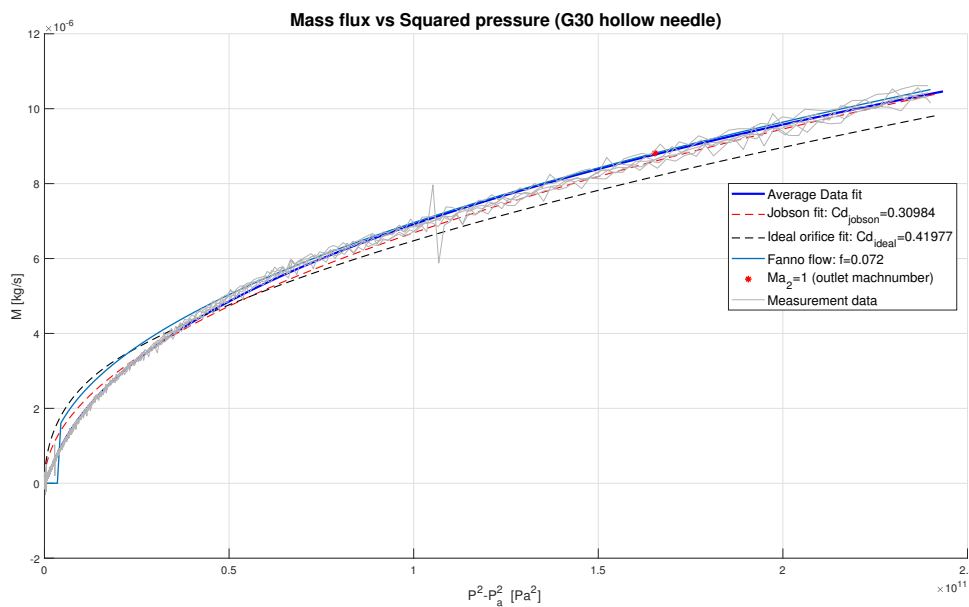


Figure B.5: Mass flux measurement with flow model fittings

From figure 2.6 it can be seen that the critical transition from laminar to turbulent flow occurs at a quadratic pressure difference of:  $P_{critical} = 5 \times 10^{10} \text{ Pa}^2$ . At this point the Fanno fit in figure B.5 starts to deviate from the measurement data. This is because a constant wall roughness may only be assumed in the case of

full turbulent flow. For this reason the Fanno flow model does not fit for pressures below the critical transition pressure.

The ideal orifice and jobson flow models are used in turbulent orifice flows and are generally not applicable when a capillary is considered. Despite this fact the models are fitted on the capillary flow. It can be seen that the Jobson fit shows good agreement with the data for both laminar and turbulent flow regimes, the ideal orifice fit shows less agreement. The length of the capillary is short (17 mm) so this might be the reason that the Jobson (orifice) equation has a good fit. For small squared pressure differences:  $P^2 - P_a^2 < 1 \times 10^{10}$ , none of the theoretical models shows a good fit. For these small pressure differences a 3rd order polynomial is fitted, see figure B.6.

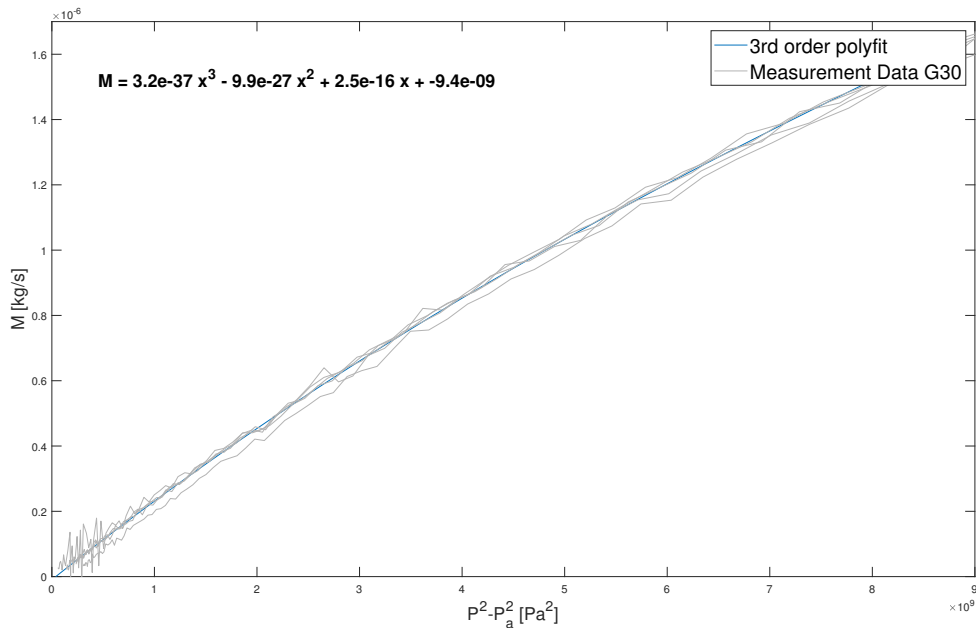


Figure B.6: Mass flux measurement G30 with 3rd order polynomial fit

## Restriction measurement

To understand the mass flow through this needle type of restriction, flow measurements are performed. This is done by using the measurement set-up discussed in appendix ... The goal of this measurement is to find the flow model that suits best to this type of restrictor element. This restriction model can then be implemented in extended air-bearing studies to achieve an optimized air bearing design. Multiple restrictor elements are measured, to get an indication of manufacturing tolerances and their influence on the mass flux. From the rather tight tolerances in table 2.1, one expects minor mass flux deviations between the individual needles.

### B.2.2. G26 measurement results

Blunt (G26) syringe needles with an inner diameter of:  $d = 248 \mu\text{m}$  are measured. Six needles are tested, each needle is measured once due to a lack of time, therefore this measurement should be used as indication of mass flow only. A data fit that is valid for both small- and large pressure differences is not found. This has to do with the fact that the flow is in the laminar to turbulent transition zone. A cubic polyfit has been found that fits the data at the total pressure range, see figure B.7.



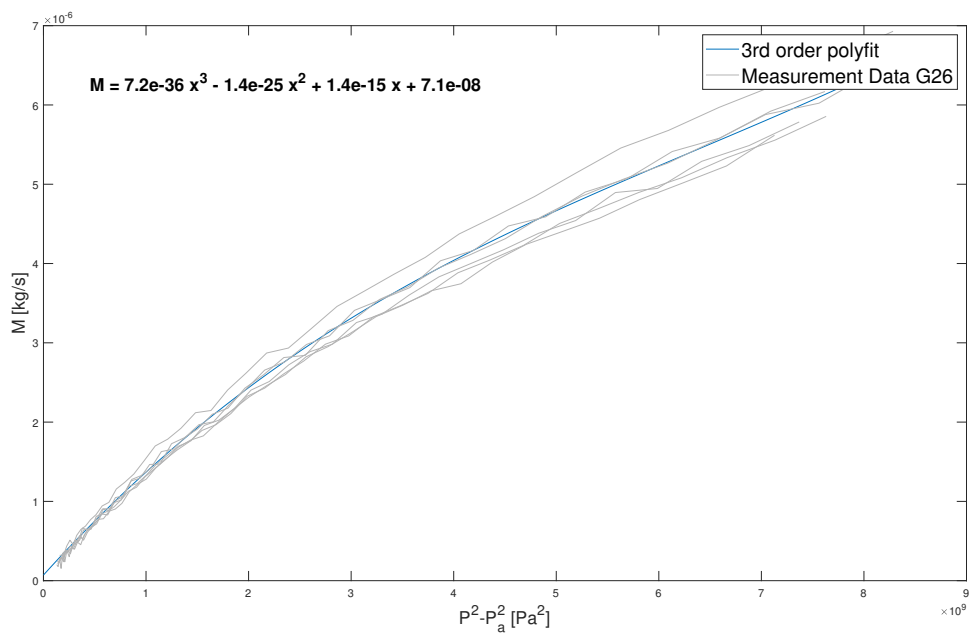


Figure B.7: Mass flux measurement G26 with 3rd order polynomial fit



# C

## General flow equations

### C.1. Laminar pipeflow equations

In [55] the momentum equations for fully developed flow are derived using the Navier Stokes equations A.4. It is assumed that the medium is incompressible, Newtonian and there is a no slip condition at the wall. The flow profile for a pressure driven (Poiseuille) flow is parabolic and depicted at the right hand side in figure C.1. The flow profile for one moving plate and no pressure gradient (Couette flow) is depicted at the left hand side in figure C.1.

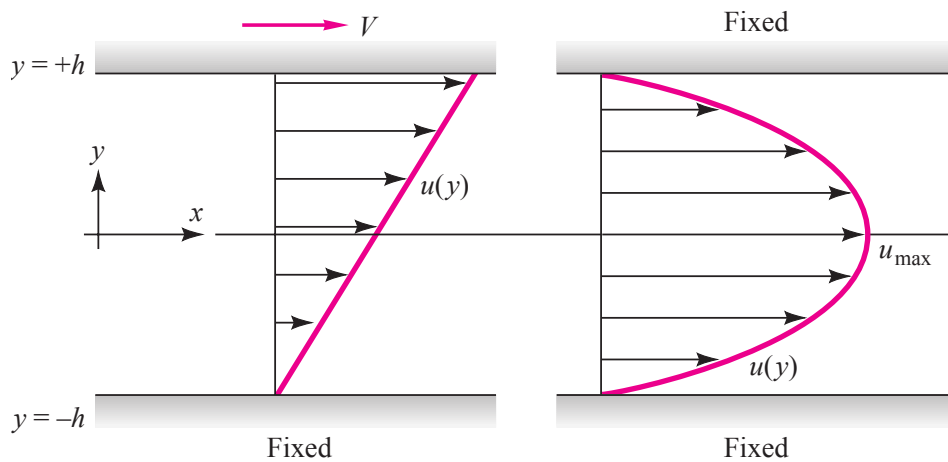


Figure C.1: Incompressible viscous flow between parallel plates: Couette flow and Poiseuille flow (from [55, p. 269])

The flow in the channel due to a pressure gradient is described by:

$$u(y) = -\frac{dp}{dx} \frac{h^2}{2\eta} \left(1 - \frac{y^2}{h^2}\right) \quad (C.1)$$

The maximum velocity occurs at the centreline ( $y = 0$ ), inserting gives:

$$u_{max} = -\frac{dp}{dx} \frac{h^2}{2\eta} \quad (C.2)$$

These flow profiles are valid for developed laminar pipe flow with radius  $R$  and length  $L$ , the volume flow ( $Q$ ) through the pipe is derived:

$$Q = \int u dA = \int_0^R -\frac{dp}{dx} \frac{R^2}{2\eta} \left(1 - \frac{r^2}{R^2}\right) 2\pi r dr = \frac{\pi R^4 \Delta p}{8\eta L} \quad (C.3)$$

The mass flow through the pipe can be found by multiplication with the density, for the compressible flow case the ideal gas law from equation A.13 is used. Rewriting and integration of the volume flow equation gives:

$$\dot{m} = \rho Q = \frac{1}{R_s T} \int \frac{\pi d^4}{128 \eta L} p dp = \frac{\pi d^4}{256 L} \frac{\Delta p^2}{\eta R_s T} \quad (\text{C.4})$$

## C.2. Thin film flow

Analytical functions for mass flow and pressure can be derived in the case of 1D thin film flow between two parallel plates. The steady-state polar Reynolds equation describes this type of flow and is used as starting point:

$$\frac{1}{r} \frac{\partial}{\partial r} \left( \frac{r p h^3}{12 \eta R_s T} \frac{\partial p}{\partial r} \right) = 0 \quad (\text{C.5})$$

Since the plates are parallel, the gap height is not a function of the spatial coordinate, removing all constants gives:

$$\frac{\partial}{\partial r} \left( r p \frac{\partial p}{\partial r} \right) = 0 \quad (\text{C.6})$$

When solving the part between the brackets a solution for pressure is found with two integration constants  $C_1$  and  $C_2$

$$p(r)^2 = C_1 \ln r + C_2 \quad (\text{C.7})$$

The pressure at the inner- and outer radius is known, this gives two boundary conditions:  $p(r = r_i) = p_i$  and  $p(r = r_o) = p_o$ . Implementing these in equation C.7 gives the solution for laminar flow through a long thin parallel film [52], see equation C.8.

$$p(r) = p_o \sqrt{\left( \frac{p_i}{p_o} \right)^2 - \frac{\ln(r/r_i)}{\ln(r_o/r_i)} \left( \left( \frac{p_i}{p_o} \right)^2 - 1 \right)} \quad (\text{C.8})$$

The mass flux through a boundary in this parallel film is found using the pressure distribution in equation C.8 and its derivative w.r.t to  $r$ . The mass flux can be found by using part of the Reynolds equation, see C.9.

$$\dot{m} = \frac{r h^3}{12 \eta R_s T} p \frac{\partial p}{\partial r} \quad (\text{C.9})$$

Substitution of C.8 in C.9 and integration along an edge from: 0 to  $2\pi$ , gives the dimensioned mass flux through the thin parallel film, as a function of the pressure difference, see C.10.

$$\dot{m} [\text{kg s}^{-1}] = G_{tf} (p_i^2 - p_o^2) = \frac{\pi h^3}{12 \ln(r_o/r_i) \eta R_s T} (p_i^2 - p_o^2) \quad (\text{C.10})$$

All constants are grouped in one parameter  $G_{tf}$ , called the thin film conductivity. This constant describes the inverse of the flow resistance through the thin film.

# D

## Extra dynamics single inlet bearing

Supplementary graphs illustrating the influence of different design variables on the dynamic behaviour of the single-inlet-centrally-fed aerostatic bearing, for design see table 2.2.

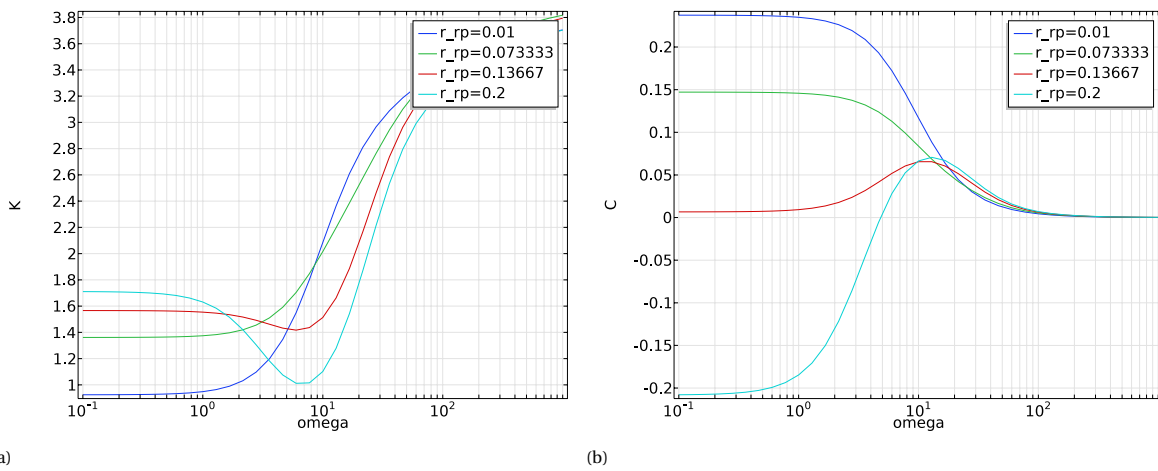


Figure D.1: Stiffness and damping at different frequencies and restrictor radii

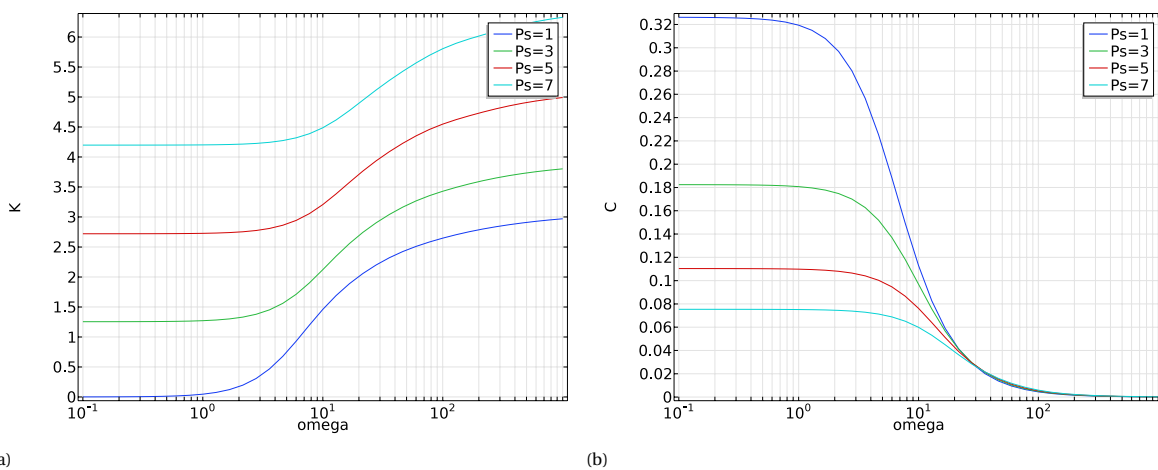


Figure D.2: Stiffness and damping at different frequencies and supply pressures

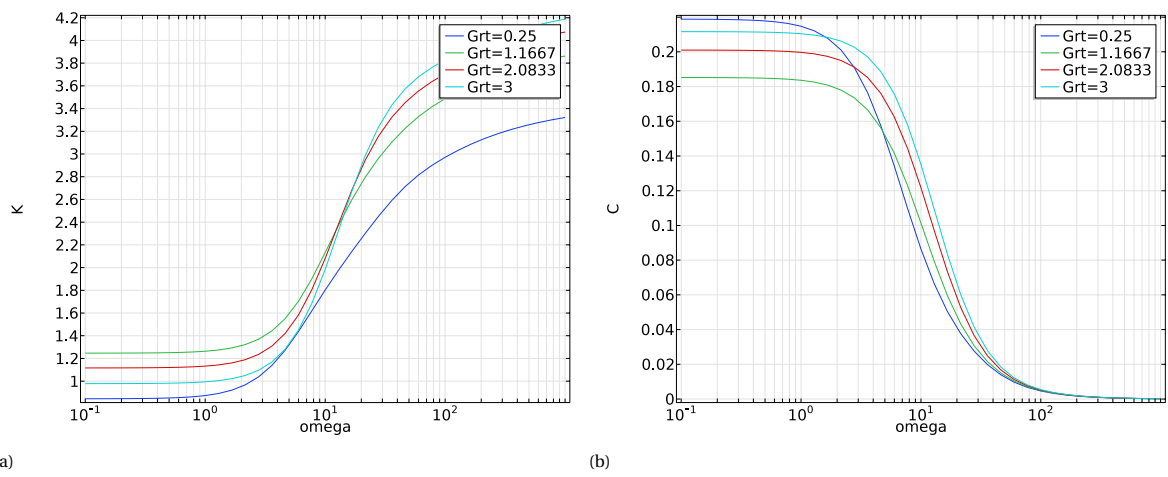


Figure D.3: Stiffness and damping at different frequencies and inlet conductivities

# E

## Manufacturing

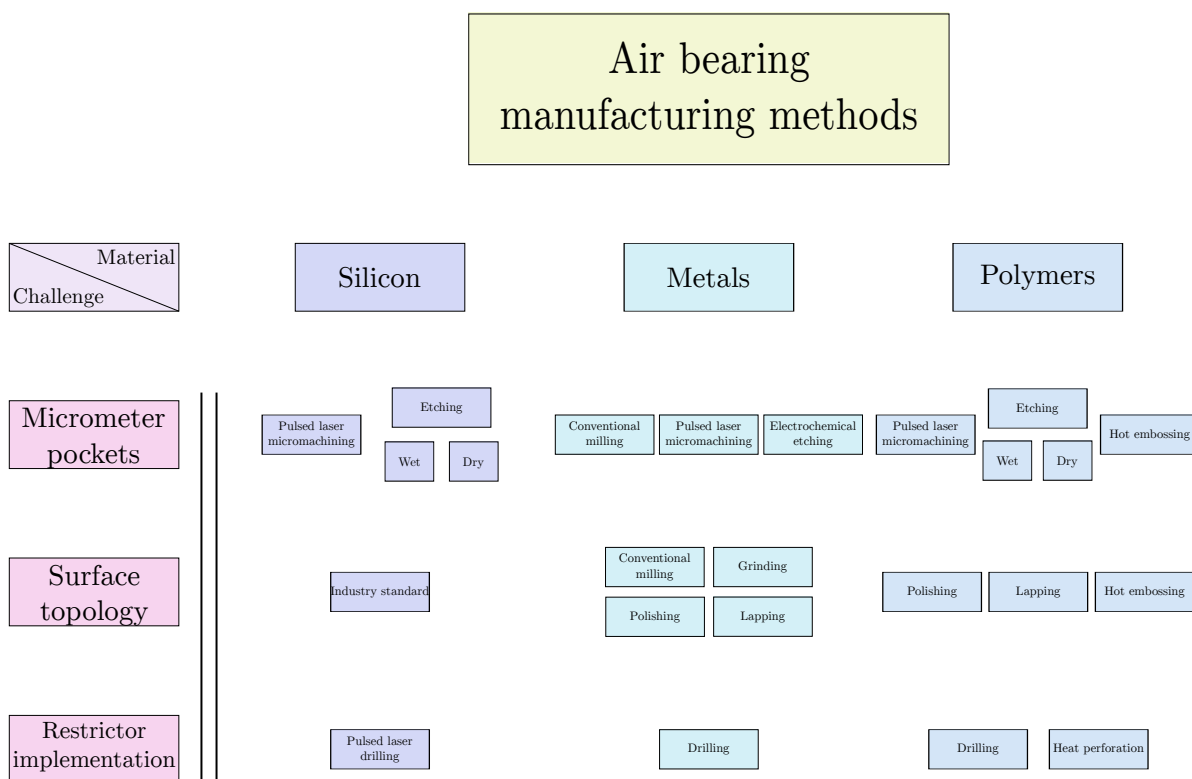


Figure E.1: Overview of manufacturing methods

### E.1. Lathe

This method is used in [21] to obtain shallow pockets in a flat surface. Although it is possible to get pockets with well defined radii and micrometer depth it takes lots of trial and error to get the desired specifications. Another downside is that only circular pockets can be made. And there's no way to make multiple pockets in one step since the design has to be axisymmetric. A positive aspect of the lathe is that it can be used to flatten the surface of a cylinder quite well as is proved by [21]. He achieved an average roughness of  $R_a = 0.3\mu\text{m}$  and an acceptable waviness of  $3\mu\text{m}$  peak to peak.

Because this method is thoroughly tested in [21] it is not useful to repeat it. Time is put in finding a faster and more reliable method to create shallow pockets. However the lathe can be used to construct a flat structural base that can be used as manifold and as support for another layer that has micro scale pockets in it.

Table E.1: Lathe summary

Pro	Cons	Comments
<ul style="list-style-type: none"> <li>proved method</li> <li>well defined radii</li> <li>ability to make flat surface and pocket</li> <li>cheap 'in-house' method</li> </ul>	<ul style="list-style-type: none"> <li>not easily repeatable</li> <li>axisymmetric designs only</li> <li>one pocket at the time</li> </ul>	In theory it is not possible to make micrometer scale features on a normal lathe. Only with a lot of patience and trial and error it is possible.

## E.2. Pulsed laser micromachining

A short pulse UV laser is available in the lab that is used to cut or engrave micro scale features in various materials. The challenge with this laser is that it takes a lot of testing to find the right machine settings. A recent study [24] is done by a student investigating the manufacturability of silicon cantilevers using this laser. In this research a few laser recipes are described that may be useful. Unfortunately this research focuses on cutting instead of engraving micrometer features in a surface. Therefore tests with different settings and materials must be performed to know if this is a promising manufacturing method. Samples were made using stainless steel and silicon.

The quality of the engraved samples is quantified by examining: debris, geometric accuracy, surface roughness and waviness. After using the laser the samples need to be cleaned to improve the quality. In the lab two methods of cleaning are available: ultrasonic cleaning and wet etching. The problem with the laser is that there is little known about the settings. Finding the optimal settings for every material and desired profile can take months. Therefore a limited number of settings and samples is tested to get some knowledge about this manufacturing method. Two features are made in the surface: a circular hole and a laser etched square. The quality of the holes should be good enough to be used as a restrictor and the etched squares gives an indication of how well a pocket or groove can be made in the material.

The following parameters can be adjusted: firing rate, laser speed, diode current, number of drill levels, drill steps, hatch pattern, repetitions and laser power. As a starting point parameter values are taken from [24].

Table E.2: Laser settings of different materials

Material	Firing-rate	Speed	Diode current	Level	Step	Lines	Gap	Repetition	Energy output
Stainless steel, thickness 100 $\mu\text{m}$	50 kHz	20 $\text{mm s}^{-1}$	6.44 A	-	-	1	20 $\mu\text{m}$	10-50	10-100
Silicon wafer, thickness 300 $\mu\text{m}$	15 kHz	15 $\text{mm s}^{-1}$	6.5 A	-	-		15 $\mu\text{m}$	10	100

### E.2.1. Stainless steel

In the lab thin 100 $\mu\text{m}$  thick stainless steel sheets are available that are used to engrave small squares as discussed. The laser parameters are given in table E.2, all parameters are kept constant except the number of repetitions and the energy output. These two are varied in steps of 10, this gives a matrix of  $5 \times 10$  squares where bottom left is the most repetitions and least amount of power and bottom right most power and repetitions, see figure E.2. After etching the sample is cleaned using an ultrasonic cleaner, this removes most of the burned material making the sample easier to analyse. To analyse the etched sample the Bruker white light interferometer is used <sup>1</sup>. In figure E.3 the first two columns of the sample are pictured, it can be seen that top left the square is very shallow and the depth increases when going to bottom left. In the second column the power is increased to 20 % and more material is removed. Figure E.4 gives the red and blue part that are highlighted in figure E.2.

Desired is an etch depth between 1 $\mu\text{m}$  and 3 $\mu\text{m}$  since this is a characteristic depth for a shallow pocket. From the measurements using the white light interferometer it can be concluded that the laser etched pockets exceed this limit by tens of microns. With very low power the pockets are shallow, however the surface becomes very rough and the pocket is undefined, see the sample in the left bottom corner of figure E.2 and the measurement in figure E.5a. Increasing the power results in a better ablation of the material, see figure E.5b. More settings are tested using stainless steel but the production of a well defined shallow pocket using this method did not give the desired results.

<sup>1</sup>blabla Bruker link



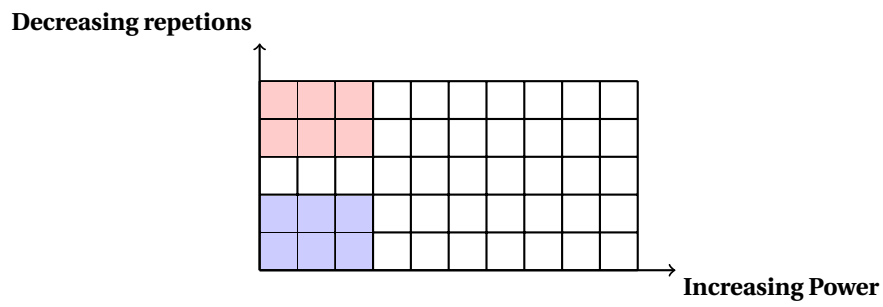


Figure E.2: Etched squares sample

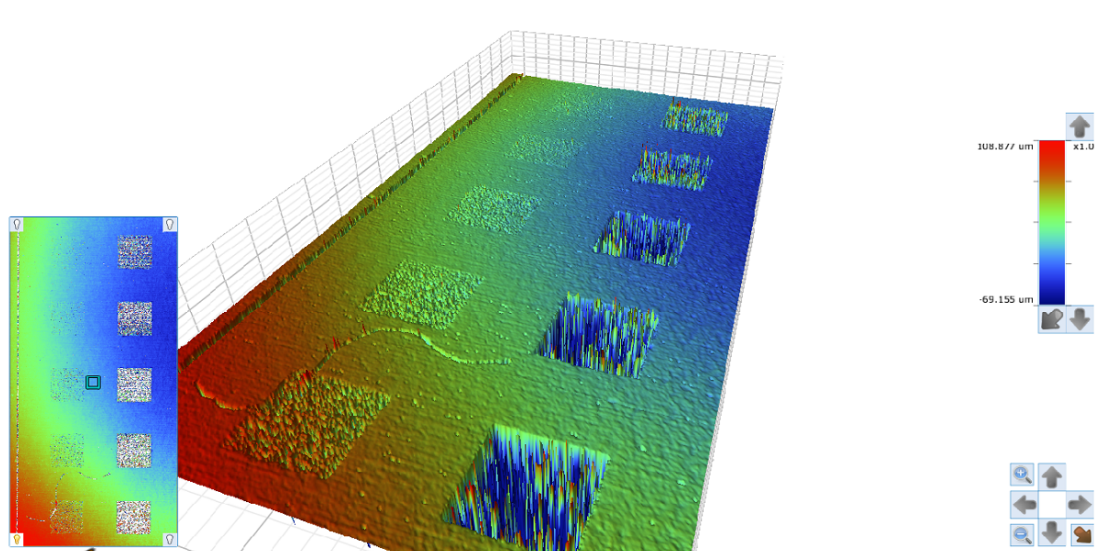
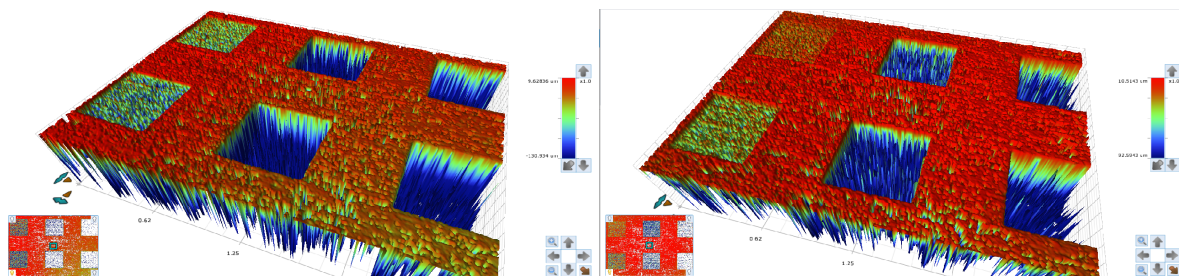


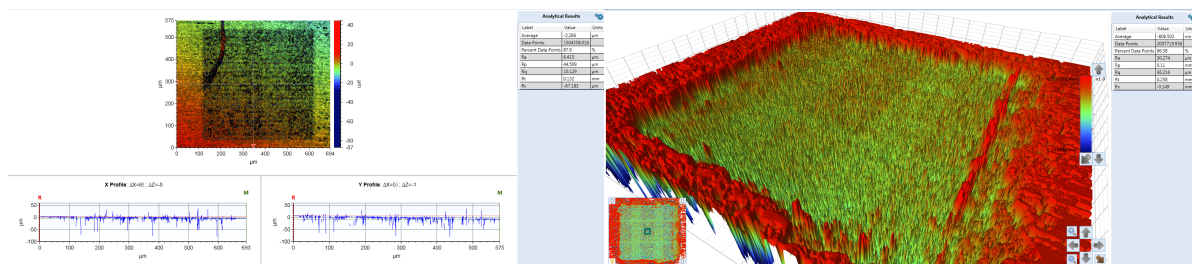
Figure E.3: 3D image of left part of the sample



(a) Blue part of figure E.2

(b) Red part of figure E.2

Figure E.4: Surface profiles of etched stainless steel sample



(a) Sample with: 10% power and 50 repetitions

(b) Sample with: 100% power and 50 repetitions

Figure E.5

The creation of small holes that can be used as a restriction is discussed in [43]. Nice well-defined orifice restrictions were created in stainless steel using this laser. The outer diameter of the hole was 140 $\mu\text{m}$  on top and 90 $\mu\text{m}$  at the bottom, this difference is a result of the taper angle of the laser beam. The taper angle of 15deg is not an issue in thin sheets like the 100 $\mu\text{m}$  thick stainless steel sheet that is used in [43]. However when a thicker material is used it might be the case that the laser beam cannot penetrate the sample and no hole is created. The creation of orifice restrictor holes in stainless steel as described in [43] is not repeated here.

### E.2.2. Silicon

Since the tests in stainless steel did not give the desired results other materials are tested, this section describes the etching in mono-crystalline silicon. A silicon wafer can possibly be used as a bearing surface since it is extremely flat. A polished wafer has a roughness below 1 nm and a flatness that is smaller than 1  $\mu\text{m}$ . In [24] research is done in cutting through silicon wafers and testing the roughness of the cut-plane and mechanical properties. Etching micrometer pockets in Silicon is not treated in this report, therefore multiple test samples are made. As a starting point some general laser settings that are used to cut the wafers are now used to etch shallow squares in the surface, settings can be found in table E.2.

In the silicon test samples the laser power, number of repetitions and line density of the hatch profile are varied and the results are obtained using a white light interferometer. After the samples are processed by the laser they are cleaned using the ultrasonic cleaner. Again a matrix of squares is etched where along the x-axis the power increases (10 – 100%) and along the y-axis the number of repetitions (5 – 30) increases, see figure E.6. The squares are filled with a line type hatch with a spacing of 10 $\mu\text{m}$  between the lines. The etched square in figure E.6a has high power and only 5 repetitions, the average depth of the pocket is 31 $\mu\text{m}$ . Decreasing the number of repetitions makes the pattern in the pocket rougher because repeating smoothes the surface. Now the number of repetitions is doubled to 10 in figure E.6b and the pocket depth increases to 50 $\mu\text{m}$ .

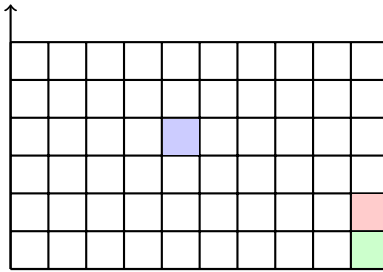
The influence of the laser power on the pocket depth can be seen in figure E.6c. The power is too low to evenly evaporate the silicon, this results in a rough surface that has a depth of around 15 $\mu\text{m}$ . When the power is lower than 50% the results become worse, this is not an option to obtain a well defined pocket of a few micro meters.

Other tests are done with different hatch profiles such as: lines with a closer spacing, lines under an angle and net or honey type of hatch profiles. The roughness inside the pocket becomes better when a denser hatch profile is used, however the pocket becomes deeper since there is more laser beam exposure at the surface. The best result in terms of a shallowness is found with low power settings (50%) and a very dense line hatch (2.5 $\mu\text{m}$  between the lines). The result is given in figure E.7, it is clear that the pocket is very rough and not well defined with a depth of around 6 $\mu\text{m}$ . This is a shallow pocket but since a depth of around 2 $\mu\text{m}$  is desired the result is still infeasible.

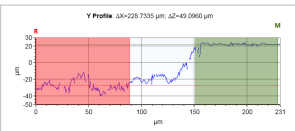
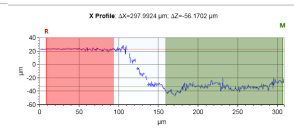
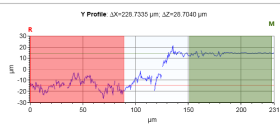
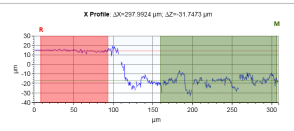
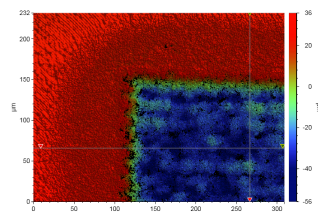
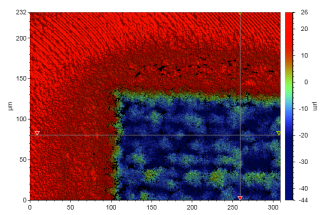
Until now only: the power, number of repetitions and the hatch density are varied, the laser firing rate and the speed are kept constant at the values given in table E.2. When there is less exposure by the laser on the surface, the pockets might become shallower therefore the laser firing rate and speed are varied, an overview of the sample is given in figure E.8. The number of repetitions is: 15, the line hatch distance is 2.5 $\mu\text{m}$  and the power is fixed at 100% since this gives the best ablation and surface quality. After laser engraving the samples are cleaned in an ultrasonic cleaner for 2 min and examined using the white light interferometer. Height profiles of the four corners of the sample matrix are given in figure E.8. As expected the upper left corner (yellow sample) has the shallowest pocket with a depth of around 8 $\mu\text{m}$  since the amount of energy applied to the surface is minimal.

Various tests have been done with lower number of repetitions and different speeds and firing rates. Samples with zero repetitions give the shallowest results so these will be discussed further. Squares with a line type of hatch with 2.5 $\mu\text{m}$  between the lines are etched with a power of 100% while the firing rate and speed are varied, see figure E.9. Again the surface is examined using the white light interferometer, see figure E.9 to get an indication of the etching depth. With some of the settings a shallow pocket is etched with a depth between two and three micrometer. Unfortunately the bottom of the pocket has a very rough surface so the geometry is not well defined. When the pocket depth decreases the roughness of the etched surface becomes more important. The roughness can be improved by increasing repetitions or hatch line density. The problem is

Increasing repetitions 5-30

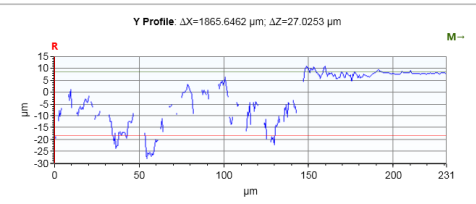
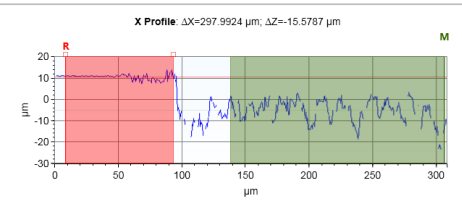
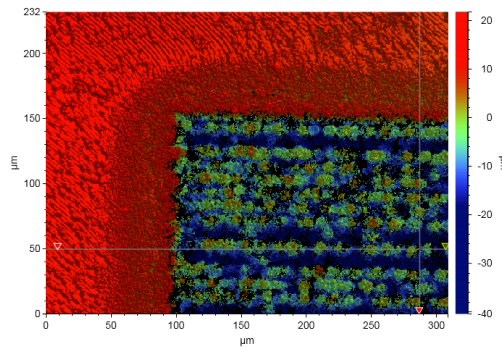


Increasing Power 10-100%



(a) Green etch

(b) Red etch



(c) Blue etch

Figure E.6: Surface profiles of etched Silicon with varying repetitions and power

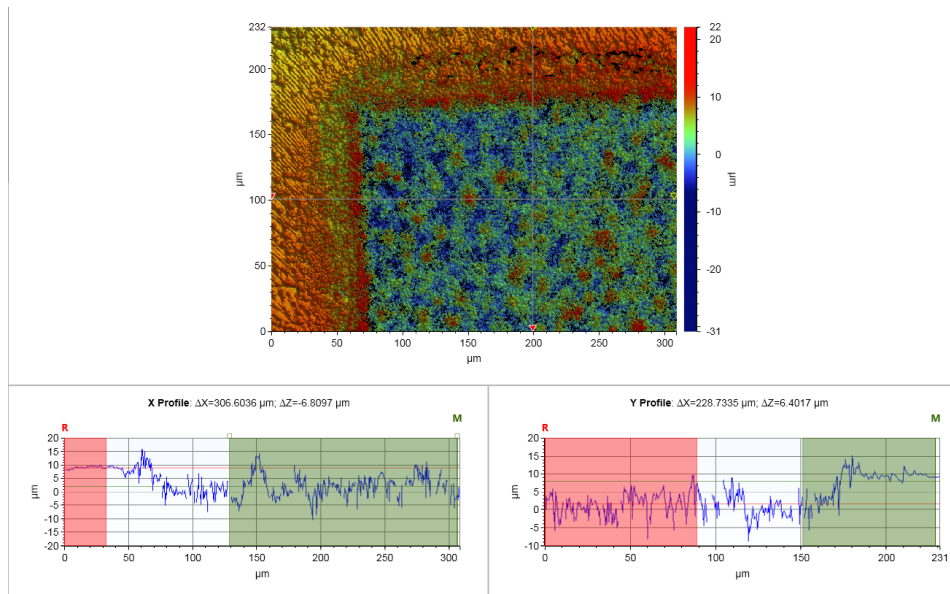
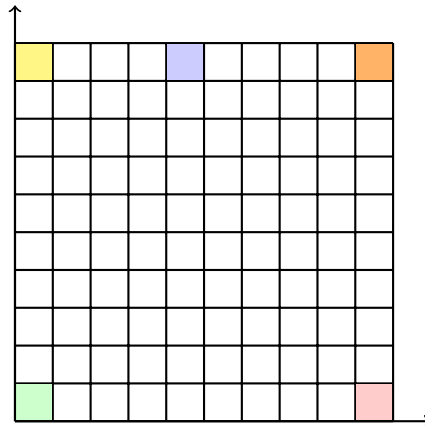


Figure E.7: Silicon sample: power=50 %, hatch line distance=2.5 μm

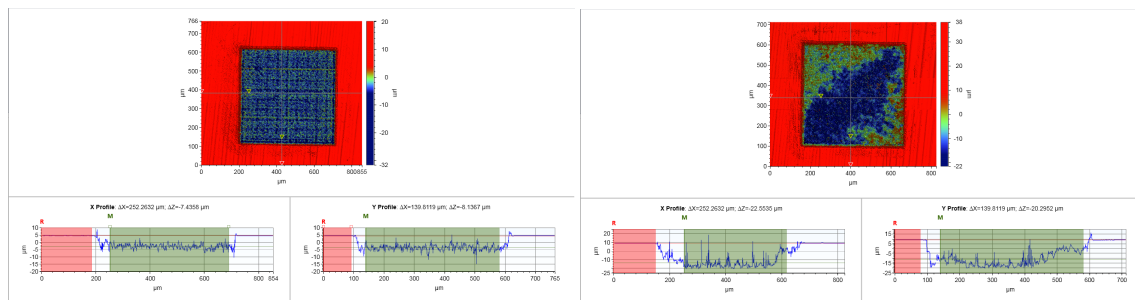
this generates more exposure and a deeper etch, so other methods need to be found.

In [24] potassium hydroxide, also known as KOH, is used to etch the silicon wafer and obtain a better edge and surface roughness. The KOH etchant removes silicon preferably along the (100) plane so it will influence the existing geometry that is cut by the laser, furthermore it attacks oxides such as  $SiO_2$ . This last feature is useful in removing recast material and debris to make a 'clean' cut. Wet etching the laser etched samples with a KOH solution might improve the surface quality since sharp peaks might dissolve faster than a flat surface. A solution is made with 30% KOH and 70%  $H_2O$ , according to [41] the etch rate in (100) direction is:  $0.024 \mu\text{m min}^{-1}$  when the solution is at a temperature of  $20^\circ\text{C}$ . Now a number of samples with rough but shallow pockets are put in the wet etch bath and the results are given in figure E.10. As one can see there is no improvement concerning the roughness inside the pocket, even after three hours of etching. Outside the pockets the surface of the polished wafer gets rougher due to the anisotropic etch behaviour of the KOH solution. This indicates that the material dissolves due to the KOH solution but unfortunately it does not result in a flattened shallow pocket. There are other wet etch solutions like hydrofluoric acid that may give better results, however these are very toxic and are not allowed to use at the chemical lab facility at the faculty.

Speed  $10-28 \text{ mm s}^{-1}$

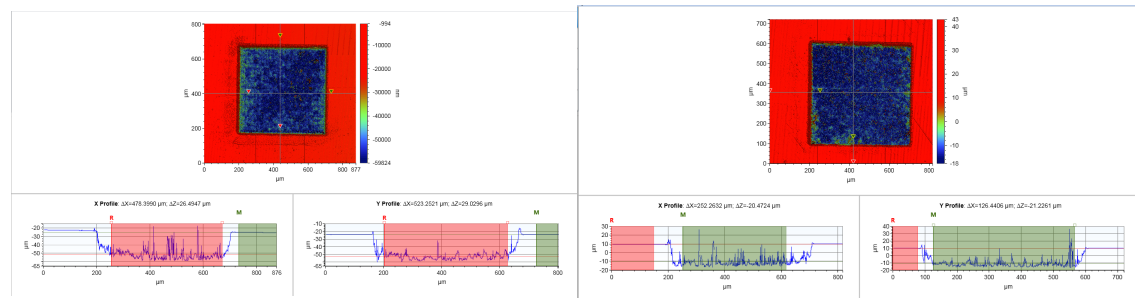


Firing rate 10-55 kHz



(a) Yellow etch

(b) Orange etch

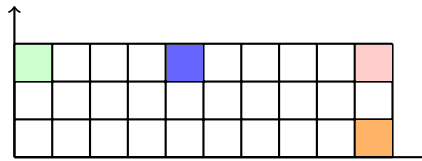


(c) Green etch

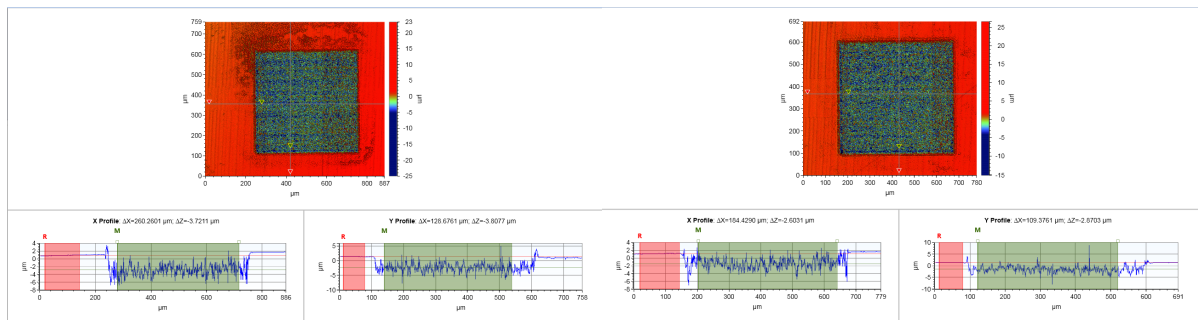
(d) Pink etch

Figure E.8: Surface profiles of etched Silicon with varying speed and firing-rate

Firing rate 1-5 kHz

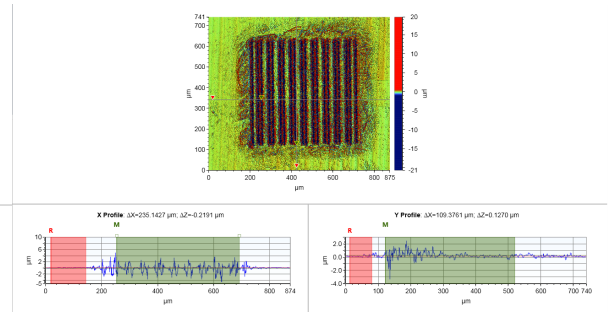
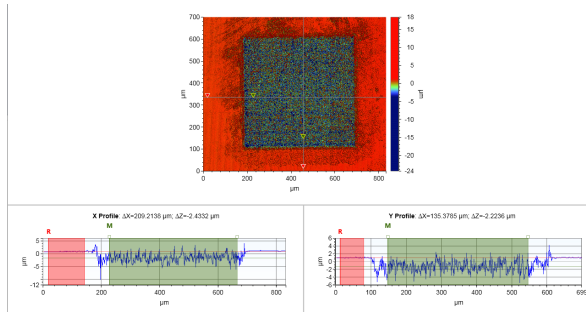


Speed 35-53 mm s<sup>-1</sup>



(a) Green etch

(b) Blue etch



(c) Pink etch

(d) Orange etch

Figure E.9: Surface profiles of etched Silicon

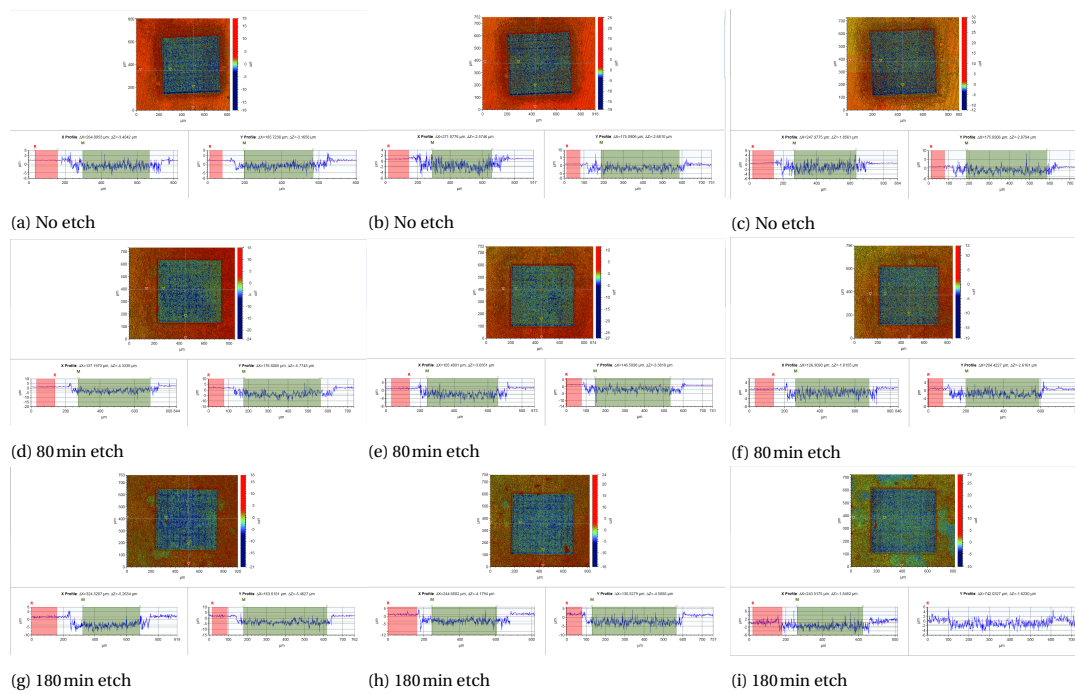


Figure E.10: Multiple samples with different wet etch durations

To conclude, the short pulse UV laser can be used to create micrometer scale pockets in a polished silicon wafer. However the minimum depth of the pockets is around  $8\mu\text{m}$  which is not shallow enough in this specific air bearing application. The roughness inside the etched pockets is a function of: laser power, hatch line density and number of repetitions. Tuning all laser parameters is a delicate task but some settings are available. A great number of tests have been done and creating a desired pocket depth of ( $2\mu\text{m}$ ) is probably not possible with short pulse laser etching.

Table E.3: Pulsed laser micromachining summary

Pro	Cons	Comments
<ul style="list-style-type: none"> <li>Advanced geometries possible</li> <li>Flat silicon wafers can be used</li> <li>Pockets with a depth of <math>8\mu\text{m}</math> possible</li> <li>'in-house' method</li> </ul>	<ul style="list-style-type: none"> <li>Non-linear process so hard to find parameters</li> <li>Unable to make shallow pocket</li> <li>Very slow process</li> <li>Laser ablation introduces roughness</li> </ul>	This could be an option for somewhat deeper pockets. A laser with higher pulse frequency might be able to produce shallow pockets.

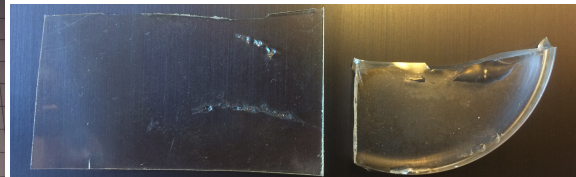
### E.3. Oxygen plasma etching of Topas®

A plasma is an ionised gaseous substance that, when given momentum is able to clean or etch a surface. Besides the etching that is done using the momentum of the plasma, chemical reactions between the plasma and substrate occur, resulting in material removal. At the faculty an oxygen plasma cleaner is available to clean different kinds of substrates. Unfortunately oxygen is the only gas that is connected and cannot be used to etch silicon, for this a different type of gas like:  $CF_4$ ,  $SF_6$  or  $CHF_3$  must be used. These are not available so a different type of material is taken that can be etched by an oxygen plasma. Cyclic olefin copolymer (COC) is a relatively new class of polymers that is also used in optics. The surface roughness is very low and similar to a polished wafer while the waviness is determined by the structural layer that is used, the sheet thickness and residual stresses in the sheet. This oxygen plasma cleaner has never been used to etch features in a surface and it is unsure if it is suitable for such purpose. A few tests are performed using Topas® that has a glass transition temperature of around 70 °C. No extensive theoretical study is done on the etch rate of this material in this specific set-up, since it is probably easier and faster to just do some tests.

The first test is done with maximum power of 99W because more power should give higher etch rates. To see if material gets removed by the plasma part of the Topas® sheet is covered with a PDMS mask and the plasma is turned on for 30 min, a picture of the result is in figure E.11a. In this picture the Topas® is at the top and the PDMS mask at the bottom. It can be clearly seen that the Topas® is bent and burned as a result of the heat during the process. Another test is done with less power 60W and a duration of 15 min, this result is in figure E.11b. This last test left some mask material at the Topas® because of the high temperatures. Despite the lower power and etching time this substrate is still effected by heat. Both etched samples are examined using the white light interferometer and no height step can be seen at the interface of the mask and Topas® sample. The absence of a height step is probably a result of the low glass transition temperature, this causes flow of material during the etch process. A solution could be to use a COC that has a much higher glass transition temperature, this is done in the following section.



(a) Oxygen plasma etch of Topas® (Tg=70 °C), 99W, 30 min



(b) Oxygen plasma etch of Topas® (Tg=70 °C), 60W, 15 min

The Topas® COC that is used in the previous section was not suitable to use in the plasma etcher, now Topas® (6015S-04)[1] with a glass transition temperature of 158 °C is tested. Part of the sheet is covered with a PDMS mask and then placed in the plasma cleaner, the result after 30 min of etching at 99W is given in figure E.12. A clear height step of around 200 nm can be seen at the place where the mask is applied on the Topas® substrate. This is a promising result so another test is done with the same material but now with an etching time of 2h, the result is given in figure E.13. After two hours of etching a clear height step of 2.5 μm can be seen in the surface. These figures of the surface profile are at a location where the PDMS mask nicely covers the substrate. At figure E.13c a zoomed in picture of the tip is depicted, the interface is very rough due to inappropriate adhesion of the mask. Adhesion can be improved by making sure the PDMS has a very good surface finish without debris, further both the mask and the Topas® substrate must be cleaned properly using an ultrasonic bath.

This method can very well be used to create micrometer pockets in a flat surface, more tests will be done



using a mask with circular features. Reducing the etch time will result in a shallower pocket, finding the correct etch time is done by trial and error. The plasma flow over the surface affects the etch rate as well, tiny mask features and using a thick mask will slow down the etch rate.

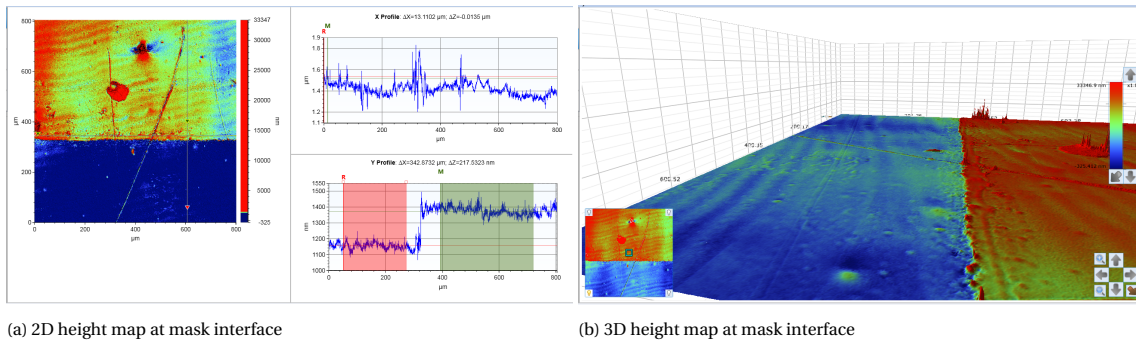


Figure E.12: Topas® ( $T_g=158^\circ\text{C}$ ) oxygen plasma etch at: 99W, 30 min

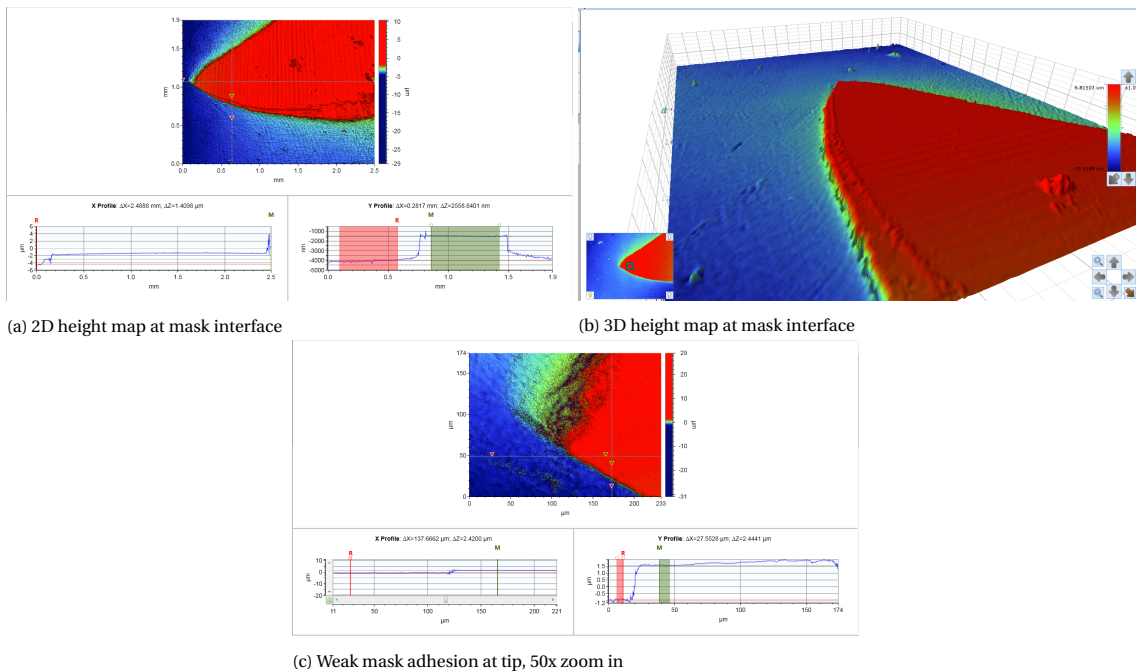


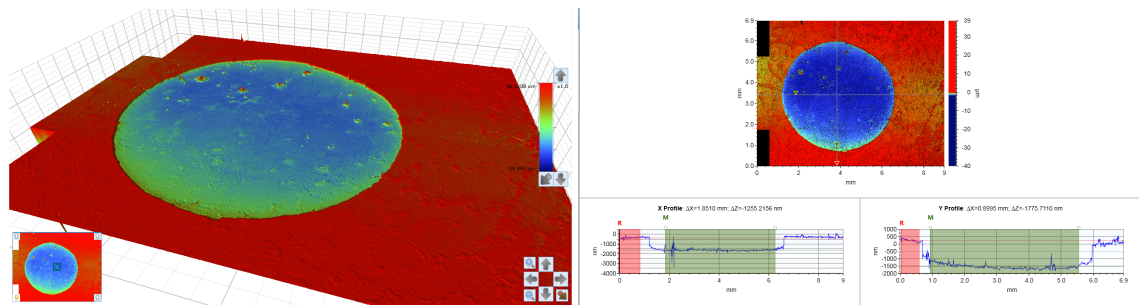
Figure E.13: Topas® ( $T_g=158^\circ\text{C}$ ) oxygen plasma etch at: 99W, 120 min

More tests are done using Topas 6015S-04 and 6017S-04 where the last one has a glass transition temperature of  $T_g = 178^\circ\text{C}$ . Both Topas grades are used and no significant difference in etch rate or surface quality is detected. In figure E.14 a circular pocket with a diameter of 5 mm is etched. The sample is etched for 75 min, this gives an average pocket depth of:  $1.5\mu\text{m}$ . At some spots the materials is not removed resulting in small islands. This is probably caused by improper cleaning of the surface before etching. Contamination functions as an extra unwanted mask.

The mask thickness is also important when a uniform material removal is desired, especially when small features need to be etched. An example is in figure E.15 where a hole with a diameter of 0.5 mm is etched. The used mask was too thick compared to the small pocket's diameter. This resulted in malfunctioning plasma flow through the mask gap and deposition of material. A bulge can be clearly seen instead of a shallow pocket.

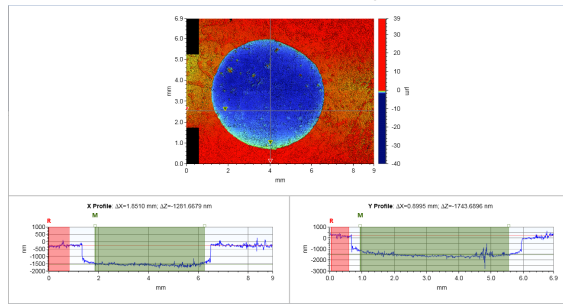
### E.3.1. Groove manufacturing

When an air inlet or outlet needs an uniform pressure distribution at a certain bearing radius, a groove can be used as virtual pocket [52]. A groove can be made by using a mask insert with a smaller diameter than



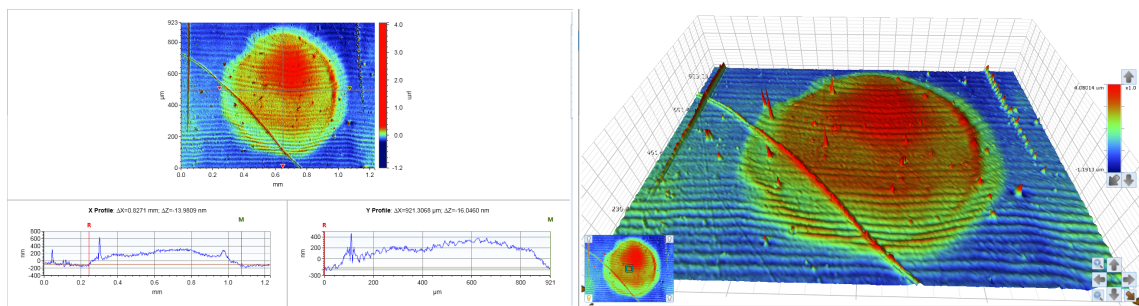
(a) 3D height map of circular pocket

(b) 2D height map at centre



(c) 2D height map

Figure E.14: Topas® (T<sub>g</sub>=158°C) oxygen plasma etch at: 99 W, 75 min



(a) 2D height map of small pocket

(b) 3D height map of small pocket

Figure E.15: Oxygen plasma etch of Topas® (T<sub>g</sub>=158°C), 99 W, 75 min

the pocket diameter. In this initial attempt the insert is centred by hand, therefore the groove may vary in width. The result after 5 h of etching is in figure E.16, the depth is around:  $7.3\mu\text{m}$ . It can be seen that the overall surface roughness of the sample stays good, even after 5 h of etching. The mask thickness that is used to create this small groove is only  $0.5\text{mm}$  this results in proper material removal.

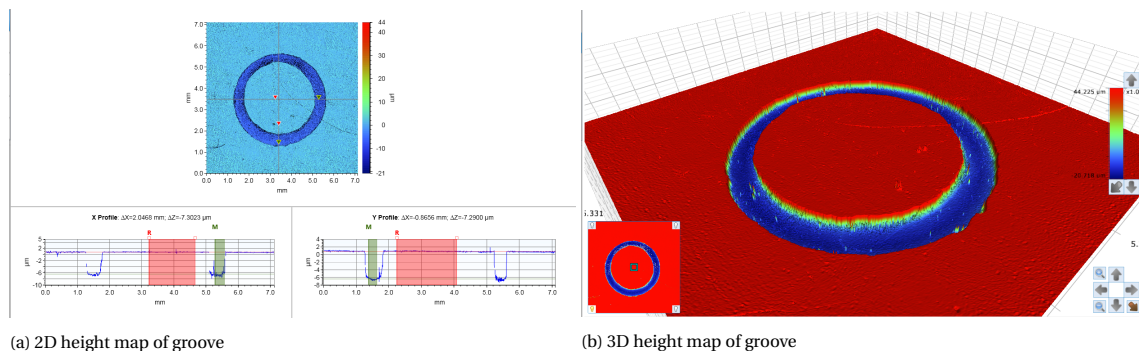


Figure E.16: Oxygen plasma etch of Topas<sup>®</sup> 5h etch time

Table E.4: Topas oxygen plasma etching summary

Pro	Cons	Comments
<ul style="list-style-type: none"> <li>Advanced geometries possible</li> <li>Excellent defined geometry</li> <li>Every pocket depth is possible</li> <li>Uniform material removal, low roughness</li> <li>'in-house' method</li> </ul>	<ul style="list-style-type: none"> <li>Etch rate has to be empirically determined</li> <li>Any contamination weakens mask adhesion</li> <li>Only possible with polymers with high <math>T_g</math></li> <li>Mask thickness and surface contamination influences etch</li> </ul>	<p>A proper method to create any shallow geometry. in a flat surface</p> <p>Etch parameters like: mask thickness and etch time must be determined empirically.</p>

## E.4. Wet etching Si wafer

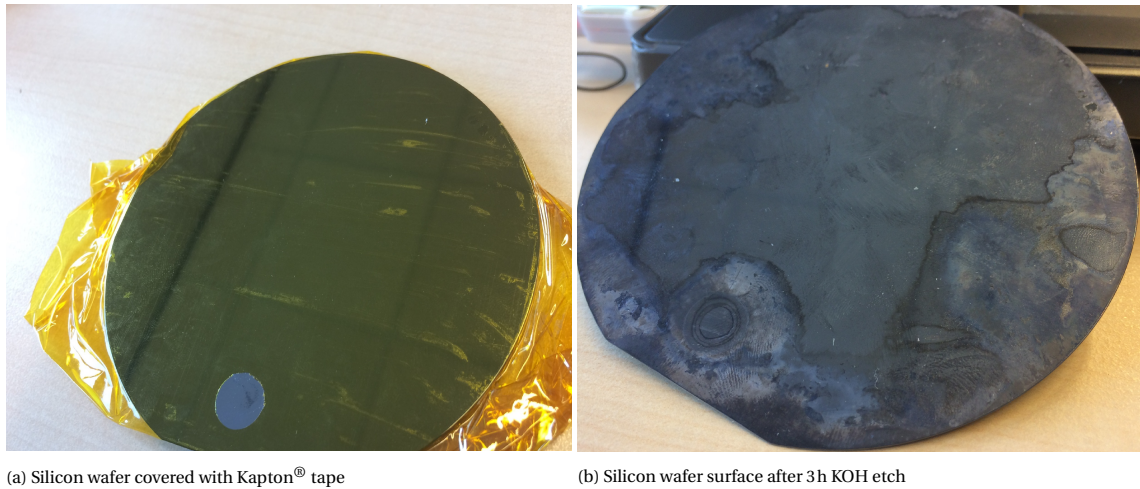
In section E.2 experiments are done using a KOH wet etch to improve the surface texture of the laser etched silicon. It is possible to wet etch a circular pocket of a few micrometers in depth in a cleanroom lab facility. Unfortunately using the cleanroom is very expensive and therefore not suitable to make some prototypes in a cheap manner. Besides the costs, it takes a couple of weeks of training to be allowed to use the cleanroom. The question arises whether it is possible to manufacture these micrometer pockets outside an expensive cleanroom facility. Therefore tests are done in the chemical lab at the faculty.

A short summary of steps that are normally taken in a cleanroom to wet etch a pattern in a silicon wafer are:

1. Extensive cleaning of the wafer using: RCA1[17], RCA2[10] and hydrofluoric acid (HF) cleaning steps
2. Application of a photoresist masking layer
3. Photolithography, development and cleaning
4. Anisotropic KOH wet etch step
5. Removal of photoresist

At the faculty few of the aforementioned facilities are available so some alternatives are tried. To clean the wafer the oxygen plasma cleaner is used together with a brief cleaning using isopropyl alcohol. The plasma cleaner is able to remove organic contamination [47] and might therefore be a replacement for the chemical RCA-1 cleaning procedure. This cleaning procedure does not remove metal ions from the silicon wafer so these remain present. The same holds for the native oxide layer that is normally removed by the extremely aggressive hydrofluoric acid. After this alternative cleaning of the wafer a mask has to be applied to protect some parts against the etchant. Applying a photoresist of the right thickness and properties on the wafer is not very easy. This because the photoresist needs to bond to the surface which might be hard since the surface is not properly cleaned. Furthermore there are issues regarding the pre-baking, UV lightning, development and photoresist removal processes. An easier way is sought to cover certain parts of the wafer and is

found in using Kapton<sup>®</sup> tape. This tape is made of polyimide and does not contain any other materials or a separate glue layer. It adheres air tight to the cleaned silicon surface and with a small mask and knife a circle can be made, see figure E.17a. Other methods to make features in the tape can also be used like: laser cutting the tape or using an automatic cutter tool.



The masked wafer is put in a 30 wt% KOH aqueous solution at a room temperature of 20°C, this gives an etch rate of  $0.024\mu\text{m min}^{-1}$  [41]. To see if the mask holds the etch time is set at 3h which should give a pocket that is deeper than  $4\mu\text{m}$ . After the etch is done the Kapton<sup>®</sup> tape is removed and the result is in figure E.17b. It can directly be seen that the etchant got underneath the Kapton<sup>®</sup> mask, this occurred around the circle and at the edges of the wafer. This under etching makes that there's no well defined pocket. In figures E.18a and E.18b the profile of the wafer surface at the location of the pocket is given. There appears to be a low frequent waviness at the surface with a circle contour in the valley. There are two challenges that need to be solved: improve the mask to limit the under etching and remove more contamination from the surface. The first measure makes sure that the surface outside the pockets does not change and improves the pocket shape. The second measure improves the etch process, since any contamination affects the etch rate in a certain direction. A better cleaning of the wafer also improves the adhesion of the Kapton<sup>®</sup> mask. At this first attempt the wafer is only cleaned before the tape is applied, cleaning again right before starting the etch might give improvements. If under etching remains a major problem it might be possible to use a photoresist mask, however this introduces new challenges.

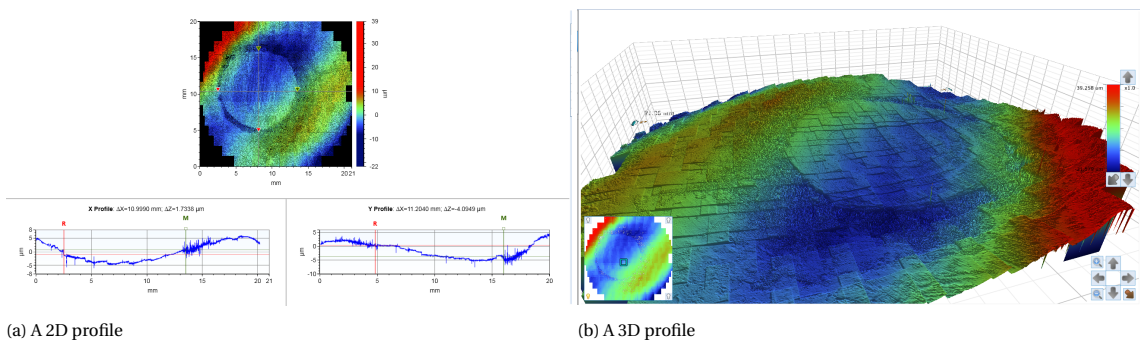


Figure E.18: Surface profiles of the 30 wt% KOH etched wafer, etching time: 3h

One more test is done using a hot KOH etch bath of 60°C. This higher temperature is chosen since it reduces the etch time and this might be beneficial to reduce under etching. Before applying the Kapton<sup>®</sup> tape the wafer is ultrasonic cleaned in acetone and cleaned in the oxygen cleaner. After applying the tape the masked wafer is again cleaned in the oxygen cleaner. Then the 30 wt% KOH etch at 60°C is performed for 12min, the results are in figure E.19. Again under etching of the mask occurred, this was visible during

the etching and it is visible in the surface profile as well. The circle that can be seen is etched due to an imperfection in the wafer surface. As said before a knife is used to cut out the mask, this damages the wafer. This groove is attacked by the etchant and is therefore visible, unfortunately there is no sign of a pocket being etched. This concludes that wet-etching a well defined pocket in a silicon wafer is a hard task when not all facilities are available. In a cleanroom all the chemicals and devices are available but this comes at high costs as stated before.

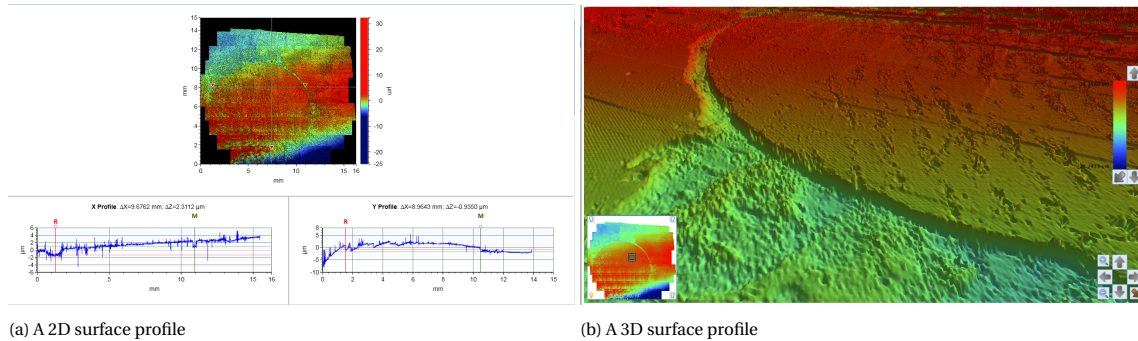


Figure E.19: Surface profiles of the 30 wt% KOH etched wafer, etching time: 12 min, temperature:60 °C

## E.5. Surface waviness

Now it is clear that shallow pockets can be made in Topas<sup>®</sup>, the next step is to inspect the waviness across the bearing surface. In an ideal case the air bearing is designed to function at a nominal fly-height of 10µm. This means that the bearing- and counter surface must be almost perfectly flat or have a perfect fit. The sensitivity of the flatness of the bearing’s characteristics must be determined in a final design model. In this section the flatness of the Topas<sup>®</sup> sheets is mapped. Some methods to improve the flatness are proposed and tested on test pieces.

### E.5.1. Topas<sup>®</sup> sheets

The Topas<sup>®</sup> sheets have a size of: 190 × 150mm<sup>2</sup>, the flatness of half a sheet is measured using the white light interferometer, see figure E.20. The measurement is corrected for tilt to get a clear picture of the waviness over the surface. The Topas<sup>®</sup> sheets are produced by melting small pellets of material and put it in a mould. The small bend in the sheet is probably caused by the non-linear cool down process of the mould. When a bearing with a diameter of 50 mm is desired, a flat 'sweet-spot' in the sheet might be available. A closer look is taken at the centre part of the figure E.20 sheet, a circular shape is cut-out, see figure E.21.

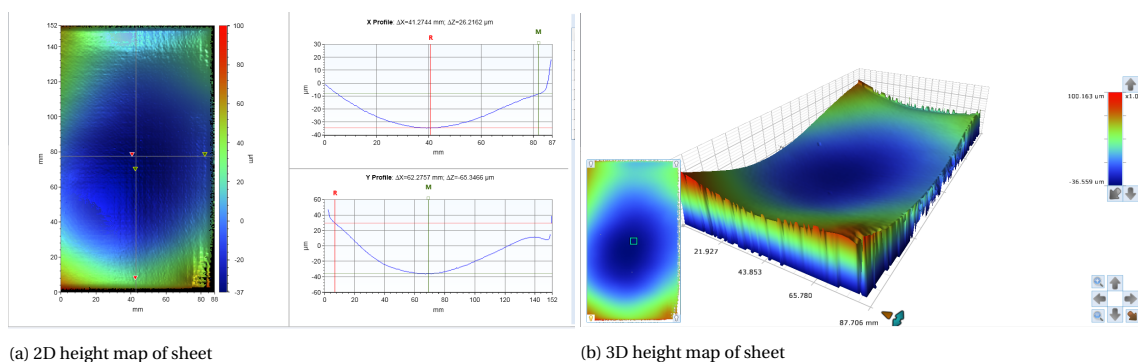


Figure E.20: Flatness of Topas<sup>®</sup> sheets

The part of the sheet with the two cut-outs is the flattest part found. From figure E.21 it can be noticed that the disk has a concave surface profile with a peak to peak flatness of around 13µm. This is unfortunately too much in an bearing design so a solution has to be found. There are three options to solve this problem:

- Reduce the bearing area

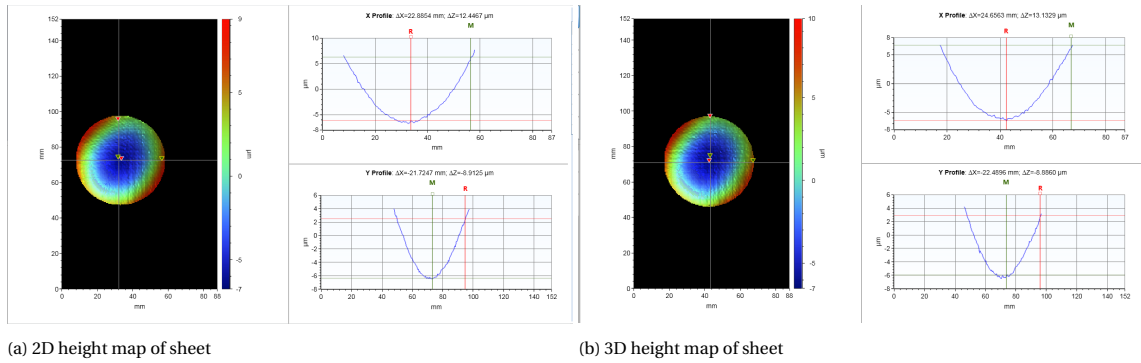


Figure E.21: Flatness of 50mm diameter disk cut-outs

- Flatten the Topas<sup>®</sup> bearing surface
- Find a counter surface with an exact opposite surface topology

### E.5.2. Reduce bearing area

It is more facile to obtain a flat surface when a smaller bearing diameter is used, this is the first and easiest option. However, decreasing the bearing's surface area, limits the load capacity and makes it harder to implement other bearing features due to scaling. So this first options might be used but the other options are investigated first.

### E.5.3. Flatten the Topas<sup>®</sup> bearing surface

The second option is to remove the waviness or minimising it, to reach an acceptable value. This can be done by: deforming the surface or by material removal. Permanent deformation of Topas<sup>®</sup> is done by heating the material to the glass transition temperature ( $T_g$ ) and then apply it on a flat counter surface. This process is called 'hot embossing' and is a common method to create microfluidic devices in Topas<sup>®</sup> [23]. In hot embossing a shape, for instance a microchannel is transferred from a mold to the Topas<sup>®</sup> surface. The main parameters to influence this process are: temperature and pressure. In this case there is no transfer of micro size features but only the application of a flat counter surface, for which a silicon wafer is used.

A circular shaped Topas<sup>®</sup> disk with a diameter of 50mm is aligned and sandwiched between two silicon wafers. This 'sandwich' is placed in a chemical oven and heated at the glass transition temperature for 30 min. The door of the switched off oven remained closed overnight to have a very slow cool-down process, bypassing steep temperature gradients. In this initial test no extra pressure is applied. Before the sample is treated in the oven it has a similar concave surface topology as the sample in figure E.21. After treatment in the oven the surface topology is depicted in figure E.22.

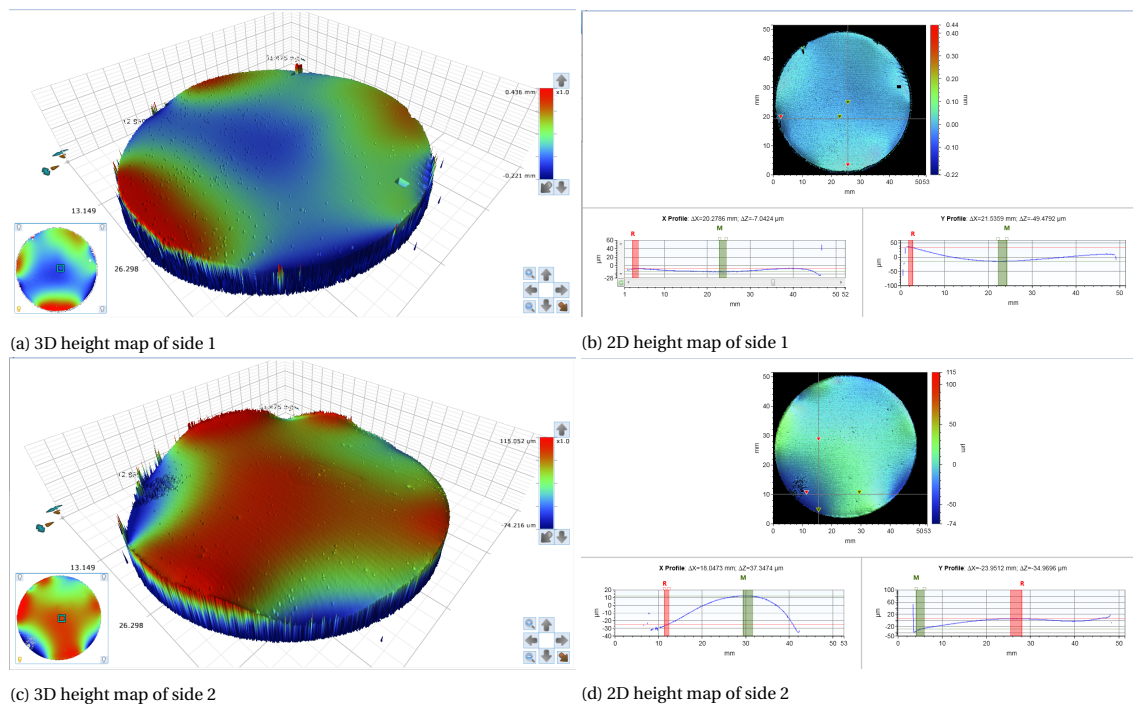


Figure E.22: Surface topology of a Topas<sup>®</sup> disk after 30 min at  $T = T_g$

From figure E.22 it can be seen immediately that the surface is deformed. The prediction was that the Topas<sup>®</sup> disk would 'copy' the 'perfectly' flat wafer surface, unfortunately something else happened. It can be seen that the surface is heavily deformed, with a large waviness up to  $50\mu\text{m}$ . This could be caused by a slight bending of the silicon wafer and thermal effects. It is likely that the surface got deformed by non-linear cooling of the wafer and sample and a lack of pressure.

Heat deformation of the surface to eliminate the waviness did not give the desired results, therefore other methods that are based on material removal, are investigated. Several machining methods exist that are used to get the desired surface finish of a work piece. The following machining methods are discussed: lapping, polishing and grinding.

With lapping a flat surface is made by making mechanical contact with a rotating plate. An abrasive paste is applied between the work piece and rotating plate [30], different materials can be lapped including polymers. Sub-micron flatness can be achieved over large surface areas while maintaining nanometre scale roughness. Lapping is in fact the same as polishing but then with the aid of an extremely flat counter surface. Unfortunately the TU Delft does not have such a machine and outsourcing comes at costs and inflexibility.

At the department of materials science a polishing lab is available, this facility is used to prepare metal samples for microscopic examination. In [21] an attempt was made to flatten the surface of a stainless steel bearing, using this same facility. It is possible to obtain a very low roughness, giving a mirror like surface finish. However, the waviness is determined by the flatness of the counter surface and an evenly distributed normal pressure during polishing. These last two conditions are not the case when using the hand polishing disks in the lab facility. It is decided not to use the facilities in the polishing lab but to build a simple test set-up. Instead of a compliant polishing disk a silicon wafer is used as a counter surface, the wafer is placed on a flat stone table. Then a polishing paste with abrasive diamond particles ( $d = 1\mu\text{m}$ ) is put between the Topas<sup>®</sup> disk and the silicon wafer, see figure E.23a.

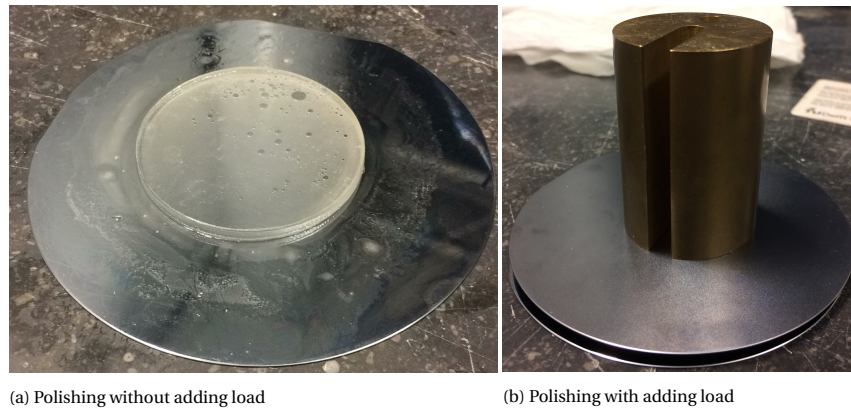


Figure E.23: Polishing of a Topas<sup>®</sup> disc using a silicon wafer as counter-surface

Now the disc is manually displaced along the wafer while floating on a film of polishing paste. It is tried to apply a uniform normal pressure during polishing. After a while the disc adheres at some points to the silicon wafer. This happens when at one point the load increases causing the disc to bend a little. The highest displacement, as a result of bending is at the centre of the disc, this results in more material removal. This gives the concave shaped profile in figure E.23 after the polishing is done. It can be seen that this polishing made the flatness only worse. Another test is done by applying a weight to distribute the normal force more evenly. Then the second wafer is moved with an in-plane motion, see figure E.23b. This method distributes the normal force more evenly but still causes bending of a non-flat sample. This causes non-uniform material removal resulting in a concave surface profile, see figure E.25.

It can be concluded that the Topas<sup>®</sup> disc deforms during the polishing resulting in a parabolic surface profile. Now the Topas<sup>®</sup> disc is connected to a structural layer to improve the bending stiffness of the sample.

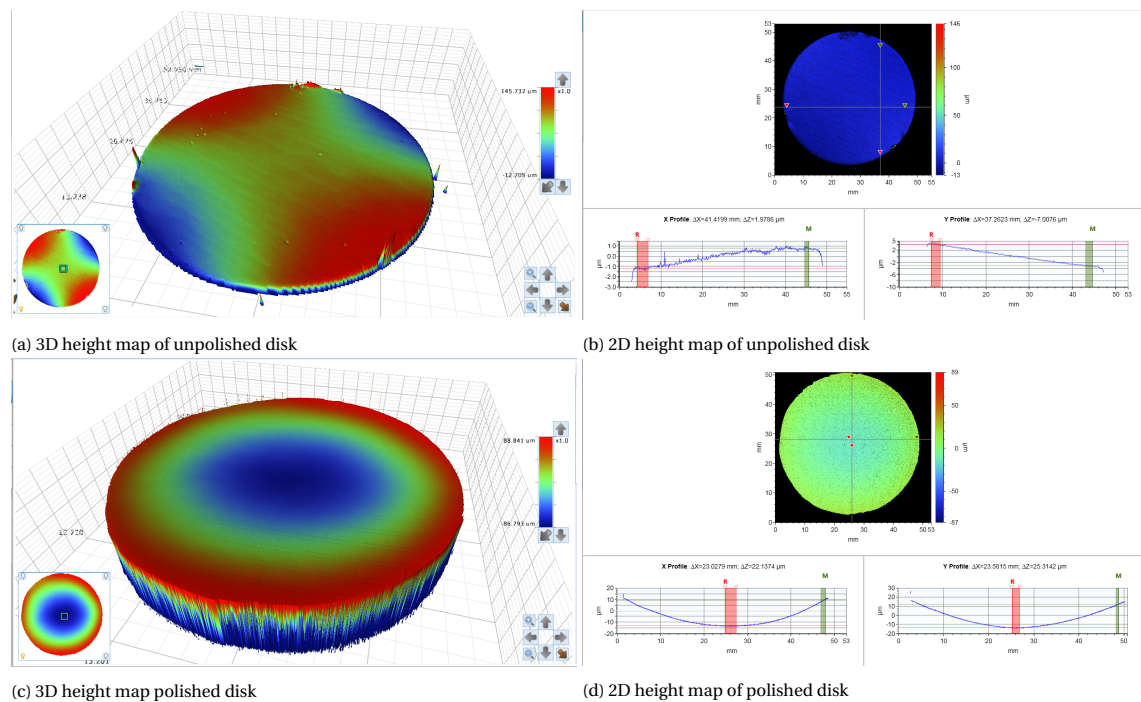


Figure E.24: Polishing of Topas<sup>®</sup> disc with  $d = 1 \mu\text{m}$  abrasive particles



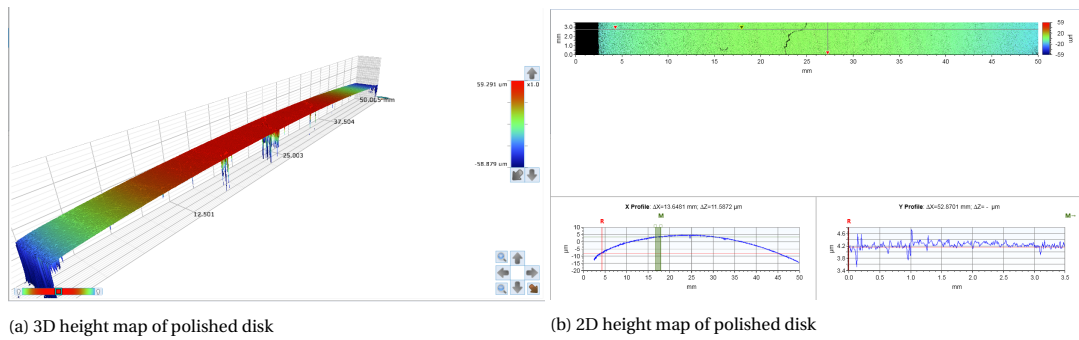


Figure E.25: Polishing of a Topas<sup>®</sup> disc with constant normal load  $W_n = 0.5\text{ kg}$

If the Topas<sup>®</sup> disk is only bended and if it has a very uniform thickness, polishing might be unnecessary. Connecting the Topas<sup>®</sup> disk with a uniform layer of glue to a flat basis might be good enough. If the Topas<sup>®</sup> surface shows a waviness after this structural adhesion step, a polishing step can always be carried out.

Very recently a grinding machine is purchased by the faculty machine shop, it is able to flatten metals and ceramics. A work piece has to be clamped on a magnetic rotating table, therefore only magnetic materials can be processed. First steel disks with a diameter of 50 mm are milled on a lathe. Then they are flattened on both sides with the grinding machine giving a peak to peak flatness of around 1 μm, see figure E.26. The ground surface shows a grooved pattern of high frequent peaks with an amplitude of around one micron.

This grounded steel disk has to be connected to the Topas<sup>®</sup> disk by means of an adhesive layer. Topas<sup>®</sup> is a low surface energy plastic, meaning that it is difficult to glue. The glue must have a uniform film thickness and must be able to withstand the high temperatures during the plasma etching process that is performed afterwards. For these reasons the: '3M DP8805NS low odour acrylic adhesive [3]' is used. It can withstand temperatures up to 150 °C and contains glass beads to control the bond line thickness. The only uncertainty is whether it will bond to Topas<sup>®</sup> since it is not specifically designed for low surface energy materials. However, according to [22], the surface energy can be increased by treating the sample with an oxygen plasma. This is the same process as used in etching the sample but with shorter exposing time and without a mask.

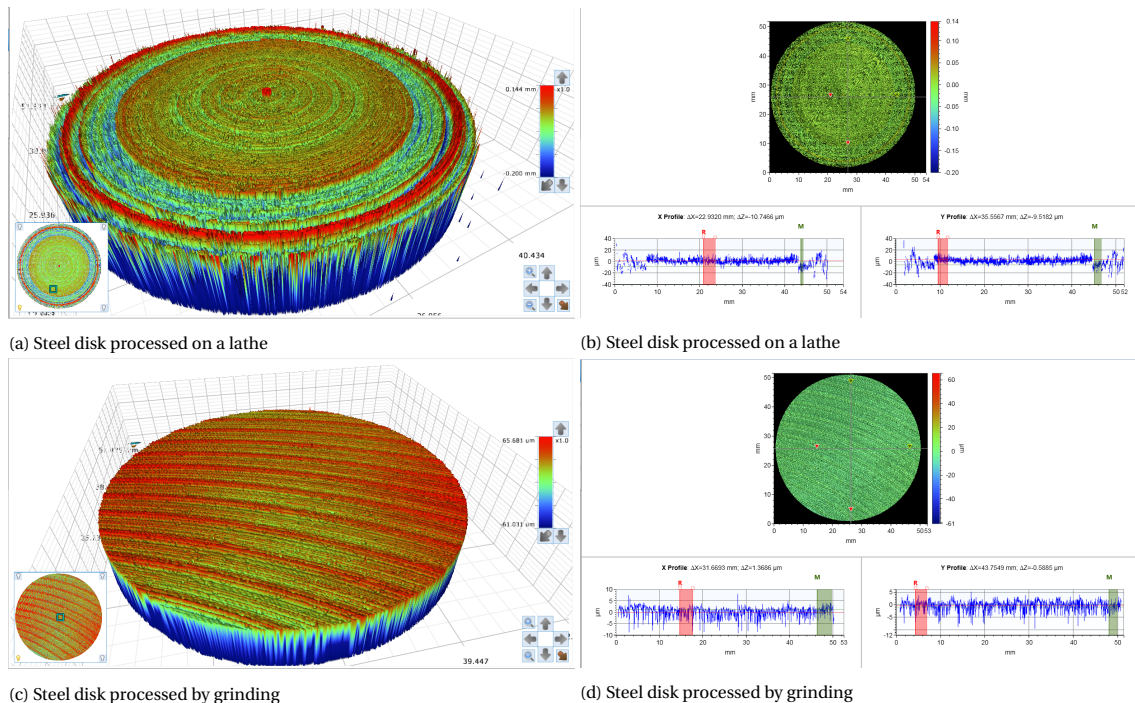


Figure E.26: Milling and grinding of a steel disk

During curing of the glue layer a constant uniform pressure is applied by using a press. Application of

pressure eliminates most of the trapped air bubbles in the glue layer. After glueing, the Topas top layer is milled to obtain a diameter of 50 mm. This milling introduces micro-cracks that are growing towards the centre as a result of residual stress in the glue layer. The cracks are subsurface meaning they do not influence the final surface topology after pocket plasma etching. The Steel-Topas configuration is depicted in figure E.27. The glue seems to have a good adhesion to both surfaces without any delamination. Interferometer inspection shows that this glued Topas top layer still has an unacceptable waviness, this requires further steps.

First the the flat wafer polishing method in figure E.23 is repeated. Bending of the Topas top layer is constraint by the adhesive layer. It is expected to have a more uniform material removal compared to the unconstrained case. Multiple displacement patterns like: circles, 8-figures and straight lines are tried using different normal loads. After a while the Topas tends to stick to the silicon, this is caused by a vacuum between the concave Topas surface and flat silicon surface. Despite the use of different procedures there is no success in flattening the surface using this method. Professional 'hand' lapping plates have a cross hatched or spiral grooved surface pattern. The cutting edges of these grooves enhance material removal and drain the surplus of diamond paste and Topas particles. The absence of these grooves, incorrect diamond paste and non-uniform normal force all contribute to an non flat surface.



Figure E.27: Steel-Topas configuration with adhesive layer

#### **E.5.4. Find a counter surface with an exact opposite surface topology**

For proving the concept of a low stiffness air bearing it is sufficient to limit displacement to out-of-plane motion only. Finding a counter surface that fits the bearing surface precisely, is only possible when the surfaces are formed by each other. There are two options: material removal by using abrasive particles or by hot-embossing with a different polymer. This second polymer must have a lower glass transition temperature than Topas to prevent bonding.

##### **Material removal method**

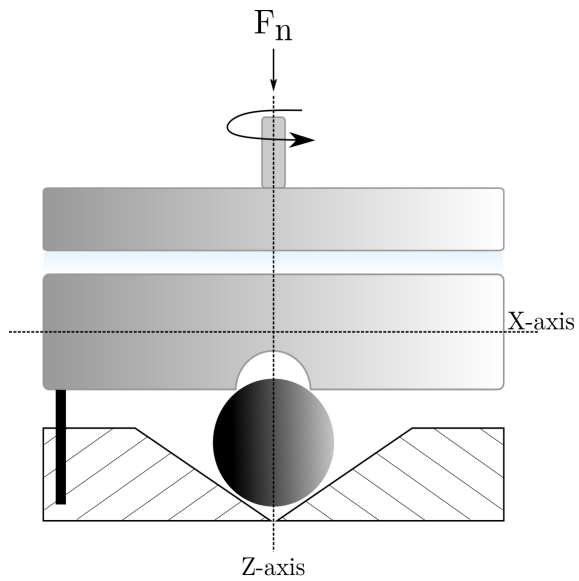
In this method two surfaces are placed at each other with an abrasive film in between, see figure E.28. One of the surfaces is slowly rotated by using a milling machine. It is impossible to get the two planes perfectly parallel. For this reason one of the discs is allowed to have some degrees of freedom to achieve perfect alignment during polishing. This ensures that only a minimum of material has to be removed, reducing processing time.

The stationary surface is placed on a spherical bullet to allow roll and pitch motions around the in-plane  $x$  and  $y$  axes. In-plane displacements are also constrained by the bullet, the out of plane displacement is constrained by the compressive normal force of the counter surface. This ball joint still allows rotations around the  $z$ -axis, a pin is placed to constrain this rotation.

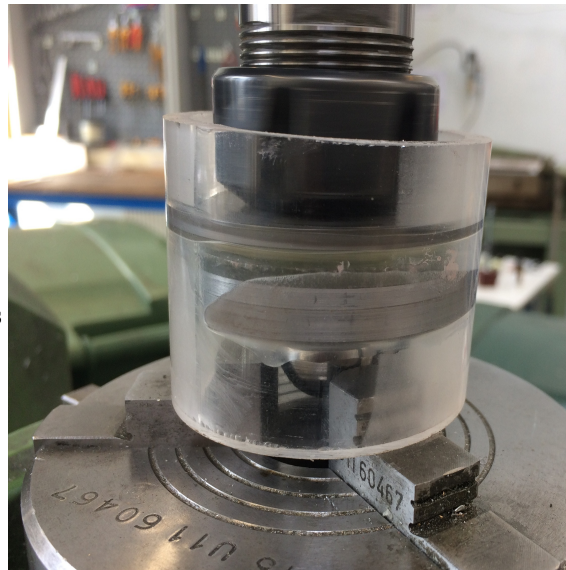
The two disks are made of a steel base that is adhered with glue to the Topas sheet material. Then the upper disk is rotated, first with a rather viscous polishing solution and in later experiments with different kind of 'more viscous' lapping paste. One starts with an abrasive solution that has large grain size to have a higher material removal rate. To get a smooth surface finish the final step is done with a small grain size solution. The normal force is controlled by a weight at the mill's lever arm, this ensures a constant pressure between

the surfaces.

After turning on the mill it is noticed that the ball joint has the desired effect. This is shown by a small tip-tilt motion that compensates the parallel misalignment of the two surfaces. After a few minutes of polishing the surfaces are inspected.



(a) Graphical representation of automated polishing set-up



(b) Automated polishing set-up

Figure E.28: Bearing and countersurface polishing using an abrasive film



# F

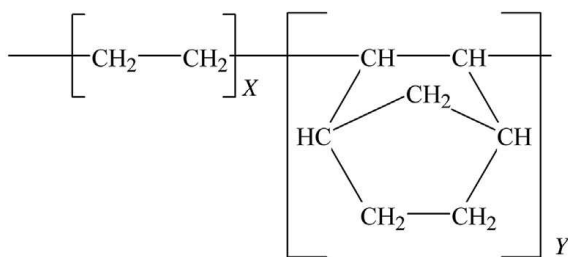
## Topas

Topas<sup>®</sup> is a trade name for cyclic olefin copolymers (COC), a relatively new class of polymers. It is used in packaging, optics and medical devices, some properties are:

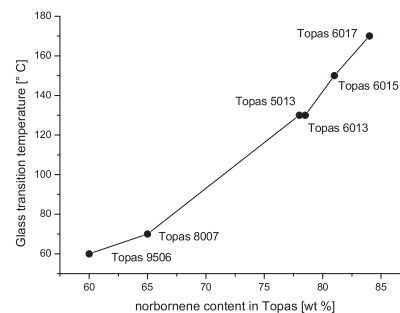
- High transparency
- Extremely low water absorption
- Good chemical resistance
- High rigidity, strength and hardness
- Variable heat deflection temperature up to 170°C

Topas<sup>®</sup> COC is an amorphous poly-olefin made by a chain copolymerisation process of ethylene ( $C_2H_4$ ) and norbornene ( $C_7H_{10}$ ) in varying ratios, see figure E.1a [31]. In the chemical structure of COC the ethylene part can be recognised at the X and the norbornene part at Y in figure E.1a.

The ratio of norbornene and ethylene determines the grade of the Topas. The Topas product nomenclature contains a four digit number. The first two digits indicate the viscosity number and last two digits describe the heat deflection temperature ( $HDT$ ) or glass transition temperature ( $T_g$ ). Higher grades have a higher temperature resistance as can be seen in figure E.1b.



(a) Chemical structure of COC [31]



(b) Heat resistance as function of norbornene percentage [26]

Figure E.1: Topas<sup>®</sup> COC properties

Since Topas is an amorphous thermoplastic the shear modulus ( $G$ ) is a function of temperature [2], see figure E.2. This also means that the material is suitable for fabrication methods like injection moulding, extrusion and hot-embossing. After processing, Topas is known for its high dimensional stability. In figure E.2 it can be seen that when the temperature exceeds the glass transition point, the structural strength of the material starts to decay rapidly.

Topas is very resistant to acids and bases but can be attacked by non-polar solvents such as toluene and sec-butyl-benzene [2]. Like all olefins, Topas has a very low surface energy. This means a hydrophobic surface

with a poor surface wettability making it hard to glue. Oxygen plasma treatment can increase the surface energy by implementation of polar functional groups [22]. Oxygen plasma treatment is also suitable to dry-etch polymers including Topas [36].

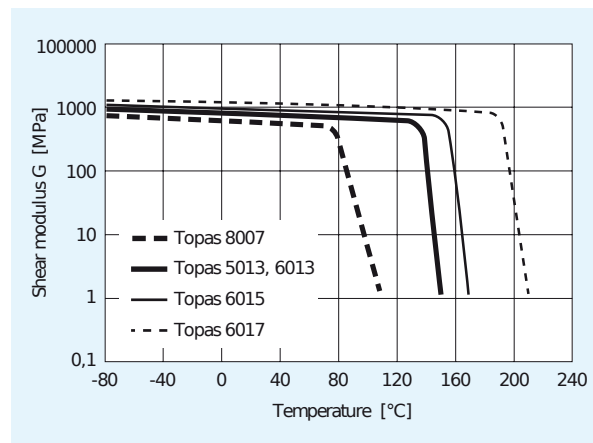


Figure E2: Shear modulus as function of temperature for different Topas grades [2]

# G

## Metrology specifications and settings

The measurement set-up has a number of different hardware and software elements. The specific settings of the sensors and data acquisition is summed in this appendix.

The capacitive sensors from microsense are PME property and consist of a probe and a gage with adjustable jumper settings. The gage processes the sensor signal and provides an analog voltage signal which can be fed into the data acquisition for automated and more precise measurements. To measure the supply- and vacuum pressures, a T-piece is placed before the restrictions and a MPX5700 series pressure sensor is placed. This sensor gets a supply voltage from the DAQ and returns a voltage signal that is proportional with absolute or differential pressure, see figure G.2 for linearity.

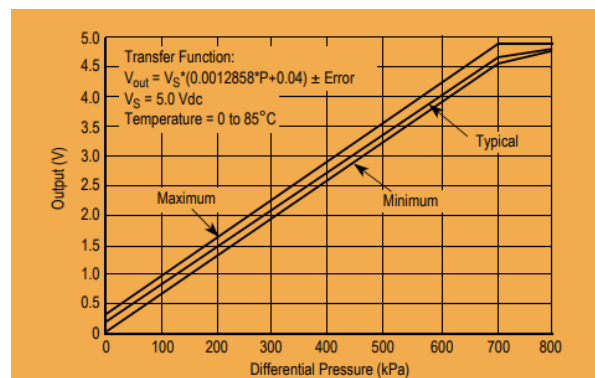
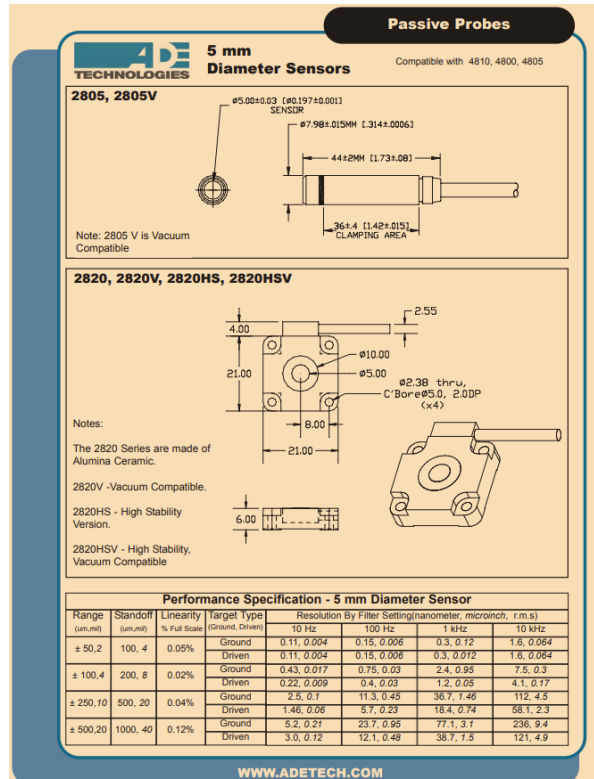
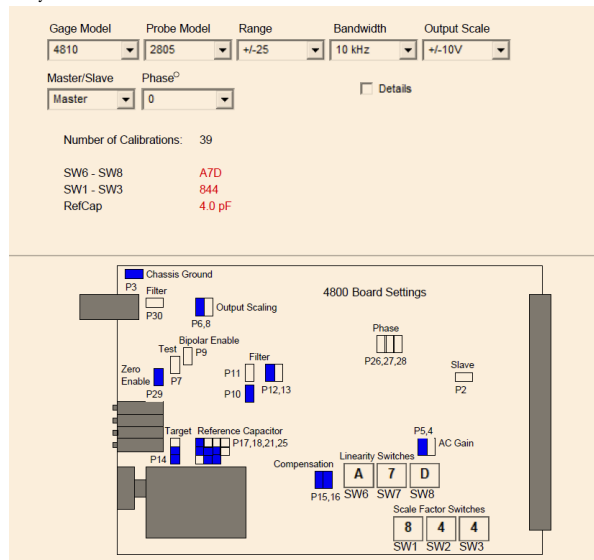


Figure G.2: The MPX5700 series pressure sensor calibration data provided by NXP manufacturer.

A data acquisition system from National Instruments (USB-2611) is used to feed all the signal data to the laptop. This device has a high sampling rate of 50 kS/s, when a total of five channels are used. Labview software is used to read all the data provided by the DAQ and to store it with the correct time stamp. The same labview data file is used to simultaneously operate the supply pressure valve by feeding a periodic saw-tooth shaped voltage signal.



(a) The capacitive probe specifications by microsense manufacturer



(b) The gage model jumper settings for a range of: 50µm and a BW of 10kHz. Note that the slave and master jumper settings should be based on the number of probes that measure the same target to minimise interference.



### Bus-Powered M Series Multifunction DAQ for USB — 16-Bit, up to 400 kS/s, up to 32 Analog Inputs, Isolation

#### NI USB-6210, NI USB-6211, NI USB-6212, NI USB-6215, NI USB-6216, NI USB-6218

- Up to 32 analog inputs at 16 bits, up to 400 kS/s (200 kS/s scan rate)
- Up to 2 analog outputs at 16 bits
- Up to 32 TTL/CMOS digital I/O lines
- Two 32-bit, 60 MHz counter/timers
- Digital triggering
- NI-FPGA 2 and NI-MCAL calibration technology for improved measurement accuracy
- NI signal streaming for 4 high-speed data streams on USB
- Bus-powered
- Available with CAT I isolation
- 1-year warranty
- Additional warranty and calibration services available

#### Operating Systems

- Windows Vista (32- and 64-bit)/XP/2000

#### Recommended Software

- LabVIEW
- LabVIEW SignalExpress
- LabWindows/CVI
- Measurement Studio

#### Other Compatible Software

- Cf, Visual Basic .NET
- ANSI C/C++

#### Measurement Services Software (included)

- NI-DAQmx driver software
- Measurement & Automation Explorer configuration utility
- LabVIEW SignalExpress LE



Family	Bus	Analog Inputs	Resolution (bits)	Max Rate (S/s)	Analog Outputs	Analog Input Resolution (bits)	Max Rate (S/s)	Range (V)	Digital I/O	32-Bit Counter	Isolation
USB-6210	USB	16	16	250 kS/s	0	16	250 k	+10	4 DIO DQ	2	—
USB-6211	USB	16	16	250 kS/s	2	16	250 k	+10	4 DIO DQ	2	—
USB-6212	USB	16	16	400 kS/s	2	16	250 k	+10	32 DIO	2	—
USB-6215	USB	16	16	200 kS/s	2	16	250 k	+10	4 DIO DQ	2	80V CAT I
USB-6216	USB	16	16	400 kS/s	2	16	250 k	+10	32 DIO	2	80V CAT I
USB-6218	USB	32	16	250 kS/s	2	16	250 k	+10	8 DIO DQ	2	80V CAT I

Table 1. NI USB-621x Selection Guide

Figure G.3: Overview from the NI about the DAQ2611

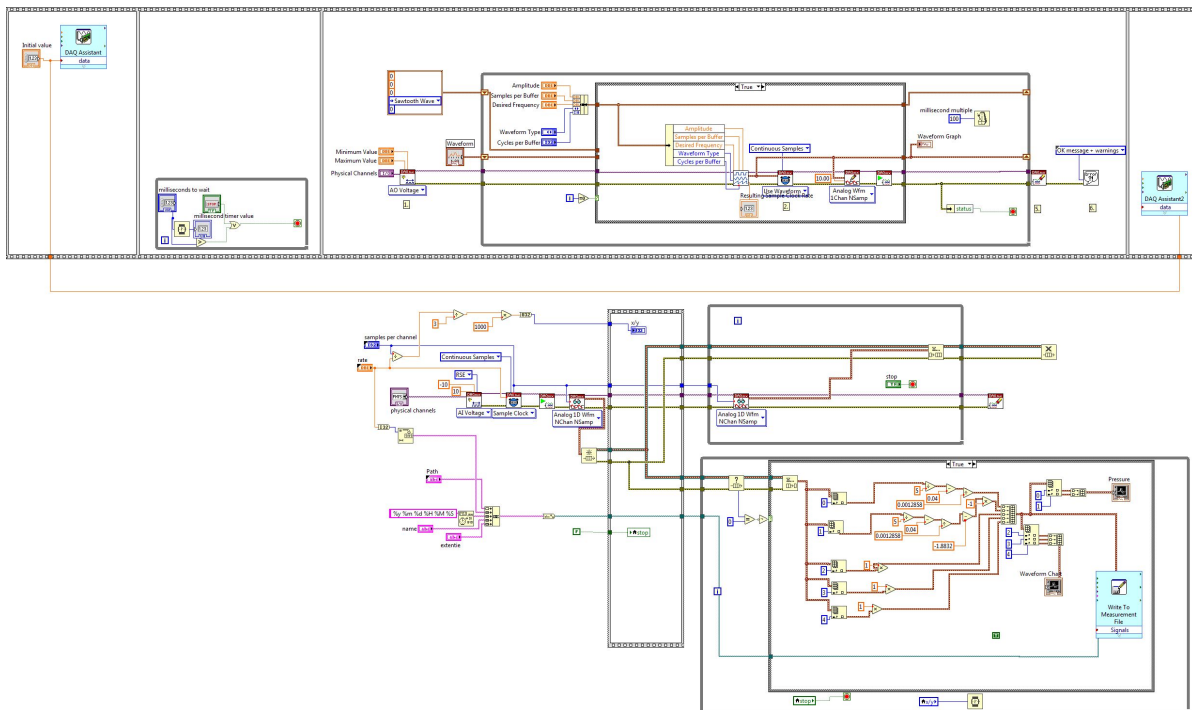


Figure G.4: Labview code to actuate the valve and to harvest all sensor data



# Bibliography

- [1] Technical data sheet. 49(0):3–4, 1805.
- [2] Topas Cyclic Olefin Copolymer Brochure. [www.topas.com](http://www.topas.com), 2006. URL [www.topas.com](http://www.topas.com).
- [3] 3M Industrial Adhesives and Tapes Division. 3M Scotch-Weld Low Odour Acrylic Adhesives DP8805NS. Technical report, 2017.
- [4] Gorka Aguirre, Farid Al-Bender, and Hendrik Van Brussel. A multiphysics coupled model for active aerostatic thrust bearings. *IEEE/ASME International Conference on Advanced Intelligent Mechatronics, AIM*, pages 710–715, 2008. doi: 10.1109/AIM.2008.4601747.
- [5] Gorka Aguirre, Farid Al-Bender, and Hendrik Van Brussel. A multiphysics model for optimizing the design of active aerostatic thrust bearings. *Precision Engineering*, 34(3):507–515, 2010. ISSN 01416359. doi: 10.1016/j.precisioneng.2010.01.004. URL <http://dx.doi.org/10.1016/j.precisioneng.2010.01.004>.
- [6] F. Al-Bender. *Contributions to the design theory of circular centrally fed aerostatic bearings*. Phd thesis, Katholieke Universiteit Leuven, 1992.
- [7] F. Al-Bender and H. Van Brussel. Tilt characteristics of circular centrally fed aerostatic bearings. *Tribology International*, 25(3):189–197, 1992. ISSN 0301679X. doi: 10.1016/0301-679X(92)90048-R.
- [8] Farid Al-Bender. On the modelling of the dynamic characteristics of aerostatic bearing films: From stability analysis to active compensation. *Precision Engineering*, 33(2):117–126, 2009. ISSN 01416359. doi: 10.1016/j.precisioneng.2008.06.003.
- [9] A. Andrisano and A. Maggiore. Theoretical and experimental analysis of an externally pressurized porous gas thrust bearing. *Tribology International*, 11(5):285–288, 1978. ISSN 0301679X. doi: 10.1016/0301-679X(78)90059-2.
- [10] Mark Bachman. RCA-2 Silicon Wafer Cleaning. *UCI Integrated Nanosystems Research Facility*, 2:1–3, 2002.
- [11] G. Belforte, T. Raparelli, V. Viktorov, and A. Trivella. Discharge coefficients of orifice-type restrictor for aerostatic bearings. *Tribology International*, 40(3):512–521, 2007. ISSN 0301679X. doi: 10.1016/j.triboint.2006.05.003.
- [12] Michael R. Bryant, Steven A. Velinsky, Norman H. Beachley, and Frank J. Fronczak. A Design Methodology for Obtaining Infinite Stiffness in an Aerostatic Thrust Bearing. *Journal of Mechanisms Transmissions and Automation in Design*, 1986. ISSN 07380666. doi: 10.1115/1.3258753.
- [13] S. H. Chang, C. W. Chan, and Y. R. Jeng. Numerical analysis of discharge coefficients in aerostatic bearings with orifice-type restrictors. *Tribology International*, 90:157–163, 2015. ISSN 0301679X. doi: 10.1016/j.triboint.2015.04.030.
- [14] Ming-Fei CHEN and Yu-Ting LIN. Dynamic Analysis of the X-shaped Groove Aerostatic Bearings with Disk-Spring Compensator. *JSME International Journal Series C*, 2004. ISSN 1344-7653. doi: 10.1299/jsmec.45.492.
- [15] Xue Dong Chen, Jin Cheng Zhu, and Han Chen. Dynamic characteristics of ultra-precision aerostatic bearings. *Advances in Manufacturing*, 1(1):82–86, 2013. ISSN 21953597. doi: 10.1007/s40436-013-0013-6.
- [16] R. Dupont. Robust rotor dynamics for high-speed air bearing spindles. *Precision Engineering*, 40:7–13, 2015. ISSN 01416359. doi: 10.1016/j.precisioneng.2014.12.008.

- [17] Fridman. RCA-1 Silicon Wafer Cleaning. *Film*, 2:2–4, 1960.
- [18] Qiang Gao, Wanqun Chen, Lihua Lu, Dehong Huo, and Kai Cheng. Aerostatic bearings design and analysis with the application to precision engineering: State-of-the-art and future perspectives. *Tribology International*, 135(February):1–17, 2019. ISSN 0301679X. doi: 10.1016/j.triboint.2019.02.020. URL <https://doi.org/10.1016/j.triboint.2019.02.020>.
- [19] Bernard J Hamrock. Fundamentals Fluid Film Lubrication of. *Nasa Publication 1255*, pages 301–318, 1991.
- [20] P. L. Holster and J. A H Jacobs. Theoretical analysis and experimental verification on the static properties of externally pressurized air-bearing pads with load compensation. *Tribology International*, 20(5):276–289, 1987. ISSN 0301679X. doi: 10.1016/0301-679X(87)90028-4.
- [21] R. P. Hoogeboom. Design and experimental validation of low stiffness aerostatic thrust bearings. Technical report, Delft University of Technology, 2016.
- [22] Shug June Hwang, Ming Chun Tseng, Jr Ren Shu, and Hsin Her Yu. Surface modification of cyclic olefin copolymer substrate by oxygen plasma treatment. *Surface and Coatings Technology*, 202(15):3669–3674, 2008. ISSN 02578972. doi: 10.1016/j.surfcoat.2008.01.016.
- [23] R K Jena, C Y Yue, Y C Lam, P S Tang, and A Gupta. Comparison of different molds (epoxy, polymer and silicon) for microfabrication by hot embossing technique. *Sensors and Actuators B*, 163:233–241, 2012. doi: 10.1016/j.snb.2012.01.043. URL [https://ac.els-cdn.com/S0925400512000664/1-s2.0-S0925400512000664-main.pdf?{}\\_tid=5415c2d8-3da4-4293-a7b2-843444762d90{&}acdnat=1523278905{ }3f1c7f2d58875f626cc7d9a91ee5725d](https://ac.els-cdn.com/S0925400512000664/1-s2.0-S0925400512000664-main.pdf?{}_tid=5415c2d8-3da4-4293-a7b2-843444762d90{&}acdnat=1523278905{ }3f1c7f2d58875f626cc7d9a91ee5725d).
- [24] Boran Jia. Evaluation of a Fast Prototyping Method: Thermal Damage in Pulsed Laser Micromachining. Technical report, 2016.
- [25] D A Jobson. On the flow of a compressible fluid through orifices. *Proceedings of the Institution of Mechanical Engineers*, 169(1):767–776, 1955. ISSN 0020-3483. doi: 10.1243/PIME\_PROC\_1955\_169\_077\_02. URL [http://pme.sagepub.com/lookup/doi/10.1243/PIME{}\\_PROC{}\\_1955{}\\_169{}\\_077{}\\_02](http://pme.sagepub.com/lookup/doi/10.1243/PIME{}_PROC{}_1955{}_169{}_077{}_02).
- [26] Dan M Johansen. Investigation of Topas ® for use in optical components. Technical report, Technical University of Denmark, 2005.
- [27] Albert Kingsbury. EXPERIMENTS WITH AN AIR-LUBRICATED JOURNAL. *Journal of the American Society for Naval Engineers*, 1897. ISSN 15593584. doi: 10.1111/j.1559-3584.1897.tb05692.x.
- [28] Technical Library. Chemicals - Technical Library Syringe Needle Gauge Chart, 2016. URL <https://www.sigmaldrich.com/chemistry/stockroom-reagents/learning-center/technical-library/needle-gauge-chart.html>.
- [29] N. Maamari, A. Krebs, S. Weikert, and K. Wegener. Centrally fed orifice based active aerostatic bearing with quasi-infinite static stiffness and high servo compliance. *Tribology International*, 129(May 2018): 297–313, 2019. ISSN 0301679X. doi: 10.1016/j.triboint.2018.08.024. URL <https://doi.org/10.1016/j.triboint.2018.08.024>.
- [30] Ioan D. Marinescu, Eckart Uhlmann, and Toshiro K. Doi. *Handbook of lapping and Polishing*. 2007. ISBN 1574446703. doi: 10.1201/9781420017632.
- [31] Laurence W. McKeen. Polyolefins and Acrylics. *The Effect of Temperature and other Factors on Plastics and Elastomers*, pages 341–370, 2014. ISSN 0717-6163. doi: 10.1016/B978-0-323-31016-1.00007-6. URL <http://linkinghub.elsevier.com/retrieve/pii/B9780323310161000076>.
- [32] Hajime Onda. Development of a unique, high precision linear motor integrated air slide table, and its application to laser beam writers. *Optical Review*, 1999. ISSN 13406000. doi: 10.1007/s10043-999-0088-2.
- [33] M. Park. Elastic orifices for gas bearings. *Final report. Washington DC: National Aeronautics and Space Administration (NASA)*, Aug(SP-5029), 1965.

- [34] M. J. D. Powell. A view of algorithms for optimization without derivatives. *Mathematics Today-Bulletin of the Institute of...*, 2007. ISSN 1361-2042.
- [35] Terenziano Raparelli, Vladimir Viktorov, Federico Colombo, and Luigi Lentini. Aerostatic thrust bearings active compensation: Critical review. *Precision Engineering*, 44:1–12, 2016. ISSN 01416359. doi: 10.1016/j.precisioneng.2015.11.002. URL <http://dx.doi.org/10.1016/j.precisioneng.2015.11.002>.
- [36] K. Rasmussen. Advanced dry etching studies for micro- and nano-systems. page 129, 2014. URL [http://orbit.dtu.dk/en/publications/advanced-dry-etching-studies-for-micro-and-nanosystems\(d79d6390-c330-4729-aa70-b2d3a0f87269\).html](http://orbit.dtu.dk/en/publications/advanced-dry-etching-studies-for-micro-and-nanosystems(d79d6390-c330-4729-aa70-b2d3a0f87269).html).
- [37] Osborne Reynolds. On the Theory of Lubrication and its Application. *Philosophical Transactions of Royal Society of London A*, 1886. ISSN 0261-0523. doi: 10.1098/rstl.1886.0005.
- [38] Seung Kook Ro, Soohyun Kim, Yoonkeun Kwak, and Chun Hong Park. A linear air bearing stage with active magnetic preloads for ultraprecise straight motion. *Precision Engineering*, 34(1):186–194, 2010. ISSN 01416359. doi: 10.1016/j.precisioneng.2009.06.010.
- [39] W.B. Rowe and G.T.F. Kilmister. A theoretical and experimental investigation of a self-compensating externally pressurised thrust bearing. *Proceedings of the 6th International Gas Bearing Symposium*, March(D1):1–13, 1974.
- [40] Robert Munnig Schmidt, Georg Schitter, Adrian Rankers, and Jan van Eijk. *The design of high performance mechatronics: High-tech functionality by multidisciplinary system integration: 2nd revised edition*. Los Press, 2014. ISBN 9781614993681. doi: 10.3233/978-1-61499-368-1-i.
- [41] Ismail A. Shah, Benjamin M.A. van der Wolf, Willem J.P. van Enkevort, and Elias Vlieg. Wet chemical etching of silicon {111}: Etch pit analysis by the Lichtfigur method. *Journal of Crystal Growth*, 311(5):1371–1377, 2009. ISSN 00220248. doi: 10.1016/j.jcrysgro.2008.12.021. URL <http://linkinghub.elsevier.com/retrieve/pii/S0022024808013778>.
- [42] A.H. Slocum. *Precision Machine Design*. Society of Manufacturing Engineers, 1992.
- [43] Jelle Snieder. Development of an Air-Based Contactless Transport Demonstrator. Technical Report September, Technical University Delft, 2017.
- [44] R. Snoeys and F. Al-Bender. Development of improved externally pressurized gas bearings. *KSME Journal*, 1(1):81–88, 1987. ISSN 1738494X. doi: 10.1007/BF02953383.
- [45] P. T. Stanev, F. Wardle, and J. Corbett. Investigation of grooved hybrid air bearing performance. *Proceedings of the Institution of Mechanical Engineers, Part K: Journal of Multi-body Dynamics*, 218(2):95–106, 2004. ISSN 14644193. doi: 10.1243/146441904323074558.
- [46] H. M. Talukder and T. B. Stowell. Pneumatic hammer in an externally pressurized orifice-compensated air journal bearing. *Tribology International*, 36(8):585–591, 2003. ISSN 0301679X. doi: 10.1016/S0301-679X(02)00247-5.
- [47] Amorn Thedsakhulwong and Warawoot Thowladda. Removal of carbon contamination on silicon wafer surfaces by microwave oxygen plasma. *Journal of Metals, ...*, 18(2):137–141, 2008. URL <http://www.material.chula.ac.th/Journal/v18-2-2/137-141THEDSAKHULWONG.pdf>.
- [48] A. Trivella, T. Raparelli, F. Colombo, V. Viktorov, and G. Belforte. Performance of Externally Pressurized Grooved Thrust Bearings. *Tribology Letters*, 37(3):553–562, 2009. ISSN 1023-8883. doi: 10.1007/s11249-009-9550-3.
- [49] Andrea Trivella, Guido Belforte, Vladimir Viktorov, Terenziano Raparelli, and Federico Colombo. Comparison between grooved and plane aerostatic thrust bearings: static performance. *Meccanica*, 46(3):547–555, 2010. ISSN 0025-6455. doi: 10.1007/s11012-010-9307-y.
- [50] Richard Turton. A new approach to nonchoking adiabatic compressible flow of an ideal gas in pipes with friction. *The chemical engineering Journal*, 30:159–160, 1984. ISSN 15253198. doi: 10.1089/ind.2013.0035.

- [51] Eizo Urata. A flow rate equation for subsonic Fanno flow. *Proceedings of the Institution of Mechanical Engineers, Part C: Journal of Mechanical Engineering Science*, 227(12):2724–2729, 2013. ISSN 09544062. doi: 10.1177/0954406213480295.
- [52] Anton van Beek. *Advanced engineering design, Lifetime performance and reliability*. TU Delft, 2009. ISBN 978-90-810406-1-7. URL [https://books.google.nl/books/about/AdvancedEngineeringDesign.html?id=NKGD0AAACAAJ&redir\\_esc=y](https://books.google.nl/books/about/AdvancedEngineeringDesign.html?id=NKGD0AAACAAJ&redir_esc=y).
- [53] J. van Rij, J. Wesselingh, R. A J van Ostayen, J. W. Spronck, R. H. Munnig Schmidt, and J. van Eijk. Planar wafer transport and positioning on an air film using a viscous traction principle. *Tribology International*, 42(11-12):1542–1549, 2009. ISSN 0301679X. doi: 10.1016/j.triboint.2009.03.013. URL <http://dx.doi.org/10.1016/j.triboint.2009.03.013>.
- [54] N Verbruggen. Air-based contactless positioning of thin substrates. Technical report, Delft University of Technology, 2017.
- [55] Frank White. *Fluid Mechanics*. Mcgraw-Hill Education, Boston, 2010. ISBN 0077422414. doi: 10.1111/j.1549-8719.2009.00016.x.Mechanobiology.
- [56] S. Yoshimoto, Y. Nakano, and T. Kakubari. Static characteristics of externally pressurized gas journal bearings with circular slot restrictors. *Tribology International*, 17(4):199–203, 1984. ISSN 0301679X. doi: 10.1016/0301-679X(84)90021-5.
- [57] S. Yoshimoto, J. Tamura, and T. Nakamura. Dynamic tilt characteristics of aerostatic rectangular double-pad thrust bearings with compound restrictors. *Tribology International*, 32(12):731–738, 1999. ISSN 0301679X. doi: 10.1016/S0301-679X(00)00004-9.
- [58] Mhia Zaglul, Takeshi Mizuno, Yuji Ishino, and Masaya Takasaki. Control Engineering Practice Active vibration isolation using negative stiffness and displacement cancellation controls : Comparison based on vibration isolation performance. *Control Engineering Practice*, 37:55–66, 2015. ISSN 0967-0661. doi: 10.1016/j.conengprac.2014.12.004. URL <http://dx.doi.org/10.1016/j.conengprac.2014.12.004>.